THE FLUID SHEAR STRESS ENVIRONMENT OF THE NORMAL AND CONGENITAL BICUSPID AORTIC VALVE AND THE IMPLICATIONS ON VALVE CALCIFICATION

A Dissertation
Presented to
the Academic Faculty

By

Choon Hwai Yap

In Partial Fulfillment
Of the Requirements for the Degree of
Doctor of Philosophy in Bioengineering

Department of Biomedical Engineering
Georgia Institute of Technology
December 2011

THE FLUID SHEAR STRESS ENVIRONMENT OF THE NORMAL AND CONGENITAL BICUSPID AORTIC VALVE AND THE IMPLICATIONS ON VALVE CALCIFICATION

Approved by:

Dr. Ajit P. Yoganathan, Advisor
Department of Biomedical Engineering
Georgia Institute of Technology

Dr. Rudolph L. Gleason Jr.
School of Mechanical Engineering
Georgia Institute of Technology

Dr. Don P. Giddens
Department of Biomedical engineering
Georgia Institute of Technology

Dr. Hanjoong Jo
School of Biomedical Engineering
Emory University

Dr. Ari Glezer
School of Mechanical Engineering
Georgia Institute of Technology

Dr W. Robert Taylor
Department of Medicine
Emory Unviersity

Date Approved: 12 August 2011

ACKNOWLEDGEMENTS

I would first like to thank my first uncle, Dr. Yap Leong Ping, for his words of wisdom, which prompted me to pursue a doctoral degree in the first place. He told me that if I go after money or power, I will always be frustrated, but if I pursue my true passion, then I will truly live. Even though I realized later that he missed out telling me how tough getting a Ph.D. might be, I sucked up those words and ended up living a dream for these graduate school years.

I wish to acknowledge my family, and the support they've given me to enable my thesis work. Dad's encouragements and support in all forms played a very essential role. He understood that I wanted to chase this passion, and jumped at the first moment when I suggested to him that I might want to do this, to offer his support. I dedicate this thesis to Mom, who passed away in 2002, and who used to keep telling me I should be a medical doctor. I bailed on that after watching gory movies of surgery in high school. But I guess still I ended up being a doctor of some kind, and I think she will still be happy with it. Thanks to my brother, Choon Hong, sister-in-law, Avril, and sister, Hui Zhong, who's presence always gave me comfort, and gave me strength; to my nephews Jared and Joshua, and niece Jane, who made my time every time I vacationed and visited home.

I wish to acknowledge my girlfriend, Fontaine, for sharing my life, and walking with me through good and tough times. Her presence gave me a peace and calm in the mind, and I could work for days at ends without feeling fatigue. She reminded me of the need to balance practicality and dream, which is most likely a good advice.

A big thank you to Dr Y, short for Dr Yoganathan, my advisor. He provided all the opportunities that I needed to complete a thesis and more, for which I am very grateful. I appreciated both his boot camp training in the lab, which toughened me and trained me to be a highly independent intellectual, and his holiday season invitations to his house if I didn't have anywhere to go. Further, the enigmatic philosophical advice from his alias, Dr. Boz, was always interesting and got me thinking. Thanks to my committee members, Dr. Giddens, Dr. Glezer, Dr. Gleason, Dr. Jo, and Dr. Taylor. Their critical inputs and willingness to spend time with me shaped my thesis over the past years. Special thanks to Dr. Glezer for insisting on the inclusion of sections 5.2.5 and 6.2.4 and 7.1.1.

Enablement of this thesis also came in the form of the fun-loving companionship from members of the Cardiovascular Fluid Mechanics Lab. They are truly great friends and colleagues. Thanks to L. Prasad Dasi for helping me swim through a mess of confusion in the initial years, and to Neelakantan Saikrishanan for generously contributing time to sharpen my work in the later years. Their in-depth intellectual inputs were critical to my work. Neelakantan also provided PIV data on the valve flow fields. Thanks to Kartik B. and Murali Padala for their technical exchanges which helped me establish myself in the lab. Thanks to Swetha Rathan for assisting in much of the biology work, and for the comradeship in these work. My sincere gratitude goes also to Shiva Arjunon, Erin Spinner, Chris haggerty, JP Rabbah, Maria Restrepo, Elaine Tang, Brandon Chaffins, Arvind Santhanakrishnan, Andrew Siefert, Jorge Jimenez, Reza Khiabani and Lauren Couch for being very supportive colleagues. Colly Mitchell, LaKeisha Wheaton, Gail Spatt, Cosetta Hill, Sandra Maffrey and Susan Camp, thank you

for assisting in the administrative tasks. To my friends in the neighboring labs, William Wan, Laura Hansen, Ruaya Wang, David Bark, Julia Raykin, Julia Henkels, and Michael Zaucha, thanks for being there, and for helping out during time of emergency supply shortages. Thanks to William Wan, David Bark, David Murphy, Peng Meng Kou, Julia Raykin, Ai Ping Hu, whose good company helped me vent out frustration, and to whom I can chat just about anything.

My gratitude also goes to the undergraduate assistants who worked with me and contributed to this thesis or aided in my doctoral training in being a mentor: Gowthami Tamilselvan, Katie Wallon, Samiya Hussain, Mike Weiler, Elizabeth Morris, Roy Rusly, Ramya Parthasarathy, and Erin Keller. In particular, Gowthami has assisted in many of the LDV experiments leading to this thesis. Her industriousness is commendable and very much appreciated.

I wish to acknowledge Holifield Farms, Covington, GA for donating porcine heart samples that enable this thesis work. This thesis work was also supported by National Heart, Lung and Blood Institute grant number: HL-07262, and kind donations by Tom and Shirley Gurley.

Most of all, thanks to God, who provided, walked me through tough times, and gave me his love.

TABLE OF CONTENTS

LIST OF TABLES

LIST OF FIGURES

LIST OF SYMBOLS AND ABBREVIATIONS

AV - Aortic Valve

BAV - Bicuspid Aortic Valve

LDA - Laser Doppler Anemometry

LDV - Laser Doppler Velocimetry

PIV - Particle Image Velocimetry

PMT - Photomultiplier box

RSA - Real Time Signal Analyzer

α - Geometric angle

α_L - Half angle of LDV laser beams

α_c -Taper angle of the cone in the cone and plate

D_e - initial beam diameter of LDV probe

d_f - Fringe spacing of LDV probe volume

d_m- Width of LDV probe volume

d_k - Kernel of power spectral density

δ - boundary layer thickness

E - LDV beam expansion ratio

ED - Ejection duration

f - Frequency of light beam

Φ - Power spectral density

HR – Heart rate

h_c - Gap between apex of cone and the plate

λ - Light wavelength

l - Characteristic length scale

l_m - Length of LDV probe volume

n - refractive index

P - Probability

Q - Volumetric flow rate

r_c - radial coordinate of cone and plate

r - radial coordinate

Re - Reynold's number

R - radius of channel

R_y - Auto-correlation function (interpolated)

R_r - Auto-correlation function (original)

ρ - Density

t - Time

τ - Shear stress

μ - Dynamic Viscosity

u_i - ith component velocity

V - velocity

V_f - LDV probe volume velocity

V_{PD} - Volume of the LDV probe volume

ν - Dynamic viscosity

ω_c - Angular velocity

ω_n - Fourier frequency

x_i - ith coordinate

SUMMARY

Calcific aortic valve disease is highly prevalent, especially in the elderly [1]. Every year, aortic valve disorders are associated with over 40,000 deaths [2] and 95,000 surgeries are performed on the aortic valve in the US. Majority of aortic calcification cases are termed idiopathic, indicating our lack of knowledge on the exact mechanism causing the disease. Our current knowledge on how to prevent or cure the disease is also limited. The current treatment for the disease is the replacement of the valve with prosthetic valves, which has limited durability, and is associated with many complications.

Thus far, ex vivo investigations have provided evidence that the aortic valve's biological response is very sensitive to mechanical forces, including fluid shear stresses [3-7]. Shear stresses were shown to be anti-inflammatory and oxidative as opposed to static culture [4], and adverse patterns of shear stresses can cause inflammatory responses to the valve [5], which is known to be a precursor to valve sclerosis and calcification. Further, it has been suggested that the localization of calcification nodules on the aortic surface of the valve leaflet is due to "disturbed fluid shear stress" on the aortic surface, and "undisturbed fluid shear stress" on the ventricular surface [8, 9]. All these have led to the hypothesis that adverse fluid shear stress environment play a role in leading to valve calcification.

The case of the congenital bicuspid aortic valve provides a good test bed for this hypothesis. The bicuspid valve is a geometric deformation in the valve where two of the three leaflets are fused together at birth and occurs in 1-2% of the population [10, 11].

Bicuspid valve patients suffer from drastically increased risk of aortic valve calcification [12, 13]. Since the drastic change in the bicuspid valve geometry may have drastically changed its mechanical environment, the bicuspid valve is a good case for investigating the hypothesis that mechanical forces influence the calcification disease process.

This thesis seeks to investigate this hypothesis. It seeks to first characterize the fluid shear stress mechanical environment of the aortic valve leaflets, both in the normal tricuspid aortic valve and the malformed bicuspid aortic valve. It also seeks to investigate the effects of various shear stress characteristics of these valves on the biological response of the aortic valve tissues.

Since aortic valve calcification is a major cause of mortality and morbidity, studies undertaken by this thesis in investigating the mechanical environment of the valve and the biological responses elicited by this environment is important. Further, there is insufficient data in the literature on shear stresses experienced by the aortic valve leaflet, and this lack of understanding of the aortic valve shear stress environment could be a bottleneck for further research work to completely understand the pathways to aortic valve calcification.

The specific aim 1 of this thesis, a method for performing experimental measurement of time-varying shear stress on aortic valve leaflets under physiologic flow conditions was first developed, based on the Laser Doppler Velocimetry technique, and was systematically validated. This method was then applied to both the aortic surface and the ventricular surface of the aortic valve, in specific aim 2, using suitable *in vitro* valve models and an *in vitro* pulsatile flow loop. It was found that the peak shear stress on the aortic surface was approximately 20 dyn/cm^2. Aortic surface shear stresses were elevated

during mid- to late-systole, with the development of the sinus vortex, and were low during all other instances. In the axial direction, aortic surface shear stresses were mostly uni-directional. Aortic surface shear stresses were observed to increase with increasing stroke volume and with decreasing heart rate. On the ventricular surface, shear stresses had a systolic peak of approximately 70 dyn/cm^2. During late systole, due to the Womersley effect, shear stresses were observed to reverse in direction to a substantial magnitude for a substantial period of time. Thus ventricular shear stresses were bi-directional.

In specific aim 3, an *in vitro* bicuspid aortic valve model was constructed and shear stresses experienced by its leaflets were measured. It was found that due a moderately stenotic bicuspid valve can have turbulent forward flow, and highly unsteady shear stresses on the aortic surface of the valve leaflets. This unsteadiness manifested as both an high frequency fluctuation about the ensemble mean within each cardiac cycle, as well as a cycle-to-cycle magnitude differences.

To demonstrate that the measured shear stresses can have an effect on the aortic valve biology, ex vivo experiments were performed in specific aim 4 to determine the effects of these various shear stress characteristics on the biological response of porcine aortic valve leaflets, using the cone and plate bioreactor. It was found that unsteady shear stress measured in the bicuspid valve elicited elevated calcification responses. Further, a series of sinusoidal waveforms of different magnitude and frequencies were tested on the bioreactor, and it was found that low shear stresses and high frequency shear stresses resulted in an elevation of calcification responses. This indicates that aortic valve

endothelium may have similar mechanobiology response to shear stress as vascular endothelium, where low and oscillatory fluid shear stresses can cause sclerosis.

CHAPTER 1

INTRODUCTION

Aortic valve calcification is a degenerative disease of the aortic valve which results in the deposition of calcium minerals on the valve leaflets. This disease has a high prevalence: it has been reported that 2% of the elderly population has severe aortic valve stenosis due to calcification [1]. Aortic valve calcification leads to aortic stenosis and regurgitation, and eventually heart failure, and is a major cause of mortality and morbidity: every year, in the US alone, aortic valve disorders are associated with over 40,000 deaths [2], and resulted in 95,000 surgeries being performed, making aortic valve surgery the second most common cardiac surgery after coronary bypass procedure. Worldwide, 170,000 aortic valve replacement surgeries are performed annually [14].

Aortic valve calcification is especially severe in patients with bicuspid aortic valves. The bicuspid aortic valve is a congenital disease where two of the three leaflets of the aortic valve are fused together, and has a high prevalence of 1-2% of the population. Individuals with bicuspid aortic valve suffer from sclerosis and calcification 10-20 years earlier than normal individuals [12, 13], and make up 50% of calcific aortic stenosis patients [10, 11].

The exact mechanisms of the aortic valve calcification are currently unclear. This has led to a bottleneck for development of better disease treatment therapies, or for the formulation of preventive therapies. Due to its prevalence, the need to understand the mechanisms of aortic valve calcification in both the normal tricuspid aortic valve individuals and bicuspid aortic valve patients is critical.

Ex vivo studies have suggested that mechanical forces such as fluid shear stress play an important role in mediating valve biology and pathobiology, and could play a role in the development of this disease [3-7]. Fluid shear stress, as opposed to static culture, was found to be protective against pro-inflammatory and pro-oxidative expressions in cultures of valvular endothelial cells [4]. Certain patterns of shear stresses, however, were found to be "adverse", resulting in the up-regulation of inflammatory markers in valve leaflet tissues [5]. Further, it has been speculated that the reduced shear stresses on the non-coronary leaflet of the aortic valve (AV) due to the lack of coronary flow is responsible for the increased susceptibility to calcification of that leaflet [13].

Thus, a complete understanding of the shear stress mechanical environment of the aortic valve leaflets may be essential to understand the pathways to aortic valve calcification. It has been hypothesized that the exposure of the two sides (aortic and ventricular surfaces) of the valve leaflet to different shear stress environments could be responsible for the preferential formation of calcification lesions on the aortic surface of the aortic valve [8, 9]. Thus, there is a need to characterize the shear stress environment on both surfaces. Further, despite evidence that genetic factors play a role in the bicuspid aortic valve calcification, it has been hypothesized that altered mechanical environment of the bicuspid aortic valve due to the significant change in the geometry of the valve could play a role in promoting calcification. There is thus a need for a comprehensive understanding of the fluid shear stress environment of the bicuspid aortic valve, and the difference in this shear stress environment compared to that of the normal tricuspid aortic valve.

The major objectives of this thesis are to characterize fluid shear stresses on the leaflets of the normal aortic valve and the congenital bicuspid aortic valve, and to investigate if these shear stresses can up-regulate or down-regulate patho-biological expressions the leaflets.

The mechanical environment of the aortic valve is not completely characterized. The fluid shear stress environment, in particular, is poorly studied: there have been no experimental measurements of fluid shear stresses on aortic valves subjected to dynamic, physiological conditions. The work in this thesis thus addresses these gap of knowledge. Further, the data from this thesis show that mechanical forces could be a pathway through which bicuspid aortic valves calcify faster than normal tricuspid aortic valves, suggesting that, contrary to conventional beliefs, calcification in the bicuspid aortic valve calcification may not be completely due to genetic defects, but could be due to a combination of genetics factors and exposure to adverse mechanical forces.

In chapter 2, an in depth literature review is presented, so as to provide a background to the thesis, and significance and motivation for the proposed work, leading to the hypothesis and specific aims in chapter 3. The methodologies employed in this thesis are presented in chapter 4 and the results in chapter 5. The research findings will be discussed in chapter 6, to understand the implications of the results and the limitations of the study. The conclusions of the work are discussed in chapter 7, highlighting the major findings and briefly summarizing their implications. Finally, recommendations for future directions are provided in chapter 10.

CHAPTER 2

BACKGROUND AND SIGNIFICANCE

2.1. The Cardiac Valves and the Cardiac Cycle

The heart is the main source of energy for circulation in the body. It consists of four chambers: the right atrium, right ventricle, left atrium and left ventricle. Blood returning from systemic circulation flows from the vena cavae to the right atrium, which are then channeled into the right ventricle, before entering the pulmonary arteries into pulmonary circulation for oxygenation. Blood returning from the lungs enters the left atrium are channeled into the left ventricle before being pumped into the aorta for systemic circulation.

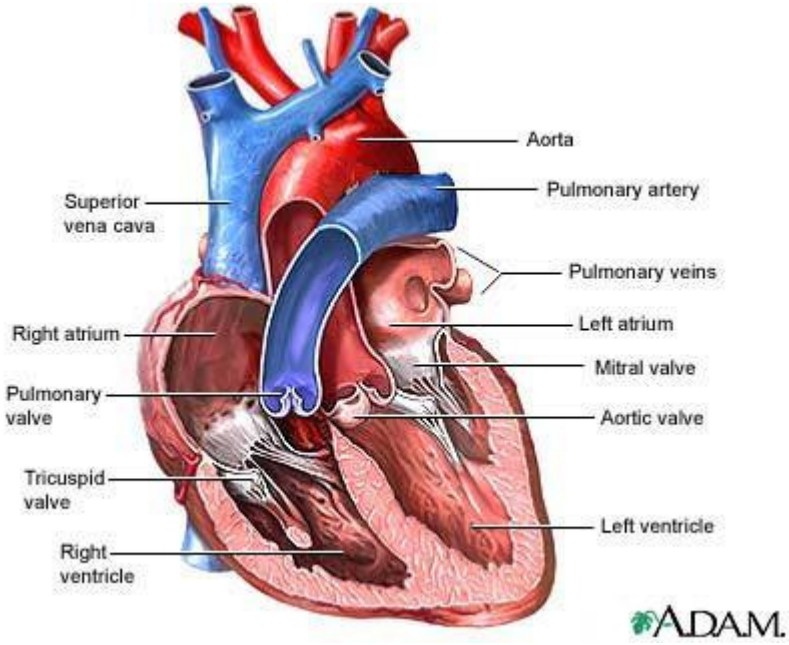

Figure 2-1. *The anterior view of the human heart, illustrating the the cardiac chambers, heart valves and adjoining great arteries and veins. Adapted from* *http://www.ncbi.nlm.nih.gov/pubmedhealth/PMH0003450/figure/d19e1789*

The four cardiac chambers undergo contractile motions to pump blood to the downstream chamber, with the aid of cardiac valves to control the direction of flow. During systole, the two ventricles contracts to impart high pressure on blood to force blood out of them through the outflow tracts (pulmonary artery for the right ventricle and aorta for the left ventricle). During diastole, the ventricles relax, and blood flows in to fill them from the atria passively. During end diastole, atrial contraction provides active pumping to aid blood flow into the ventricle.

The cardiac valves control the direction of blood flow by acting as one-way valves, opening when blood flows in one direction, but closing when blood flows in the reversed direction. The atrio-ventricular valves facilitate the flow of blood from the atria into the ventricle and prevent leakage of blood from the ventricle to the atria. These valves include the mitral valve, which is situated in the left heart, and the tricuspid valve, which is situated in the right heart. The semi-lunar valves facilitate flow from the ventricles into the great arteries, and prevent leakage of blood from these arteries back into the ventricle. Semi-lunar valves include the aortic valve in the left heart and the pulmonary valve in the right heart.

The cardiac valves open and close passively due to differential pressures across them generated by actions of the cardiac chambers. During systole, ventricular contraction increases pressure in the ventricle. The atrio-ventricular valves remain closed since ventricular pressure is higher than atrial pressure. The semi-lunar valves on the other hand, open when ventricular pressure exceeds arterial pressure. At the end of systole, with the relaxation of the ventricles, ventricular pressures decrease. When ventricular pressure is lower than arterial pressure, the semi-lunar valves close.

The period immediately thereafter is known as the iso-volumetric relaxation phase, where declining ventricular pressure is still higher than the atrial pressure and the atrio-ventricular valves have not yet opened, thus ensuring that ventricular blood volume is constant. All four valves are thus closed at this stage. When ventricular pressure decreases to less than the atrial pressure, the atrio-ventricular valves open to allow ventricular filling. At the end of diastole, the ventricles commence contraction again. When ventricular pressure reaches the atrial pressure, the atrio-ventricular valves close. The period immediately thereafter is known as the iso-volumetric contraction phase, where the increasing ventricular pressure is still lower than the arterial pressure, and the semi-lunar valves have not yet opened. The heart experiences systole again when the ventricular pressures are above arterial pressure.

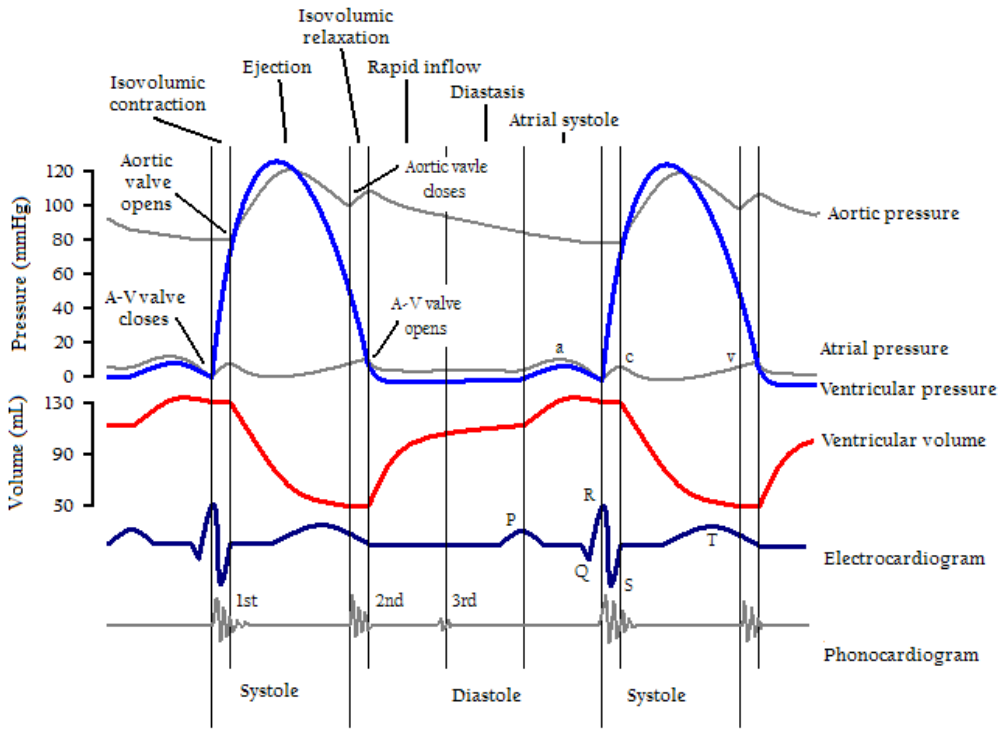

Figure 2-2. *Pressure and volume of the left heart cardiac chambers, the pressure in the ascending aorta, the electrocardiogram and the phonocardiogram over the cardiac cycle. Adapted from http://commons.wikimedia.org/wiki/File:Cardiac_Cycle_Left_Ventricle.PNG*

The durations of the cardiac cycle is approximately 35% systole, and 65% diastole, which for the normal adult resting heart rate of 70 beats/min, translate to approximately 300 ms and 560 ms, respectively. The iso-volumetric contraction and relaxation durations are very short in comparison to these two phases.

2.2. The Aortic Valve Anatomy and Tissue Structure

2.2.1. Anatomy

The aortic valve is the semi-lunar valve between the left ventricle and the aorta, within the base of the aorta, known as the aortic root. The normal aortic valve consists of three leaflets. The inferior base of the leaflet is connected to the annulus, which is a fibrous ring embedded in the fibers of the ventricular septum and the anterior leaflet of the mitral valve. The annulus of the aortic valve separates the aorta from the left ventricle, and superior to this ring are bulges in the wall known as the sinus of Valsalva, or aortic sinuses. Each bulge aligns with the center of a specific valve leaflet. At the top of the sinuses, where the sinus bulge transitions to the tube-like ascending aorta is termed the sinotubular junction.

Two of the sinuses give rise to coronary arteries that branch off the aorta, providing blood to the heart itself. The aortic valve sinuses and the corresponding valve leaflets are named according to the presence of the coronaries. The sinus with the right coronary artery ostium is known as the right coronary sinus, and the leaflet in front of this sinus is known as the right coronary leaflet. The sinus with the left coronary artery ostium is known as the left coronary

leaflet. The sinus without any coronary attachment is the non-coronary sinus, and the associated leaflet is the non-coronary leaflet.

The superior base of the leaflet is connected to the valve commissure, which inserts into the aortic root walls. The aortic valve commissures provide load-bearing support to the leaflet when they are closed to resist high transvalvular pressures.

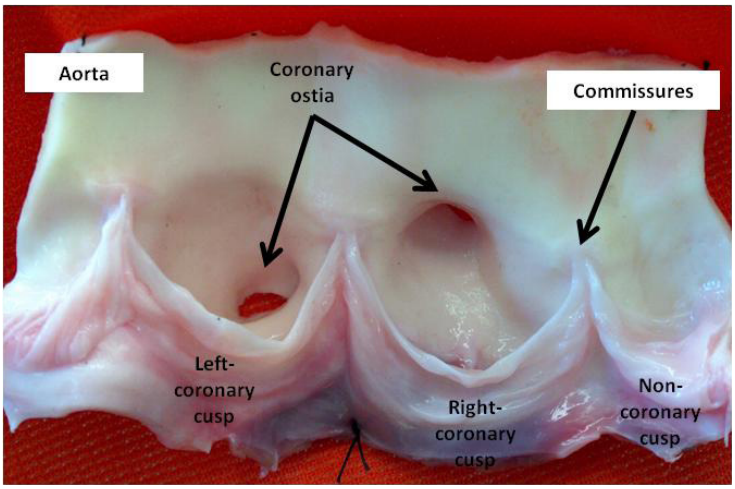

Figure 2-3. *the aortic valve, cut open along an axial line and laid out flat, demonstrating the anatomy of the valve. Adapted from [15].*

Swanson et al. [16] characterized the dimensions of the aortic root by making rubber molds of human aortic valves under suitable pressures. Their results are shown in figure 2-4. The axial length of the sinus was found to be 0.87 times the annulus diameter and the radial width of the sinus was found to be 0.73 times the annulus diameter. The length of the coapted leaflet was found to be 0.7 times the annulus diameter. By assuming that the leaflet length will not change between diastole and systole, Swanson et al. calculated the motion of the valve leaflet during the opening phase [17] theoretically. They reported that the axial length of the leaflet to be 0.7 times the annulus diameter when it is fully opened,

which is also shown in figure 2-4. Later studies by Yap et al, however, showed that the valve leaflets changes in length between systole and diastole, because the leaflets are stretched further in the radial direction under the much higher diastolic trans-leaflet pressure [18]. Yap et al. showed that leaflet radial lengths during diastole are 1.33 times that during systole. Thus the more accurate estimate of the axial length of the leaflet during systole is 0.5 times the annulus diameter.

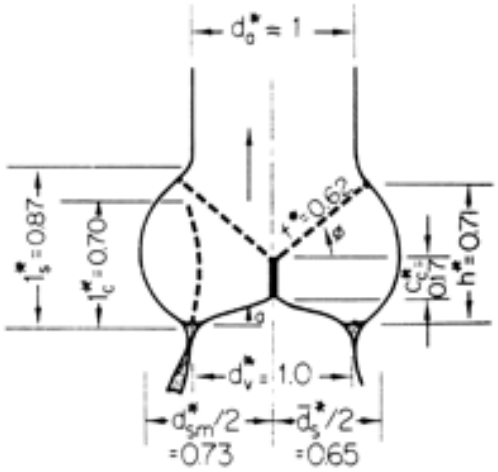

Figure 2-4. *Dimensions of the aortic root as measured by Swanson et al. [16]. All dimensions are listed as multiples of the annulus diameter, dv.*

2.2.2. Tissue Structure

The aortic valve leaflets are lined with endothelial cells and are composed of collagen, elastin, proteoglycans, protein polysaccharides and interstitial cells in a three layered structure, as shown in figure 2-5. The layer facing the aorta is termed the fibrosa, and is the major fibrous layer within the leaflet. It consists mainly of trunk collagen bundle chords in the circumferential direction, interlaced with radially-aligned elastin fibers [19]. The layer covering the ventricular side of the leaflet is a thin layer called the ventricularis

and is composed of elastin fibers interspersed with some collagen. The ventricularis presents a very smooth surface to the flow of blood [20], while the fibrosa surface is visibly undulating under the microscope. The central layer of the leaflet, called the spongiosa, contains variable loose connective tissue, proteins and sugars (in the form of glycos-amino-glycans and other glyco-proteins), has reduced amount of protein fibers and is normally not vascularized. It is thought that the semi-fluid nature of the spongiosa provides the valve leaflet with deformability, allowing the exterior layers of fibers to slide over each other during bending and stretching [21-23]. The collagen fibers within the fibrosa and ventricularis are unorganized in the unstressed state, but when a stress is applied, they become oriented primarily in the circumferential (or width) direction [20, 24]. The amount of transvalvular pressure required to align the collagen fibers from the relaxed state has been reported to be as low as 1mmHg [25].

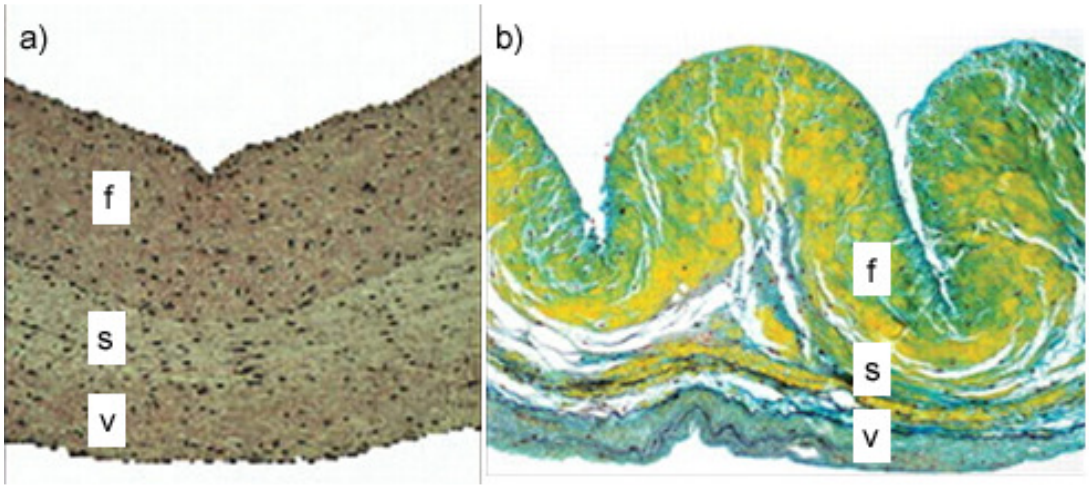

Figure 2-5. *(a) H&E stain of a cross section of the aortic valve, adapted from [26]; and (b) Movat Pentachrome stain of a cross section of the aortic valve, adapted from [27], showing the three distinct layers with different composition. "f", "s" and "v" indicate fibrosa, spongiosa and ventricularis respectively.*

2.3. Aortic Valve Fluid Mechanics

2.3.1. General Fluid Mechanics of the Aortic Valve

The aortic valve is a highly dynamic organ, involving rich dynamics and interaction between fluid and the valve. At the beginning of systole, the valve leaflets rapidly open, and blood rapidly accelerates through the valve with a positive gradient (higher pressure upstream in the ventricle than downstream in the aorta). At about the first third of systole, forward flow velocities are at their peaks. Thereafter, flow begins to decelerate to zero at the end of systole under the influence of adverse pressure gradient (the ventricle is at the end of its contraction phase, and ventricular pressure drops below aortic pressure). The systolic pressure gradient required to accelerate blood through the healthy aortic valve is in the order of a few millimeters of mercury. However, diastolic pressure differences reaches 80 mmHg across the closed valve.

In the healthy adult, systolic blood reaches peak velocity of 1.35 ± 0.35 m/s. For children, this value is slightly higher at 1.5 ± 0.3 m/s [28]. Flow in the aorta immediately downstream of the valve is pulsatile in nature, and in normal resting adults, heart rate is approximately 70 beats/min. The Reynolds number of peak flow in the aorta ranges from 2000 to 4000 [29], and the Womersley number of the flow is approximately 36 [30]. Under these conditions, according to the study by Nerem et al, turbulence will not be triggered in the flow [30]. Even though Reynolds number reaches the transitional level, they are not high enough for turbulence to develop within the short systolic duration.

Further, during systole, vortical flow develops in the sinuses, which is induced by the forward flow. These vortices was first described by Leonardo da Vinci in 1513, and they have been extensively investigated primarily through the use of *in vitro* models [31, 32].

More recently, phase contrast magnetic resonance imaging provided evidence of their presence in humans [33, 34], one demonstration of their measurement is shown in figure 2-7. It has been hypothesized that these vortices create a transverse pressure difference that pushes the leaflets towards the center of the aorta and towards each other at the end of systole, thereby helping with the valve closing process and minimizing regurgitation of blood. However, *in vitro* work showed that the axial pressure difference alone is sufficient to close the valve [32]. Without the sinus vortices, the valve still closes, but the closure is not as quick as when the vortices are present, and the velocity of the leaflet closure motion is not as rapid [35].

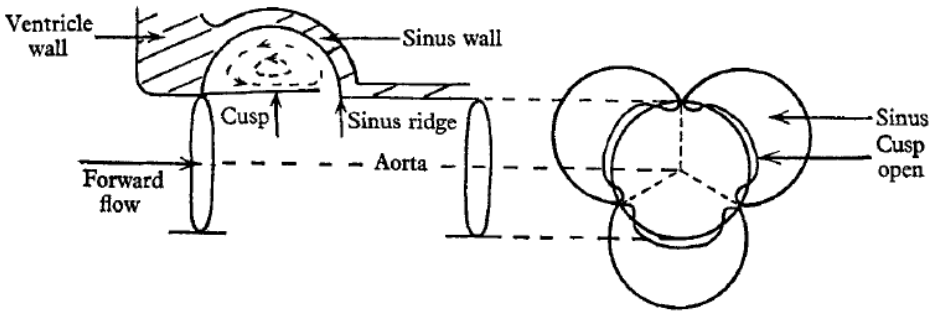

Figure 2-6. *Schematic of the sinus vortex, as studied by Bellhouse et al [36].*

Based on these existing literatures on the fluid flow around the aortic valve leaflets, it can be conceived that the ventricular surface of the valve leaflets will experience different shear stresses from the aortic surface of the valve leaflets. The ventricular surfaces form the boundary of the systolic forward flow jet, and should experience much higher than the shear stresses on the aortic surface of the leaflets. On the aortic surface, shear stresses are conceivably related to the sinus vortex flow.

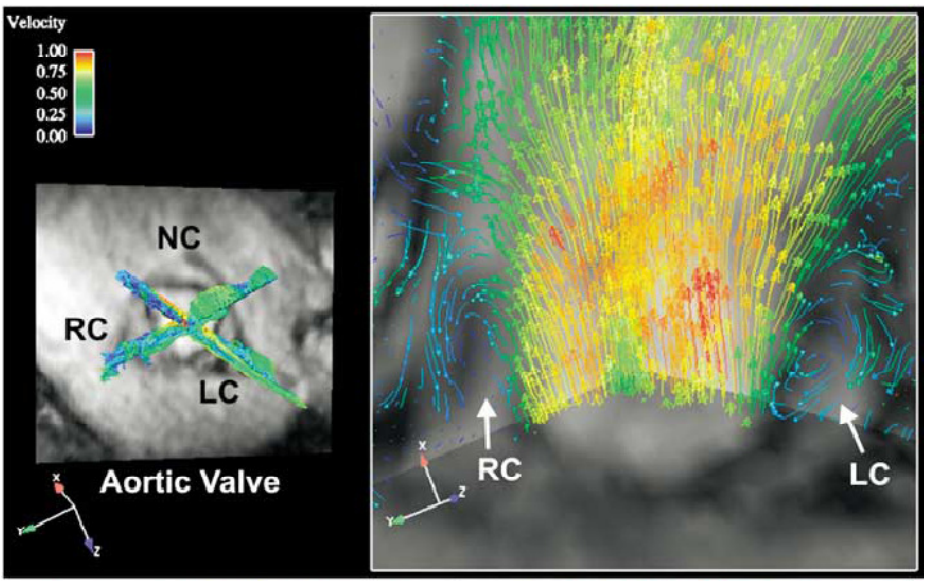

Figure 2-7. *Three-directional velocity vectors along two dimensional planes, acuiqred from a healthy subject with PCMRI, showing vortices in the right coronary sinus (RC) and left coronary sinus (LC). Adapted from [34]*

2.3.2. Experimental Aortic Valve Fluid Mechanics Measurements

Experimental measurements of the fluid mechanics in the aorta or near prosthetic valves have been extensively performed. As early as 1968, Ling et al used hot-film anemometry to measure shear stresses in the descending aorta of open-chested dogs [37], and found wall shear stresses to be in the range of 80-160 dynes/cm^2. They further presented flow profiles qualitatively matching those of the Womersley solutions. Nandy and Tarbell used flush mounted hot film anemometry to measure shear stresses in a plastic model of the aorta and aortic root with a tri-leaflet bioprosthetic valve, and reported that wall shear stress in the sinus bulge to be very unstable with large beat-to-beat variation [29]. Yoganathan et al used LDV to measure the flow profiles and Reynolds shear stresses downstream of a variety of prosthetic valves [38], while Lim et al used PIV to evaluate flow and Reynolds shear stresses downstream of tri-leaflet bioprosthetic valves [39]. Despite extensive studies in the fluid mechanics of native and

prosthetic aorta / aortic valve, none of these studies focused on measuring shear stresses on the surface of the aortic valve leaflet.

More recently, new non-invasive techniques such as MRI and Doppler Ultrasound has been used for quantification of vessel wall shear stress *in vivo*. Brands *et al.* [40] used pulsed wave Doppler ultrasound to measure the flow profile in carotid arteries in human volunteers using a novel wall filtering algorithm, and they obtained flow profile data at spatial resolution of 250 μm, and found wall shear rates to be between 393/s and 805/s. Efstathopoulos et al acquired PCMRI of human ascending aortas with the 1.5 T scanner and used a linear method for the estimation of the wall shear stresses, and reported wall shear stress in the vicinity of 1-10 dyn/cm^2 [41]. However, these techniques have low spatial and temporal resolution and may not be able to resolve shear stresses on the aortic valve completely.

To date, only one study has attempted to assess shear stress on the surface of a heart valve leaflet. Weston et al performed LDV measurement on the ventricular surface of a polymeric valve under steady flow conditions *in vitro* [42]. Their results are shown in figure 2-8. Peak wall shear stress on the ventricular surface of the valve was measured to be approximately 20, 40 and 80 dyn/cm^2 for steady flow rates of 7.5, 15 and 22.5 L/min respectively. However, since this study is performed under steady flow condition, the evolution of shear stresses over the cardiac cycle could not be reported. Further, the flow profile of forward flow under dynamic condition is necessarily different from that under steady flow condition, as explained by the Womersley solution of pulsatile flow, and thus these measurements may not represent the true aortic valve leaflet fluid shear stress environment.

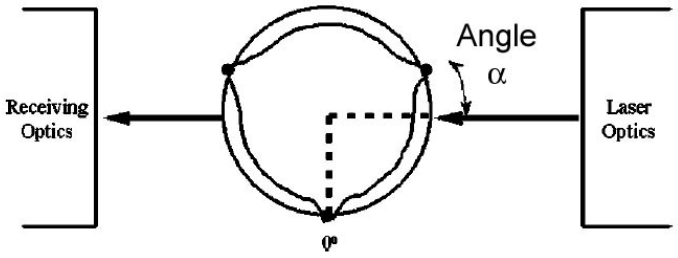

Figure 2-8a. *Schematic of measurement of fluid shear stress on aortic valve leaflet surface by Weston et al [42].*

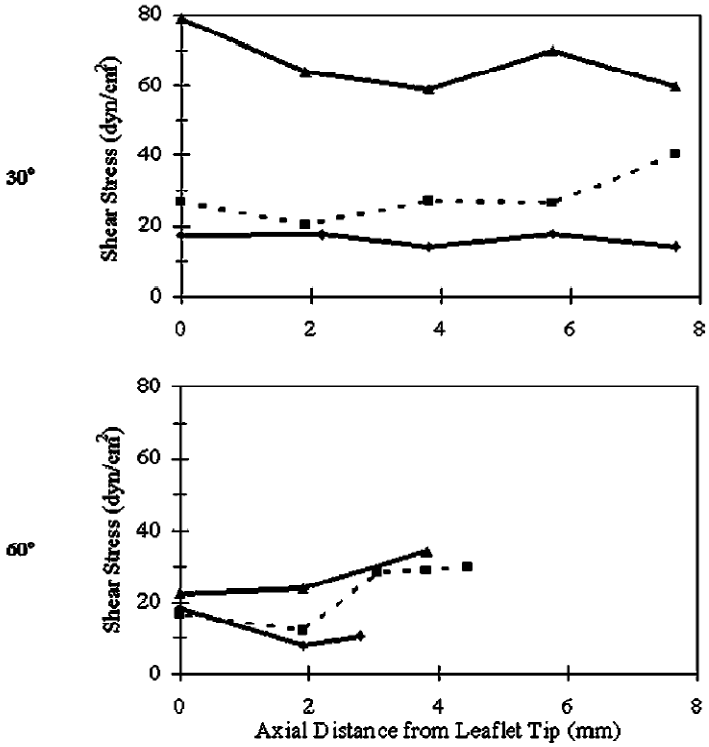

Figure 2-8b. *Shear stresses measurement results by Weston et al [42]. The angle on the left corresponds to* α *in figure 2-8a.*

Experimental measurement of shear stresses on the surface of aortic valve leaflets is technically challenging. As discussed above, non-invasive scanning modalities do not have sufficient resolution to resolve these shear stresses. With *in vitro* techniques, the dynamic motion of the valve leaflet poses difficulties for hot film anemometry, which is

typically used on stationary surfaces, and there are difficulties with in situ calibration. With Laser Doppler Velocimetry or Particle Image Velocimetry, issues with making measurements on a dynamic surface, and issues with making measurements on a light scattering biological surface have not been resolved. There is currently no experimentally collected data in the literature on physiologic fluid shear stress experienced by the aortic valve leaflet. It is thus important to address this gap in the literature.

2.3.3. Computer Simulations of Fluid Mechanics of the Aortic Valve

To make up for the lack of experimental data, computational fluid dynamic and fluid-structure interaction simulations were performed to obtain the shear stress environment of the aortic valve leaflets. Ge et al [43] performed quasi-steady simulations of flow in a tri-leaflet aortic valve, and observed systolic aortic surface shear stresses in the order of 0-8 dyn/cm^2, and systolic ventricular surface shear stresses in the order of 50-100 dyn/cm^2. Their results are shown in figure 2-9. The ventricular surface shear stresses were observed to be aligned with the streamwise direction. The aortic surface shear stresses showed heterogeneity in directions, and evolved over time. However, the aortic root geometry used in the simulation was not physiologic: an axis-symmetric "barrel" sinus chamber was modeled instead of tri-lobed sinus chamber.

Morsi et al performed simulations of the opening phase of a trileaflet valve in a tube, and reported shear stresses at various locations on the aortic valve [44]. Large spatial heterogeneity of shear stresses was observed, most likely associated with the geometry of the leaflet in its open state. The simulation, however, only reached a Reynolds number of

600, shy of the 4000 expected in the aortic valve, and further, there no sinuses were modeled.

De Hart et al. performed coupled fluid-structure interaction simulations of the complete aortic root [45], and reported complex leaflet motion during the opening and closing phases. The results are shown in figure 2-10. This simulation achieved a higher Reynolds number of 1500, but is none-the-less lower than the physiologic Reynolds number. Fluid shear stresses on the surface of valve leaflets were not reported, although it appeared possible to obtain this from the simulation.

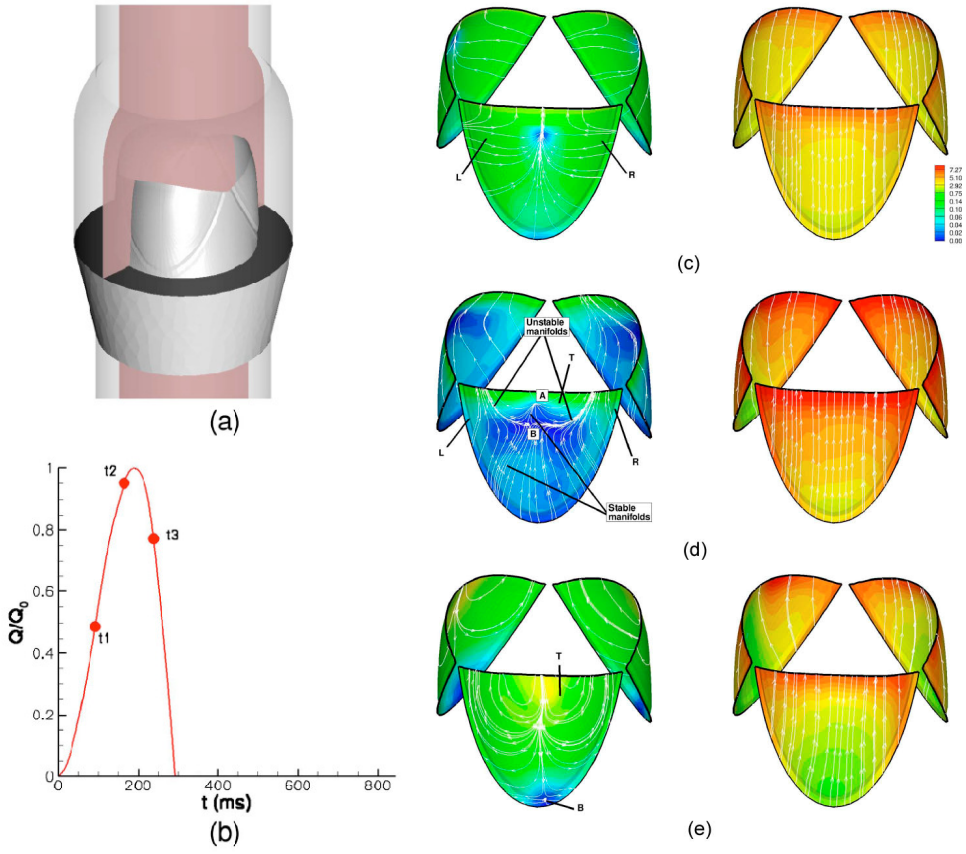

Figure 2-9. *Quasi-steady simulation of fluid mechanics in the trileaflet aortic valve by Ge et al [43]. (a) Geometry of the simulation; (b) systolic time points for which shear stresses are shown; (c) shear stresses on the aortic surface (left) and ventricular surface (right) of the valve leaflets.*

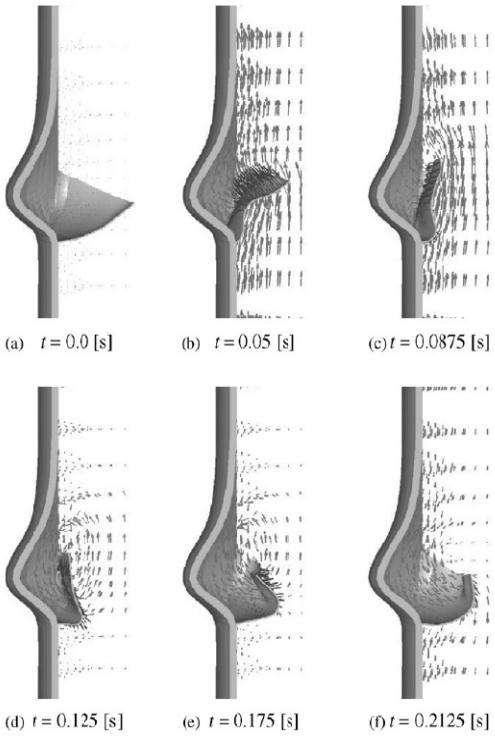

Figure 2-10. *Fluid-structure Interaction simulations in a trileaflet aortic valve, demonstrating the complexity of fluid flow and leaflet motion during opening/closing phases.*

Weinberg et al. [46, 47] performed fluid structure simulations on the aortic root at physiologic transvalvular pressures, and included forward flow velocities above 1.5 m/s. their results is shown in figure 2-11: they reported peak ventricular surface shear stress of 38 dyn/cm^2, and peak aortic surface shear stress of 3 dyn/cm^2. Ventricular shear stresses were reported have no shear reversals, where else the aortic shear stresses were reported to have reversals. Shear stresses on the aortic surface were reported to be zero during all of diastole.

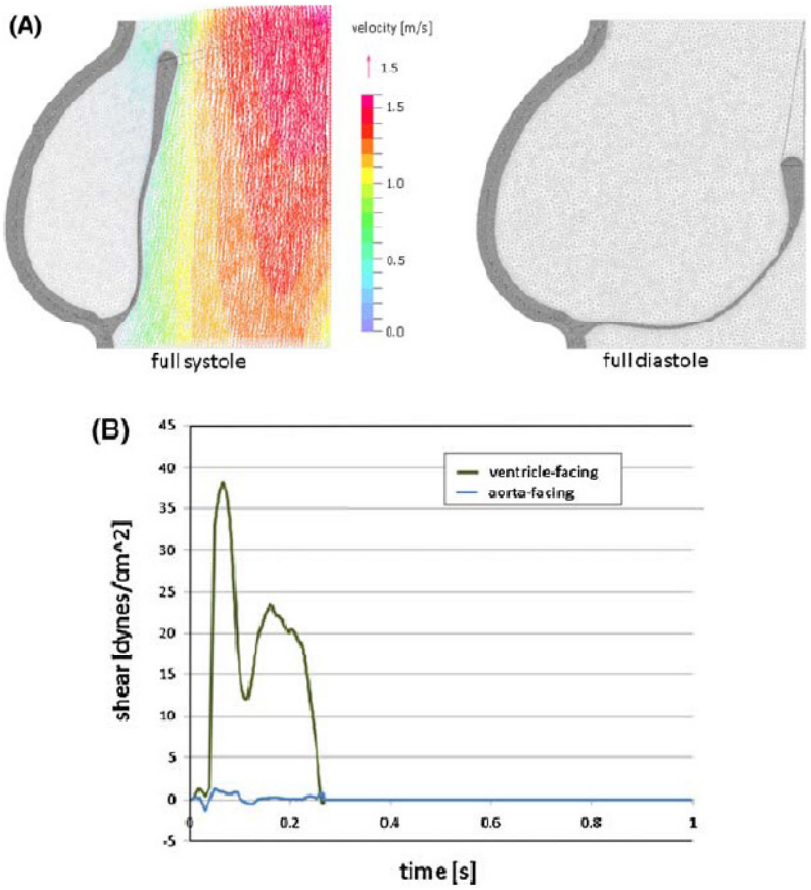

Figure 2-11. *Results of simulations by Weinberg et al. [46], showing (A) flow in the aortic root during systole and diastole; and (B) shear stresses experienced by the ventricular and aortic surfaces.*

These studies collective demonstrated the complex dynamics of flow and shear stresses on the aortic valve leaflets. However, the task of numerically modeling the aortic valve have its own challenges: there were complications in modeling the anisotropic and heterogeneous fiber architecture and solid mechanical properties, in meshing the fluid-solid boundaries and updating the mesh to capture leaflet dynamics, in modeling the complete closure of the valve leaflet to separate fluid into two domains (upstream and downstream), in modeling transitional flow and turbulence, and in achieving Reynolds number of peak flow at physiological levels. Further, simulations require the validation of

modeling assumptions, and thus require experimental data for support. Also, some experimental data is necessary for a comprehensive understanding of fluid shear stress environment of the aortic valve.

2.4. Aortic Valve Solid Mechanics

2.4.1. Valve Leaflet Mechanical Properties

Like most biological tissues the aortic valve leaflets are anisotropic, inhomogeneous and viscoelastic. The collagen fibers within each leaflet are mostly aligned along the circumferential direction. Elastin fibers are present at a lesser concentration than collagen and are mostly oriented radially. This fiber structure accounts for the anisotropic properties of the valve. The variation in thickness and composition across the leaflets is responsible for their inhomogeneous material properties. Although the aortic valve leaflet as a whole is asymmetric in its distensibility, the basal region tends to be relatively isotropic while the central region shows the greatest degree of anisotropy [48]. Mechanical testing of elastin structures from the fibrosa and ventricularis separately have shown that the purpose of elastin in the aortic valve leaflet is to maintain a specific collagen fiber configuration and return the fibers to that state during cyclic loading [49].

Billiar et al. tested porcine aortic valve leaflets and found that their response curve was similar to those of collagen fibers, with an exponential increase in stress with strain [50]. With increasing stress, the leaflets exhibit three distinct responses consecutively, starting a low stiffness "toe" region, moving on to a transitional "heel" region, and a high stiffness "linear" region (figure 2-12). This is in accordance to the fiber architecture of the valve leaflet: the "toe" region represents the uncrimping of the collagen fiber curls

and the elastic response of elastin, while the "linear" region represents the stretching of already straightened collagen fibers [25]. As expected, the leaflet as a whole was found to have higher stiffness in the circumferential direction than in the radial direction. Further, dynamic testing has revealed that at physiological loading rates, the leaflet material behaves elastically although the leaflets are viscoelastic in nature [51, 52]. The leaflet is capable of undergoing large, rapid anisotropic strains in response to transvalvular pressures and return to its original configuration when unloaded with little hysteresis and creep, leading to its association with the term "quasi-elastic". Performing engineering analysis of the valve structures, Christie el. al. concluded that stress in the leaflets in the circumferential direction is the primary load bearing element, which is in line with the presence of collagen fiber bundles oriented circumferentially [20]. Radial stress was found to be small compared to circumferential stress in the closed valve.

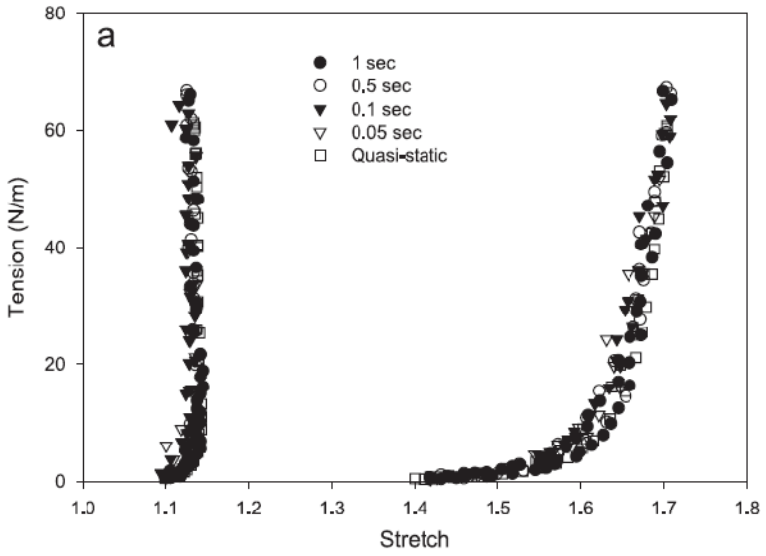

Figure 2-12. *Mechanical response of fresh aortic valve leaflet to equi-biaxial stress at different loading rates, demonstrating the anisotropy of the tissue as well as the insensitivity of the tissue to loading rates, adapted from Stella et al. [51]*

2.4.2. Aortic Root Dynamics

During the cardiac cycle, the heart undergoes translation and rotation due to its contraction pattern. As a result, the base of the aortic valve varies in size and also translates and twists. The dynamics of the aortic root are a result of the combination of passive response to pressures on both sides of the valve as well as active contractions of the muscular shelf on the anterio-medial segment of the annulus. Using marker fluoroscopy in sheep, Dagum et al [53] characterized the aortic root motion. During iso-volumetric contraction, the annulus and sinotubular junction undergo rapid circumferential expansion and the aortic root increases in longitudinal length without shear or torsion. During ejection phase, the annulus undergoes circumferential contraction whereas the sinotubular junction continues to expand, and the aortic root undergoes non-uniform shearing which results in torsional deformation. During the iso-volumetric contraction, the aortic root undergoes further circumferential contraction at both the annulus and the sinotubular junction, and experiences further shearing and torsional deformation, as well as longitudinal compression. During early diastole, the annulus and sinotubular junction recoils from its dynamically loaded configuration by expanding, and the root is elongated and untwisted from its motion during the other phases. Torsional deformation has been described to be non-uniform over the three sinus segments.

2.4.3. Valve Leaflet Dynamics

The systolic motion of the aortic valve can be described in three phases: the rapid opening phase, the slow closing phase, and the rapid closing phase. The rapid opening phase lasts for about 60 ms, when leaflets rapidly open at an average speed of 20 cm/s,

the valve opens to the fullest extent, and blood accelerates through the valve. The slow closing phase, which lasts for 330 ms, is when the bulk of ejection occurs, and valve leaflets move approximately 13 mm. The rapid closing phase occurs during late systole, lasts for 40 ms and witnesses leaflet speed of 26 cm/s [35].

Earlier experiments in measuring the physiologic deformations of the aortic valve leaflets involves using marker fluoroscopy, in which the aortic valve leaflets were surgically tagged with radio-opaque markers and imaged with high speed X-rays [24]. The leaflets were found to be longer during diastole than systole in both the radial and circumferential direction, as is expected due to the high transvalvular pressure across the closed aortic valve stretching the leaflets. Yap et al. [18] characterized the deformational dynamics of the aortic valve leaflets *in vitro* at high spatial and temporal resolution, and showed that average diastolic stretch ratio of the valve to be 15%-18% in the circumferential direction and 45%-54% in the radial direction at the base and belly regions of the valve. It was found during diastole, the leaflets rapidly loads up to the peak stretch ratios, and plateaus at approximately the same stretch ratio until the rapid unloading phase at end diastole. During systole, however, the valve stretches slightly in the radial direction (to a lesser extent than during diastole) due to drag forces induced by forward flow, it compresses slightly in the circumferential direction due to Poisson's effect of radial stretch. It has been reasoned that the stretching of the valve leaflets during diastole is useful in allowing leaflets to come together and achieving proper coaptation, and that the shortening of the leaflets during systole reduces obstruction of the aorta during the ejection of blood [20].

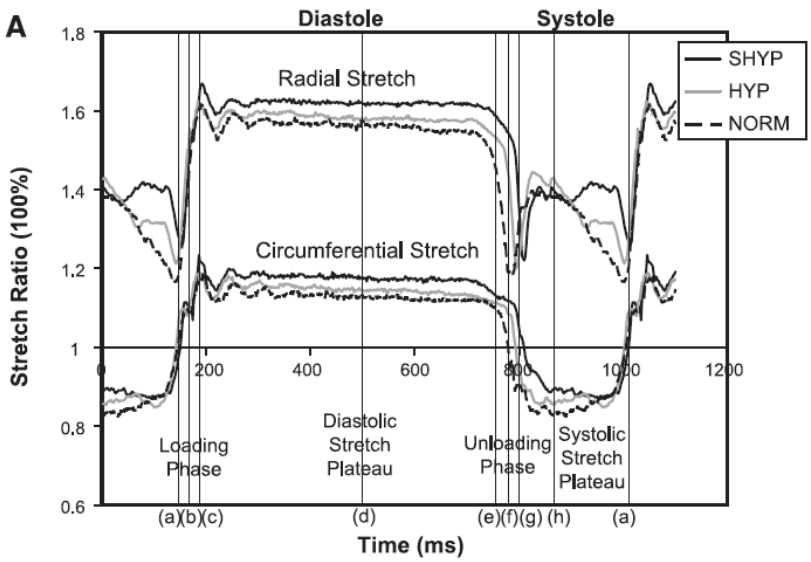

Figure 2-13. Dynamic Deformational Characteristics of the aortic valve leaflet over the cardiac cycle, reported by Yap et al. [18]. Stretch is higher in the radial direction. During diastole, the leaflet is stretched in both radial and circumferential direction. During systole, the leaflet is stretched in the radial direction by drag forces imparted by forward flow, and contracts in the circumferential direction due to Poisson's effect.

Drastic changes in valve area described above are results of the valve reacting to the stresses in a passive manner. It is currently unclear if active contractions of aortic valve cells play a role in the deformation dynamics of the leaflets. Active contractions of aortic valve cells have been studied and were found to be able to impart very small forces at physiological biochemical stimulations [54]. On the other hand, stimulants such as serotonin and endothelin were found to alter the stiffness of valve leaflets at the post-transitional zone of the response curve (high stiffness zone) significantly [55]. It is unclear if the stiffness of the pre-transitional zone (low stiffness zone) is altered, which is the main determinant of the amount of stretch suffered by the leaflets under physiologic loads. Active cell contraction has been also observed to impart additional bending stiffness to the valve leaflet [56]. This is an important consideration because the aortic valve leaflet experiences substantial bending during the cardiac cycle: valve leaflet is

convex curved toward the ventricle during diastole and curved towards the sinus when open, with the base of the valve leaflet bent to allow the opening. It is hypothesized that leaflet cell contractions is a regulatory mechanism of leaflet kinematics, and biochemical cues are used to control leaflet stiffness tone to influence function.

2.5. Aortic Valve Diseases

The aortic valve serves two important functions: (1) facilitating the outflow of blood from the ventricle into the aorta during systole; and (2) preventing blood flow back into the ventricle during diastole. Aortic valve disease occurs when there is a breakdown in either of these functions, and can result in mortality or serious morbidity. Aortic stenosis occurs when the aortic valve fails to open sufficiently to allow ejection of sufficient amount of blood during the short ejection phase, resulting in insufficient blood available for circulation. Aortic regurgitation occur when the aortic valve fails to close properly, and blood leaks back from the aorta into the ventricle, resulting in loss of energy available for circulating the blood. Both of these conditions can lead to heart failure and death.

Aortic valve disorders are associated with 41,132 deaths and 49,000 hospital discharges in 2010 in the US alone [2]. Every year, nearly 95,000 procedures are performed on the aortic valve, making aortic valve surgeries second onto the coronary bypass procedure [57, 58]. Further, the number of people requiring aortic valve surgery is expected to triple by 2050 [59]. Calcific aortic stenosis is the most common cause of aortic valve disorders. In the Euro Heart Survey covering more than 25 countries, aortic stenosis was the most frequent lesion, accounting for 43% of all patients having valvular

heart disease [2]. Among the elderly above 65 years old, the aortic valve was normal in 70%, sclerotic without outflow obstruction in 29% and stenotic in 2% [60].

2.5.1. Aortic Valve Calcification

Currently, the exact mechanism or the cause of aortic valve calcification is not well understood. A calcified aortic valve has increased thickness, collagen fiber disarray, and deposition of calcium predominantly on the aortic surface. Such a morphology result in the aortic valve having a drastically reduced leaflet flexibility, disabling the native valve kinematics and function, resulting in aortic valve stenosis and/or regurgitation [61]. The majority of aortic valve calcification has an idiopathic etiology. Recent studies, however, has shown that aortic sclerosis, which leads to calcification, is an active process akin to atherosclerosis, involving chronic inflammation involving macrophage and T-lymphocyte migration, basement membrane disruption and lipid infiltration, and active leaflet calcification mediated by cell differentiation [13]. Further, calcium depositions on the valve leaflet appear to be associated with cellular degradation products rather than the extracellular matrix fibers, suggesting that active tissue degeneration is responsible for the calcification rather than the passive deposition of calcium [62].

Figure 2-14. *Calcified human aortic valve. Arrow indicates a calcium nodule. Adapted from http://www.heart-valve-surgery.com/heart-surgery-blog/2010/04/27/aortic-stenosis-progression-calcified-leaflet/*

Stewart et al reported on the risk factors of aortic valve calcification. These factors include age (twofold increased risk for every 10 year increase in age), male gender (twofold excess risk), present smoking (35% increase in risk) and a history of hypertension (20% increase in risk) [63]. Other significant factors included height and high lipoprotein-a and low density lipoprotein cholesterol levels, and body weight [63, 64]. These risk factors are similar to those of atherosclerosis, leading investigators to propose that aortic valve sclerosis and atherosclerosis are different manifestation of the same disease [64].

2.5.2. The Congenital Bicuspid Aortic Valve Disease

One of the most significant risk factors for aortic valve calcification is the congenital bicuspid aortic valve (BAV) [63], where two of the three aortic valve leaflets are fused together at birth (figure 2-15). The BAV is the most common congenital malformation of the heart and great vessels, affecting 1-2% of the population, or about four million US

citizens [10, 11]. Clinically, there are a number of BAV morphologies. Classification systems had to be drawn up to comprehend the BAV characteristics [10, 65, 66]. The fusion of the leaflet can take place between any of the three original valve leaflets, as shown in figure 2-16. The most common morphology, however, is the fusion of the left and right valve leaflet, being observed in 86% of BAV patients. As demonstrated in figure 2-17, the fusion of the valve leaflets can result in the formation of a raphe, which is a thick fibrous tissue ridge along the line of fusion, where the commissure is supposed to be, but which was instead, degenerated. BAVs with more than one raphe or with no raphe also exist, but the more common morphology is that with one raphe. Sievers et al provided a more complete classification of the BAV morphologies [66] (figure 2-17).

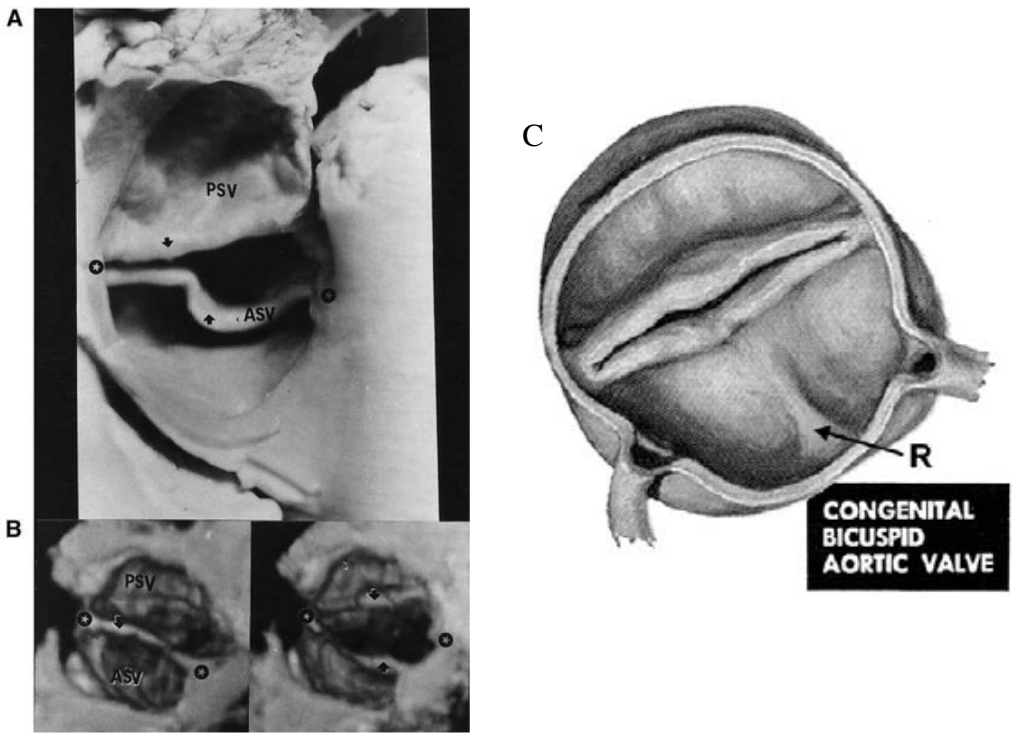

Figure 2-15. *(A) Black and white photographic image of a BAV, and (B) the Echocardiographic images of the valve during the (left) closed and (right) opened phases. Adapted from [67]. (C) schematic of the BAV, R indicates the Raphe, adapted from [68].*

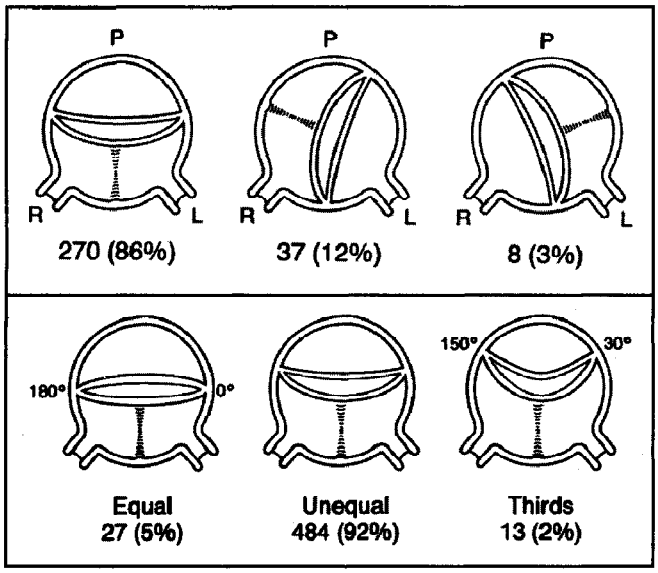

Figure 2-16. *Classification system of BAVs with one raphe, and the clinically observed relative frequency of occurrence of each morphology. Adapted from [65].*

main category: number of raphes	0 raphe - Type 0		1 raphe - Type 1			2 raphes - Type 2
	21 (7)		269 (88)			14 (5)
1. subcategory: spatial position of cusps in Type 0 and raphes in Types 1 and 2	lat 13 (4)	ap 7 (2)	L – R 216 (71)	R – N 45 (15)	N – L 8 (3)	L – R / R – N 14 (5)
2. subcategory: VALVULAR FUNCTION						
I	6 (2)	1 (0.3)	79 (26)	22 (7)	3 (1)	6 (2)
S	7 (2)	5 (2)	119 (39)	15 (5)	3 (1)	6 (2)
B (I + S)		1 (0.3)	15 (5)	7 (2)	2 (1)	2 (1)
No			3 (1)	1 (0.3)		

Figure 2-17. *Classification system proposed by Sievers et al. covering cases where no raphe or more than one raphe were observed. Representations of the BAV are illustrated as viewed from the surgeon's position with the left coronary sinus on the left side. The numbers indicate number of cases observed, with the number in parenthesis being the percentage of all observations. L, left coronary sinus; R, right coronary sinus; N, non-coronary sinus; I, insufficiency; S stenosis; B, balanced valvular lesion; No, normal function.*

The BAV is usually an isolated defect in between 20% and 50% of the cases. It is associated with majority of coarctation of the aorta cases, with 50% of Turner's syndrome cases, 60% of supra-valvular aortic stenosis cases, 30% of ventricular septal defect cases, and between 19% and 30% of Shone's Syndrome. Due to the valve morphology, the BAV can be stenotic and cause an eccentric outflow jet [68, 69]. The BAV, however, is not intervened during childhood unless significant symptoms of stenosis is observed, when balloon valvuloplasty is used as the treatment. Later in childhood and into adolescence, aortic regurgitation can develop, and aortic stenosis eventually develops in adulthood to due leaflet calcification. Aortic valve stenosis is associated with between 15% and 71% of BAV cases, between 1.5% and 3% of aortic regurgitation cases, between 9.5% and 40% of infective endocarditis cases, and about 5% of aortic dissection cases [11]. Further, patients with a BAV experience leaflet calcification about two decades earlier than people with normal aortic valves [12, 13]. These indicate a significant elevation in the risk of valve calcification for BAV patients.

Currently, the exact cause of the BAV is not completely understood. The observation of familial clustering in BAV has led to the proposition that genetic defects caused the morphology [70, 71]. Some researchers proposed abnormal behavior of neural crest cells as a possible etiology [72], since neural crest cells are involved in the development of semi-lunar valves. Others proposed molecular abnormality such as fibrillin-1 deficiency in extracellular matrix that leads to abnormal valvulogenesis as the cause [73]. Lee and colleagues noted that mice lacking endothelial nitric oxide synthase as predisposed to form BAV [74]. More recently, Garg et al [75] described evidence that mutations in the signaling and transcriptional regulator NOTCH1 is associated with the manifestation of

bicuspid aortic valve and with aortic valve calcification. One family of European-American decent spanning 5 generations with 11 cases of congenital aortic valve anomalies including 6 BAVs were studied, and it was found that every case of NOTCH1 mutation had congenital disease. Out of 7 cases where the subject showed mutations of the NOTCH1 gene, 4 had the BAV, and 5 had aortic valve calcification. Garg et al proposed the pathway for which NOTCH1 affects calcification: NOTCH1 transcripts repress the activities of RUNX2, a central transcriptional regulator of osteoblast cell fate, and defects in NOTCH1 could have led to de-repression of calcium deposition that caused aortic valve calcification. NOTCH1 messenger RNA is abundantly transcribed in fetal heart mesenchyme, the precursor to the valves and the endothelial layer, suggesting an important role in valvulogenesis, corroborating with Garg et al.'s hypothesis. Nonetheless, the direct relationship between the lack of NOTCH1 and the tendency of aortic valve tissues to calcify has yet to be proven.

On the other hand, the role of mechanics in calcification of BAVs cannot be neglected. Since drastic geometric of the aortic valve and aortic root occurs in the BAV, it is highly probably that there will be changes in the mechanical environment. Robicsek et al. [76] obtained human bicuspid aortic valves of individuals who died of non-cardiac causes. These valves were tested in *in vitro* flow loops and the leaflet dynamics were studied. Three valves were studied, and they were all noted to be stenotic. The images of the valves showed that the orifices were elliptical, and the fused leaflet had reduced mobility and blocked flow somewhat. The authors noted that the opening and closure mechanism contained considerable irregularities, such as whipping and trembling, which they attributed to the presence of turbulence, even though no direct engineering analysis

was performed to demonstrate the presence of turbulence. Further, these valves were noted to depend heavily on extensive folding and creasing in order to achieve opening and closing, and the closed valve contains significant waviness along the line of coaptation, which is most likely a compensatory mechanism to increase the free edge length, and allow a larger valve orifice area to be opened.

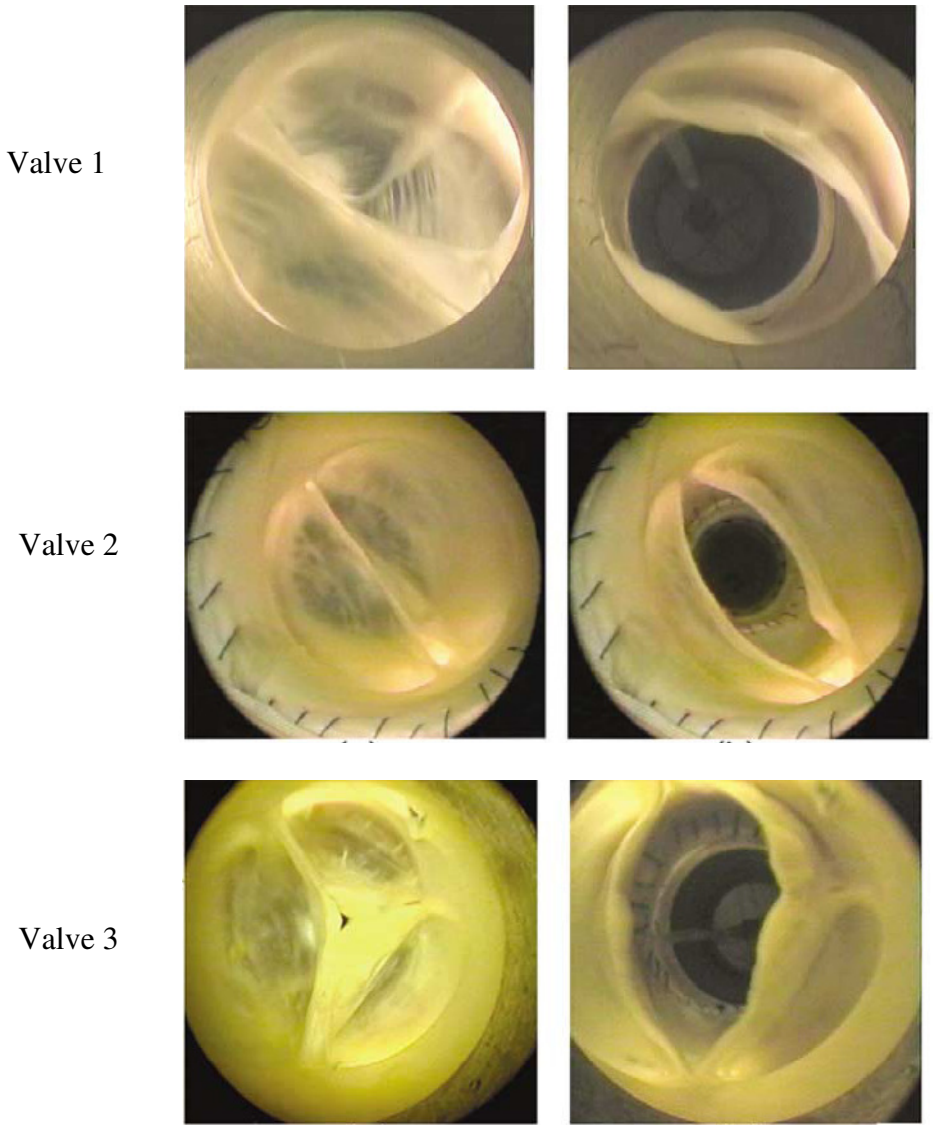

Figure 2-18. *Aortic view of three human bicuspid aortic valves, tested in an in vitro flow loop. The fused valve leaflet has a raphe where the commissure should have been. The orifice of the BAV appeared oval, the fused leaflet appeared less mobile than the normal leaflet, and appeared to block flow somewhat. Adapted from [76].*

Robicsek et al.'s work provided a basis for suspecting that the fluid mechanical environment of the BAV will be completed altered from the normal aortic valve. Since aortic valve tissues are very sensitive to altered mechanical environment, as discussed in section 2.5, and it is likely that the drastically altered mechanical environment of the BAV play a role in causing increased risk of calcification in the BAV. This notion is corroborated with studies showing that similar cellular and molecular mechanisms exist in BAVs and normal aortic valves [77], and thus if the normal aortic valve is mechanosensitive and can calcify from an altered mechanical environment, the BAV may also have the same response. The above sets up the hypothesis that BAV calcification is caused by a combination of genetic and hemodynamic factors, not just genetic factors.

The debate of whether mechanics or genetics were responsible for co-morbidities observed in BAV patients occurred in the medical community for the case of aortic dilation. Tutarel et al [78] responded to Robicsek et al.'s study by stating that the sample size of their study was small, while the geometric variation of BAV is known to be large; and that a study by Yasuda et al [79] showed that the dilatation rate of the aortic root between BAV patients after aortic valve replacement, and those without valve replacement were the same, indicating that improved hemodynamics did not regress the dilatation rate of the aorta. This suggests that the tissue level defect, perhaps genetic, instead of hemodynamics is responsible for aortic dilation. On the other hand, den Reijer et al. [69] showed through MRI studies of BAV patients that out flow from BAVs are more angled than normal subjects, and the outflow jet angle correlated with the rate of aorta dilatation, representing a counter-evidence to Yasuda et al.'s study. These studies are but a small sample of a large body of conflicting evidence debating the relative

importance of hemodynamics and genetics in BAV morbidities. On the subject of leaflet calcification, however, there were few studies to directly demonstrate role of either tissue defects or hemodynamics.

In order to test this hypothesis, a good characterization of the mechanical environment of the BAV is first needed, including the fluid shear stresses that the BAV leaflets experiences. Further, we need to understand the response of aortic valve leaflet tissues exposed to BAV mechanical environment.

2.6. Treatment of Aortic Valve Disease

Currently, calcific aortic stenosis is treated with valve replacement. The diseased native aortic valve is replaced with a prosthetic valve. Prosthetic valves have been successfully used in heart valve replacements for over 40 years, and are capable of extending lives for about 10-20 years. However, prosthetic valves will eventually fail, or the patient will eventually die from complications related to the prosthetic valves. Thus, there is no satisfactory therapy for aortic valve calcification currently.

There are three broad categories of prosthetic aortic valves: mechanical valves, biological valves, and trans-catheter valves (Figure 2-19). Mechanical valves are prosthesis manufactured from non-biological tissues. There are currently three basic designs or classifications: the ball and cage, the tilting disc, and the bileaflet. Mechanical valves result in the exposure of blood to high shear stresses during forward flow (since the valve components are rigid and some component obstructs flow [38, 80, 81]) and during diastolic blood leakage (since many mechanical valve cannot provide complete

occlude, and have small holes where blood leaks back at high velocities [82, 83]). High shear stresses causes platelet activation and blood lysis, which lead to thrombosis. Further, certain valve designs result in regions of low velocity fluid recirculation, which lead to thrombosis as well. Thrombosis in patients can result in thromboembolic events, where blood clots break loose, and get lodged in smaller vessels, resulting in heart attacks, strokes or other organ failures. Patients with mechanical valve implants must therefore be under a life-long anti-coagulation therapy, which is harmful [84].

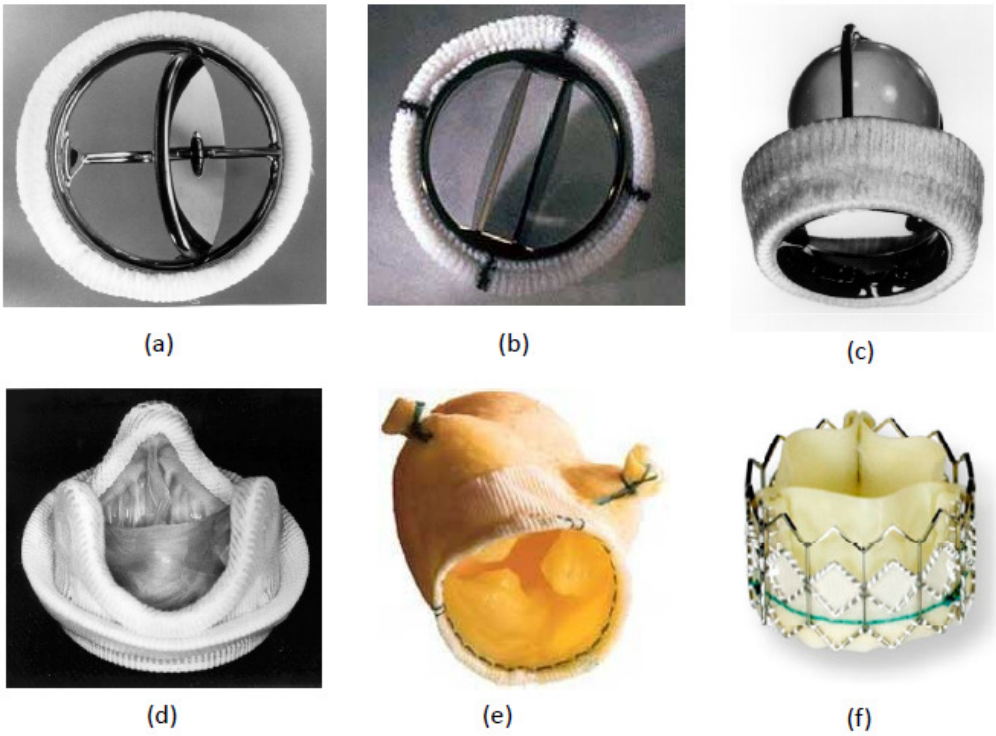

Figure 2-19. Various prosthetic valve designs. (a) a tilting disc mechanical valve; (b) a bileaflet mechanical valve; (c) a ball and cage mechanical valve; (d) a porcine bioprosthetic valve; (e) a porcine stentless valve; and (f) a trans-catheter valve. Adapted from [85] and http://www.heart-valve-surgery.com/heart-surgery-blog/2009/09/01/sapien-aortic-valve-replacement-trial/

Biological valves are prosthesis manufactured from animal tissues, usually from cows, horses or pigs. These valves can be made from animal pericardium or from the actual aortic valve of these animals. Biological valves are aggressively treated to prevent host immune rejection of the prosthesis, and consequently, they cannot be biologically assimilated into the host cardiovascular system, resulting in a lack of regeneration of the valve tissues. Biological valves thus fail eventually due to structural failures after extended duration of wear and tear.

Trans-catheter valves are the newest addition to the prosthetic valve market. Although they are essentially biological valves delivered through catheters, these valves deserve a spate classification due to the novelty of their implantation mechanism, and due to the different target patients (trans-catheter valves are implanted in patients who have high risk of mortality under the surgical valve replacement therapy). Trans-catheter valves suffer from similar shortcomings of biological valves, and have further performance shortcomings: over 50% of these valves have regurgitation, of which most cases are peri-valvular regurgitation.

The current therapy for calcific aortic stenosis is far from satisfactory. Although they do improve patient standard of living, they have limited durability and may cause blood damage, stroke and blood-related complications. There is thus a need for a greater understanding of the disease and its possible causes, such that improved therapies can be derived in future.

2.7. Aortic Valve Mechanobiology

2.7.1. Adverse Mechanical Forces' Role in Aortic Valve Calcification

One of the hypotheses on the cause of aortic valve calcification disease is that adverse mechanical environment elicits adverse biological responses from the aortic valve leaflets, which on the chronic basis leads to calcification.

Past investigations have shown that the aortic valve leaflet is biologically sensitive to its mechanical environment. Isolated mechanical forces, including membrane tension, pressure, and fluid shear stresses were shown to affect the remodeling, inflammatory and oxidative responses of aortic valve leaflet tissues in *ex vivo* and *in vitro* experiments [3-6, 86-91]. Since these responses are relevant to clinically observed aortic valve calcification [92], it has been proposed that the cause of calcification could be exposure to adverse mechanical force environments.

In terms of the effects of pressure on valve biology, Xing et al showed that valve leaflet responded biological to cyclic pressure in a magnitude and frequency dependent manner [6, 86]. For example, increase in pressure magnitude and decrease in pressure frequency increased collagen and sGAG synthesis. Warnock et al reported that elevated cyclic pressure significantly down-regulated osteopontin and up-regulated VCAM-1, indicating inflammation [93].

In terms of the effects of membrane tension on valve biology, Balachandran et al [88] reported that cyclic stretch stimuli maintained the levels of α-SMA at the native level, but statically incubating the leaflets reduced the α-SMA levels, and that cyclic stretch induced an increase in collagen content and decrease in sGAG content of valve leaflets. Balachandran et al. [3] further found that excessive cyclic stretch resulted in increased

apoptosis and adverse remodeling responses, which are responses relevant to aortic valve calcification. Metzler et al. [91] stretched aortic valve endothelial cells seeded on flexible membranes, and reported that reduced stretch as well as excessive stretch elicited inflammatory responses. Inflammatory markers such as VCAM-1, ICAM-1 and E-Selectin were up-regulated at these conditions. This indicated that alterations from the native environment can lead to pathology. Merryman et al. [94] stretch whole leaflet tissues in a uniaxial stretch bioreactor, and found that elevated levels of TGF-β1, in the presence of cyclic stretch, can result in synergistic increase in contractile and biosynthetic proteins, indicating that TGF-β1 could be an important cue in eliciting calcification disease.

In terms of the effects of fluid shear stress on valve biology, Butcher et al. [4] showed that the exposure aortic valve cells to shear stress down-regulated inflammatory and oxidative gene expressions, as opposed to static culture. These observations were made after microarray comparisons of RNA from aortic valve cells cultured under 20 dyn/cm^2 steady shear stresses or under static condition. Sucosky et al. [5] found that exposing the valve leaflets to altered, non-physiological shear stresses up-regulated inflammatory responses, which is a mechanism highly involved in valve calcification. Valve remodeling was also found to be affected by shear stresses: Platt et al. [87] found that shear stresses can regulate levels of Cathepsin L and MMPs in porcine aortic valve leaflets. This is significant because valve remodeling and activities of MMPs are known to be involved in human valve calcification [95]. All of these studies showed that certain patterns of shear stresses or lack of which can elicit pathological responses relevant to aortic valve calcification, suggesting that fluid shear stresses play a role in calcification.

A number of other studies described findings of various aspects of aortic valve leaflet biology which were affected by altered specific mechanical forces, and Butcher et al provided a review of the field of aortic valve mechanobiology studies [96].

The hypothesis that adverse mechanical environments play a role in aortic valve calcification is corroborated by clinical observations. For example, epidemiological studies have demonstrated a correlation between hypertension and the occurrence of aortic valve calcification: Rabkin provided a review of several epidemiology studies, and found that hypertension was related to aortic valve sclerosis with an odds ratio of 1.23-1.74 [97], indicating that hypertensive individuals are more likely to develop aortic valve sclerosis. A possible explanation for this is as such: hypertension imparts excessive pressure on valve leaflets to cause additional tension and stretch in the leaflets, which on the chronic basis, may have elicited active pathological cellular processes to cause calcification.

In terms of fluid shear stresses, it has been observed that the non-coronary leaflet of the aortic valve is more susceptible to calcification, which may be explained by the reduced shear stresses from the lack of diastolic coronary flow [13]. Further, calcification nodules on aortic valve leaflets have been observed to be exclusively localized on the aortic surface of the leaflets. It has been proposed that this phenomenon is due to the exposure of the aortic surface to disturbed shear stresses, which elicited pathological biological response that leads to calcification; whereas the exposure of the ventricular surface to undisturbed shear stresses protected the ventricular surface to pathological responses and prevented calcification [8, 9]. On the other hand, however, some investigators attributed this side specificity of calcification to differing phenotype of

endothelial cells on either side of the valve leaflet: Simmons et al. [98] profiled transcriptional expression of valvular endothelium isolated from both sides of porcine aortic valve leaflets, and found over 584 transcripts which were differentially expressed. Multiple inhibitors of calcification were significantly less expressed by the fibrosa side, which may have contributed to the exclusive localization of calcification to the fibrosa side.

2.7.2. *Ex Vivo* Experimentation

The investigation of the role of fluid shear stresses in aortic valve calcification biology can be performed with *ex vivo* experimental methodologies. Some important preliminary work by past investigators essential to this thesis is reviewed here.

Ex vivo culture experiments involve harvesting aortic valve leaflets from the slaughterhouse within 20 minutes of slaughter, transporting the valves to the laboratory in ice-cold sterile PBS, and then cultured in them in sterile bioreactors. Previous work using an organ culture system, which cultures the entire porcine aortic root in a pulsatile flow loop filled with culture media, has shown that such treatment of porcine aortic valve leaflets can preserve the native biology and structure of the valve tissues [99]. The native levels of collagen, sGAG and elastin were maintained, and so were the number of apoptotic and proliferating cells. The level of α-SMA expression was qualitatively preserved, the endothelial lining appeared to retain its native structure and the general tissue structure as shown by Hemotoxylin and Eosin stain on leaflet sections was preserved.

Further, the cone and plate bioreactor can be used to study the effects of shear stresses on the biology of aortic valve leaflets. This bioreactor has been extensively validated, as detailed by Sucosky et al [100]. This bioreactor consist of a dish with a plate at the bottom, where aortic valve tissues are held flush to the surface of the plate; and a cone at a small distance above the plate, which is rotated by a servo motor with a specific pattern programmable into the motor controller (Figure 2-20). The rotational motion of the cone will induce rotations in the media fluid between the cone and the plate, which will result in shear stresses imparted on the valve leaflet surface in the circumferential direction. Figure 2-20 shows the schematic of the cone and plate system. Shear stress on the plate is calculated by the equation:

$$\tau_w = \rho \nu \omega_c \left[\frac{r_c}{h_c + r_c \alpha_c}\right] \qquad \text{(Equation 2-1)}$$

Where τ_w is the wall shear stress, ρ and ν are the density and the viscosity of the fluid, ω_c is the angular velocity of the cone, and r_c is the radial coordinate of the point of shear stress calculation on the plate, h_c is the gap between the apex of the cone and the plate, and α_c is the cone taper angle, which is 0.5 degrees. This equation for calculating shear stress experienced by the plate is validated by computational fluid dynamics simulation of the cone and plate bioreactor, as well as by Laser Doppler Velocimetry measurements of the apparatus. Further, the actual rotational velocity measured by the tachometer on the motor was shown to match the desired velocity programmed into the controller.

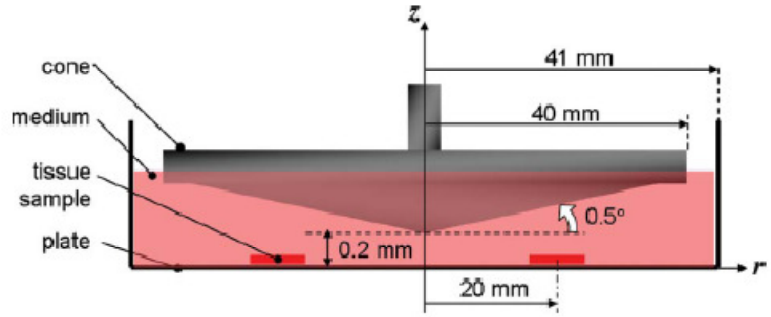

Figure 2-20. *Schematic of the cone and plate bioreactor. Adapted from [100].*

Since *ex vivo* experiments can only be performed for a limited period of time, an osteogenic media was developed to accelerate the calcification response of the valve leaflets, so that the calcification response to different mechanical forces can be studied. Methods associated with the use of the osteogenic media is detailed by Balachandran et al [89]. The osteogenic media is composed of normal Dulbecco's modified Eagle's media supplemented with 10% fetal bovine serum; 1mM β-glycerophosphate; 10 µm dexamethasone; 4.7 mM phosphates; and 1ng/ml TGF-β1. Porcine aortic valve leaflets cultured under this media was observed to form calcium nodules close to the endothelial layer similar to clinically observed calcification nodules [15, 89], as shown in figure 2-21.

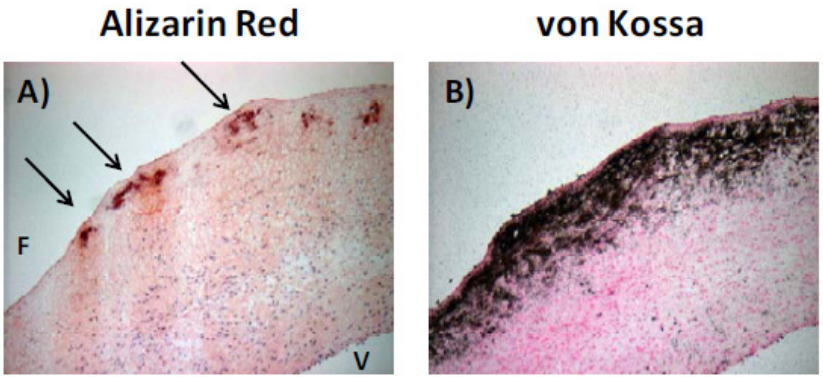

Figure 2-21. *Alizarin Red and von Kossa stains on thin sections of aortic valve leaflet cultured in the osteogenic media in an ex vivo experiment, demonstrating calcium nodule formation. Adapted from [15]*

2.8. *In Vitro* Velocimetry Techniques

In this sub-section, the fundamentals of Laser Doppler Velocimetry and Particle Image Velocimetry, which are two techniques heavily used in this thesis, is reviewed.

2.8.1. Laser Doppler Velocimetry

Laser Doppler Velocimetry (LDV), also known as Laser Doppler Anemometry (LDA), is a technique for measuring the velocity of fluids. In LDV, a pair of collimated, monochromatic and coherent laser beams cross at the probe volume or the measurement point within the flow. These two beams are usually obtained by splitting a single beam, thus ensuring coherency between the two. Due to these characteristics of the laser beams, they will interfere at the probe volume, and generate a set of straight light fringes, alternating between light and darkness at fixed fringe spacing. The fringe spacing can be calculated from following equation:

$$d_f = \frac{\lambda}{2 \sin \alpha_L} \quad \text{(Equation 2-2)}$$

where λ is the wavelength of the laser light in the fluid media and α_L is the half angle of the laser beam in that media. When a particle moves through these fringes, it will scatter a signature pattern of light that alternates between brightness and darkness, known as the Doppler Burst. Characteristics of the Doppler burst, such as its dominant frequency component can be used to calculate the velocity of the particle.

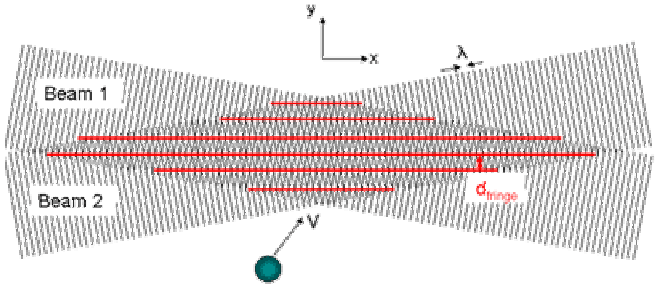

Figure 2-22a. *LDV laser fringes resulting from the interference of two coherent, collimated, monochromatic beams. Adapted from http://www.erc.wisc.edu/ldv.php.*

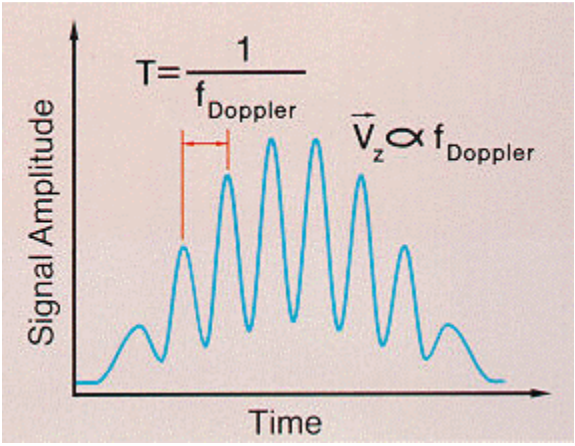

Figure 2-22b. *Doppler Burst pattern resulting from a particle crossing the LDV probe volume fringes. Adapted from http://clients.dedicatedconsulting.com/aerometrics/ldv.html.*

To allow the resolution of the direction of the particle motion within the probe volume, a frequency shift in one of the two laser beams is induced, through the use of a Brag cell. A frequency shift of 40 or 80 MHz is usually induced. This frequency shift will cause the fringe pattern to move in a specified direction at a constant speed. The velocity of particles within the probe volume fringes will then be calculated as the Doppler shift from the speed of the fringes themselves.

$$V_f = \frac{\text{Doppler frequency}}{\text{probe volume fringe spacing}} \qquad \text{(Equation 2-3)}$$

In LDV, each pair of laser beam provides the capability for measuring one velocity component. Two or three pairs of laser beams can be used concurrently, each with a unique light wavelength (typically green, blue and purple), and can be used to make measurements at the same point in the fluid. Coincident measurements of more than one velocity component can be done this way, which improves the data quality.

The use of LDV in a fluid media of different optical density will require careful consideration of the optical distortions. If the beams always pass through flat surfaces, beam angle distortion and the light wavelength distortions will cancel out, leaving the fringe spacing the same as if there is no change in optical density. However, if the beam angle is altered disproportionately from the light wavelength distortion, then the fringe spacing needs to be recalculated with equation 2-2. Further, the probe volume dimensions (width d_m, and length l_m) will have a different dimension in a media or different optical density, according to the following equations:

$$d_m = \frac{4\lambda f}{\pi D_e E} \quad \text{(Equation 2-4)}$$

$$l_m = \frac{d_m}{\tan \alpha_L} \quad \text{(Equation 2-5)}$$

where λ is the wavelength of the laser light in the media, f is the focal length, D_e is the initial beam diameter, E is the beam expansion ratio, and α_L is the half beam angle in the media. Due to Snell's law, displacement of the LDV probe will lead to a different displacement of the probe volume, and this needs to be accounted for.

2.8.2. Particle Image Velocimetry

PIV is another optical method for measuring fluid flow velocities (figure 2-23). PIV allows the measurement of an entire field of velocity at a time. The fluid is again seeded with micro-particles, which are assumed to faithfully follow the flow dynamics of the fluid around it. A pair of PIV images is acquired in order to compute the flow field. For each PIV exposure, a laser sheet is used to illuminate a plane within the flow body, such that all the particles within this plane will be illuminated, and a digital camera positioned to view the laser sheet plane at a normal angle, is used to acquire an image of the illuminated particle. The illumination of the plane of interest is tightly synchronized with the acquisition of the image through external trigger controls between the camera and the laser. In this manner, two images are taken with very short time difference between them, or two exposures to the same image with this time difference are taken. The pattern of particle motion between these two images can be used for velocity field computation.

The computation of velocity field is achieved through a cross correlation algorithm for image pairs. Each camera image is divided into rectangular regions called interrogation areas, and the correlation between interrogation areas in the first image to interrogation areas in the second image displaced by a certain distance is obtained, which corresponds to the degree of match in the two particle images with a displacement in the viewing window in the second image. The peak in the cross correlation map signifies the most probable velocity of the particular interrogation area. In this manner, the entire field of velocity vectors can be obtained. To speed up computation, discrete fast Fourier transformation is used in the processing.

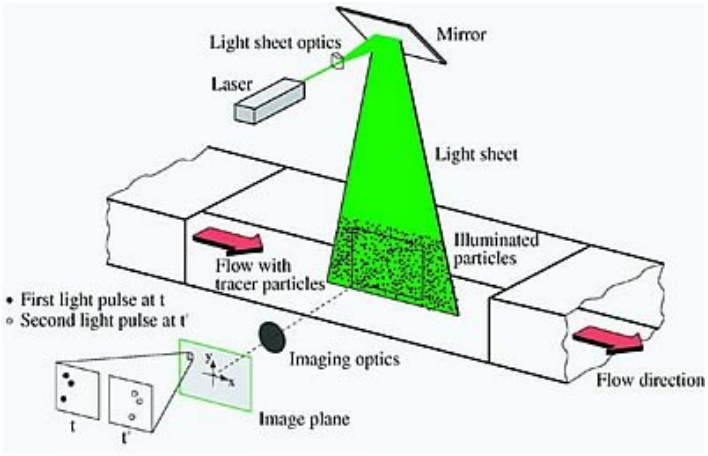

Figure 2-23a. *The setup for performing Particle Image Velocimetry. Adapted from http://www.dlr.de/as/en/DesktopDefault.aspx/tabid-183/251_read-12796/gallery-1/gallery_read-Image.5.1574/*

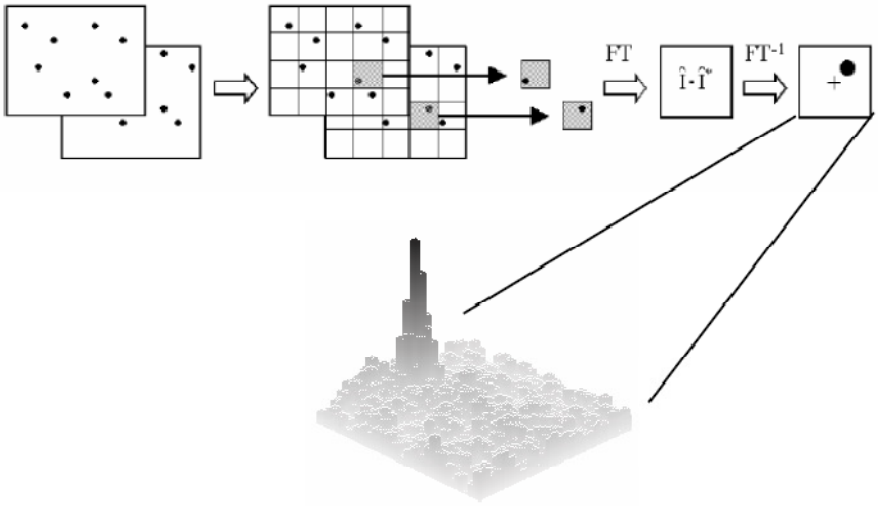

Figure 2-23b. *Processing sequence of PIV raw image pairs. Each image is divided into smaller interrogation windows. The image intensities of the interrogation windows from the two images are cross-correlated to obtain the most probable particle displacement. Adapted from [101].*

CHAPTER 3

HYPOTHESIS AND SPECIFIC AIMS

3.1. Rationale for Thesis Research

The work in this thesis will characterize the shear stress environment of the aortic valve leaflet in the normal tricuspid aortic valve and the congenital malformed bicuspid aortic valve using an *in vitro* setting. Further, preliminary ex vivo culture experiments will be conducted to investigation the effects of the various shear stress characteristics on biology of the valve leaflet tissues.

The urgency of this research can be demonstrated in the prevalence of the disease [1, 2], and in the morbidity and mortality risk associated with it [60]. It has been hypothesized that adverse mechanical forces play a role in causing aortic valve calcification [96, 98], and there are evidence that adverse mechanical forces (including fluid shear stress) can elicit pathological responses from valve leaflets similar to human aortic valve calcification [3-7]. Yet, the fluid shear stress environment of the aortic valve is incompletely understood, and data is lacking in the literature, further pointing to the urgency of the current work.

To date, only one study has attempted to experimentally measure the magnitude of shear stresses on the ventricular surface of the aortic valve [42]. This study, however, was performed with steady and fully developed flow through the aortic valve. The resulting velocity profile and thus leaflet surface shear stresses will be different from that of a pulsatile flow, due to flow development and Womersley effect in the pulsatile case. Several authors have attempted simulations of the aortic valve, and have reported shear

stresses. These studies, however, are idealized and have shortcomings. For example, Ge et al [43] performed quasi-steady simulations of flow through a tri-leaflet aortic valve, and although they showed complex fluid leaflet shear stress results, it is uncertain if the fully pulsatile case will be similar to the quasi-steady case. Morsi et al [44] performed simulations of the aortic valve taking into account fluid-structure interactions in the valve. However, no sinuses were modeled, and the bulk flow rate was modeled to the peak Reynolds number of 600, much smaller than the physiological Reynolds number, which is about 6000. The state of the art of numerical simulation techniques face challenges in simulating the aortic valve, such as difficulties in modeling the complete closure of the valve, in achieving sufficiently high Reynolds number, in meshing the fluid structure boundary with sufficient resolution, and in modeling the mechanical behavior of the valve leaflets.

The lack of complete understanding of the shear stress environment may be one of the bottlenecks to furthering our understanding of the calcification and remodeling mechanisms involved with the aortic valve. For example, in *ex vivo* culture experiments investigating the effects of fluid shear stresses on the biology of the aortic valve tissues / cells, steady and fixed-magnitude shear stresses were used [4, 87, 102], or idealized shear stress waveforms such as sinusoidal waveforms were used [5, 100]. These waveforms differ from the actual shear stress waveforms, but in the face of lack of further information, idealized waveforms have to be used. It is unclear if the results reported in these studies will change if realistic shear stress waveforms are used. The proposed work on characterizing the shear stress mechanical environment of the normal aortic valve serves to cover this gap in the literature.

The proposed work on studying the shear stress environment of the bicuspid aortic valve is important because of the high prevalence of bicuspid aortic valve disease [10, 11]. The bicuspid aortic valve case serves as a good test bed for the hypothesis that fluid shear stress may play a role in aortic valve calcification and inflammation mechanisms. The bicuspid valve has a significantly altered geometry, indicating that the fluid mechanical environment could most likely be significantly different. Further, the bicuspid valve is associated with significantly higher risk of leaflet calcification [12, 13], which may be partially a result of drastically altered mechanical environment. Hence both the fluid shear stress environment of the bicuspid valve leaflets and the biological response of aortic valve tissues to this shear stress environment deserve investigation.

With a good understanding of the mechanical environment of both the normal tricuspid aortic valve and the malformed bicuspid aortic valve, we can perform detailed mechanobiology experiments investigating the biological pathways that lead to calcification. Such knowledge may eventually inspire novel pharmacological curative or preventive therapies targeting specific intermediate proteins or nucleic acids in the pathway. The proposed *ex vivo* culture experiments in the current study serve as prelude to these investigations, providing preliminary data on what specific shear stress characteristics elicit patho-biological response from aortic valve tissues.

3.2. Hypothesis

The Hypothesis for this thesis is that:

The hemodynamic and anatomic characteristics of the aortic valve alters its fluid shear stress environment

3.3. Specific Aims

3.3.1. Specific Aim 1: Establishment of a Method for Measuring Shear Stress on the Surface of Aortic Valve Leaflets

In this specific aim, the methods for measuring shear stresses on the aortic valve leaflets *in vitro* are developed. A method for tracking the position of the valve leaflet using the intensity of the back-scattered LDV laser light and a method for measuring two-dimensional dynamic shear stresses on the surface of the aortic valve leaflet surface are developed. A series of validation experiments will then be performed: (1) The back-scattered light leaflet tracking method will be validated on both a static valve leaflet surface as well as on a dynamic object; (2) the ability of the LDV to make velocity measurements very close to the surface of a biological tissue will then be validated using steady flow loops; (3) calculations will be performed to ensure that laser vibrometry / interferometry effects are not adversely affecting velocity measurements despite the motions of the valve leaflets; (4) correction factors for optical distortions in the beam angle due to refractive index differences between the flow loop fluid and the acrylic chamber will be derived; (5) an order of magnitude analysis will be performed to estimate the errors involved in the misalignment between the LDV probe and the valve leaflet surface; (6) calculations will be made to ensure that the LDV measurement spatial resolution is sufficient to resolve velocities within the boundary layer of flows in the aortic valve.

The proposed methods of viscous shear stress measurements, however, will not be validated in the case where the valve leaflet was dynamic, due to difficulty in obtaining the true shear stress for comparison with the measurements. Validation will be only

performed for the leaflet tracking method, and for velocity and shear stress measurements with a stationary leaflet. However, the valve leaflet dynamics will be investigated to show that the motions (velocities and accelerations) are small during the fully opened and fully closed positions when shear stresses were obtained, such that the stationary leaflet validation is expected to be sufficient.

3.3.2. Specific Aim 2: Measurement of Shear Stresses on the Leaflets of the Normal Tricuspid Aortic Valve

In this specific aim, the dynamic fluid shear stresses environment experienced by the normal tricuspid aortic valve leaflets will be measured. Using the validated method developed in specific aim 1, shear stresses will be measured at the center of the aortic surface of the leaflet of a native tissue valve model, and measurements will be performed under various hemodynamic conditions spanning various stroke volumes and heart rates, to investigate the effects of stroke volume and heart rate on shear stress. Further, using two transparent polymeric prosthetic tricuspid valve as the valve models, shear stresses experienced by the ventricular surface of the normal tricuspid aortic valve will be measured. A theoretical model for ventricular surface shear stresses will be developed, as an order of magnitude analysis to obtain the general features of ventricular surface shear stresses, and applied to *in vivo* hemodynamics to predict general characteristics of aortic valve ventricular surface shear stresses *in vivo*. The characterization of the ventricular surface shear stresses will allow the comparison of differences in shear stresses experienced by the two surfaces of the aortic valve. The theoretical model does not completely mimic in vivo geometries, given that it assumes a straight tube geometry, but

is intended as a order of magnitude study to obtain general features of the shear stress waveforms.

3.3.3. Specific Aim 3: Measurement of Shear Stresses on Leaflets of the Aortic Surface of the Congenital Bicuspid Aortic Valve.

In this specific aim, the dynamic fluid shear stress environment experienced by the leaflets of the congenital bicuspid aortic valve will be characterized and compared to that of the normal tricuspid aortic valve. A congenital bicuspid aortic valve model will first be constructed by surgical manipulation of fresh porcine aortic root tissues. Shear stresses will then be measured on the aortic surface of the bicuspid aortic valve model leaflets. The shear stress data will be analyzed for magnitude and stability, and compared to those measured in the normal aortic valve leaflet.

3.3.4. Specific Aim 4: *Ex Vivo* Studies of the Effects of Fluid Shear Stresses on Porcine Aortic Valve Leaflet Biology

In this specific aim, preliminary work investigating the effects of various fluid shear stress patterns on the biology of aortic valve leaflets will be performed. Fresh porcine aortic valve leaflets will be cultured in the cone and plate bioreactor and exposed to various shear stress patterns of varying shear stress magnitudes, frequencies, and unsteadiness. Further, the valve leaflets will also be exposed to salient features of fluid shear stresses experienced by the bicuspid aortic valve, as measured in specific aim 4. The culture media will be supplemented with osteogenic factors to accelerate calcification responses of the tissues. The amount of calcification resulting from exposure

to each type of shear stress pattern will then be assayed for and compared with qualitative stains of samples on glass slides (Alizarin Red and Von Kossa) and a quantitative colorimetric assay (the Arsenazo calcium assay).

CHAPTER 4

MATERIALS

In this section, all equipment and supplies utilized in this thesis are described. The flow loops used for specific aims 1 to 3 are first described. Next, the valve models used for specific aims 2 and 3 are described. Thereafter, the LDV system, the PIV system and the ex vivo culture system (the cone and plate system) are described.

4.1. Flow Loops

Velocity measurements were performed with LDV in three different flow loops. The first two flow loops were used for validation of methods in specific aim 1, while the third flow loop was used for measuring shear stresses in various valve models in specific aims 2 and 3.

The first was a straight tube steady flow loop with a piece of fixed and dyed porcine aortic valve leaflet attached to the wall (figure 4-1). This piece of valve tissue was obtained from the local slaughterhouse and fixed within the 12h of obtaining it. The second flow loop was composed of the valve model connected to a centrifugal steady pump, such that steady flow through the valve could be set up (figure 4-2). In this flow loop, steady flow conditions allowed the valve leaflet to stay at the opened position in a relatively motionless manner, so that the motion of valve leaflets such as that in the pulsatile flow loop will not confound velocity measurements, such that validation work can be performed in a simplified environment.

The first two flow loops were utilized to verify that the reflection of laser light on the surface of the valve leaflet would not cause inaccuracies in velocity measurements close to the leaflet surface, and that the point of zero velocity corresponded with the leaflet location indicated by the back-scattered light intensity leaflet tracking method, described in section 5.1.3.2, indicating that the no-slip condition applied. In the first flow loop, the measured velocities were checked to ensure agreement with theoretical expectations. The second loop was set up to provide an extension to the validation work provided by the first flow loop. It was more similar to the physiologic pulsatile flow loop than the straight tube flow loop (first flow loop).

The third flow loop was composed of the valve model exposed to physiologic pulsatile flow conditions (figure 4-3), which was the setting of the dynamic fluid shear stress data obtained. For all three flow loops, the working fluid used was a 36% glycerin aqueous solution with blood-matching dynamic viscosity, so as to preserve *in vivo* flow characteristics. This blood-analogue fluid was selected also because it was not damaging to native tissues, and was fairly close to the optical density of the acrylic plastic chambers, minimizing distortions caused to the LDV laser beam path. This fluid had density of 1.087 g/cm3, dynamic viscosity of 3.5 cSt, and kinematic viscosity of 3.8 cP, and a refractive index of 1.39. In contrast, the refractive index of the acrylic chambers was 1.49.

The three flow loops are described in greater details in the following sub-sections.

4.1.1. Flow Loop 1: Straight Tube Steady Flow Loop

The straight tube steady flow loop is shown in figure 4-1. The loop was driven by a centrifugal pump (Model 2E-N, Little Giant Pump Company, Oklahoma City, OK),

which was immersed in a fluid reservoir, and controlled by a variable transformer (SC-10M 10 Amp Variable Transformer, China). A compliance chamber was placed downstream of the pump to smooth out pressure and flow oscillations to achieve relatively constant flow. Flow was channeled into an acrylic tube 35 cm in length and 1.91 cm in internal diameter before being channeled back to the reservoir.

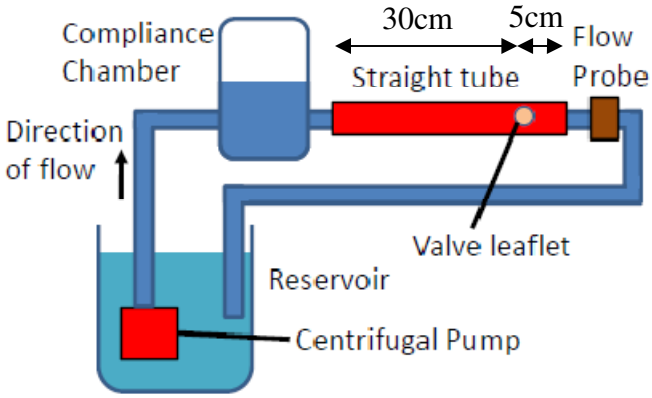

Figure 4-1: *Schematic of the 1st flow loop: steady flow loop with a circular tube cross-section with a piece of native aortic valve leaflet glued to the wall.*

A piece of aortic valve leaflet was excised from a fresh porcine heart, fixed overnight in 0.1% gluteraldehyde, and dyed black with a tissue dye (Black Shandon® Tissue Marking Dye, Thermoelectron Corporation, Pittsburgh, PA) . This piece of leaflet was then attached to the wall of the tube with conventional cyano-acrylic glue 30 cm from the flow entrance and 5 cm from the flow exit. Two flow rates were generated in the flow loop for experimentation: 3.5 L/min and 7 L/min. Flow was measured with an ultrasonic inline flow probe connected to a flow meter (T108, Transonic System, Ithaca, NY).

4.1.2. Flow Loop 2: Valve Model Steady Flow Loop

The valve model steady flow loop is shown in figure 4-2. Similar to the first flow loop, the second flow loop was also driven by a centrifugal pump (Model 4E-34N, Little Giant Pump Company, Oklahoma City, OK) controlled by the same variable transformer, and contained a similar compliance chamber to smooth out pressure and flow variations. Flow measurements were performed with the same flow probe and meter (T108, Transonic System, Ithaca, NY). The only difference from the first loop was the substitution of the valve model for the straight tube. The valve model is described in 4.2.2, and engineering drawings for the chamber can be found in appendix A1. 7 L/min and 14 L/min of flow were generated in the flow loop for experimentation. These were within the range of physiologic flow rates in the aortic valve (0-25 L/min) but not too high to cause instabilities such as leaflet fluttering.

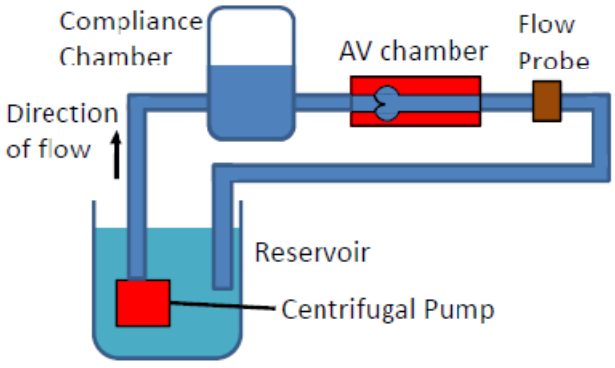

Figure 4-2: *Schematic of the 2nd flow loop: steady flow loop with the native tissue valve model.*

4.1.3. Flow Loop 3: Valve Model Pulsatile Flow Loop

The third flow loop was the Georgia Tech Left Heart Simulator, a pulsatile flow loop capable of generating physiologic pressure and flow waveforms, as shown in figure 4-3. This flow loop has been used in several previous works [81, 103-105].

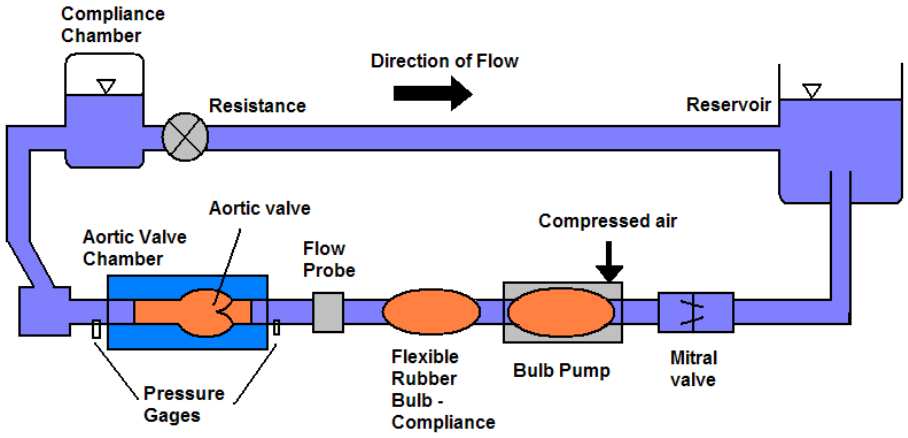

Figure 4-3: *Schematic of the 3rd flow loop: pulsatile flow loop with either the native tissue valve models (normal and congenital bicuspid valve models) or the polymeric valve model. This loop is dubbed the Georgia Tech Left Heart Simulator in the Literature, and is capable of mimicking physiologic flow and pressure conditions [81, 103-105].*

Circulation in this loop was driven by a bulb pump - a silicone bulb encased within an acrylic and metal housing. The fluid-filled bulb was rhythmically compressed by injecting compressed air into the space surrounding the bulb within the housing. Compressed air was provided by an air compressor (Craftsman model 921 air compressor, Sears Holdings Corp., IL). Compressed air delivery was controlled by 3 solenoid valves (model 56C-12-111CA, MAC Valves Inc., Wixom, MI), which in turn was controlled by a custom built pulse programmer (schematic shown in figure 4-4). The pulse programmer box was programmed to provide 120V AC power to solenoid valves during specific durations within the cardiac cycle to turn the solenoid valves on. Solenoid valves allowed

compressed air to pass through them when they were turned on, but would block air flow when turned off. Solenoid valve 1 and 2 were turned on during systole to provide pressure to compress the bulb and drive fluid flow. At the end of systole, solenoid valves 1 and 2 were off, and solenoid valve 3 was turned on to allow pressurized air surrounding the bulb to escape, thereby allowing the bulb to relax and "ventricular/bulb" filling to occur. Since the solenoid valves were 2-state valves (either opened or closed), two solenoid valves were used to control the systolic phase to provide greater degree of freedom in generating systolic waveforms. The timing of turning on these two valves could be adjusted with the pulse programmer box and the amount of air delivered by each valve can be tuned by adjusting the resistances to provide desired outcomes.

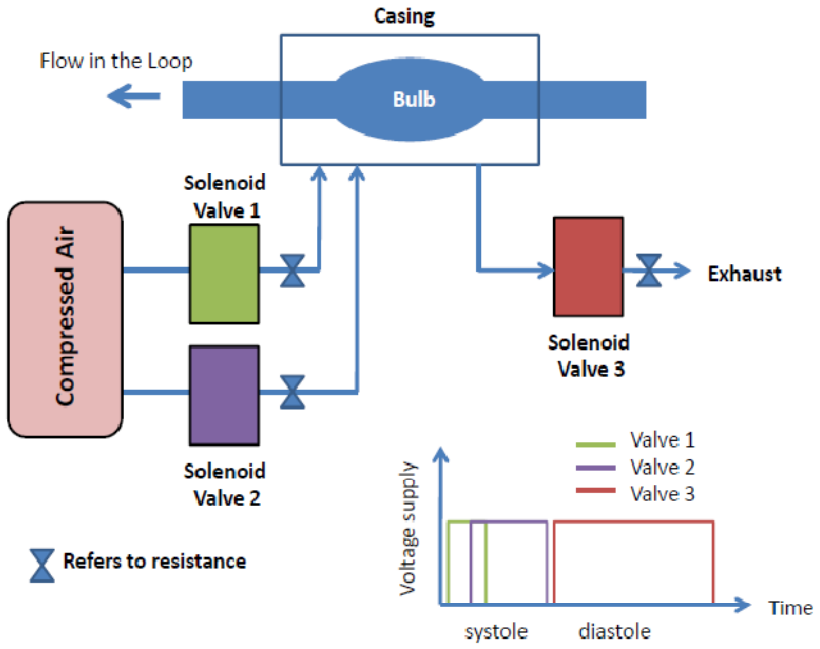

Figure 4-4. *Schematic of the mechanisms of the bulb pump. The plot at the lower right shows the timing of voltage supplies (120V) provided to the different solenoid valves.*

In the flow loop, a bi-leaflet mechanical valve upstream of the bulb pump acted as the mitral valve. The subject aortic valve model being studied was placed downstream of

the bulb pump. A compliance chamber and a resistance clamp simulated the compliance and resistance of the cardiovascular system, and were placed downstream of the aortic valve. The compliance chamber consisted of a cylindrical chamber 13 cm in diameter and 23 cm in height, and has an inlet and outlet connected to the loop at the bottom of the chamber. Air trapped at the top of the chamber acted as the complaint material; by controlling the volume of air in the chamber, the level of compliance in the loop can be controlled. The resistance, on the other hand, consisted of a pinch clamp on the soft rubber tubing portion of the loop.

Pressures and flow in this loop were measured with commercial electronic probes. Aortic pressure was measured approximately 10 cm downstream of the annulus of the aortic valve, while ventricular pressure was measured approximately 5 cm upstream of the annulus of the aortic valve. Pressure was measured via ports mounted flush with the loop tubing wall, perpendicular to the flow direction. These ports were connected to commercial pressure gages (Baxter Uniflow pressure transducer, Baxter Healthcare corp., Irvine, CA), which were connected to a pressure meter (Cardiomed CM 4008, Medi-Stim, Oslo, Norway). Flow, on the other hand, was measured with an inline flow probe connected to a flow meter (T108, Transonic System, Ithaca, NY). The probe was located upstream of the ventricular pressure gage port, approximately 10 cm upstream of the aortic valve annulus. No compliant material was used for the loop tubing between the aortic valve and the flow probe, to ensure that the measurements were accurate.

The outputs of the pressure meter and the flow meter were routed to the Data Acquisition System (DAQ, National Instruments, Austin, TX) and were recorded at 500 Hz for 10-30 cycles. The data acquisition system consisted of the I/O box (BNC-2110,

National Instruments, Austin, TX), which was connected to the electronic card (DAQCard-6036E, National Instruments, Austin, TX), which was placed in communication with a laptop computer through the PCMCIA port. The DAQ system was controlled by a custom-written Labview® program, known as the DAQANAL. The program allowed the acquisition of up to 8 channels of analogue signals (-10V to 10V) at up to 500 Hz, over multiple cycles.

4.2. Valve Models

In the current thesis, three valve models are employed: (1) the polymeric valve model; (2) the native tissue normal aortic valve model; and (3) the native tissue congenital bicuspid aortic valve model. The polymeric valves were used for specific aim 2, where ventricular surface shear stresses were measured, taking advantage of their transparent leaflets, which provided optical access to the ventricular side. The native tissue normal aortic valve models were also used in specific aim 2, but for aortic surface shear stress measurements, and the native tissue BAV valve models were used in specific aim 3. The BAV valve model was inserted into the two-lobed sinus chamber while the polymeric and normal native tissue valve models were inserted into the three-lobed sinus chamber.

4.2.1. The Polymeric Valve Model

Two tri-leaflet polymeric valves (AorTech, Europe) were used as valve models for measuring ventricular surface shear stresses. These valve models are shown in figure 4-5a and 4-5b. The valve leaflets are made of high silicone polyurethane copolymer

(Elast-Eon^{TM}), and valve frames are machined from poly-etheretherketone. Two valves of slightly different geometry were studied, and their characteristics are listed in table 4-1. Valve 1 was axially longer than valve 2 due to the extension of the polyurethane leaflets by about 1.1mm above the stents, but had a smaller valve orifice.

Table 4-1. *Geometric dimensions of the two polymeric valve models used for ventricular surface shear stress measurements.*

	Valve 1	**Valve 2**
Annulus Inner diameter (in mm)	24.0	24.8
Height (in mm)	17.1	16.0
Leaflet thickness (in μm)	120	150

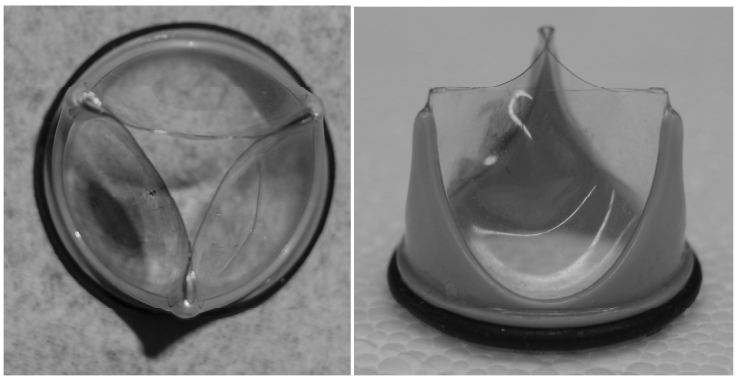

Figure 4-5a. *The first polymeric valve model.*

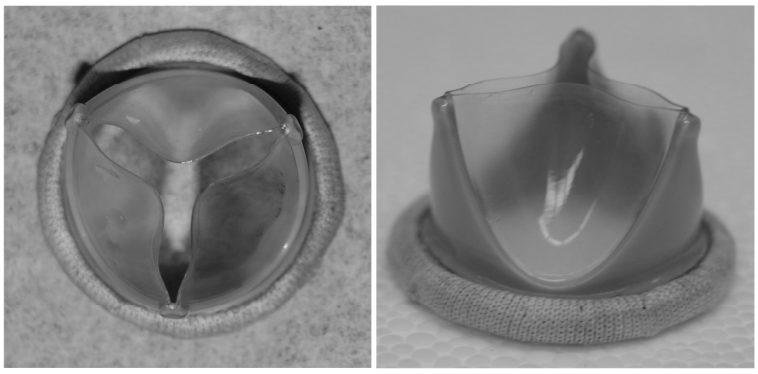

Figure 4-5b. *The second polymeric valve model.*

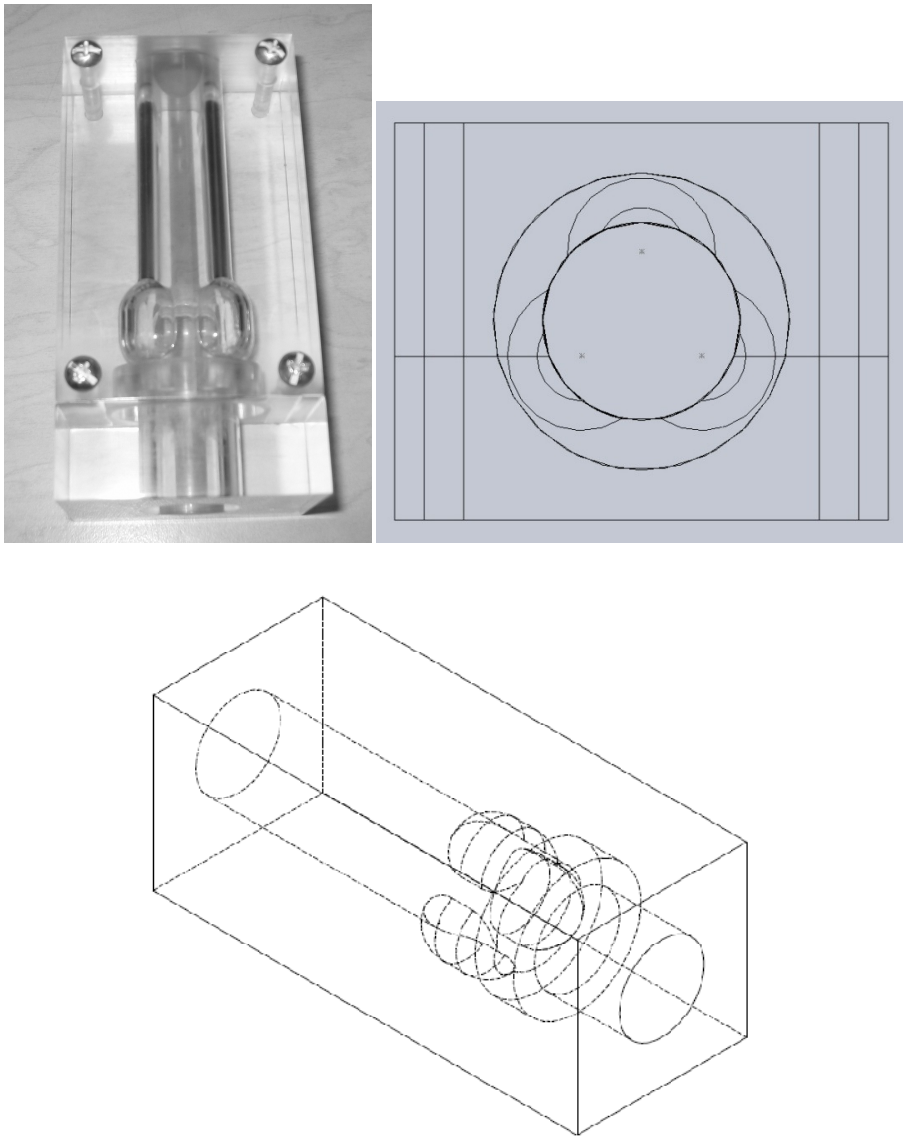

Figure 4-6. *The idealized sinus geometry normal aortic root chamber, machined from acrylic plastic. This chamber is used to house valve models in the flow loop. Engineering drawings for the chamber with dimensions are provided in Appendix A1.*

The polymeric valve was inserted into a clear acrylic aortic chamber with idealized tri-lobed sinuses so as to provide optical access for LDV measurements, and the valve and chamber collectively constituted the valve model. To mimic physiologic geometry, the acrylic aortic chamber was carefully designed to dimensionally match

those noted earlier in rubber casts of human aortic roots [24]. The axial length of the sinus space was set to be 0.9 times the annulus diameter, and the sinus radial width (from the center of the chamber) was 0.76 times that of the annulus diameter. The valve chamber is shown in figure 4-6. The engineering drawings of the chamber with dimensions are provided in Appendix A1.

4.2.2. The Native Tissue Normal Aortic Valve Model

The valve model used as the model for normal aortic valve was constructed from a fresh porcine aortic valve harvested from the local slaughterhouse. This valve is shown in figure 4-7. The fresh porcine valve was trimmed of its sinus walls, sutured to a plastic ring with three stents. It was then inserted into a clear acrylic aorta chamber with idealized tri-lobed sinuses so as to provide optical access for LDV work. The valve itself had an approximate diameter of 21mm, and height of 19mm (from base to commissure). The valve leaflets were colored black with tissue dye (Black Shandon® Tissue Marking Dye, Thermoelectron Corporation, Pittsburgh, PA) to reduce the reflection of LDV laser light off the leaflet surface. The same acrylic aorta chamber as that used for the polymeric valve models was used for this valve model.

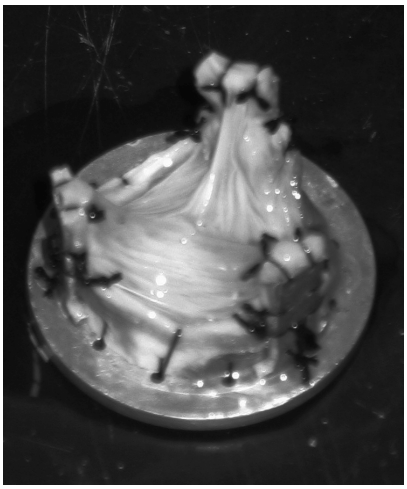

Figure 4-7. *The native tissue valve model of the normal aortic valve, trimmed and sutured to a tri-stented ring.*

4.2.3. The Native Tissue Congenital Bicuspid Aortic Valve Model

The valve model for the congenital bicuspid aortic valve was similarly constructed from fresh porcine tissues. A fresh porcine aortic root was harvested from the local slaughterhouse, and surgically modified as follows (figure 4-8): (1) the aorta was opened longitudinally between the right and left coronary leaflets; (2) two to three millimeter strips of the aortic wall was excised from the longitudinally cut edge; (3) triangular portions of the right and left coronary leaflets were excised, and the same two leaflets were then sutured together to form the fused leaflet of the BAV. While resecting and suturing the tissue, care was taken that the resultant fused leaflet was mobile, and to prevent creating too much stenosis; (4) the sinus walls of the root were trimmed away and the valve was sutured to a dual-stented plastic ring. The valves were modeled after the human BAVs studied by Robicsek et al. [76], discussed in section 2.5.2. A fusion of

the right and left coronary leaflet was chosen because this is the most common morphology of BAV, also discussed in section 2.5.2.

The entire remaining valve apparatus was fixed in 0.1% gluteraldehyde solution for 24h under mild aortic pressure (approximately 25 mmHg) such that the valve would not degrade under lengthy experimental durations. The valve was then inserted into an aortic chamber with idealized bi-lobed sinus geometry (figure 4-9). The chamber was made of acrylic to provide optical access during LDV measurements. The engineering drawings for this chamber with dimensions are show in Appendix A2. The valve in chamber was then inserted into a pulsatile flow loop and exposed to physiologic hemodynamics, and evaluated for its resemblance to clinically observed BAVs.

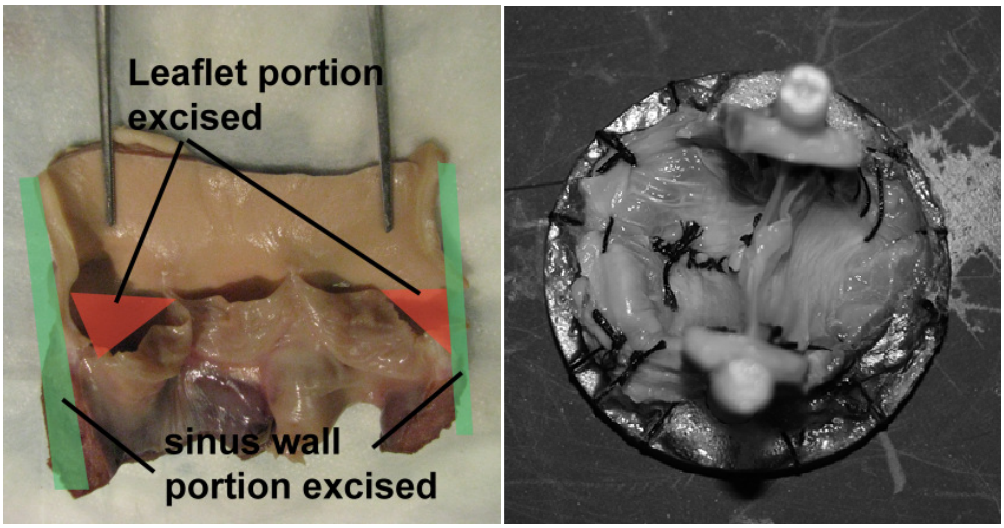

Figure 4-8. *(left) The procedure for constructing the native tissue bicuspid aortic valve model. The aortic root was first cut open, the two constituent leaflets of the fused leaflet were trimmed and a thin strip of the aortic root at the cut-edge was trimmed as well. The two constituent leaflets of the fused leaflet were sutured together and the valve was sutured to a bi-stented ring. (right) the final product: the bicuspid aortic valve model.*

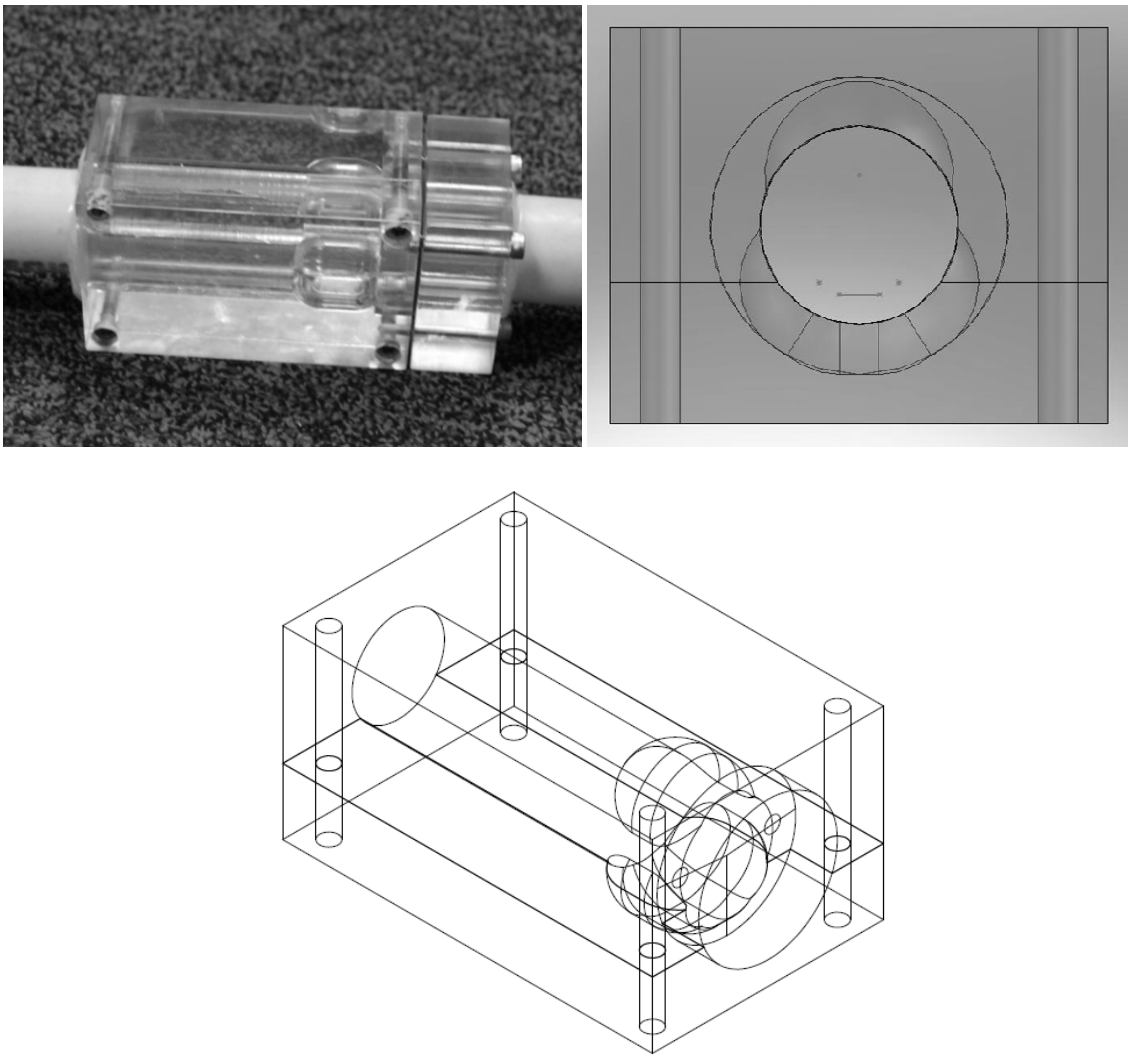

Figure 4-9. *The aortic root chamber used for the bicuspid aortic valve mode, having tow sinus spaces instead of three. Engineernig drawings of this chamber with dimensions are shown in Appendix A2.*

4.3. Laser Doppler Velocimetry Materials

4.3.1. Working Fluid Particle Seeding

The working fluid of the flow loops was seeded with silicon carbide micro particles (model 10081, TSI Inc., Shoreview, MN) to aid LDV velocity measurements. These particles had a mean diameter of 1.5 μm and density of 3.2 g/cm^2. To ensure that the fluid

was not over seeded, calculations were performed to determine the equation relating amount of seeding and the probability of having more than one particle in the probe volume. The probability of having more than one particle in the probe volume was kept to 0.2%, and the corresponding particle seeding was used as the maximum allowable amount of seeding. This would ensure that there was low chance that more than one particle will reside within the LDV probe volume, which might result in measurement dropouts.

4.3.2. Laser Doppler Velocimetry System

A fiber optic, three-component, coincident LDV system (Aerometric System, TSI Inc., Shoreview, MN) was used to measure 1D velocities in the steady flow loops and 2D velocities in the pulsatile loop with the valve models. A 4 W Argon-ion laser was coupled to a fiber drive unit, allowing color separation of the incoming primary beam. A two-component fiber optic transceiver probe with a 100 mm focal length lens was connected to the fiber drive. The resulting optics train produced an ellipsoidal probe volume, which, after accounting for the relative optical density between the flow loop fluid and air, had dimensions of 19 μm by 126 μm. Doppler signals were processed with Fast Fourier Transform based real-time signal analyzers (RSA-1000, TSI Inc., Shoreview, MN).

The LDV system had the following components (Figure 4-10): (1) Plasma tube and fiber drive; (2) transmitter and receiver; (3) computer terminal and velocity information output.

Plasma tube - A 5 W, Argon-ion laser plasma tube (Model 70 Innova, Coherent, Santa Clara, CA) was used to generate the primary multi-line laser beam, which was

subsequently passed through a fiber optic drive (Aerometrics, Sunnyvale, CA). The multi-line laser beam, which consists of different wavelength laser beams, was split by a beam splitter within the fiber drive into two beams of approximately equal intensity. The frequency of one of these beams was shifted by 40 MHz using a Bragg cell within the fiber drive, and it is referred to as the secondary beam. The two beams were separated into their green (514.5 nm), blue (488 nm), and violet (476.4 nm) components by a prism inside the fiber drive. Each of the three pairs of resulting beams, i.e. green, blue and violet beams, was channeled into a beam coupler, which is linked to two transceivers by a series of fiber optic cables.

Transmitter and Receivers - For 2D LDV measurements (using only green and blue beams), only one transceiver acting as both a transmitter and receiver was used, and the acquisition mode was backscattering. The naming convention for the different scattering mode is referenced from the receiver in relation to the direction of the incident beams. Within the transceivers, each of the beams was passed through a lens with a 100 mm focal length. The sample volumes created by the intersection of the two colored, paired beams in the water glycerin solution were ellipsoids with a major axis of 126 μm and a minor axis of 19 μm. To measure the three orthogonal components of velocity, the three sample volumes of each color were positioned orthogonal to each other and spatially superimposed.

The plane of the calculated 2D velocity vectors map was orthogonal to the direction of the incident beams as illustrated in Figure 4-11. The velocity vectors measured by the green beams moved from left to right, while those measured by the blue

beams moved into or out of the page depending on the direction of the intersecting primary and secondary blue beams.

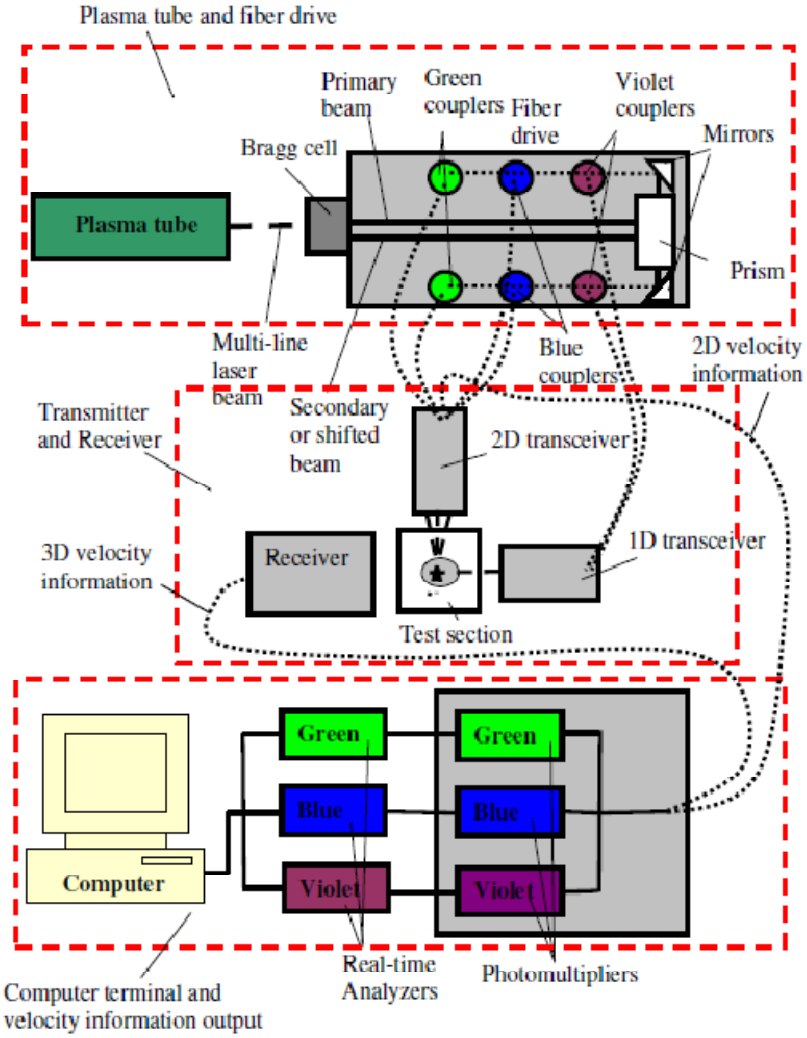

Figure 4-10. *The LDV system employed for shear stress measurements. Adapted from [101].*

The intersection of the two beams created an interference pattern of bright and dark bands of light within the probe volume. Because one of the intersected beams in each color pair has a frequency shifted by 40 MHz relative to the other, the interference pattern moved with a characteristic velocity. Thus, the reflective particles used to seed

the flow generated a light signal called a Doppler burst as they passed through this interference pattern (Figure 4-11). When the particle crossed the bright bands of the interference pattern, a peak in the light signal was observed. Conversely, a valley in the Doppler burst was observed when the particle passed through the dark bands. The mobile interference pattern of the sample volume enabled particles of near-zero velocity to generate a Doppler burst and allowed differentiation between particles of positive and negative velocity.

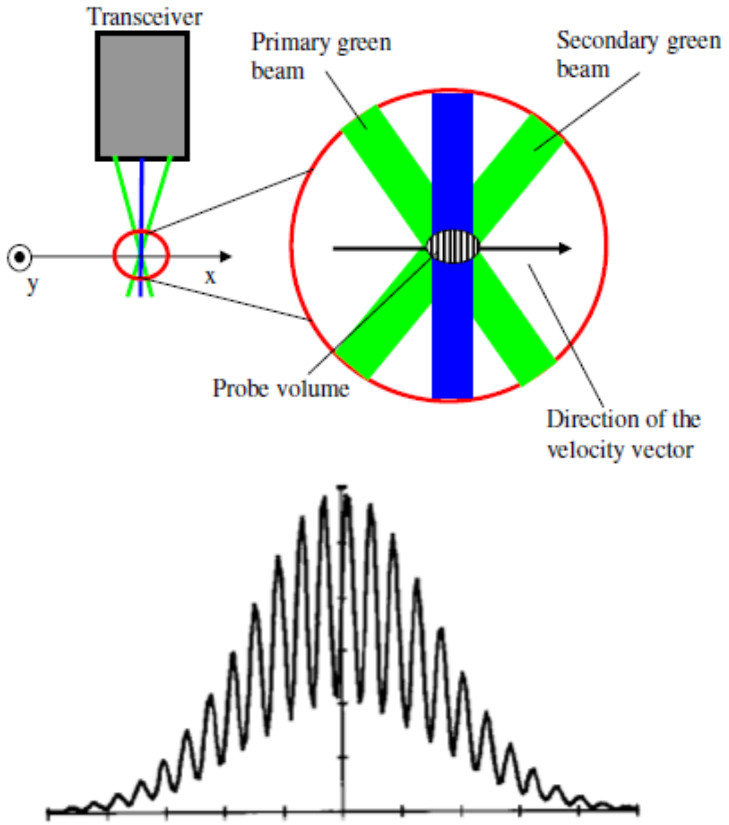

Figure 4-11. *Direction of measurement of velocities: green lasers measure in plane velocities, while the blue lasers measure out-of-plane velocities; and the Doppler Bust signals received by the transceiver when a particle traverse the probe volume, produced because the particle moves through alternating regions of brightness and darkness due to interference between the pair of lasers. Adapted from [101].*

Computer terminal and velocity information output – The Doppler bursts from the passing particles were picked up by the fiber optic receiver that was focused on the superimposed probe volumes. These Doppler signals were transmitted through a series of fiber optic cables to three photomultiplier tubes. A band pass optical filter, allowing the passage of only green, blue, or violet light, covered the optical inlet to each of these tubes. The photomultiplier tubes amplify and convert the light signals into voltages for signal processing. This signal processing was performed by three real-time fast Fourier transform Doppler signal analyzers. The signal processors calculated the velocity of each particle that generated a Doppler burst using the distance between the interference fringes and the frequency with which the particle crossed the fringes. The fringe crossing frequency of a particle was calculated as an average of the inverse of the time between successive peaks in the Doppler burst. The distance between successive bright bands within the sample volume was derived from basic optical theory. The laser Doppler Velocimetry system required no calibration, as the velocities measured were calculated from known superposition properties of light. The cycle time of the velocity measurements was recorded by a 16 bit resettable clock (Aerometrics, Sunnyvale, CA). This clock was triggered by a signal from the pulse generator, and this same signal also opened the pneumatic solenoid valve for the compression of the flexible bulb. The resettable clock created a linear increase in voltage in response to increasing cycle times. This increase, when sampled digitally, effectively divided the 860 ms cycle time used in the pulsatile flow experiments into 55 255 discrete intervals.

4.4. Particle Image Velocimetry System

The PIV system used consisted of a pair of pulsed Nd:YAG lasers (17mJ, 532nm, 9-ns duration), used with a combination of spherical and cylindrical lenses to illuminate the central longitudinal plane within the regions of interest. The PIV images were captured with a CCD camera (Model 1101MPRO, Lavision, Germany) of 1600x1200 pixels in resolution, which were positioned to view the measurement region normal to the laser illuminated plane. The laser sheet thickness was estimated to be about 0.5 mm. The same pulsatile flow loop (flow loop 3, described in section 4.1.3) which was used for LDV analysis was used for PIV analysis. The flow loop fluid was seeded with Rhodamine-B coated melamim resin micro-particles 2-20 microns in size (FPP-RhB-10, Dantec Dynamics A/S, Copenhagen, Denmark). These particles reflects orange light (590nm) when excited by the green PIV laser light, and the camera was fitted with an orange filter (NT48-086, Edmund Optics Inc., Barrington, NJ), such that light not scattered by particles can be filtered out.

4.5. Cone and Plate Ex Vivo Culture Experimental Materials

4.5.1. The Cone and Plate Bioreactor

The cone and plate apparatus has traditionally been used to measure the viscosity of fluid. This apparatus was previously redesigned to act as a bioreactor for culture of aortic valve leaflet tissues [100]. Detailed engineering drawings of all parts of the bioreactor are in Appendix A4, the bioreactor operating manual is attached in Appendix D, and the protocol for performing ex vivo experiments with the bioreactor is described in Appendix C.

The bioreactor consists of a dish with 9 tissue wells, as shown in figure 4-10. A cover plate was secured above the plate, with a hole (6.1 mm in diameter) above each well. Each well was filled with 1% agarose (Acros Organic pure powder Agarose, Thermo Fisher Scientific, NJ) as tissue holder, and the valve leaflet samples, trimmed to circular pieces, were placed on top of the agarose. The cover plate was then utilized to secure the tissues to the well, ensuring that the tissues were flushed to the surface of the place. The cone and plate dish was filled with media fluid, and a cone with a shallow taper angle of 0.5^{o} was positioned such that its apex was 0.2 mm above the plate.

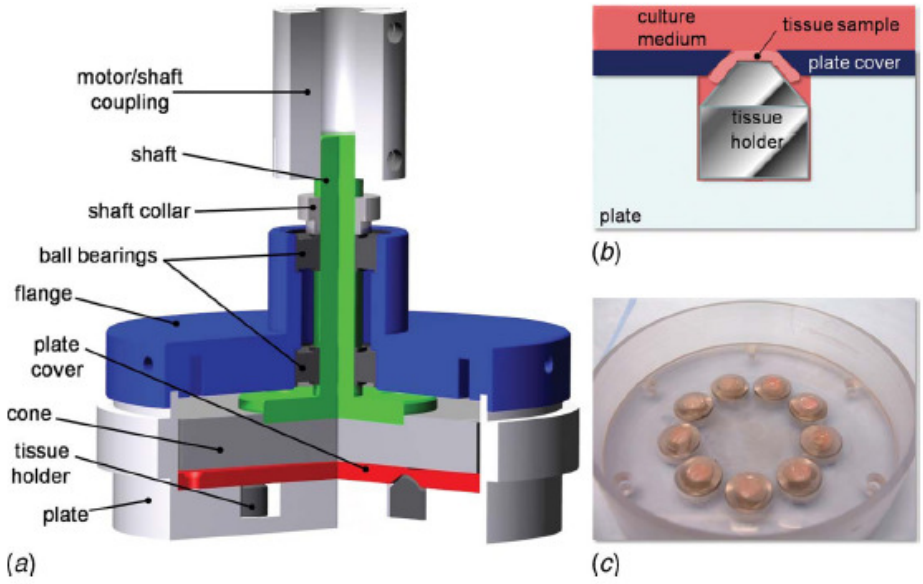

Figure 4-10. *(a) CAD model of the cone and plate apparatus, drawn to the correct proportions; (b) the schematic of the tissue holder design, where 1% agarose is used as the tissue holder; and (c) picture of the plate with tissues held in it. Adapted from [100].*

The cone was coupled to a servo motor (Model SM232AE-NPSN Brushless Servo Motor, Parker Hannifin Corp., Rohnert Park, CA) which was controlled by a servo drive

(Model GV6K Gemini Servo, Parker Hannifin Corp., Rohnert Park, CA). The motors were programmed by the Motion Planner© software (version 4.3.2.0, Parker Hannifin Corp., Rohnert Park, CA). A perfusion system consisting of a reservoir of media, powered by a slow moving peristaltic pump (Model SP202.100, APT Instruments, Rochester, IL) was installed to continually re-circulate the media within the cone and plate bioreactor, to prevent incidences of drying. This cone and plate bioreactor was validated by previous work, as described in section 2.5.

4.5.2. *Ex Vivo* Experiment Materials

Fresh porcine aortic valve leaflets were used for tissues for the ex vivo experiments. These were harvested from the local slaughterhouse within 20 minutes of slaughter, transported to the laboratory in ice-cold sterile 1X phosphate-buffered solution (P3813, Sigma Aldrich, St. Louis, MO), and were prepped for experimentation within 6h of slaughter. Round pieces of valve leaflets were then cut from the belly region under a sterile fume hood, and mounted in the cone and plate bioreactor. The cone and plate was inserted into an incubator and the samples were cultured for 72 h.

An osteogenic media was used as the culture media to stimulate accelerated valve calcification. The media consists of Dulbecco's modified Eagle Media (DMEM; Sigma-Aldrich, St. Louis, MO) supplemented with 10% fetal bovine serum, β-glycerophosphate (1 mmol/L), dexamethasone (10 μmol/L), high phosphate concentration (3.8 mmol/L), and TFG-β1 (1 ng/ml). This media has been validated in a previous publication [89], and was observed to cause calcium nodule formations in the sub-endothelial layers on the aortic surface of porcine aortic valve leaflets cultured in it.

CHAPTER 5

METHODS

This chapter provides details of all the methods used to gather data in this thesis. First, the settings for which the pulsatile flow loop is tuned to for each specific aim is discussed. Next, methods associated with the LDV were provided. These methods were used for specific aims 2 and 3, and include methods to measure velocities and calculate shear stresses, methods to track valve leaflet locations, and methods to assess the variability of shear stresses. Methods to validate these LDV techniques, where required, are also presented. Thereafter, PIV methods are described. After which, the theoretical model for calculation of ventricular shear stresses, used in specific aim 3 is presented, followed by methods related to the ex vivo culture experiments, which is used in specific aim 5.

5.1 Flow Loop Settings

The third flow loop, which is the physiologic pulsatile flow loop, was used for specific aims 2 and 3 for shear stress measurement work. For each specific aim, the loop was tuned to different settings.

In specific aim 2, where the aortic surface shear stresses were measured, the loop was run under a number of conditions: (1) different heart rates (50, 70 and 90 beats/min) at the same stroke volume of 55 ml; and (2) different stoke volumes (29, 43, 62 and 68 ml) at the same heart rate of 70 beats/min. All conditions were run under aortic pressure of 120/80 mmHg. These conditions were meant to test the effects of isolated changes in

stroke volume or heart rate. The ejection durations (*ED*) were adjusted according to clinical data [106], according to the equation:

$$ED = 367.72 - 1.20 \cdot HR \qquad \text{(Equation 5-1)}$$

where *HR* is the heart rate.

In specific aim 2, the ventricular surface shear stresses were also measured. For these studies, the loop was run under normal adult resting condition of 70 beats/min heart rate, 4.5 to 5.0 L/min cardiac output and 120/80 mmHg aortic pressure. The systolic duration was set to be 35% of the cardiac cycle or about 300 ms.

In specific aim 3, where the shear stresses of the BAV is measured, the BAV valve model was subjected to normal adult resting condition of 70 beats/min heart rate, 5 L/min cardiac output and 120/80 mmHg aortic pressure. The systolic duration was set to be 35% of the cardiac cycle or about 300 ms.

5.2 Laser Doppler Velocimetry Methods

5.2.1 Velocity Measurement

All measurements were obtained in the backscatter mode in which a single probe acted as both the transmitter and receiver for the Doppler signals, and all measurements were gated to the pulse programmer, to identify the time phase of measurements within the cardiac cycle. The LDV system was set to a 5 MHz sampling frequency.

For the first flow loop, velocity measurements were performed along the diameter of the channel from the surface of the leaflet attached to the wall to 2mm away from the leaflet, and measurement resolution was 89 μm per spatial step near the valve leaflet attached to the channel wall. This was achieved by securing the LDV probe to a two-

direction traverse mount (XY traversing stage), which has a traversing resolution of 1/1000 inch or 25.4 microns. The traverse mount allows adjustment in the two lateral directions. Its elevation was be adjusted by placing it on a vertical traverse table (Portelevator, Machine Tool Corp, Hamilton, OH). At least 1000 velocity samples were taken at every measurement location. Measurements at each location were averaged, and all average velocities were used to construct the flow profile close the valve leaflet surface. The location of the leaflet surface was obtained by the back-scattered light intensity position tracking method, described in section 5.2.3.2, which was validated using methods described in section 5.2.3.3, and was confirmed with caliper measurements.

For the second flow loop, velocity measurements were performed near the aortic surface of the opened valve leaflet, in the sinus space. Measurements were performed at 8 – 15 points along a radial line approximately perpendicular to the leaflet surface within a distance of less than 1 mm away from the leaflet aortic surface. At least 1000 velocity samples were taken at every measurement location. Measurements at each location were averaged, and all average velocities were used to construct the flow profile close the valve leaflet surface. The location of the leaflet surface was also obtained by the back-scattered light intensity position tracking method described in details in section 5.2.3.2.

Measurements in the first two flow loops were performed to validate that the LDV measurements close to a biological surface were reliable, and that the LDV laser light being reflected by the surface would not cause errors in velocity measurements close to the surface.

In the third flow loop, velocity measurements were performed at multiple points along a radial line between the sinus wall and the center of the valve, wherever optical access was possible, as shown in figure 5-1. Measurements were performed near the mid-point between the base and the free-edge of the leaflet. For the native tissue valve model, this is approximately 9.6 mm away from the base (height of the valve is approximately 19mm). For the polymeric valve, this is approximately 12 mm away from the base (height of the valve is approximately 19 mm). Velocities were measured in both the streamwise (from AV annulus to aorta) and the non-streamwise (from commissure to commissure of the AV) directions. The spatial distance between consecutive points was 89 μm after accounting for flow loop fluid optical density. At least 30,000 data points were collected at each measurement location. There are at least 300 data points in each cardiac cycle, and data were collected over at least 60 cardiac cycles. Velocity measurements were then binned into 86 phases of 10 ms each over the entire cardiac cycle according to the time of the measurements. Within each bin, at least 300 data points were collected. Within each phase, velocities from different measurement locations were used to construct the velocity profile near the leaflet surface.

For the native valve model, measurements were only performed on the aortic side of the valve leaflet. Due to the opacity of the leaflets, velocities on the ventricular side of the leaflet could not be obtained. It must be noted that fluid shear stresses experienced by the surface of the valve leaflet can only be two dimensional. Since velocity measurements were performed in two directions, shear stress could be resolved in both directions. Shear stress was calculated for the entire cardiac cycle except for the short time periods when

the valve was rapidly opening or closing. At these time points, it was difficult to accurately quantify leaflet velocity and orientation.

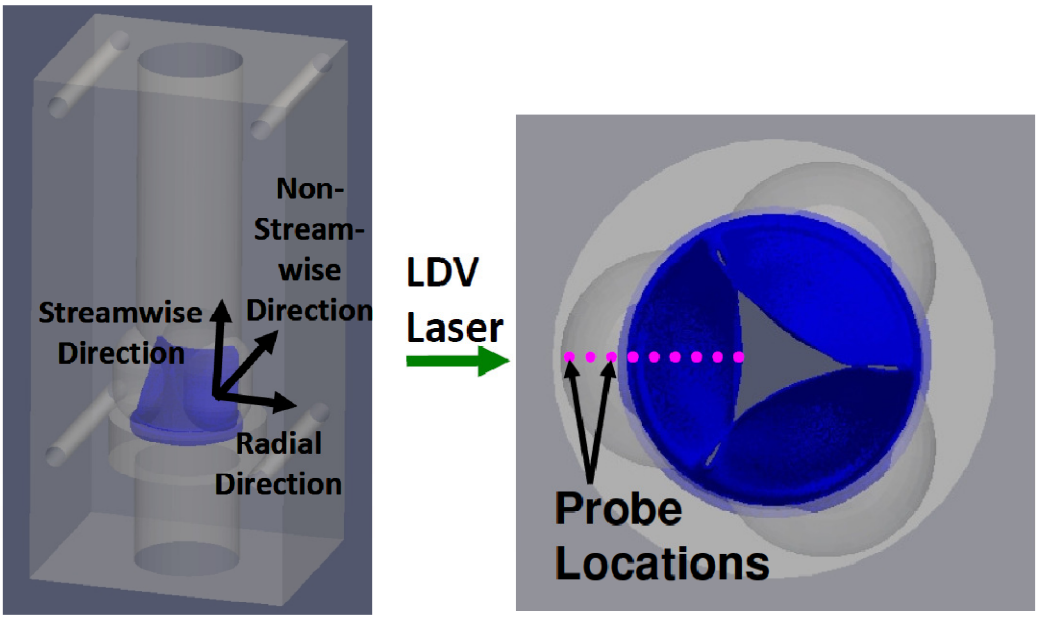

Figure 5-1. *(left) Direction convention for velocity components. (right) Schematic for the location of velocity measurements in the valve models.*

For the polymeric valves, taking advantage of the transparency of the valve leaflets, velocities were measured on the ventricular side of the leaflet, and shear stresses on the ventricular surface could be obtained. Shear stress was only calculated during systole, since there is little flow near the ventricular surface during diastole, and consequently, shear stresses are much smaller in magnitude scale than during systole.

5.2.2 Effects of optical Distortion

Since the flow loop fluid has a slightly different refractive index from that of the acrylic chamber wall (1.365 versus 1.491, respectively), the LDV beam angle may be

distorted during velocity measurements. A CAD program (SolidWorks®, Dassault Systèmes SolidWorks Corp., MA) was used to estimate the beam angle distortions at different locations. Laser beam trajectories were traced on the CAD model of the chamber in accordance to Snell's law, and the resulting beam angle was used to calculate the fringe spacing with the equation:

$$d_f = \frac{\lambda}{2 \cdot \sin \alpha_L} \qquad \text{(Equation 5-2)}$$

Where d_f is the fringe spacing, λ is the wavelength of the laser in the fluid media, and α_L is the half beam angle. Velocities measured at various locations were then corrected accordingly.

Further, the refractive index difference between the flow loop fluid and air resulted in a difference between the displacement of the LDV probe and the consequent displacement of the probe volume. The LDV probe was displaced in steps of 64 µm (which was 1/400th of an inch) by displacing the traversing stage, but this resulted in the probe volume being displaced in steps of 89 µm within the flow loop fluid media. This distortion was taken into account during shear stress computation.

5.2.3 Valve Leaflet Position Tracking

To enable shear rate computation, the location of the leaflet surface must first be correctly identified.

5.2.3.1 Leaflet Position Tracking for Native Tissue Valve

For the native tissue valve models, leaflet position tracking was done by detecting the location where the back-scattered LDV laser light intensity recorded by the LDV

probe was the highest, since intensity of light reflected from the leaflet to the probe will be maximum when the leaflet is within the probe volume. Back-scattered laser light was received by the receiver fiber of the LDV probe, and was sent to the photomultiplier box (PMT) through optical fiber cables. Raw signal output from the PMT was then recorded by the Data Acquisition System (DAQ, National Instruments, Austin, TX) at 500 Hz. At least 40 cardiac cycles of signals were recorded from the PMT and averaged to give ensemble averaged back-scattered light intensity for all time points within the cardiac cycle. This averaging was done so that the randomly received Doppler Burst signals, which were laser light back-scattered by particles in the fluid, would be eliminated, and would not contaminate the back-scattered light signals produced by the leaflet surface. At each time phase, intensity of back-scattered light was plotted over space, and had a resolution of 11.2 points / mm. A smooth curve was fitted onto these data points using a low pass filter (by applying Fourier Transformation to the data and using a cut-off frequency of the 30^{th} mode). This smooth curve was then digitized at 200 points / mm resolution, and the point of highest intensity was noted. The out-of-plane velocity of the leaflet can then be calculated from this leaflet location measurement as the displacement divided by the time steps.

5.2.3.2 Assessment of Cycle-to-Cycle Variability of Leaflet Location

The proposed method for obtaining leaflet location would yield the ensemble average leaflet position. Since the instantaneous position of the valve leaflet may vary from one cycle to the next, it was important to document the variability of the valve leaflet location. Back-scattered light intensity data obtain as per methods in section 5.2.3.1 was used for

this investigation. Back-scattered light intensity data were averaged over 3 cycles for each dataset of leaflet position so as to exclude randomly received back-scattered light from particles, and to distinguish back-scattered light from the leaflet and that from particles. 13 datasets of leaflet position were then analyzed for mean and standard deviation of leaflet positions at each time phase.

5.2.3.3 Leaflet Position Tracking for Polymeric Valve

Since the polymeric valve leaflets were transparent, leaflet position tracking cannot be performed by relying on back-scattered laser light intensity. Thus leaflet position tracking method for the polymeric valve must be different from that for the native tissue valve.

Both velocities in the sinus were small compared to velocities within the valve orifice and had small velocity profile gradients. On the ventricular surface of the valve leaflet, velocities rapidly increased with distance from the surface and had high velocity profile gradient (figure 5-2). Thus, velocity profile had gentle gradients in the sinus space but steep gradients in the valve orifice space. This change in velocity profile gradient occurred suddenly moving from the sinus space to the valve orifice space (figure 5-2). A sudden change in a quantity over space meant that there would be a spike in the spatial derivative of the same quantity. Thus there would be a spike or peak in the spatial derivative of the velocity profile gradient where the valve leaflet ventricular surface was located (as shown in figure 5-2). This method was used to track the ventricular surface of the polymeric valve during systole, when the valve was fully opened.

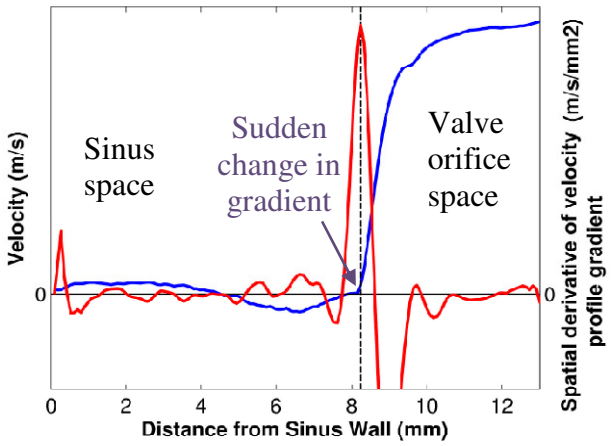

Figure 5-2. *Velocity profile (blue line) and the spatial derivative of velocity profile gradient (red line) along a radial line in the polymeric valve. At the dotted line location, the gradient of the blue line suddenly changed from a gentle slope within the sinus space to a steep slope in the valve orifice space, leading to a spike in the spatial derivative of the gradient (red line). This indicated that the leaflet ventricular surface was located at this point.*

5.2.3.4 Validation for Back-Scattered Light Leaflet Tracking Method

A validation study was performed for this method of dynamic leaflet position tracking. The method was used to track the head of an electromagnetic piston pump (Superpump, Vivitro Systems Inc., Canada), and the results were compared to the position sensor of the pump, which provide electronic sensing of the location of the pump head. A waveform generator (Arbitrary Waveform Generator, model 33120A, Agilent Technologies Inc., Santa Clara, CA) was used to provide a sinusoidal waveform input to control the motion of the piston pump. This signal is amplified with the piston pump controller box to provide 2mm of displacement amplitude in the pump head motion. The position sensing output was recorded with the same Data Acquisitions System (DAQ, National Instruments, Austin, TX) as was used to record the backscattered light intensity for the leaflet position tracking method. Data acquisition was performed at 500 Hz. The

cyclic trigger for data acquisition was simultaneously provided by the waveform generator.

5.2.3.5 Leaflet Orientation

The LDV measured velocities perpendicular to the LDV probe orientation. This direction of measured velocities, however, might not align with the valve leaflet surface orientation because the valve leaflet was dynamic, and its orientation changed over the cardiac cycle. Since shear stresses in the orientation of the leaflet surface were desired, the misalignment between the valve leaflet surface and the LDV probe alignment must be quantified and accounted for at every time point when shear stresses were calculated (figure 5-3).

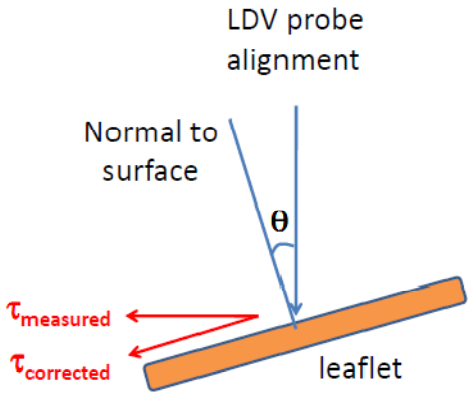

Figure 5-3. *Schematic showing how the LDV probe could be misaligned with the leaflet surface orientation (in this case, by angle θ). The measured shear stress would be perpendicular to the LDV probe alignment, but can be corrected to the parallel to the leaflet surface orientation by the squared cosine of θ.*

To quantify the misalignment, the leaflet orientation with respect to the LDV probe was measured. This was achieved by making leaflet location measurements not only along the radial line where shear stress was measured, but also at 2 additional

adjacent locations: a location 0.32 mm downstream of the measurement location and a location 0.32 mm lateral of the measurement location (0.32 mm displaced in the non-streamwise direction as defined in figure 5-1), and the leaflet orientation was calculated based on differences in leaflet location divided by distance between adjacent measurement locations. In the current study, shear stress was first computed in the directions perpendicular to the probe ($\tau_{measured}$ in figure 5-3), and later corrected to the orientation of the leaflet surface by the square of the cosine of the relative orientation angle between the leaflet and the probe ($\tau_{corrected}$ in figure 5-3).

This correction assumed that flow near to the surface of the valve leaflet would be approximately parallel to the leaflet surface. Given that the flow within the sinus was expected to manifest as a sinus vortex [31, 34], it appeared reasonable to make this assumption at the center of the valve leaflet. It must be noted that obtaining the out-of-plane velocity close the surface of the valve leaflet experimentally was challenging. One of the two LDV laser beams would have to pass through the valve leaflet in order that the probe volume would be close enough the surface of the valve leaflet to measure this (figure 5-4), which was difficult due to geometric constraints, and due to optical access constraints (since an opaque native tissue valve model was used).

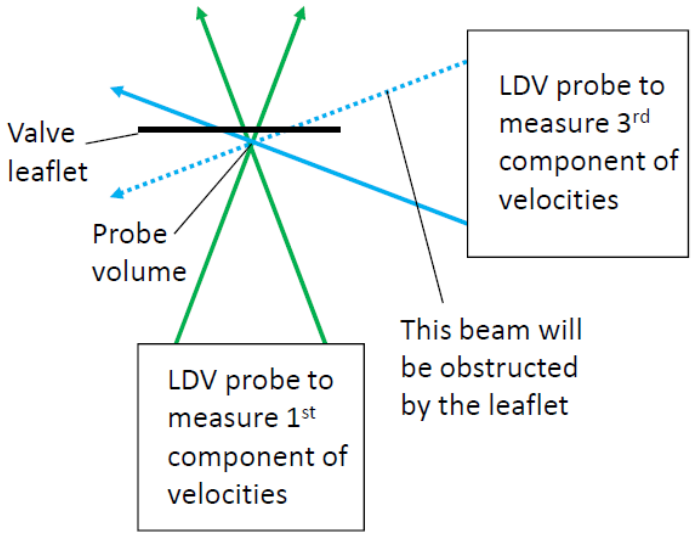

Figure 5-4. *Laser beam arrangements for measuring the 1st and the 3rd component of the velocities at a probe volume location very close the valve leaflet. The beam path in the dotted line may be obstructed by the opaque valve leaflet.*

5.2.3.6 Order of Magnitude Analysis for Errors Associated with LDV Probe-Leaflet Misalignment

Despite difficulties in obtaining radial or out-of-plane velocity components, they might be non-zero. In the case that the leaflet surface was exactly perpendicular to the LDV probe orientation, there would not be any errors due to out-of-plane velocities, since the velocities components responsible for valve leaflet surface shear stress were directly measured. However, the existence of out-of-plane velocities, when combined with misalignment between the LDV probe and the leaflet surface, could lead to errors. Thus an order of magnitude analysis for errors associated with out-of-plane velocities and probe misalignment with the leaflet surface orientation was performed.

In the current thesis, LDV Probe - leaflet surface misalignments of up to 0.15 radians were observed. The order of magnitude of errors associated with the 0.15 radians

misalignment was estimated. Three different flow fields were considered: (1) strictly streamwise pipe (Poiseuille and Womersley) flows; (2) Couette flow; and (3) Hiemenz wall impingement flow. These were chosen to cover a range of possible scenarios. Strictly streamwise pipe flows were when flow dynamics adhere to the assumptions made in the squared cosine angle correction, with no out-of-plane velocity components (velocity components normal to the wall surface). Hiemenz flow, on the other hand, was the other extreme, where certain points on the wall experiences direct impingement of fluid with small or no velocity components parallel to the wall. The cylindrical Couette flow simulated the condition where there was no out-of-plane velocity component, but the wall was curved.

5.2.4 Shear Stress Computation

In the computation of shear stress, the following assumptions were made: (1) that Newtonian mechanics, and thus Galilean Invariance was valid; and (2) that the fluid was Newtonian and isotropic. The result of these assumptions was that shear stress was independent of the reference frame, defined as follows:

$$\tau = \mu\left(\frac{\delta u_i}{\delta x_j} + \frac{\delta u_j}{\delta x_i}\right) \qquad \text{(Equation 5-3)}$$

Where μ was the dynamic viscosity of the fluid, u_i was the ith component of the velocity, and x_i was the position in the ith axis. The terms within the parenthesis were collectively known as the shear rate. In this case, i was either the stream-wise or non-stream-wise direction while j was the radial direction. Thus the first term of shear rate could be obtained with the LDV measured velocity profile by calculating the gradient of the stream-wise velocity with respect to the radial distance, at the surface of the leaflet. The

second term of shear rate could be obtained by computing the relative radial velocity of adjacent points on the leaflet surface. An order of magnitude analysis was performed to compute the relative contribution of these two terms to the overall shear rate magnitude.

It should be noted that the above expression for shear stress, equation 5-3, is valid for all frame of references, even for inertial reference frames [107, 108], which are accelerating (rectilinear or rotational) reference frames. Under accelerating conditions, additional body force terms would be needed in the Navier-Stokes equation. However, the expression of the shear stress term, which depended on the deviatoric tensor, would be dependent only on the spatial gradient of velocities and the viscosity.

For the calculations of ventricular shear stresses, the velocity profile gradient at the surface was obtained by performing a parabolic least squares fit to the 10-15 velocity data points nearest to the leaflet surface (which spanned a distance of 0.89-1.34 mm from the leaflet surface), and obtaining the gradient of the parabolic curve at the leaflet surface. Shear stresses were then obtained by the product of velocity profile gradient and kinematic viscosity. The parobolic fit was used because flow on the ventricular surface resembled that of a developing flow in a pipe, and had simple flow profile shapes close to the leaflet surface, which could be approximated with a polynomial.

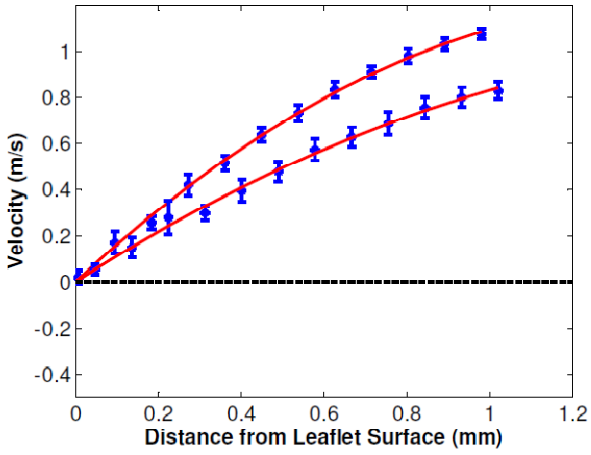

Figure 5-5. *Example of the least square parabolic curve fitting to obtain the flow profile for ventricular surface shear stress computation.*

On the aortic surface, velocity profiles near the leaflet surface sometimes had complex shapes, which were not easily approximated by simple polynomials. A different method for the interpolation is thus utilized. For the calculations of aortic surface shear stresses, the gradient of the velocity profile at the surface of the leaflet was obtained with velocities in the 15-20 velocity data points nearest to the leaflet surface. These were first used to construct a periodic waveform symmetric about the location of the leaflet surface. This was done by appending the set of data points with the mirror image of the same data points at the end further away from the valve, and by appending the resulting set of data points with the negative mirror image of the same data points at the location of the leaflet surface. An example is shown in figure 5-6. A low-pass filter was then applied to the waveform to the 15th frequency mode, before the gradient of this velocity profile waveform was computed at the leaflet location. This method ensured that the

interpolation to obtain shear rate at the leaflet surface will not be performed at the edge of a set of data, which might cause errors due to the discontinuity.

On top of calculating viscous shear stresses as described above, the Reynolds stress was estimated by getting fluctuation component of velocity (instantaneous velocity less ensemble average velocity), and getting the statistical mean of the square of the fluctuation velocity within each time bin, at the location of 1mm away from the valve leaflet. Only one component of Reynolds stress was computed because of the unavailability of the radial component of velocity (or velocity perpendicular to surface of valve leaflet): the streamwise direction Reynolds normal stress.

$$\text{Reynolds shear stress estimate} = \rho\overline{(u')^2} = \rho\overline{(u-U)^2} \qquad \text{(Equation 5-4)}$$

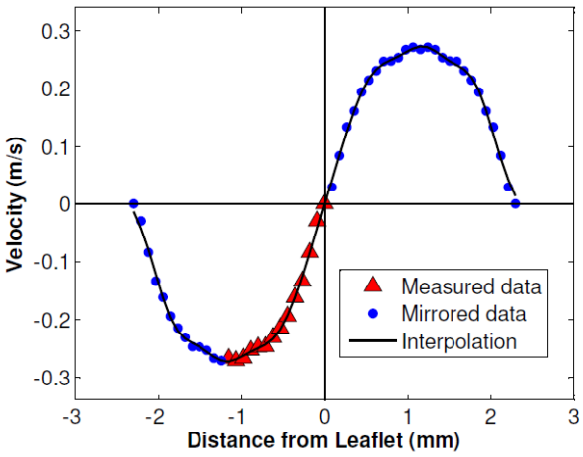

Figure 5-6. *Example of the construction of a symmetric periodic waveform using mirror images of the measured data, and the low pass filter curve fit / interpolation applied to obtain the flow profile gradient.*

5.2.5 Assessment of Errors Associated with Proposed Technique

The proposed shear stress measurement technique involves shear stress calculations based on ensemble averaged (phase-averaged) velocity profiles instead of instantaneous velocity profiles. This was performed because LDV is a point-by-point measurement technique that cannot measure velocities at multiple locations at one time point. It was thus uncertain whether the ensemble average velocity profile accurately represented the instantaneous velocity profile. The technique of locating valve leaflet also relied on a point-by-point measurement and ensemble averaging. It thus suffered from the same limitation as velocity measurements stated above. It was thus important to assess possible errors from the proposed technique.

Because measurements could only be done point-by-point, simultaneous acquisition of leaflet location and velocities was not possible, and the assessment of the uncertainty in shear stress measurement was challenging. Nonetheless 3 methods were used to estimate errors / uncertainty in the measurements: (1) estimating the change in shear rate (du/dy) that would occur with variations in the velocity closest to leaflet surface (u) and the leaflet location (y); (2) displaying the variability of measured velocities without any ensemble averaging and measured leaflet location; (3) performing a stochastic analysis to calculate the pdf of velocity profile from the pdf of individual velocities, so as to assess the variability of shear stress measurements based on variability of individual velocities. Stochastic analysis was proposed due to the inability to obtain deterministic measurements.

5.2.5.1 Estimating Error in Shear Stress from Maximum and Minimum Bounds of Velocity and Leaflet Location

The first method to estimate error utilized the maximum and minimum bounds of velocity and leaflet location. The velocity used is the one measured closest to the mean leaflet location. Shear stress was then calculated using the four possible combination of the maximum or minimum velocity and the maximum or minimum distance from leaflet surface: (1) max. velocity and max. distance; (2) max. velocity and min. distance; (3) min. velocity and max. distance; (4) min. velocity and min. distance. The highest shear stress and the lowest shear stress of the four cases was recorded and presented.

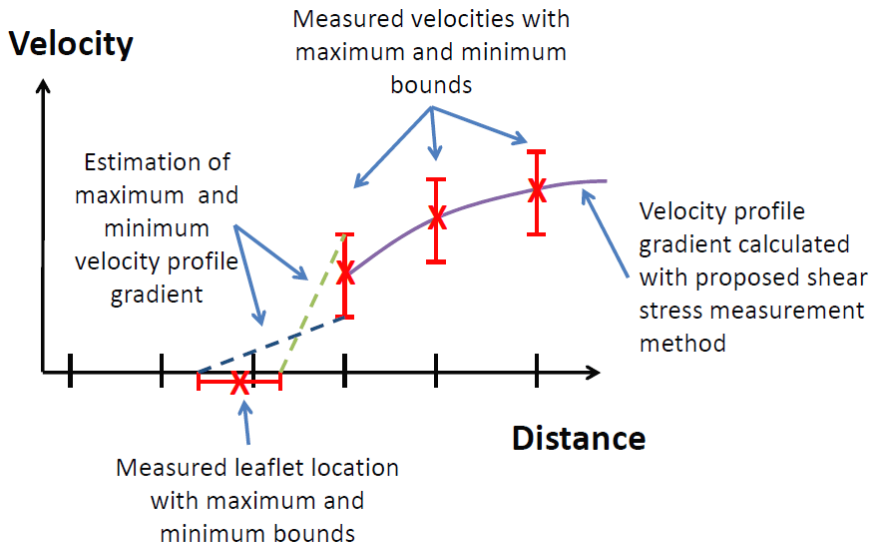

Figure 5-7. *Method to estimate errors of shear stress measurements: estimating maximum velocity profile gradient using the maximum velocity divided by the minimum distance from leaflet surface; and estimating minimum velocity profile gradient using minimum velocity divided by the maximum distance from leaflet surface.*

5.2.5.2 Displaying Variability of Measured Velocities and Leaflet Location as Indications of Errors in Shear Stress Measurement

The second method to assess errors was simply displaying the variability of measured velocities and leaflet locations to inform the reader. Raw velocity measurement data were tabulated for two cases: velocities near the aortic surface of the native aortic valve model on the 68 ml stroke volume, 70 beats/min case; and velocities near the ventricular surface of the polymeric valve model #2.

5.2.5.3 Performing Stochastic Analysis of Individual Velocity Data Points to Calculate the Variability of Shear Stress to Compute Errors in Shear Stress Measurements

The third method was to perform stochastic analysis on individual velocities to analyze for the pdf of shear stress. The stochastic was adopted because it was not possible deteministically measure shear stress, since it was not possible to simultaneously measured velocities at different points, or simultanously measure velocities and leaflet location. Stochastic analysis can give information on probable shear stress ranges given the spread of the measured velocities.

To achieve the stochastic analysis, Monte Carlo simulations were performed to calculate the pdf of fluid shear stress based on the pdf of velocity measurements at individual locations and time points. The pdf of velocities measured at any one location and time point was first obtained by fitting a least-square best-fit Gaussian function to the histogram of velocities. Two examples are shown in figure 5-8. Next, random number generation was performed according to the pdf of individual velocities. 5000 cases of

velocity profiles were then constructed from this random generation method. Shear stress was calculated for each case by obtaining a least-square best fit 4th order polynomial to the velocity profile. The resulting 5000 shear stress values were used to plot a histogram to construct the pdf of shear stress. The resulting shear stress pdf can be used to analyze the variability of the calculated shear stress, to show how variability can result from the currently proposed shear stress measurement method.

The Monte Carlo simulation could be performed based on velocity variability, but not leaflet location variability. This is because there were sufficient velocity measurements at an location and time phase to construct a histogram and estimate the pdf, but there was only 7-15 leaflet location measurements at any time phase, which was insufficient to plot the histogram for estimating the pdf of leaflet location.

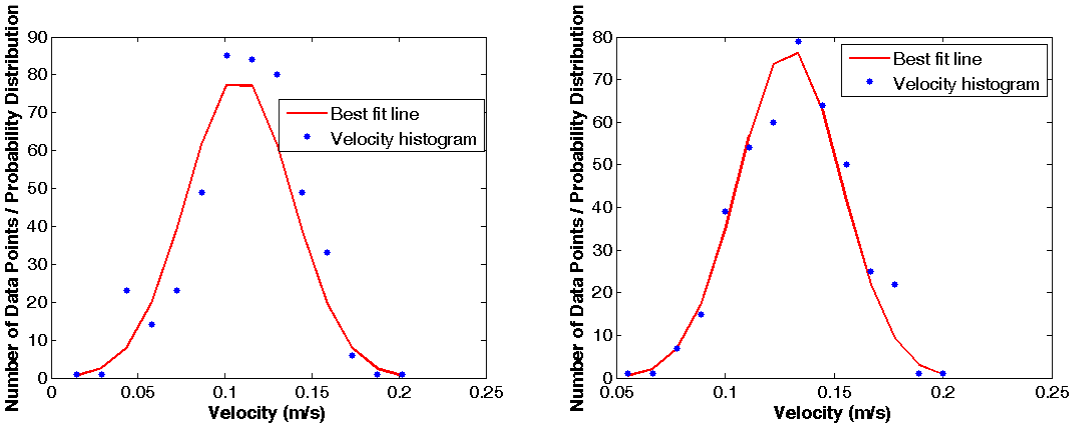

Figure 5-8. *Demonstration of the fitting of Gaussian functions to velocity histograms in order to obtain the probability distribution function of velocities measured at any single location and time point.*

5.2.6 Assessment of Variability of Shear Stresses

Despite uncertainty in the measurement technique, it was nonetheless possible to compare the variability of flow near the valve leaflet and variability in shear stresses

between the different valves and conditions, to investigate which condition or valve will result in more unsteady shear stresses. The variability of the shear stresses were studied in three methods: (1) by obtaining the standard deviation of velocities at the location of 1mm away from the valve leaflet surface, which is indicative of the variability of shear stresses on the valve leaflet surface; (2) by obtaining the one-standard-deviation bounds of the shear stresses; and (3) by obtaining the power spectral density of the velocities close to the leaflet surface, described below.

5.2.6.1 Standard Deviation of Velocities 1mm away from the Valve Leaflets

The statistical standard deviation of the velocity was calculated at the location of 1mm away from the valve leaflet at all the time bins, and was taken as an indication of velocity variability at this location. Since this location was very close to the valve leaflet surface, velocity variability at this point were indicative of the shear stress variability.

5.2.6.2 One Standard Deviation Bound of Shear Stresses

LDV velocity measurements yielded velocity data categorized into specific time phase in the cardiac cycle and specific measurement locations. At any one specific time phase and specific location, velocity data measured from multiple different cardiac cycles were averaged and the standard deviation was calculated. Methodologies for shear stress calculations, described in section 5.2.4, would yield the ensemble average shear stresses when applied to the ensemble mean of these velocity data points. When these methodologies were applied to the ensemble mean velocity data plus or minus one standard deviation, the one standard deviation bounds of shear stresses would be obtained.

5.2.6.3 Power Spectral Density Analysis

Further, a power spectral density analysis could be performed on temporally sequential velocity data points close to the leaflet, to investigate the presence of fluctuating velocity components, which would most likely lead to fluctuating shear stresses. This analysis would allow the investigation of the nature of shear stress unsteadiness in the BAV model compared to the normal aortic valve model.

Since shear stresses could only be obtained for ensemble averaged values, shear stress values were unsuitable for this power spectral density analysis. Velocities measured very close to the valve leaflet surface, however were temporally sequential data points, and could be used for the power spectral density. In this thesis, velocities measured 1 mm away from the valve leaflet surface were used for this analysis. These velocities were first used to calculate the fluctuating velocity components, which are the instantaneous velocities less the ensemble average velocities, and which describe the deviation of velocities from the ensemble average values. The fluctuating velocity components were then used in the power spectral analysis.

Since the input data for power spectral analysis had non-uniform time spacing between consecutive data points, additional treatment were required. Two methods were used for this purpose: (1) the sample and hold method, as described by Adrian et al. [109], and (2) the sample and hold method with refinement to the autocorrelation function, as described by Moreau et al. [110].

The sample and hold method involved re-sampling the existing data at a regular time interval, and at every re-sampling time point, velocity was assumed to take the value

of the immediately previous LDV measurement (figure 5-9). In the current study, this re-sampling was done at 1000 Hz. This sampling rate was chosen because it was higher than the average data rate of 400 Hz.

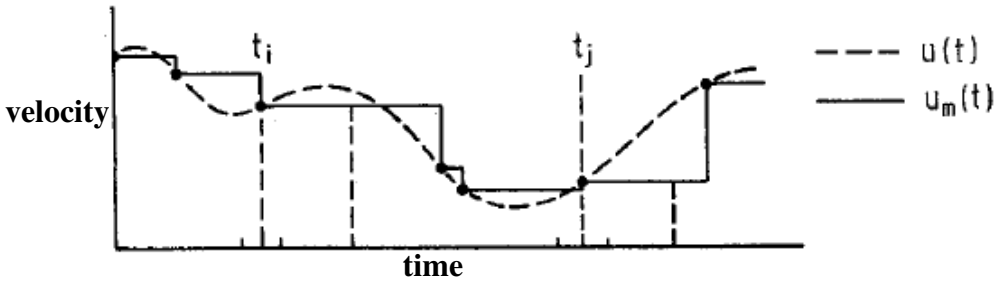

Figure 5-9. *Illustration of the sample and hold method. u(t) is the actual velocity over time, while $u_m(t)$ is the sample and held velocity waveform, which assumed that velocities stay at the previously measured value until a new measurement could be made. Adapted from [109].*

Under the first method, sample and hold without refinement, the resulting uniformly spaced signal from the sample and hold re-sampling (y) exercise was used to calculate the autocorrelation function R_{SH} as per equation 5-5:

$$R_{SH}(k) = \frac{1}{N}\sum_{l=0}^{N-k-l} y(l \cdot \delta t) \cdot y\big((l+k) \cdot \delta t\big) \qquad \text{(Equation 5-5)}$$

where dt is the time interval between the velocity samples (1 ms), N is the total number of data points, and ($0 \leq k \leq P$), where P corresponded to the value of k for which the amplitude of the autocorrelation could be neglected. P was taken to be 2000, which is approximately 2.3 cardiac cycles, and thus sufficiently long a delay for the autocorrelation amplitude to be neglected. Next, the power spectral density was calculated as the discrete Fourier transformation of the autocorrelation function:

$$\Phi(f) = 2 \cdot \delta t \cdot [R_{SH}(0) + 2\sum_{k=1}^{P-1} R_{SH}(k) \cdot \cos(2\pi f k \cdot \delta t)] \qquad \text{(Equation 5-6)}$$

Under the second method, the sample and hold method with refinement to the autocorrelation function, the same sample-and-held re-sampled data was used to calculate the autocorrelation function as per equation 5-5. The resulting auto-correlation function was then refined for bias due to non-uniform time spacing as per Equation 5-7.

$$R_r(k) = c(\alpha) \cdot R_y(k) + \frac{1 - c(\alpha)}{2} \cdot \left[R_y(k-1) + R_y(k+1)\right] + [1 - c(\alpha)] \cdot \left[R_y(0) - R_y(1)\right] \cdot d(k)$$

(Equation 5-7)

where

$$d(k) = \begin{cases} 1 & where\ k=0 \\ 0 & otherwise \end{cases} \qquad \text{(Equation 5-8)}$$

and

$$c(\alpha) = \frac{1+e^{-2\alpha}}{(1-e^{-\alpha})^2} \qquad \text{(Equation 5-9)}$$

and

$$\alpha = \lambda r \cdot \delta t \qquad \text{(Equation 5-10)}$$

where λr was the mean data rate. The power spectral density of the signal was then calculated using the equation:

$$\Phi(f) = 2 \cdot \delta t \cdot [R_r(0) + 2 \sum_{k=1}^{P-1} d_k(f) \cdot R_r(k) \cdot \cos(2\pi f k \cdot \delta t)] \quad \text{(Equation 5-11)}$$

where

$$d_k = \begin{cases} 0.5(1 + \cos[\pi f k/(F_s \kappa)]) & for\ [fk/F_s] < \kappa \\ 0 & otherwise \end{cases} \qquad \text{(Equation 5-12)}$$

where f was the discrete frequency, Fs is the frequency of sample-and-hold re-sampling (1000) and κ was the parameter arbitrarily chosen. κ was assumed to be 5, similar to the value used by Moreau et al.

5.2.7 Estimation of Boundary Layer Thickness

To show that the LDV velocity measurements had sufficiently fine temporal resolution to resolve the boundary layer flow, an order of magnitude analysis to estimate the boundary layer thickness was carried out.

Boundary layer thickness could be estimated using the Blasius solution of the Navier-Stokes for steady flow near a solid surface, and by using the solution to the Stoke's problems of oscillating flat plate. According to the Blasius solution, the boundary layer thickness should be [107]:

$$\delta = 5 \cdot Re^{-0.5} \cdot l \qquad \text{(Equation 5-13)}$$

Where d was the boundary layer thickness, Re was the Reynolds number and l was the horizontal length scale. According to the solution to Stoke's problems, the boundary layer thickness should be [107]:

$$\delta = 3 \cdot Re^{-0.5} \cdot l \qquad \text{(Equation 5-14)}$$

Estimations of the boundary layer thickness were performed for all the shear stress measurement cases. Actual flow near the valve leaflets would have several characteristics which were not modeled in these calculations. For example, flow near the valve would not be steady and developed like the Blasius flow, and would not have exactly the same velocity profile as the Stoke's solution. Thus while these calculations could not predict exact values of boundary layer thicknesses near the valve leaflet, they could predict its order of magnitude.

5.3 Particle Image Velocimetry Methods

Phase-locked 2D PIV was performed in the downstream and sinus regions of the BAV valve model and the native tissue normal aortic valve model to obtain the two-dimensional instantaneous flow fields. This was performed to compare the differences in the flow fields in the BAV versus the normal aortic valve.

The PIV cameras were positioned to view the measurement region normal to the laser illuminated plane. The laser sheet thickness was estimated to be about 0.5 mm. The same flow loops used for LDV was used for PIV analysis. The resolution of the images taken was 30 μm/pixel, with the particles images occupying between 3-5 pixels.

DaVis 7.11 software (Lavision, Germany) was used to analyze the PIV images. PIV cross-correlation vectors were computed with an initial pass of 64 x 64 pixels interrogation regions with 50% overlap reduced down to a final pass of interrogation region corresponding to 32 x 32 pixels with 50% overlap. A median filter is applied upon acquisition, where spurious vectors with velocities exceeding 5 times the average velocities of their immediate neighbor vectors were removed, and filled in with the mean of the neighboring velocities.

The measurements were phase-locked to 15 instances during systole at 25 ms intervals, and 5 instances during diastole at 100 ms intervals. At least 50 image pairs were taken at each time instance, and processed.

5.4 Theoretical Formulation for Ventricular Surface Shear Stresses

A theoretical model of pulsatile flow through the AV was formulated. This formulation can allow the estimation of ventricular shear stresses based on volumetric

flow rate waveform alone, and can be extended to *in vivo* flows. This method, however, was meant only to be an order of magnitude analysis to obtain the general features of the ventricular surface shear stresses, such as whether shear stress reversed in direction during late systole, and what the general magnitude of peak shear stress was. This is because idealizations were made during this theoretical formulation procedure, such as the assumption that the valve geometry approximated that of a straight tube, which were not entirely realistic.

The AV from the base of the leaflet to the free edge can be viewed as a slightly converging axis-symmetric tube. As a first estimate, this can be approximated to pulsatile flow in a straight tube at the same volumetric flow rate, which can be described using the Womersley solution [31] for oscillatory flow. Since the Womersley solution linearizes the Navier-Stokes equation, we can decompose the volumetric flow curve into its Fourier components, find the corresponding Womersley solution wall shear stress for each component, and then superimpose the component shear stresses to obtain the final shear stress. Volumetric flow rate was decomposed as follows:

$$Q = Q_0 + \sum_{n=1}^{N} Q_n e^{in_f \omega_n t} \qquad \text{(Equation 5-15)}$$

where Q was the volumetric flow rate, Q_0 was the temporal-mean flow rate, Q_n were the Fourier coefficients, n_f was the frequency number, ω_n was frequency, and t was time. The summation was performed to a frequency number of N=20, since additional terms had negligible effects. From the Womersley solution, shear stresses on the walls of the tube could be expressed as a function of Q_0 and Q_n as follows [111]:

$$\tau = Q_0\left(\frac{4\mu}{\pi R^3}\right) + \sum_{n=1}^{N} Q_n\left(\frac{i\mu\alpha_n{}^2}{\pi R^3}\right)\left\{\frac{J_1\left(i^{3/2}\alpha_n\right)}{i^{3/2}\alpha_n J_0\left(i^{3/2}\alpha_n\right) - 2J_1\left(i^{3/2}\alpha_n\right)}\right\}$$

(Equation 5-16)

where τ was shear stress, J_n was the Bessel function of the first kind to the nth order, α_n was the Womersley number corresponding to the frequency number of the term, and i was the square root of -1.

The theoretical model was applied first to the bulk flow rate waveform obtained from the *in vitro* experiments with polymeric valves. Shear stresses obtained from this calculation were compared with shear stresses obtained from LDV measurements for validation. The theoretical model was then applied to two *in vivo* ascending aorta volumetric flow waveforms acquired with phase contrast MRI, obtained from the literature [112, 113]. The diameter of the AV orifice was assumed to be 18 mm for data obtained from Powell et al., since subjects had a median age of 12.8 years old, and 24 mm that for data obtained from Langerak et al., since subjects were adults between ages of 24 and 31. This sizing of the valves was performed according to BSA estimates and correlation between BSA and aorta size [114].

5.5 Cone and Plate *Ex Vivo* Culture Experimental Methods

Ex vivo culture experiments were performed to investigate the effects of different shear stress waveforms on the biological response of aortic valve leaflets. From the shear stress measurements in specific aims 2 and 3, it was found that shear stresses can vary in their (1) magnitudes, (2) frequency, and (3) degree of unsteadiness with changes to

physiology. For example, changes in stroke volume and heart rate can alter the shear stress magnitude; changes in heart rate can alter shear stress frequency; and with the BAV geometry, shear stress can exhibit high unsteadiness, manifesting in the form of high frequency fluctuating shear stresses and cycle-to-cycle magnitude variations in shear stresses. The effects of these three characteristics on aortic valve biology were investigated using cone and plate ex vivo culture experiments.

5.5.1 Experimental Setup

Fresh porcine aortic valve leaflets were harvested from the local slaughterhouse and were trimmed into round samples of 8 mm diameter. The samples were cultured under various shear stress waveforms for 72 hours in the cone and plate bioreactor described in chapter 4, and an osteogenic media was used as the culture media to stimulate accelerated valve calcification. The acceleration of the calcification response will allow us to tease out the differential influence of different shear stress waveforms within short culture durations. Upon removal from the bioreactor at the end of culture period, the samples were either used for Western Blotting, or for other histological assays. In the former case, the samples were washed briefly in PBS, stored in vials and snap-frozen with liquid nitrogen. In the latter case, half of each sample was snap-frozen in optimal cutting temperature compound with liquid nitrogen, sliced into 5 μm sections, and mounted onto glass slides, while the other half was washed briefly in PBS, saved in vials, and snap-frozen with liquid nitrogen.

5.5.2 Shear Stress Waveforms

To investigate the effects of magnitude and frequency of shear stresses, perfectly sinusoidal shear stress waveforms were used. To investigate the effects of shear stress magnitude, a set of waveforms consisting of 3 waveforms at 5, 10, and 25 dyn/cm^2 peak magnitudes were used, all of which were 1 Hz in frequency. These waveforms were used because the physiological range of shear stresses measured were about 10-20 dyn/cm^2. The 1st and 3rd waveform were designed for investigating whether biological responses will change when shear stress magnitude exceeds this physiological shear stress range.

To investigate the effects of shear stress frequency, a set of waveforms consist of 3 waveforms at 1, 2, and 4 Hz was used, all of which were 10 dyn/cm^2 in peak magnitude. The 1 Hz waveform represents normal heart rate shear stress waveform, the 2 Hz waveform represents elevated heart rate waveform, such as during exercise conditions. The 4 Hz waveform represents fluctuating and unsteady shear stresses on the aortic valve leaflets, such as that observed in the moderately stenotic BAV valve.

Shear stress variability was observed in the bicuspid aortic valve. Thus to investigate shear stress instability, the shear stress waveforms measured from the bicuspid valve in specific aim 4 were used. 3 waveforms were used, as shown in figure 5-10. The first waveform is the ensemble averaged shear stress waveform measured in specific aim 4. The second waveform is one where the shear stresses alternated between (1) the ensemble average waveform; (2) the ensemble average plus one standard deviation waveform; and (3) the ensemble average minus one standard deviation waveform. This waveform represents cycle to cycle magnitude variations in shear stresses. The third waveform is one where the ensemble average waveform was superimposed with a 20 Hz

oscillation with amplitude of half of the shear stress standard deviation during systole. This waveform represented high frequency fluctuating unsteadiness of shear stresses. This condition was a speculation of what might occur in a valve, for the purpose of testing the response of valve tissues to high frequency fluctuations. It should be noted that 20 Hz can be found within the spectra of velocities in turbulent flows in the aortic valve [115, 116].

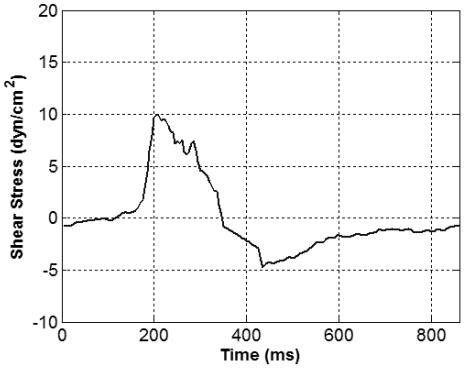

Figure 5-10a.

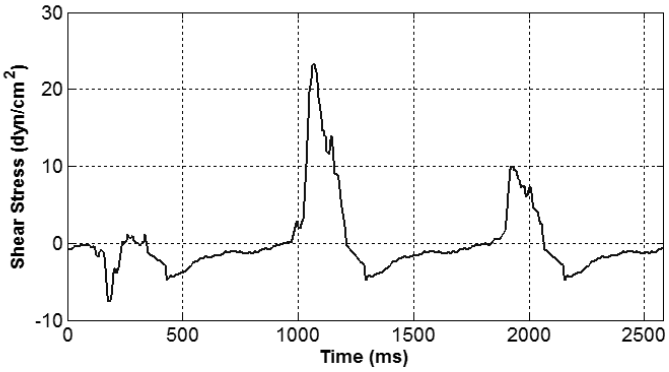

Figure 5-10b.

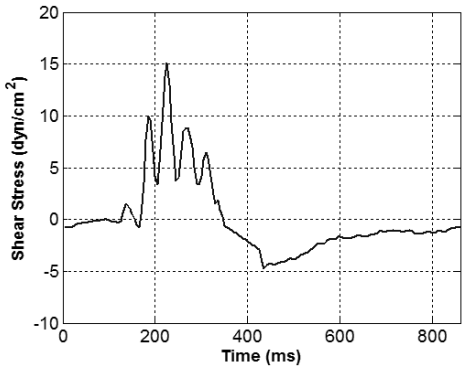

Figure 5-10c.

Figure 5-10. *Bicuspid Aortic Valve shear stress waveforms investigated using the cone and plate bioreactor. (a) the ensemble average shear stresses experienced by the center of the fused leaflet of the BAV; (2) alternation between the ensemble average shear stress, the ensemble average plus one standard deviation, and the ensemble average minus one standard deviation; and (3) the ensemble average shear stress waveform superimposed with a 20 Hz oscillation with a magnitude of half the standard deviation, during systole.*

Further, to test the hypothesis that the shear stress environment of the normal tricuspid aortic valve was not pro-calcific, but only alters shear stress environments were pro-calcific, the shear stress waveform measured in a normal tricuspid aortic valve leaflet was also used in the cone and plate ex vivo experiment (figure 5-11)

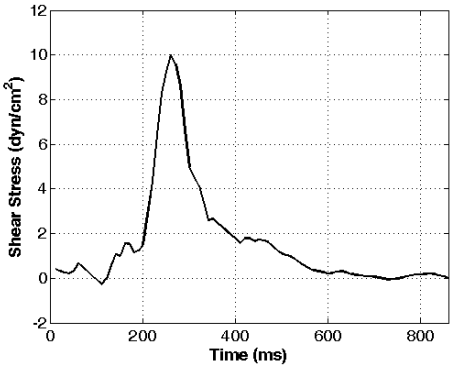

Figure 5-11. *Shear stress waveform of the normal tricuspid aortic valve, measured in specific aim 2, used as the normal valve control waveform in the cone and plate ex vivo experiments.*

Table 5-1. *List of all the shear stress waveforms investigated using the cone and plate bioreactor.*

To investigate the effects of shear stress magnitude			
	Type of Waveform	*Magnitude*	*Frequency*
1	Sine Waveform	5 dyn/cm^2	1 Hz
2	Sine Waveform	10 dyn/cm^2	1 Hz
3	Sine Waveform	25 dyn/cm^2	1 Hz

To investigate the effects of shear stress frequency			
	Type of Waveform	*Magnitude*	*Frequency*
1	Sine Waveform	10 dyn/cm^2	1 Hz
2	Sine Waveform	10 dyn/cm^2	2 Hz
3	Sine Waveform	10 dyn/cm^2	4 Hz

To investigate the effects of shear stress instability			
	Type of Waveform	*Magnitude*	*Frequency*
1	Ensemble average shear stress of the fused leaflet of the bicuspid valve	10 dyn/cm^2	1 Hz
2	Alternation between (1) ensemble average waveform; (2) ensemble average + 1 standard deviation; and (3) ensemble average – 1 standard deviation	10 dyn/cm^2	1 Hz
3	Ensemble average superimposed with 20 Hz oscillations (1/2 standard deviation amplitude) during systole	10 dyn/cm^2	1 Hz

Control Waveforms		
Type of Waveform	*Magnitude*	*Frequency*
Fresh Control – static culture	-	-
Normal tricuspid valve waveform	10 dyn/cm^2	1 Hz

5.5.3 Histology

5.5.3.1 Hematoxylin and Eosin Assay

Routine H&E staining was used to assess tissue structure to ensure no evidence of DNA aggregation, smearing or other abnormalities indicative of cell death. Hematoxylin is a basic dye that stains nucleic acids and ribosome purple or blue, while Eosin is an acidic dye that stains basic tissue structures red.

H&E staining was done automatically using a staining machine (Leica Autostainer, Vashaw Scientific, Norcross, GA). Tissue sections were first washed in water for 2 minutes prior to immersing into hematoxylin for 30 seconds. Afterwards, the slides went through water (2 minute), acid alcohol (1 second), and water (1 minute), Scott's solution (30 seconds) and were washed in water for 2 minutes. Following this, the slides were immersed in acid alcohol for 1 minute before being stained with Eosin for 30 seconds. Subsequently, the slides were run through a series of alcohols (95%: 30 seconds; 100% 1 minute; 100% 2 minutes x2) and xylene substitute (twice, each for 2 minutes) and finished in xylene. A resinous mounting agent was applied and the slides were coverslipped and allowed to dry before viewing.

5.5.3.2 Alizarin Red Assay

Alizarin Red was performed to visualize tissue mineralization. Alizarin Red S, an anthraquinone derivative, stains calcium deep red. The reaction is not strictly specific for calcium, since magnesium, manganese, barium, strontium, and iron may interfere, but these elements are usually not present in sufficient concentration to cause significant interference. Calcium forms an Alizarin Red S-calcium complex in a chelation process,

and the end product is birefringent. Frozen sections were allowed to warm up and were hydrated in PBS for 2 minutes. They were then stained in Alizarin red solution (pH = 4.1-4.3) for 5 minutes. The slides were then dehydrated in acetone-xylene, clear in xylene before being mounted in a resinous medium and coverslipped. Calcium deposits appeared orange-red when viewed under normal while light. Care was taken to wash the slides in de-ionized water before staining to prevent calcium ions in fluid on the sample from confounding results.

5.5.3.3 Von Kossa Assay

Von Kossa staining was performed to visualize tissue mineralization. In this method, tissue sections were treated with a silver nitrate solution and the silver is deposited by replacing the calcium reduced by ultraviolet light, thereby visualized as metallic silver. Briefly, frozen sections were allowed to warm up, and were hydrated in PBS for 2 minutes. They were then incubated in 1% silver nitrate solution in a clear glass Coplin jar placed under ultraviolet light for 2 hours. After washing in several changes of distilled water, excess silver nitrate was removed by incubating in 5% sodium thiosulfate for 5 minutes. The slides were rinsed in distilled water, dehydrated through graded alcohol and cleared in xylene before being mounted in a resinous medium and coverslipped. Calcium deposits appeared black when viewed under normal white light. Care was taken to wash the slides in de-ionized water before any staining to prevent calcium ions in the fluid on the samples from confounding results.

5.5.3.4 Arsenazo Assay

Experimental tissue samples were pulverized by mortar and pestle in liquid nitrogen, and collected in pre-weighed vials. After sample collection, the vials were re-weighed, and the wet weight of the tissue was calculated by the difference in the two weights measured. Following which, the ground samples were incubated in 1 M acetic acid at 4 degrees Celsius to solubilize calcium for 24 hours. The samples were then centrifuged at 20,000 rpm for 9 min, and the supernatant was collected. The supernatant as well as calcium standards were assayed for calcium content by using a calcium specific Arsenazo dye reagent (Fisher-Scientific, Waltham, MA): 25 µl of the supernatant or the calcium standard was mixed with 300 µl of Arsenazo solution in a 96 well plate in triplicates. The absorption of the various samples to 650 nm light was measured through spectrophotometry, using a 96 well plate reader (Gemini XPS Fluorescence Microplate Readers, Molecular Devices, Sunnyvale, CA). The absorption calibration curve was established with the calcium standard spectrophotometry readings, and was thereafter applied to readings from the samples. The amount of calcium per wet weight of sample tissue was then calculated.

5.5.3.5 Statistical Analysis for Histology Results

Statistical methods were used to the quantitative results from the calcium Arsenazo assay. All groups of data were first tested for normality using the Anderson-Darling test. For any comparison, when all groups of data involved were normally distributed, one-way ANOVA with Tukey-Kramer post hoc test was used to gauge differences between the groups. If any one group of data within the comparison was not

normal, then a non-parametric method was used: Kruskal-Wallis with Mann-Whitney U post hoc test. Significance at 5% and 10% were reported.

CHAPTER 6

RESULTS

The results presented in this thesis are composed of shear stress calculations based on the ensemble averaged (phase averaged) velocity profiles, measured from LDV. During the acquisition of data, however, it was noted that there was a significant spread of velocity values at various time points and spatial points. With the current data, it was uncertain whether the ensemble average velocity profile reflected the instantaneous velocity profile. The interpretation shear stress results in the current thesis must be approached with some caution. This uncertainty is consequent to the choice of using LDV as the measurement technique for calculating shear stress due to lack of a better method. LDV, being a point-by-point measurement technique, could not provide instantaneous velocity profile gradients and the back-scattered light intensity leaflet tracking method could not provide instantaneous leaflet locations. Any interpretation of shear stresses must be performed using the ensemble average and standard deviation of velocities and leaflet locations. Specifics of the analysis of the errors with the variability of velocity and leaflet location measurements are presented in section 6.2.4.1, based on methods described in 5.2.5. It should be noted that the variability of velocity and leaflet locations are likely physical phenomenon actually occurring in heart valves. Future work is needed to devise more advanced methods to study this variability and its effect on shear stress.

6.1 Specific Aim 1: Establishment of a Method for Measuring Shear Stress on the Surface of Aortic Valve Leaflets.

Specific aim 1 attempts to validate the use of LDV to measure shear stresses on the leaflets of the aortic valve models. The following validation tests and analysis (described individually in detail in the chapters 4 and 5) were performed:

(1) *Flow Seeding*: To ensure that the flow loop is not over seeded with particles to lead to measurement errors, calculations were performed to obtain maximum allowable seeding quantity.

(2) *Leaflet Position Tracking*: In the shear stress measurement experiments, valve leaflet locations were tracked using the back-scattered light intensity method. This method of tracking the position of a surface was validated on a sinusoidally moving piston pump head with known motions, to show that it could be relied upon to track the position of dynamic surfaces. The methods for this validation experiment are described in section 5.1.3.3.

(3) *Velocity Measurements Close to Biological Surface*: It was unclear if the use of the LDV to make fluid velocity measurements would result in errors due to laser light reflection from the surface of the valve leaflet. To validate that this was not the case, the LDV was used to make velocity measurements close to a biological tissue surface in the two steady flow loops, which are described in sections 4.1.1 and 4.1.2. The methods for this validation test are described in section 5.1.1.

(4) *Optical Distortion due to Refractive Index Mismatch*: To account for the optical distortion due to the refractive index mismatch between the flow loop fluid and the acrylic chamber, the CAD study of the LDV laser beam

trajectories was performed, and the correction factor for measured velocities was derived. The methods for this study are described in section 5.1.2.

(5) *Errors Associated with Misalignment Between LDV Probe and Leaflet Surface*: Since the out-of-plane or radial velocity component could not be measured, misalignment between the LDV probe and the leaflet surface can lead to errors. An order of magnitude analysis for resulting errors was performed, to validate that these errors were small. The methods for this analysis are described in section 5.1.3.5.

(6) *Boundary Layer Thickness Estimation*: An estimation of the thickness of the boundary layer was performed based on estimations of the Reynolds numbers of flows where shear stresses were measured. The methods for this analysis are described in section 5.1.6.

6.1.1 Calculations Of Optimal Seeding For LDV

It is important to control seeding density to minimize errors and velocity dropouts due to multiple particles crossing the probe volume. Having too many particles within the system could lead to multiple particles in the probe volume, which could cause velocity measurement errors and velocity dropouts. Calculations of the maximum allowable seeding were performed to minimize the probability of multiple particles within the probe volume. The following simplifying assumptions were made in the calculations:

(1) That particle interaction forces were negligible, and locations of individual particles were statistically random, and did not depend on fluid velocities.

(2) All seeding particle had sizes equal to the mean particle size.

Silicon Carbide particles were used as seeds, with the following characteristics:

Density = 3.2 g/cm3

Mean particle diameter = 1.5 microns

Thus, volume of each particle = 1.767 *10^{-18} m^3

The probe volume dimension (length l_m and width d_m) could be calculated with the following equations:

$$d_m = \frac{4\lambda f}{\pi D_e} \qquad \text{(Equation 6-1)}$$

$$l_m = \frac{d_m}{\tan \alpha_L} \qquad \text{(Equation 6-2)}$$

Where α_L was the beam half angle (8.1° in the working fluid), and *De* was the initial beam diameter (0.035 m), λ was the light wavelength, and *f* is the frequency of the light.

36% (by volume) Glycerin solution (in water) was used as the flow loop solution, giving the refractive index of the fluid media to be 1.38. The wavelengths of the green and blue laser beam in air were 514.5 nm and 488 nm, respectively. According to Snell's law, refractive indices (n) were related to light wavelengths (λ) according to the equation:

$$\lambda_{\text{fluid}} = \frac{n_{\text{air}}}{n_{\text{fluid}}}\lambda_{air} = \begin{cases} 373 & \text{Green Light} \\ 354 & \text{Blue Light} \end{cases} \qquad \text{(Equation 6-3)}$$

The focal length of the beams was 100 mm in air. The focal length (f_{fluid}) in the fluid media could be calculated by:

$$f_{\text{fluid}} = f_{\text{air}} \frac{n_{\text{fluid}}}{n_{\text{air}}} \frac{\cos \alpha_{\text{fluid}}}{\cos \alpha_{\text{air}}} = 139.3\ mm \qquad \text{(Equation 6-4)}$$

Thus the probe volumes had diameters of 18.9 microns and 17.9 microns for the green and blue light respectively, according to Equation 6-1, and lengths of 132.8 microns and 125.9 microns for green and blue light respectively, accordingly to Equation 6-2.

For the seeding density calculations, the larger probe volume (green light) was used to be conservative. The probe volume was an ellipsoid, and its volume was given by:

$$V_{PD} = \frac{4}{3}\pi\frac{d_m}{2}\frac{d_m}{2}\frac{l_m}{2} = 2.48 \cdot 10^{-14} m^3 \qquad \text{(Equation 6-5)}$$

The total volume of fluid used (V_T) was 10 L, thus the probability of any specific single particle lying within the probe volume, P_{single}, was:

$$P_{\text{single}} = \frac{V_{PD}}{V_T} = 2.48 \cdot 10^{-12} \qquad \text{(Equation 6-6)}$$

Assuming that N particles were within the fluid, the probability that no particles was within the probe volume, P_0, was:

$$P_0 = (1 - P_{\text{single}})^N \qquad \text{(Equation 6-7)}$$

The probability that there was only one particle within the probe volume, P_1, was:

$$P_1 = N \cdot P_{\text{single}} \cdot \left(1 - P_{\text{single}}\right)^{N-1} \qquad \text{(Equation 6-8)}$$

And thus the probability that there were more than 1 particle in the probe volume, P_2, was:

$$P_2 = 1 - P_0 - P_1 \qquad \text{(Equation 6-9)}$$

For a 0.2% chance of more than one particle existing in the probe volume, we could solve for *N*, the number of particles, which turned out to be $2.6*10^{10}$, or approximately 0.147 grams of particles, using the mean volume and density information given above. This seeding density (0.15 grams / 10 L of fluid) was used for LDV velocity measurements.

6.1.2 Validation for Back-Scattered Light Leaflet Tracking Method

To test the ability of LDV to accurately measure the location of a moving surface, validation experiments were carried out for the back-scattered light intensity position tracking method described in section 5.1.3.3. The LDV lasers were first used to measure back-scattered light intensity in the vicinity of a stationary valve leaflet held within the

water glycerin solution, to test if there would be a distinct difference in reflected light intensity when the probe volume was focused on the leaflet surface, versus if the probe volume was focused immediately in front or behind the leaflet. The result is shown in figure 6-1.

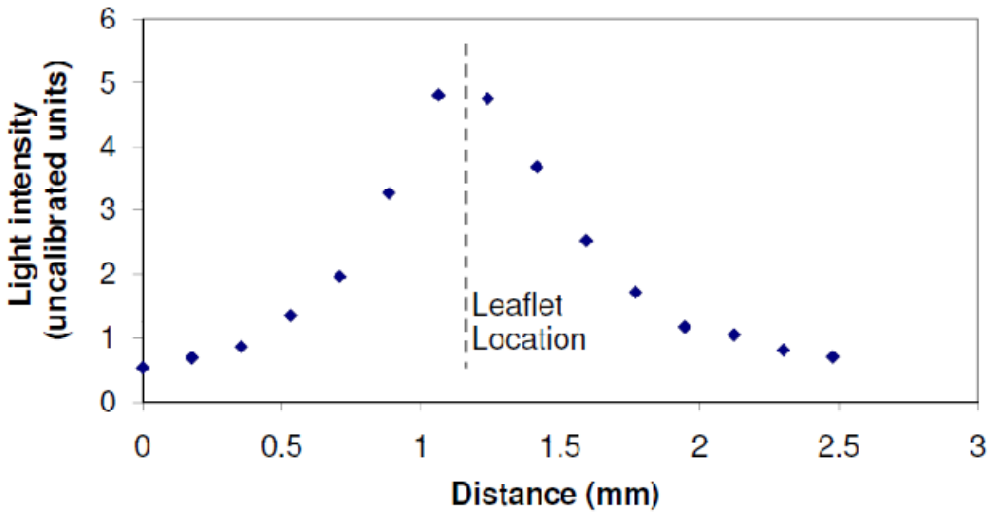

Figure 6-1. *Intensity of back-scattered LDV laser light when the probe volume is positioned at various locations near to the heart valve leaflet, a biological surface. A clear distinction in back-scattered light intensity was observed when the probe volume was placed on the leaflet surface versus when it was placed away from the leaflet surface.*

The results showed that when the probe volume was placed near the leaflet surface, there was an elevation in the intensity of the back-scattered laser light recorded by the photomultiplier box of the LDV system. When the probe volume was focused at locations in front and behind the valve leaflet, the back-scattered light intensity dropped significantly.

The ability of the leaflet position tracking method was further tested on a dynamic object: the sinusoidally moving piston pump head, as described in section 4.3.4.3. Figure 6-2 shows the back-scattered light intensity at various measurement locations and at various time points. Measurements were at various points along a straight line perpendicular to the piston pump head surface, at spatial distances of 63.5 microns between consecutive points.

This back-scattered light intensity map was analyzed with algorithms described in section 4.3.4.3 to obtain the LDV light measured location of the pump head surface, by assuming that, at any particular time point, the location of the pump head surface was the point where back-scattered light intensity was the highest. The result is plotted in figure 6-3. The true position of the piston pump head, as reported by the position sensor of the piston pump, concurrently recorded while performing the LDV light position tracking, is also plotted in figure 6-3. It can be observed that there was an excellent match in the measurements using the backscattered light leaflet tracking method and using the position sensor of the piston pump. The amplitude of the piston pump head motion differed by 0.18% on the average. The position tracking signals was delayed from the backscattered light by 4ms, and was most likely due to filters in the position sensor electronics. When the 4ms offset was corrected for, average errors given by the backscattered light reduced to 0.04%. The back-scattered light position tracking method was thus shown to accurately report the position of dynamic opaque surface.

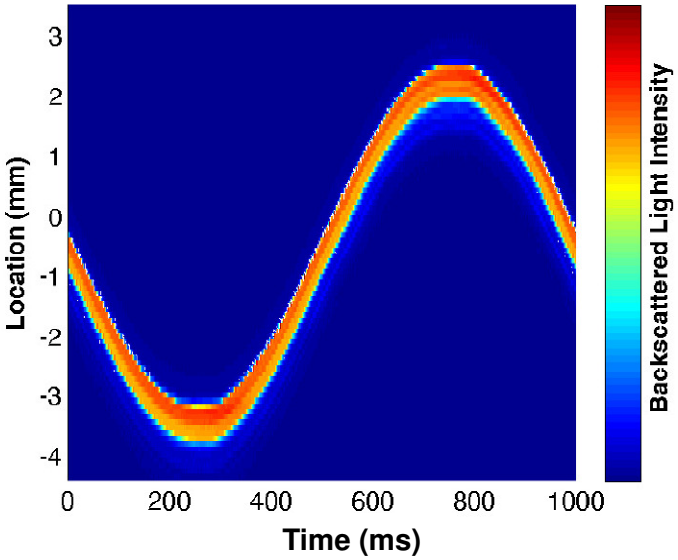

Figure 6-2. *Back-scattered LDV laser light, measured with the LDV probe volume positioned near to a sinusoidally moving piston pump head, at various locations (vertical axis), at various time in the pump head motion cycle (horizontal axis). The location of elevated reflected light intensity traced the same sinusoidal motion as the pump head.*

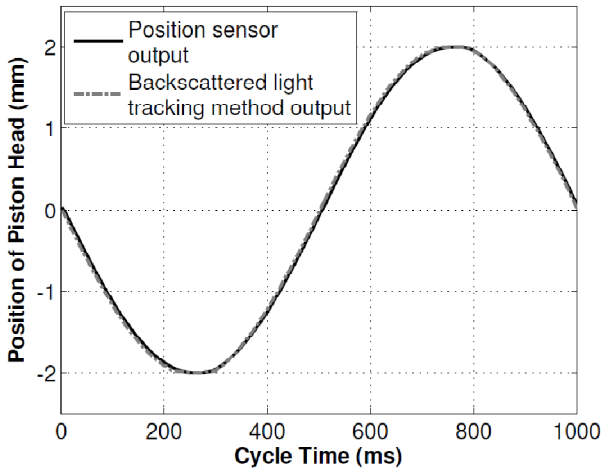

Figure 6-3. *Plot of the LDV back-scattered light measured location of the piston pump head and the location of the piston pump head as reported by the position sensor of the piston pump. A close match is observed.*

6.1.3 Measurements in the Steady Flow Straight Loop

LDV measurements of the streamwise velocity were performed near to the surface of a piece of aortic valve tissue glued onto the wall of a round tube with steady

flow to check if velocity measurements would produce errors due to reflection of the laser light from the leaflet surface. These velocity measurements are compared to those calculated from classical theoretical solutions of the round tube steady flow.

The Reynolds number of the flows generated in the tube was less than 100. This was to ensure that the entrance length of these flows were small (less than 6.3 times channel diameter [117], such that the flow would be fully developed by the time it reached the valve tissue.

Stream-wise velocity measurements (axial direction) in the straight tube are shown in figure 6-4. Tracking of the wall location was performed with the back-scattered laser light intensity method as described in section 5.1.3.3, and the wall location, which was the location with the highest intensity of back-scattered laser light, is denoted as 0 distance in figure 6-4. Velocities were not measured behind the point of highest back-scattered light intensity, since it represented the surface of the wall of the channel. For both flow rates, measured velocities showed a close fit to a parabolic profile close to the walls, with a high coefficient of determination (R^2 = 0.988-0.997), and the no-slip wall boundary condition was observable at the wall location. The standard deviation of measured velocity was 0.014 m/s on the average across different measurement locations. Based on the volumetric flow rate, the expected wall shear stresses based on Poiseuille's law were 3.01 dyn/cm2 and 6.02 dyn/cm^2, respectively. From the LDV measurements, the calculated wall shear stresses were 2.99 dyn/cm^2 and 6.00 dyn/cm^2, which matched the theoretical values well.

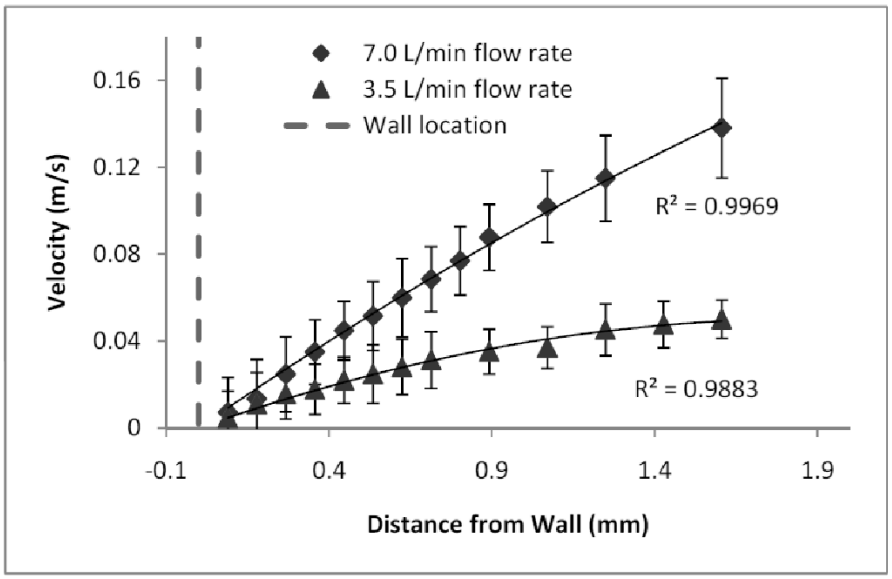

Figure 6-4. *Streamwise velocities measured near to the surface of a piece of aortic valve leaflet glued to the wall of a tube, and the theoretical parabolic flow profiles. Fully developed pipe flow was induced in the tube.*

We thus observe that reflected light from the surface of the valve leaflet did not appear to cause significant errors in the velocity measurements.

6.1.4 Measurements in the Native Valve under Steady Flow

Measurements were performed in the second flow loop (described in section 4.1.2) so as to further test whether LDV measurements can be made near the native aortic valve leaflet tissue. Stream-wise velocity measurements in the native valve model under the two steady flow rates of 7 L/min and 14 L/min are shown in figure 6-5. Forward velocities were plotted as negative for plotting clarity. The position at which the highest back-scattered light intensity was observed, which indicated that the leaflet surface was the closest to this position, was set to be 0 mm. Results showed that at this 0 mm position, the average measured velocity dropped to approximately 0 m/s, indicating that the no-slip

boundary condition was satisfied at that point. In front and behind the no-slip point, the back-scattered laser light intensity decreased as expected. Velocity measurements at various locations showed an average standard deviation of 0.026 m/s, as an indication of the measurement noise level.

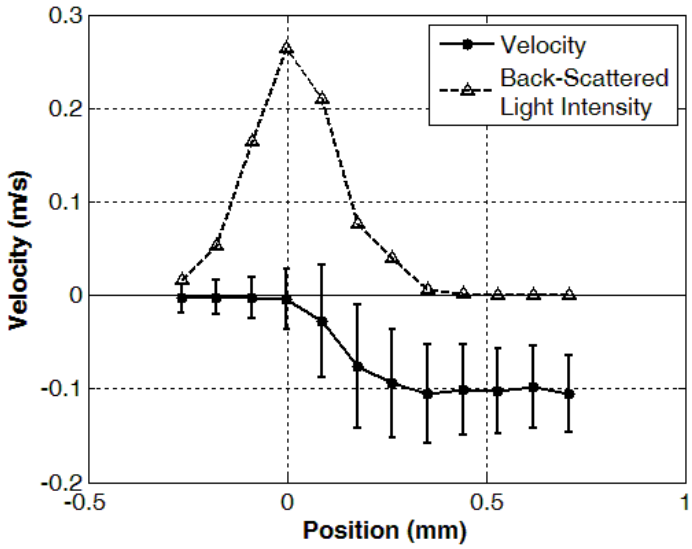

Figure 6-5a. *Back-scattered light intensity and velocity measurements close to the surface of a valve leaflet when the valve is subjected to steady flow of 7 L/min. The "no slip condition" was observed at the leaflet surface (point of highest back-scattered light intensity).*

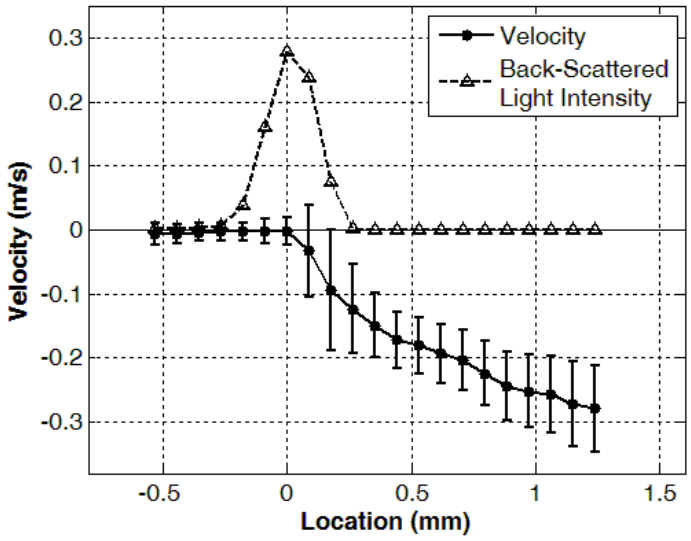

Figure 6-5b. *Back-scattered light intensity and velocity measurements close to the surface of a valve leaflet when the valve is subjected to steady flow of 14 L/min. The no-slip condition was observed at the leaflet surface (point of highest back-scattered light intensity).*

6.1.5 Correction for Optical Distortions

Since the sinus walls had a curvature, the LDV beam angle may be distorted, leading to errors in the measured velocities. The analysis of laser beam path using a CAD program was performed in accordance to Snell's law to calculate these errors, and then measured velocities were corrected accordingly.

Analysis was performed for both the BAV bi-lobed sinus chamber and the normal valve tri-lobed chamber. The analysis showed that for streamwise direction measurements, since both laser beams entered the sinus wall at a flat portion in both chambers (figure 6-6b, 6-7c), there should be no distortion to the beam angle, and thus no correction was required. In non-streamwise direction measurements, the two laser beams entered the sinus wall at points with different curvatures (figure 6-6a, 6-7a, 6-7b), and

thus beam distortions occurred. The analysis showed positioning the probe volume at various distance from the sinus wall, resulted in different levels of beam distortion, and different amount of velocity measurement errors. For the tri-lobed sinus chamber, velocity errors ranged from 0% immediately next to the sinus wall to 14.2% at 19 mm away from the sinus wall, in an almost linear fashion (figure 6-8a). For the fused leaflet sinus (larger sinus) of the BAV bi-lobed sinus chamber, the velocity errors varied linearly from 0% immediately next to the sinus wall to 12.1% at 20.5 mm away from the sinus wall (figure 6-8b). For the non-fused leaflet sinus of the BAV chamber, velocities errors were approximately 0% from the sinus wall to about 10 mm away from the sinus wall, and thereafter, it increased linearly to 3% at 16 mm away from the sinus wall (figure 6-8c). This non-linearity of the errors was due to the difference in curvatures of the points on the sinus wall where the beam entered the sinus.

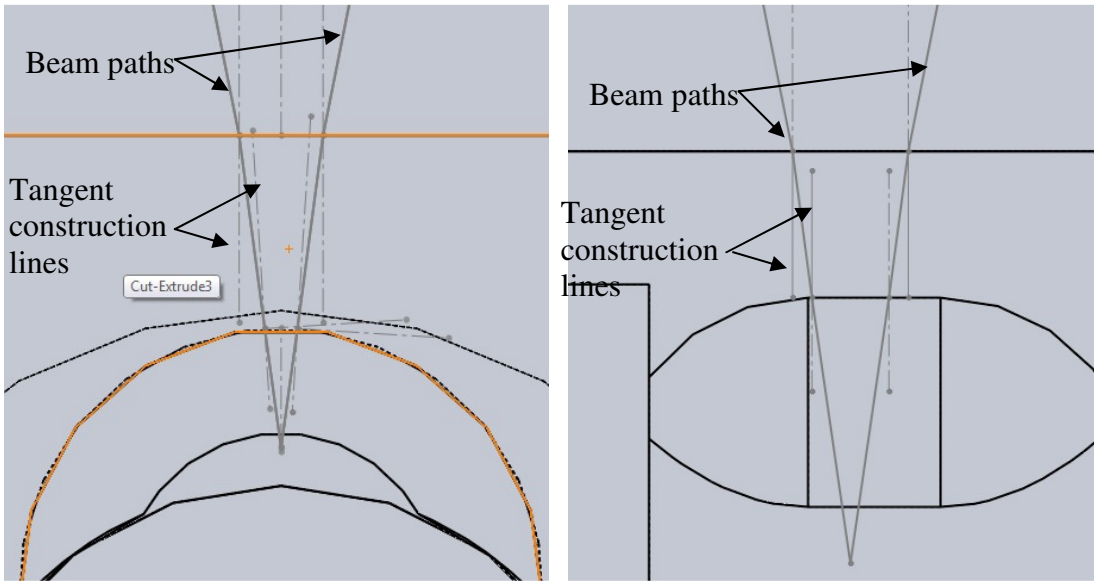

Figure 6-6. *CAD models of the beam path obeying Snell's law as the LDV laser beams enter the normal valve tri-lobed sinus chamber. (a) Streamwise velocity measurement setup; (b) non-streamwise velocity setup. Dimension tool was used in the CAD program to constrain beam paths.*

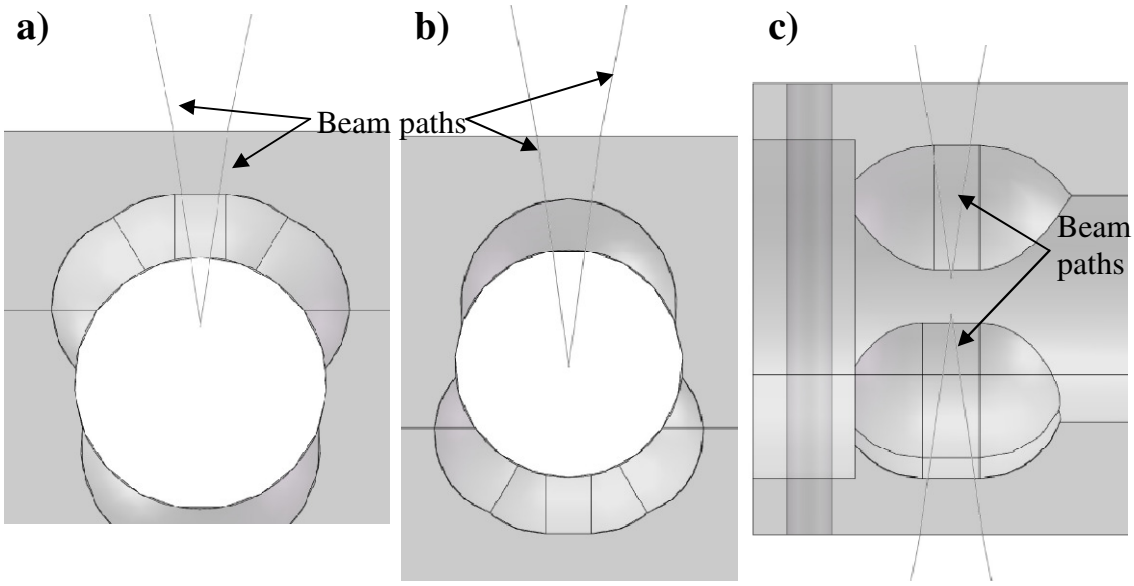

Figure 6-7. *CAD models of the beam path obeying Snell's law as the LDV laser beams enter the BAV bi-lobed sinus chamber. (a) non-streamwise velocity measurement setup for the fused sinus; (b) non-streamwise velocity measurement setup for the non-fused sinus; and (c) streamwise velocity setup for both sinuses.*

a)

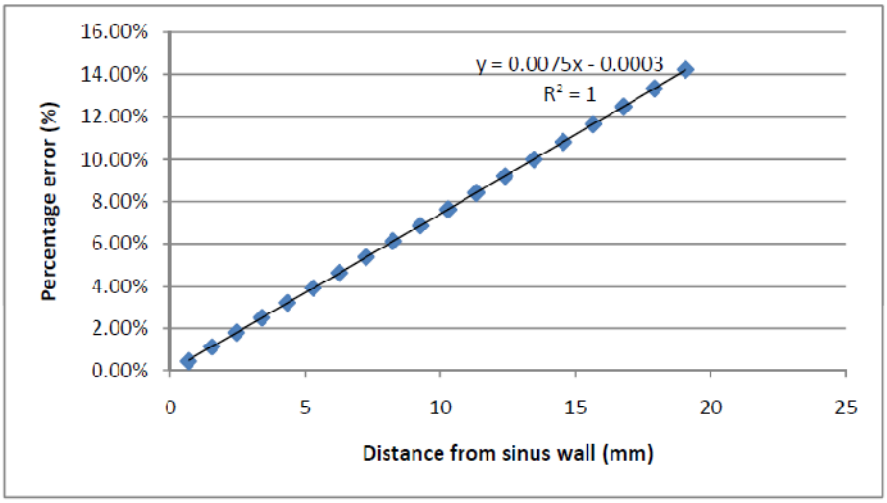

b)

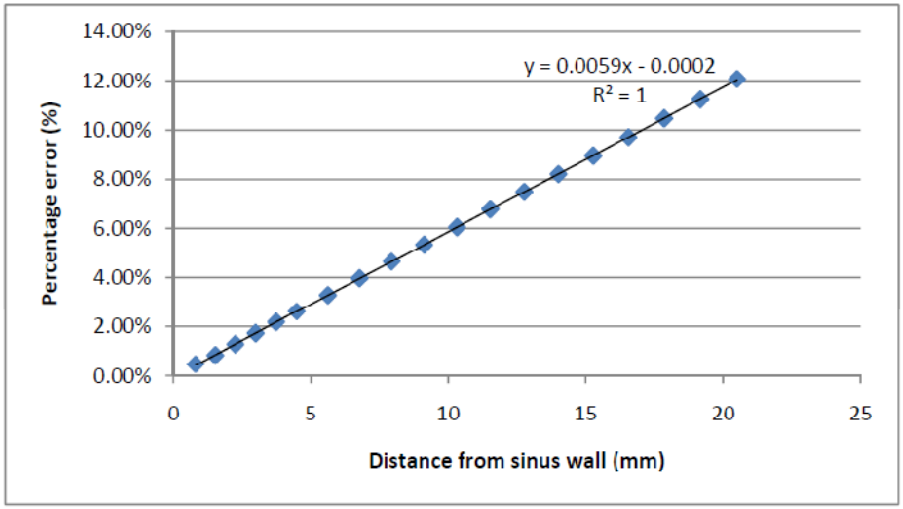

c)

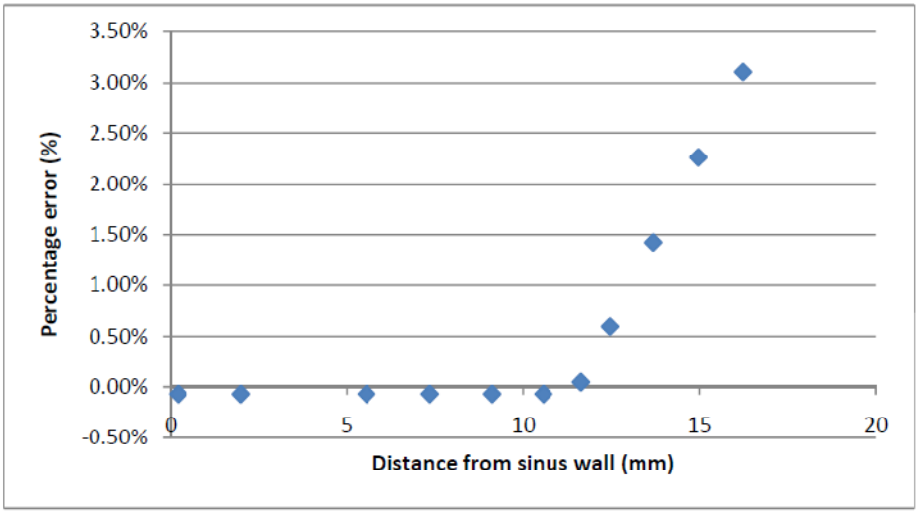

Figure 6-8. *The percentage error in non-streamwise velocities measured at various distances away from the sinus wall for (a) the normal valve tri-lobed sinus chamber; (b) the fused leaflet sinus of the BAV chamber; (c) the non-fused leaflet sinus of the BAV chamber. Since errors vary with location, measurements performed at different locations must be corrected with different factors.*

6.1.6 Order of Magnitude Analysis for Errors Associated with LDV Probe - Leaflet Surface Misalignment

During the LDV measurements, LDV probe direction was not exactly aligned perpendicular with the leaflet surface, despite being aligned perpendicular to the valve

chamber flat external surface, due to dynamics of the valve leaflet. The maximum misalignment was restricted to less than a small angle of 0.15 radians: measurements were repeated until this was achieved. Since the out-of-plane velocity was not measured, this small angle misalignment might result in errors during the computation of shear stresses, which assumed that velocities close to the leaflet surface were parallel to the surface. The order of magnitude of this error is estimated here. Different classical fluid mechanics scenarios were analyzed to cover all possibilities.

6.1.6.1 Strictly Streamwise Pipe Flows

For strictly stream-wise pipe flows, such as the Poiseuille or Womersley flow, there is no out-of-plane velocity component, and flow profiles are independent of axial location. In this case, errors caused by the 0.15 radians misalignment angle could be completely recovered with the squared cosine correction, leaving no error. This is demonstrated in the following calculations.

If velocities were sampled in the line normal to the wall, shear stress on a stationary wall (τ) was defined as:

$$\tau = \mu \frac{\delta u}{\delta y} \qquad \text{(Equation 6-10)}$$

Where μ was the kinematic viscosity, u was the streamwise velocity and y was the distance from the wall. If velocities were sampled along a slanted line α radians from the wall-normal line, computed shear stress (τ_s) is defined as:

$$\tau_s = \mu \frac{\delta u_s}{\delta y_s} \qquad \text{(Equation 6-11)}$$

Where u_s was the velocity component measured in this misalignment, which would be in the direction perpendicular to the slanted line, and y_s was the distance along the slanted

line. Since flow profiles were the same at any axial location, from geometric relationships (figure 6-9):

$$u_s = u \cdot \cos(\alpha) \qquad \text{(Equation 6-12)}$$

$$y = y_s \cdot \cos(\alpha) \qquad \text{(Equation 6-13)}$$

Thus:

$$\tau_s = \mu \cdot \frac{\delta u \cdot \cos(\alpha)}{\delta y / cos(\alpha)} = \tau \cdot cos^2(\alpha) \qquad \text{(Equation 6-14)}$$

True wall shear stress could be obtained from the shear stress measured with the misalignment corrected by the squared cosine of the misalignment angle.

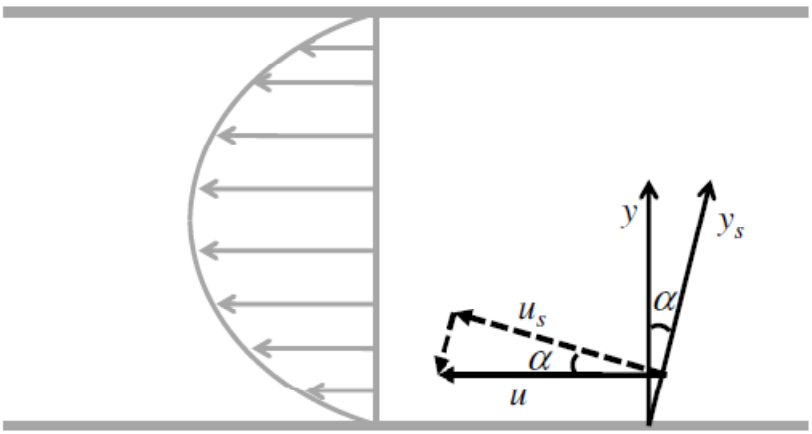

Figure 6-9. *Effects of misalignment between LDV probe and the wall surface in the Poiseuille flow. u: true velocity; u_s: measured velocity component; y: true normal to wall direction; y_s: LDV probe alignment; α: angle difference between the LDV probe alignment and the wall normal direction.*

6.1.6.2 Cylindrical Couette Flow

The Couette flow scenario was meant to test the effects of wall curvature on errors. In Couette flow, no out-of-plane velocity components existed, but the wall and flow near the wall were curved, and with the 0.15 radians misalignment, errors would

occur in velocity sampling due to errors in sampling location. This flow could be described in the cylindrical coordinates as

$$u_\theta = \tau \cdot (R - r) \qquad \text{(Equation 6-15)}$$

Where u_θ was the azimuthal velocity or the streamwise velocity, R was the radius of the curvature of the wall, and r was the radial coordinate, such that the distance from the wall was (R-r) (figure 6-10a). We could assume the length scale of the sinus space as 20mm, and thus the radius of curvature was 10mm. The vector field of this flow could be generated by Matlab® and is shown in figure 6-10a. Velocity was sampled at 89 microns intervals from the wall along the normal to the wall, and along a line slanted 0.15 radians from the normal to the wall. The resulting velocity profile is shown in figure 6-10c. The percentage error of the calculated shear stress using the slanted line was 2.2%. With the square cosine correction, the percentage error of calculated shear stress was 0.1%.

Thus the error in shear stress calculation associated with 0.15 radians misalignment was small in curved wall flow.

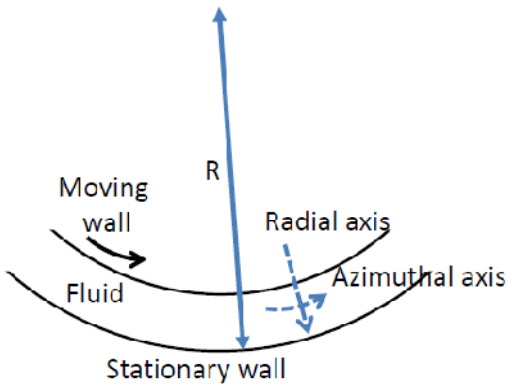

Figure 6-10a. *Schematic of the Couette flow.*

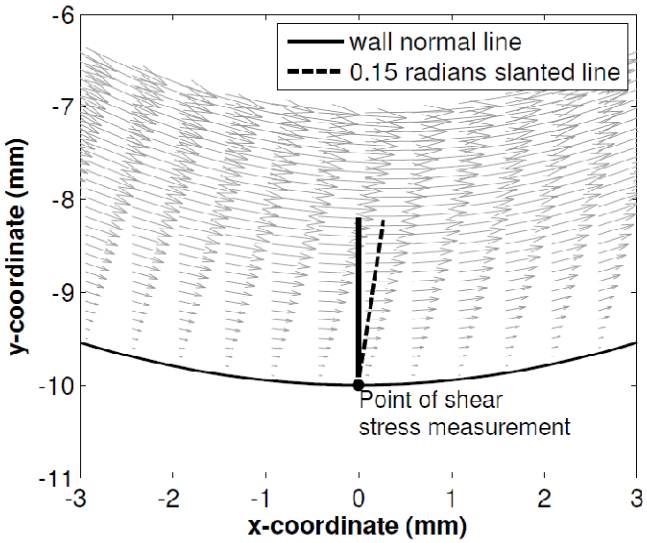

Figure 6-10b. *The Couette flow field (down-sampled from original grid), calculated according to the theoretical solution. The wall normal direction (solid line) and the 0.15 radians slanted LDV probe direction (broken line) are illustrated.*

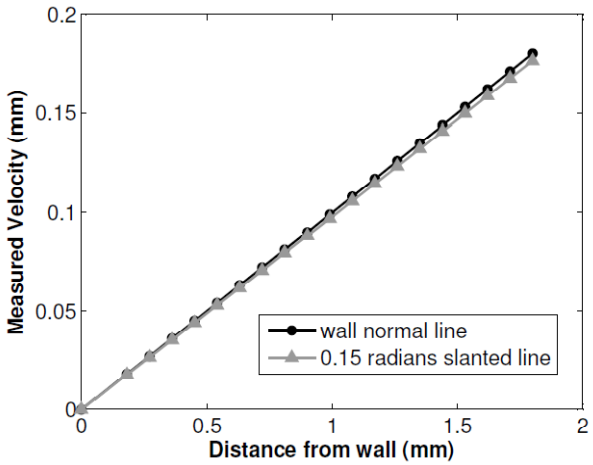

Figure 6-10c. *Velocity measurements as a function of distance from the wall, as measured along the wall normal direction (black) and along the 0.15 radians slanted direction (grey).The difference in shear stress measurement is small (0.1%)*

6.1.6.3 Hiemenz Wall Impingement Flow

In the Hiemenz flow, a free stream jet impinges on the wall, forming a flow stagnation point on the wall (figure 6-11a). This flow scenario tested for the errors due to

the presence of out-of-plane velocities. The governing equations for the flow were as follows [107]:

$$F''' + FF'' + 1 - F'^2 = 0 \qquad \text{(Equation 6-16)}$$

$$u_x = \frac{U_0}{L} x F'(\eta) \qquad \text{(Equation 6-17)}$$

$$u_y = -F(\eta)\sqrt{\frac{U_0}{L}\nu} \qquad \text{(Equation 6-18)}$$

$$\eta = y\sqrt{\frac{U_0}{L\nu}} \qquad \text{(Equation 6-19)}$$

Where x and y were the Cartesian coordinates, where (0,0) was the stagnation point, u_x and u_y were the velocities in the x and y axes, U_0 was the free stream velocity, L was the characteristic length scale, and ν was the dynamic viscosity. Equation 6-16 could be solved with Matlab. The free stream velocity scale was assumed to be 0.5m/s and length scale was 20mm, such that the simulation would be relevant to the experiments in the current study. Part of the vector field is shown in figure 6-11b.

Wall shear stress computed by sampling velocities along the wall-normal line were compared to wall shear stress computed by sampling velocities along a slanted line 0.15 radians from the wall-normal line. This comparison was done at various x-coordinates. These various x-coordinates represented flows with different out-of-plane velocity components. At the stagnation point x-coordinate, flow was almost entirely composed of out-of-plane velocities. Further away from the stagnation point, the out-of-plane velocity components gradually reduced.

The percentage error of computing shear stress using the slanted line is shown in figure 6-11e. The true wall shear stresses computed using velocities sampled along the wall-normal line is shown in figure 6-11c, and the absolute difference in computed shear

stress is shown in figure 6-11d. The results showed that errors associated with the 1.5 radians misalignment was smaller than 3% unless wall shear stresses were measured very close to the stagnation point (between -0.17 mm and 0.37 mm), indicating that unless large out-of-plane velocity components were present, the percentage error was small. Near to the stagnation point, however, wall shear stresses were very low, since velocity components parallel to the wall are small. Consequently, the absolute value of the error in shear stress computation was small despite the percentage error becoming large. Absolute error of shear stress computation near to the stagnation point (-0.17 mm < x < 0.37 mm) was smaller than further downstream (x > 0.37 mm), where percentage errors were less than 3%.

Thus errors associated with the 0.15 radians misalignment of the velocity sampling line with wall-normal line was less than 3% of relevant shear stress quantities.

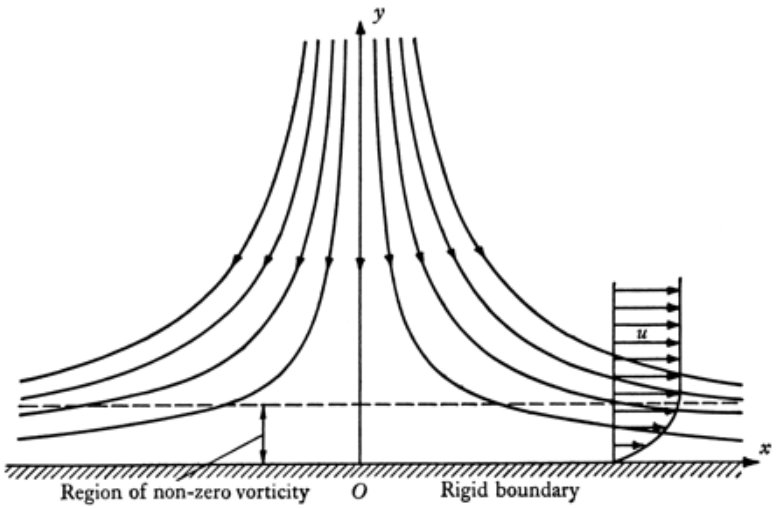

Figure 6-11a. *Schematic of the Hiemenz flow. Adapted from [118].*

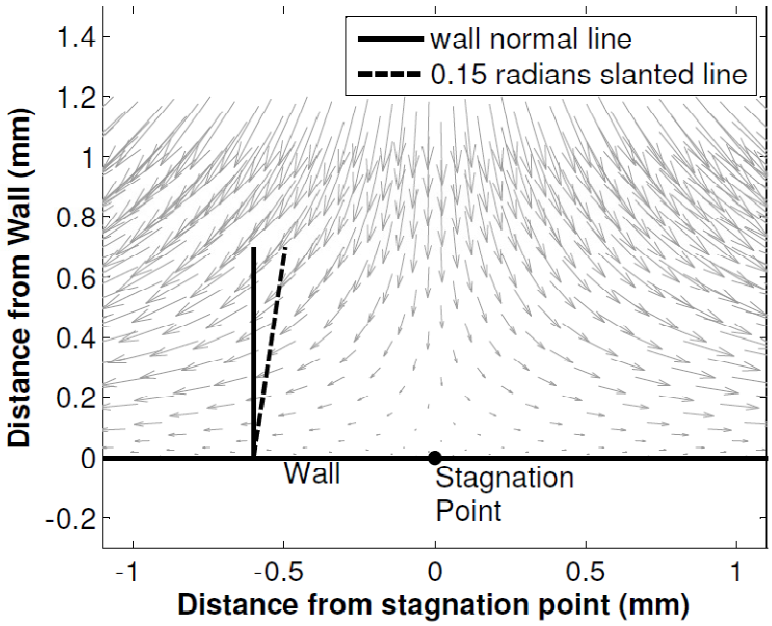

Figure 6-11b. *Vector field of the Hiemenz flow (down-sampled). The wall normal direction (solid line) and the 0.15 radians slanted LDV probe alignment (broken line) are shown. Shear stresses were computed at various wall locations, which represented the different extend of dominance of out-of-plane velocities.*

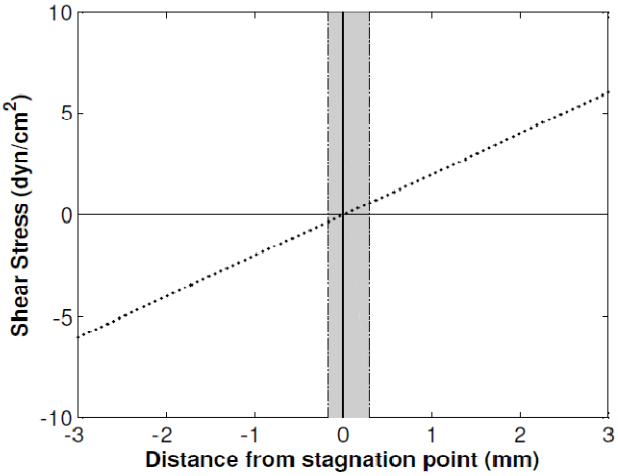

Figure 6-11c. *True shear stress at various locations on the wall, which represented various levels of out-of-plane velocity dominance. The shaded region indicates the region close to the stagnation point (shaded region). In this region, shear stresses were small.*

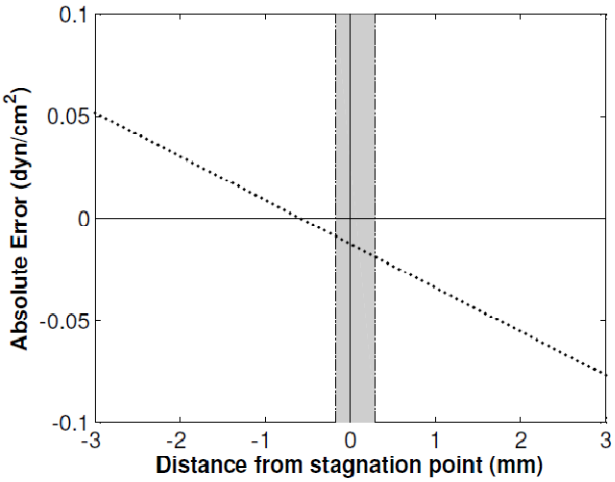

Figure 6-11d. *The absolute error in shear stresses at various wall locations: difference between shear stresses measured with the 0.15 radians LDV alignment slant and the true shear stresses. The shaded region indicates the region close to the stagnation point. In this region, absolute errors were small.*

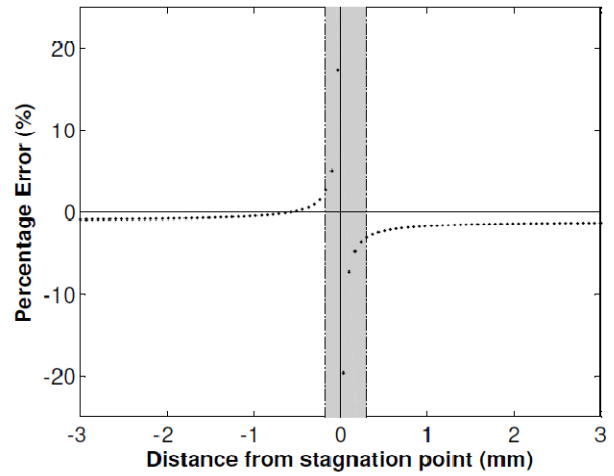

Figure 6-11e. *Percentage error in shear stress measurement due to the 0.15 radians slant in the LDV probe alignment. The shaded region indicates the region very near to the stagnation point. Errors were less than 3% everywhere except for very near to the stagnation point (shaded region). Near the stagnation point, errors were amplified because absolute shear stresses were very low.*

6.1.7 Estimation of the Boundary Layer Thickness

The radial dimension of the sinus spaces (used as the radial length scale, L_R) and maximum velocity measured in the sinuses are shown in table 6-1. Velocity scale (V_{scale}) for sinus flows were conservatively estimated by assuming that all three components of

velocity were of the same order of magnitude as the maximum measured velocity (V_{max}), which means:

$$V_{scale} = \sqrt{3V_{max}^2} \qquad \text{(Equation 6-20)}$$

For flow within the valve orifice (used for ventricular surface shear stress), the streamwise velocity dominates and thus the peak streamwise velocity was used as the velocity scale. The Reynolds number (Re) was calculated accordingly, using dynamic viscosity of $3.5*10^{-6}$ m^2. The axial length scale (L_A) was estimated to be 2cm for all cases and the boundary layer thickness (δ) was calculated according to Equation 5-11 and 5-12. The number of velocity data points within the boundary layer was also calculated using the information that spatial resolution was 89 microns. These calculations demonstrated that the measurement resolution should be sufficient to resolve the boundary layers.

Table 6-1. *Characteristic scales of various flows analyzed for in this thesis (V, L), the Reynolds number of the flows (Re), the boundary layer thickness estimation (δ) using the Blasius solution and solution to the Stoke's problems and the number of velocity data points that can be measured within the boundary layer (N) using the current spatial resolution of 89 microns.*

Cases	V_{max} (m/s)	V_{scale} (m/s)	L_R (mm)	L_A (mm)	Re	$\delta_{Blasius}$ (mm)	δ_{Stokes} (mm)	$N_{Blasius}$	N_{Stokes}
Aortic Surface of the Normal Valve	0.33	0.57	15	20	2443	2.0	1.2	22	13
Ventricular Surface of the Normal Valve	1.45	1.45	20	20	8286	1.1	0.7	12	7
Aortic Surface of the BAV fused leaflet	0.35	0.61	15	20	2614	2.0	1.2	21	13
Aortic Surface of BAV non-fused leaflet	0.69	1.19	15	20	5100	1.4	0.8	15	9

6.2 Specific Aim 2: Shear Stresses on the Leaflets of the Normal Tricuspid Aortic Valve

In this specific aim, results are presented for: (1) shear stresses measured and calculated on the ventricular surface of the aortic valve leaflet surface, and (2) shear stresses measured on the aortic surface of the valve leaflet. For the aortic surface, variation of the streamwise shear stresses with different stroke volumes and heart rates is also presented.

6.2.1 Quantification of Ventricular Surface Shear Stresses

Results for the experimental measurement of ventricular surface shear stress are first presented. Measurements are made using two polymeric valve models, hereafter named as valve 1 and valve 2. Thereafter, results of the theoretical modeling of ventricular surface shear stress and its application to *in vivo* cases are presented.

6.2.1.1 Experimental Measurement of Ventricular Surface Shear Stresses

6.2.1.1.1 Flow Loop Hemodynamics

The flow and pressure waveforms from the experiments are presented in figure 6-12. Physiological flow conditions were maintained throughout the experiments (Aortic pressure: 80/120 mmHg, cardiac output: 4.5 – 5.0 L/min, heart rate 70 beats/min), and results from the two valves are shown in table 6-2. The measured hemodynamics showed that valve 2 had a smaller forward flow pressure gradient than valve 1 for the same forward flow rate, indicating a larger orifice area. Both valves experienced oscillations in flow rate directly after closure during early diastole, with larger oscillations for valve 2.

These oscillations were an artifact of using polymeric valves, which were less flexible during valve closure and should not be observed in native valves. Since the focus of the current study was on systolic shear stresses, these oscillations should not affect results presented here. Overall, the two valves displayed small differences in hemodynamics, consistent with minor design differences between the two valves.

Table 6-2. *Hemodynamic characteristics of the two polymeric valve models.*

	Valve 1	**Valve 2**
Peak pressure gradient (in mmHg)	38	22
Mean pressure gradient (in mmHg)	24	7.2
Peak flow rate (in L/min)	20.2	21.6

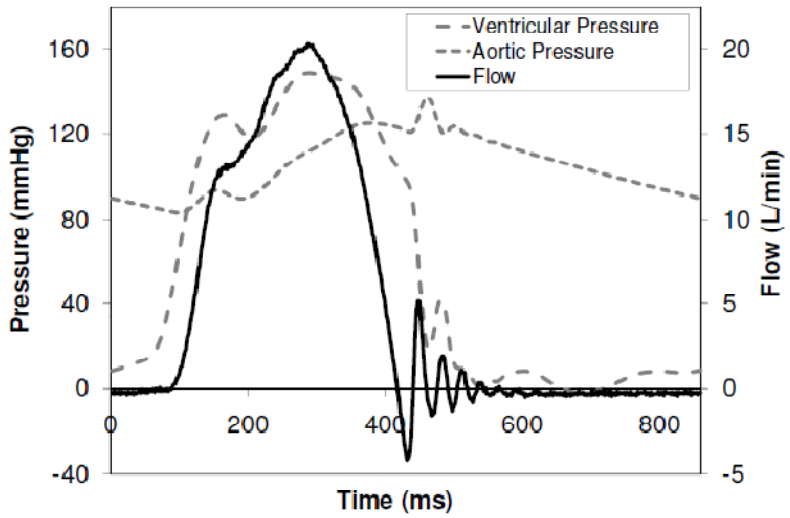

Figure 6-12a. *Hemodynamics simulated in the flow loop on polymeric valve model 1.*

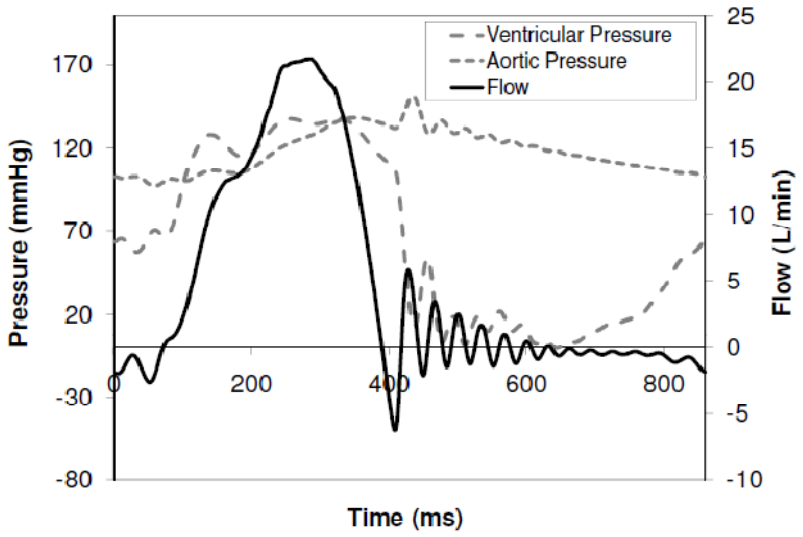

Figure 6-12b. *Hemodynamic simulated in the flow loop on polymeric valve model 2.*

6.2.1.1.2 *Leaflet Dynamics*

The reflected light intensity technique provided signals with low noise, and provided a description of the valve leaflet location along the scan line over the entire cardiac cycle. A sample of the reflected light intensity map is shown in figure 6-13a for valve 2 while the segmented leaflet location plot for both valves is show in figure 6-13b. The gradient of the segmented leaflet location gave the out-of-plane velocity of the valve leaflet. Further, valve leaflet velocities in the streamwise direction were estimated from LDV velocity measurements within 90μm from the valve leaflet surface location, assuming that the no-slip boundary condition applied at the leaflet surface.

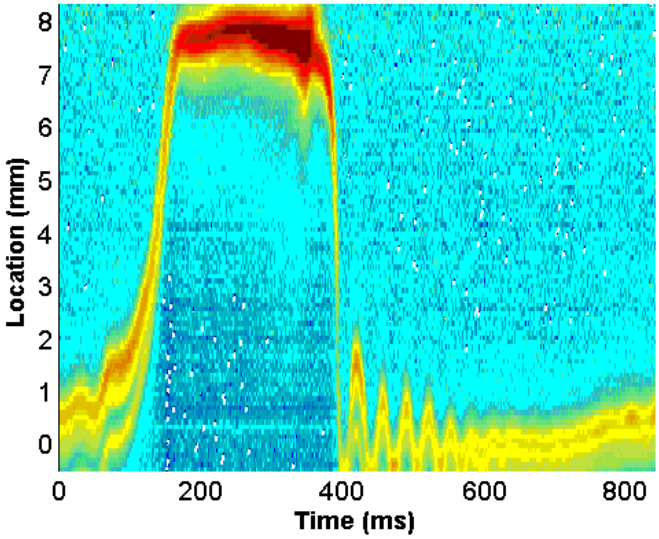

Figure 6-13a. *Back-scattered light intensity map for Valve 2, showing that the valve leaflet reflected significant amount of light sufficient for tracing its position over the cardiac cycle.*

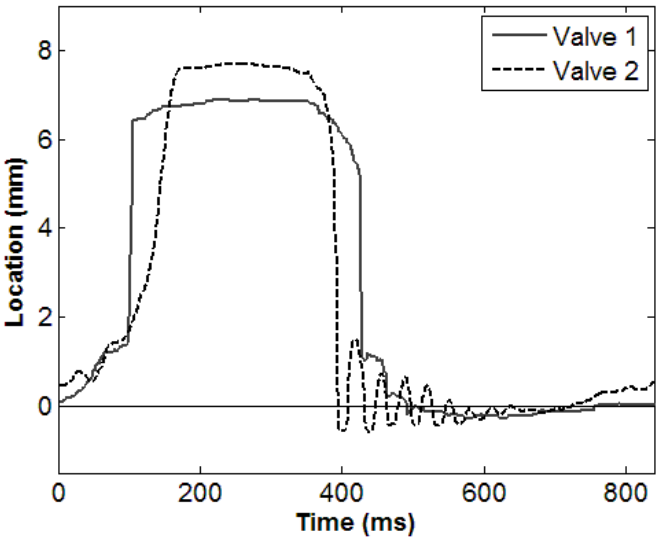

Figure 6-13b. *Valve leaflet position over the cardiac cycle for polymeric valve models 1 and 2*

For valve 1, during systole, the valve leaflet remained almost stationary in the open position. Out-of-plane leaflet velocities were less than 0.02 m/s, and streamwise

leaflet velocities did not exceed 0.03 m/s. For valve 2, systolic out-of-plane leaflet velocities were less than 0.05 m/s, and streamwise leaflet velocities were less than 0.01 m/s. In the non-streamwise direction, the average leaflet velocity was always zero, because measurements were performed along the line of symmetry. Overall, the velocities of the leaflets during the period of shear stress measurements were much smaller compared to the forward flow velocities (~1.5 m/s during peak systole). Hence, measurement errors due to in-plane and out of plane motions of the valve should be minimal.

6.2.1.1.3 Valve Geometry

Images of the valves in the steady flow loop are shown in figure 6-14. The opening angle of the valves was defined as the angle made by the valve leaflet from the annular plane. Using this definition, a fully open valve with leaflet parallel to the aortic root has an opening angle of 90°. The opening angle of the valves in the open configuration under 20 L/min steady flow condition for both valves was quantified to be 72.1^{o} in valve 1 and 77.4^{o} in valve 2.

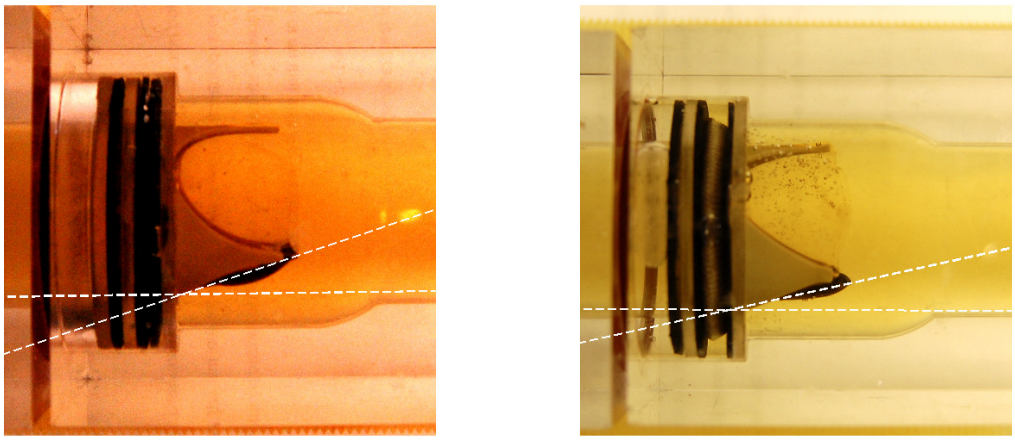

Figure 6-14. *Images of the polymeric valve models in a steady flow loop subjected to 20 L/min of steady flow, used for calculating the opening angle of the valve leaflets.*

6.2.1.1.4 *Flow Fields*

All velocity and shear stress results presented here corresponded to ensemble averaged flow, and were not identical to the instantaneous flow. Ensemble averaging preserved the dominant features which exist across all cycles, while filtering out the small scale instantaneous variations across cycles. Figure 6-15 shows the ensemble averaged velocity measurements along the interrogation line from the sinus wall to the center of the valve for valve 1, and was representative of both valves. In this figure, horizontal scan lines represent an instant in the cardiac cycle. Systole occurred between 90 ms and 400 ms. In the sinus region, low velocities were observed, and velocities were mostly low except for late systole. After valve closure, fluid motion gradually dissipated over the duration of diastole.

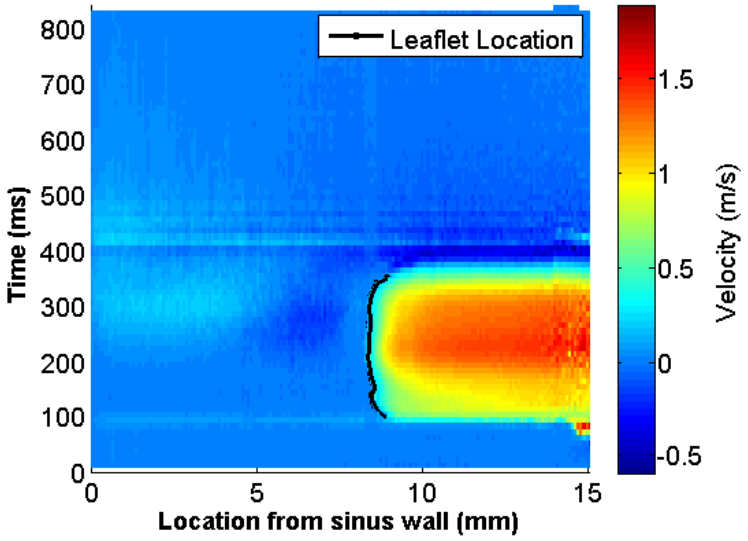

Figure 6-15a. *Sample of the phase-locked ensemble average velocities map in the streamwise direction, measured in valve 1.*

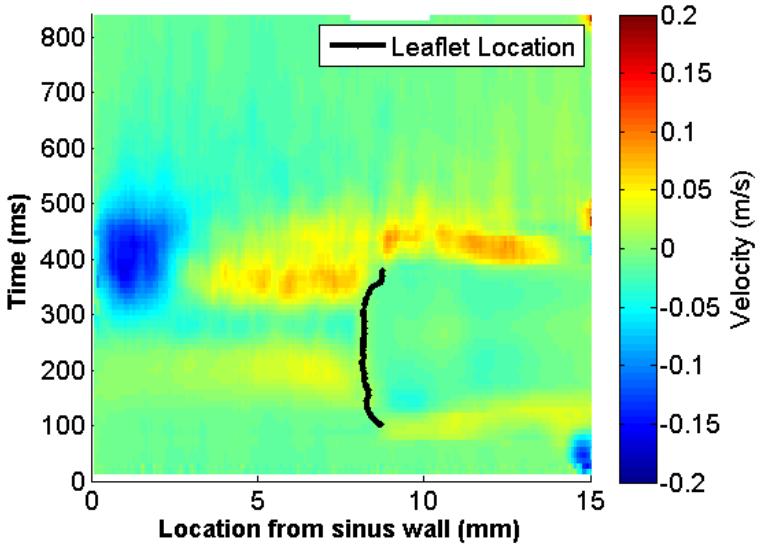

Figure 6-15b. *Sample of the phase-locked ensemble average velocities map in the non-streamwise direction, measured in valve 1*

During systole, high streamwise velocities were observed within the valve orifice. Velocities increased from near zero on the ventricular surface of the leaflet to about 1.5 m/s near the center of the valve. The ventricular surface displayed a time varying

boundary layer which was uniform across different cycles, consistent with theoretical considerations at this Reynolds number. This profile could be accurately characterized using a parabolic profile. Figure 6-16 plots the ensemble-averaged velocities with the least-square best-fit parabolic curve at two systolic time points for both valves. The coefficient of determination (R^2 value) of the fit for all the time points for all the different points on the leaflets being measured for both valves were between 0.81 and 0.99, and had an average of 0.98, demonstrating the goodness of the fit. Figure 6-28 also shows very low cycle-to-cycle variability in the measured velocities, as indicated by the standard deviations of the ensemble-averaged velocities. Thus, ensemble averaged results presented here are representative of all cycles.

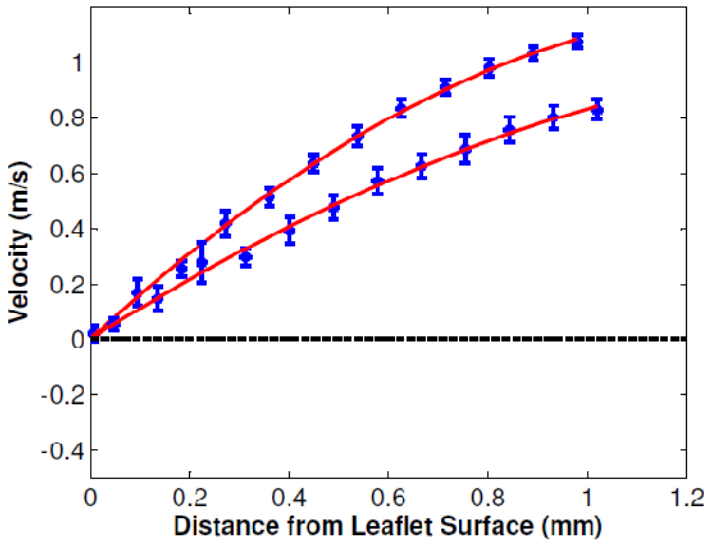

Figure 6-16. *Representative sample plot of the ensemble averaged velocities and ensemble standard deviation of these velocities versus distance from the leaflet surface, and the best fit least square parabolic curve (at 260 ms and 320 ms for valve 1), demonstrating that the parabolic profile fits well with the measured velocity.*

Figure 6-17 shows the ventricular velocity profiles at various systolic time points, as well as the flow profiles normalized by the free-stream velocity. The flow velocity was seen to attain a relatively constant value for distances greater than 1.5mm from the surface, and this was used as the free-stream velocity. As shown in figure 6-17c and 6-17d, the normalized flow profiles were observed to have a gradually decreasing gradient in the boundary layer over time, indicating the slight increase in boundary layer thickness and the occurrence of flow development. During late systole, flow reversal was observed, which manifested first in the boundary layer.

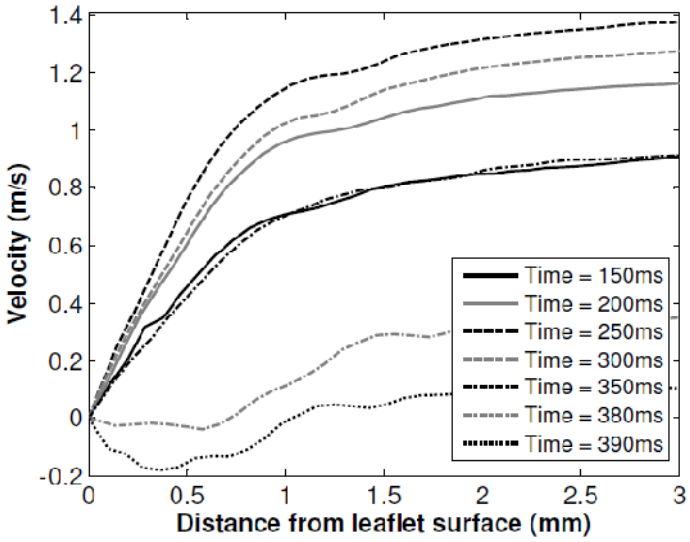

Figure 6-17a. *Ensemble average velocity profile for valve 1 near the valve leaflet surface at various time points during systole. Flow reversals were observed during late systole.*

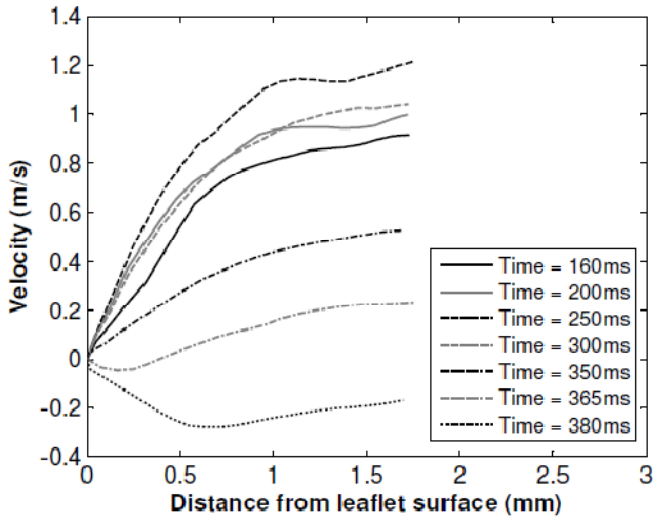

Figure 6-17b. *Ensemble average velocity profile for valve 2 near the valve leaflet surface at various time points during systole. Flow reversals were observed during late systole.*

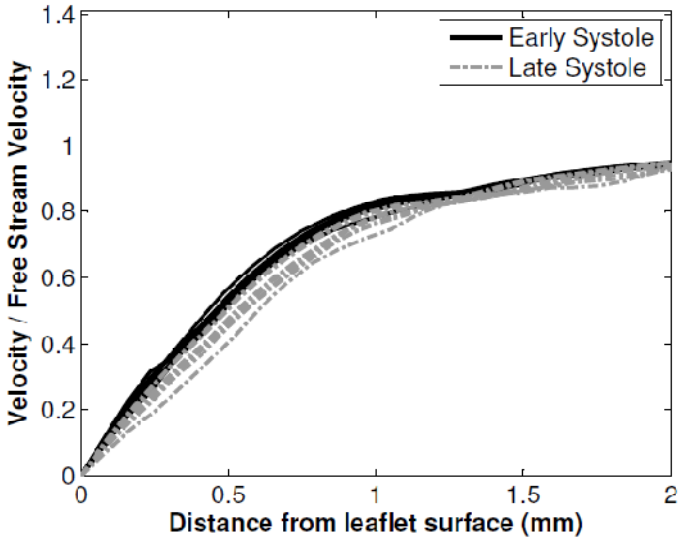

Figure 6-17c. *Ensemble average velocity profile for valve 1 near the valve leaflet surface at various time points during systole, normalized by peak velocity. Flow development was observable in the normalized profiles.*

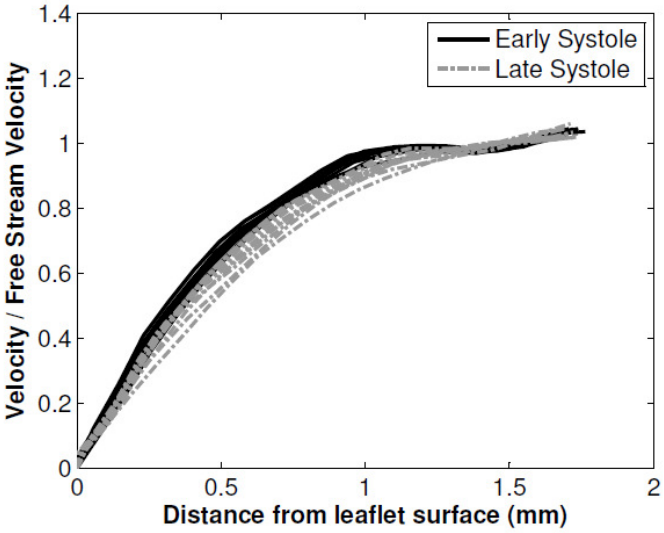

Figure 6-17d. *Ensemble average velocity profile for valve 2 near the valve leaflet surface at various time points during systole, normalized by peak velocity. Flow development was observable in the normalized profiles.*

6.2.1.1.5 *Shear Stress Computation*

This thesis adopts the following convention for describing shear stresses: "fluctuating shear stress" is defined as shear stress that has repeated variation in magnitude within a short period of time (the magnitude moves from high to low to high and repeats itself); "sinusoidal shear stress" is defined as shear stress in the shape of perfect sine waveforms.

Figure 6-18a and 6-18b plot the ventricular surface shear stresses measured for both valves. Streamwise and non-streamwise shear stresses were measured for both valves at only one location on the leaflet: point 2, which is at the center of the valve leaflet, approximately 9 mm away from the annulus. Streamwise shear stresses were also measured at a point 0.32mm upstream of point 2 (point 1) for both valves and at a point 0.32mm downstream of point 2 (point 3) for valve 2. In figure 6-18, shear stresses are

shown for the systolic durations where the valve leaflets were sufficiently stationary. As described in section 4.2.1, valve 1 had shorter closing and opening times; hence the shear stress measurement window was larger for valve 1.

Streamwise shear stress waveforms from all points for a given valve matched each other within experimental errors. The two different valves displayed similar streamwise shear stress waveforms. The waveforms had a half sinusoid shape, resembling the volumetric flow curve. The streamwise shear stress and flow curves matched identically during early systole, increasing towards their maximum values. However, the rate of increase in shear stress started trailing that of volumetric flow near peak systole (~200ms). Peak shear stress was observed about 30-55ms before peak volumetric flow rate. Peak shear stress at point 2 was 64 dyn/cm^2 for valve 1 and 71 dyn/cm^2 for valve 2. Beyond its peak, the shear stress initially decreased gently and then rapidly for the remaining duration of systole. For valve 1, the shear stress became negative about 37 ms before the flow curve, whereas this time was 27 ms for valve 2. Shear stresses remained negative during late systole for 15 ms for valve 1 and 25 ms for valve 2. The rate of decrease of shear stress was higher for valve 1 than valve 2. For both valves, the streamwise shear stress was significant at end systole (-40 dyn/cm^2 for valve 1 and 51 dyn/cm^2 for valve 2). During early systole, the shear stress curve displayed a spike, which was most likely associated with disturbance in the flow at this instant in time.

Figures 6-18a and 6-18b also show the non-streamwise shear stresses for the two valves. The overall magnitude of this component of shear stress was much smaller than the streamwise component. Except for early systole, non-streamwise shear stress was near to zero. During early systole, valve 1 displayed a small duration of positive shear

stress, before becoming negative for the entire systolic duration. The change in sign of shear stress corresponded to the spike in streamwise shear stress. Valve 2 displayed similar trends, but the positive portion of the shear stress was not recorded due to the smaller sampling window during systole. The peak non-streamwise shear stress magnitude was 8 dyn/cm^2 for valve 1 and 18 dyn/cm^2 for valve 2.

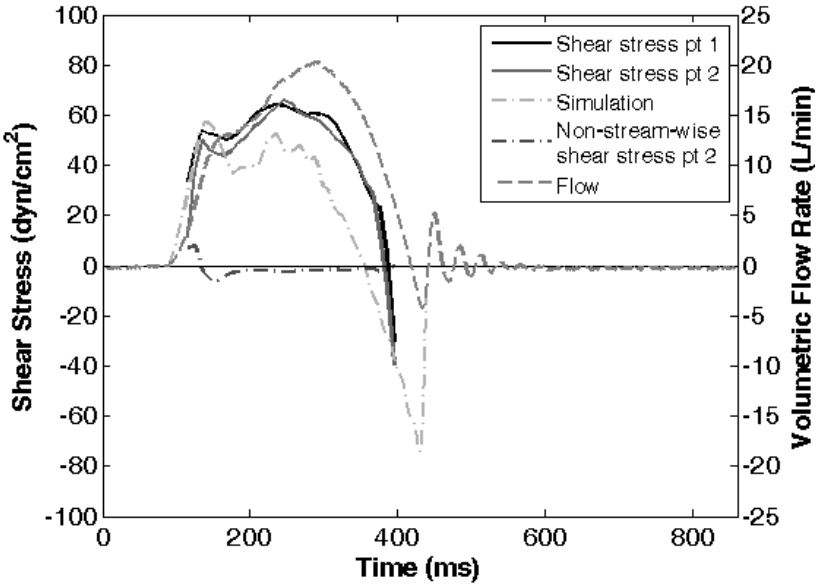

Figure 6-18a. *Plots of fluid Shear stresses on the ventricular surface of the valves computed from measured velocities for valve 1 at point 2 for both non-streamwise direction, and at points 1, 2 and 3 in the stream-wise direction. Point 2 is the center of the valve leaflet and point 1 is 0.32 mm upstream of point 2, which is in turns 0.32 mm upstream of point 3. Fluid shear stress calculated with the theoretical modeling is also plotted for comparison.*

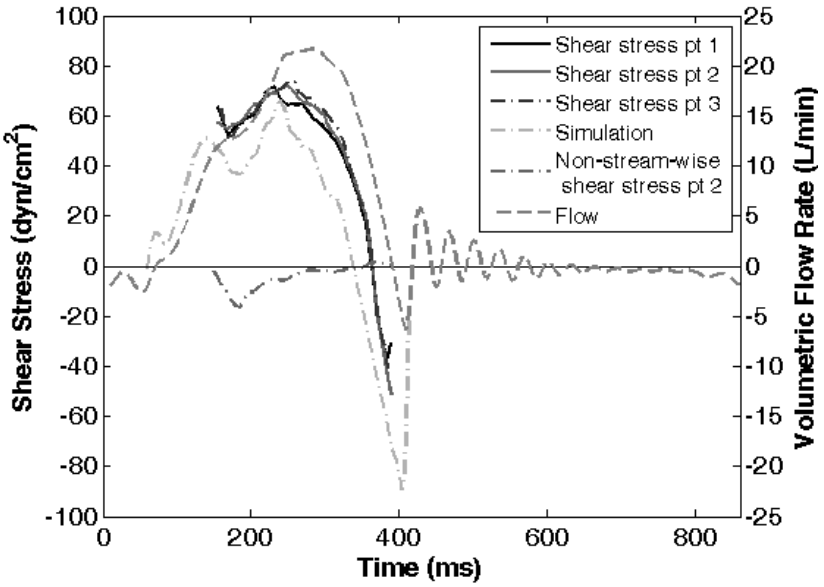

Figure 6-18a. *Plots of fluid Shear stresses on the ventricular surface of the valves computed from measured velocities for valve 2 at point 2 for both non-streamwise direction, and at points 1, 2 and 3 in the stream-wise direction. Point 2 is the center of the valve leaflet and point 1 is 0.32 mm upstream of point 2, which is in turns 0.32 mm upstream of point 3. Fluid shear stress calculated with the theoretical modeling is also plotted for comparison.*

The Reynolds Normal Stress estimations were shown in figure 6-18c. The Reynolds stress were shown to be substantial in magnitude during early and late systole, when forward flow was rapidly accelerating or decelerating, reaching as high as 165 dyn/cm^2. During the majority of systole, however, the Reynolds shear stress was found to be approximately 6 – 18 dyn/cm^2.

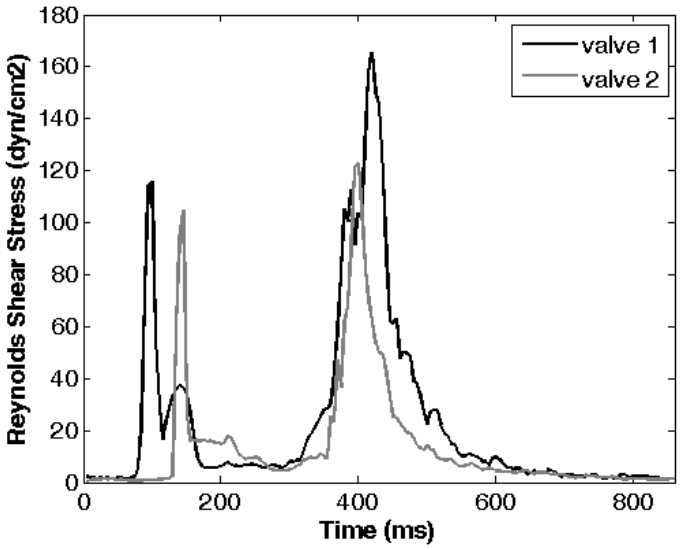

Figure 6-18c. *Reynolds normal stress in the two valves, calculated based on velocities measured at approximately 1mm away from the valve leaflet ventricular surface.*

6.2.1.2 Theoretical Modeling of Ventricular Shear Stress

The theoretical modeling for the ventricular surface shear stress using the Womersley solution was intended as an order of magnitude analysis to obtain general features of ventricular surface shear stresses. The assumption of a straight tube geometry was an idealization from the native valve in its opened configuration, and so was the assumption that there was sufficient entrance length. Even though the results of the modeling showed agreements with the measurements in the polymeric valve model, it must be noted that significant simplification assumptions were made, and the reader must interpret the results with caution.

The Womersley solution analysis was adapted to estimate shear stresses on the ventricular surface of the in vitro polymeric aortic valve model leaflet, and then applied to *in vivo* data.

6.2.1.2.1 Modeling Based on Experimental Hemodynamics

Figure 6-19 shows the raw and normalized flow profiles generated using the theoretical model of shear stresses. In figure 6-19c and 6-19d, the profiles were normalized by the centerline velocities. The Womersley solution was applied to straight tubes with 10 mm radius, nominally similar to the radii of the valves. Overall, the theoretical profiles gradually developed through systole and reversed during late systole, similar to the experimental profiles. Differences could be observed, for example, during early systole (around 150 ms), the simulations showed a point of inflexion in the flow profile slightly medial from the boundary layer, but such a profile shape was more subtle in the experimental measurements. Further, the normalized flow profile shapes showed flow development more prominently than the experimental measurements. These differences can be accounted for by the taper angle of the polymeric valves.

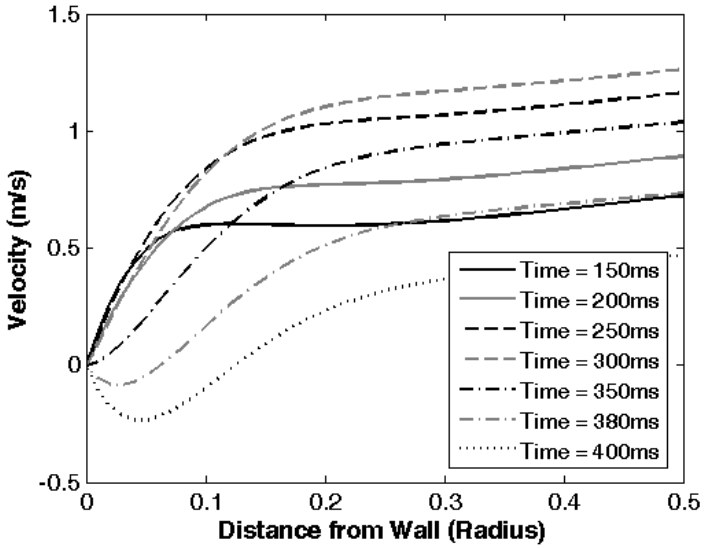

Figure 6-19a. *Flow profiles at various time points for the volumetric flow waveform of valve 1, calculated from the Womersley solution for the straight tube using the same flow rate as those used in the experiments.*

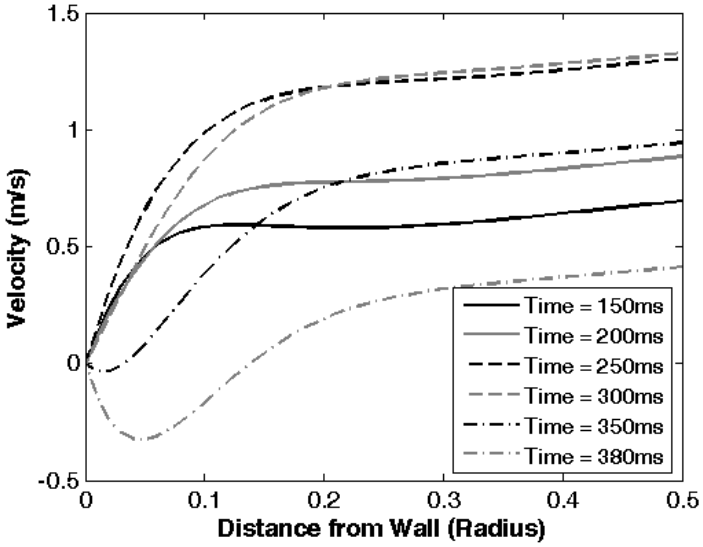

Figure 6-19b. *Flow profiles at various time points for the volumetric flow waveform of valve 2, calculated from the Womersley solution for the straight tube using the same flow rate as those used in the experiments.*

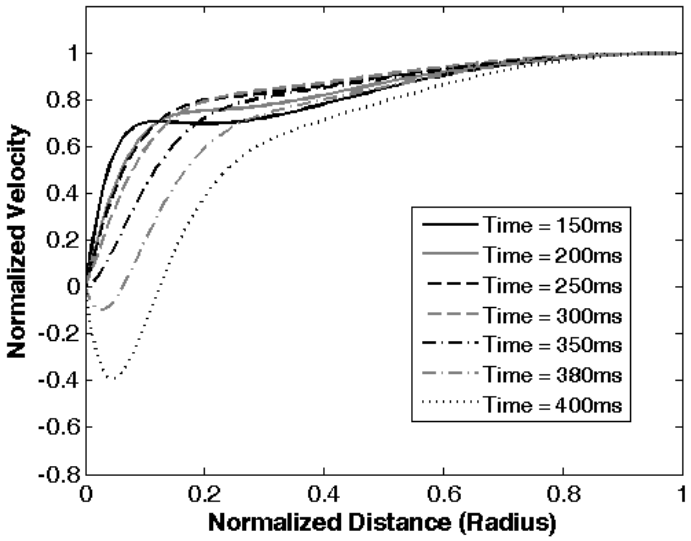

Figure 6-19c. *Flow profiles at various time points for valve 1, normalized by the tube centerline velocity, calculated from the Womersley solution for the straight tube using the same flow rate as those used in the experiments.*

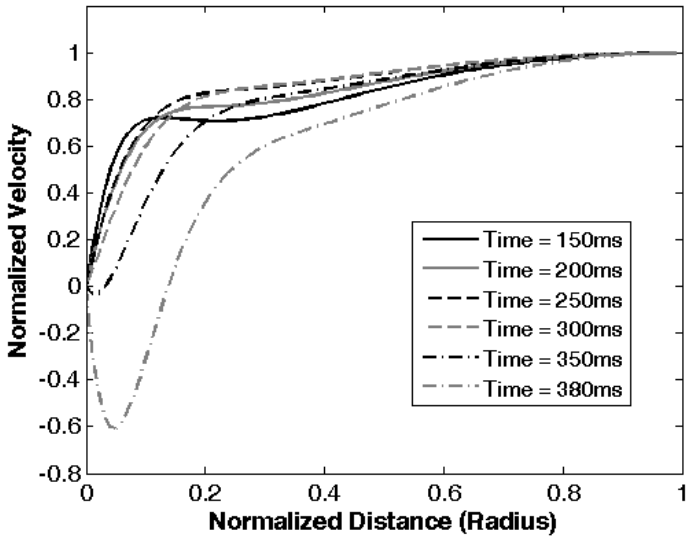

Figure 6-19d. *Flow profiles at various time points for valve 2, normalized by the tube centerline velocity, calculated from the Womersley solution for the straight tube using the same flow rate as those used in the experiments.*

Figure 6-18 also shows wall shear stresses calculated from the Womersley solution. The wall shear stress results showed similar trends as those observed in the valves. During early systole, the theoretical results matched the experimental values very well, and the spike in shear stress at 150 ms was also observed in the simulations. The maximum shear stress during the peak flow phase occurred about 50ms before peak volumetric flow occurred. During the deceleration phase, the shear stress steadily decreased and became negative during the mid deceleration phase, about 60 ms before the volumetric flow curve became negative. Shear stress reached a high negative value at end systole, before moving back to zero. The peak negative shear stress during end systole was 74 dyn/cm^2 for the valve 1, and the corresponding value for the valve 2 was 89 dyn/cm^2. Compared to the shear stresses in the valves, the simulated straight pipe

shear stresses had smaller magnitudes in the forward direction, but higher magnitudes in the reverse direction, and the shear stress became negative earlier during late systole.

The shear stress magnitude deviation between the LDV measurements and the theoretical simulations are plotted in figure 6-20. In valve 1, this deviation is initially slightly negative, but increases over the duration of systole to about 39 dyn/cm^2. In valve 2, this deviation has a similar behavior to valve 1, except that during mid to late systole, deviations are slightly lower in magnitude than in valve 1.

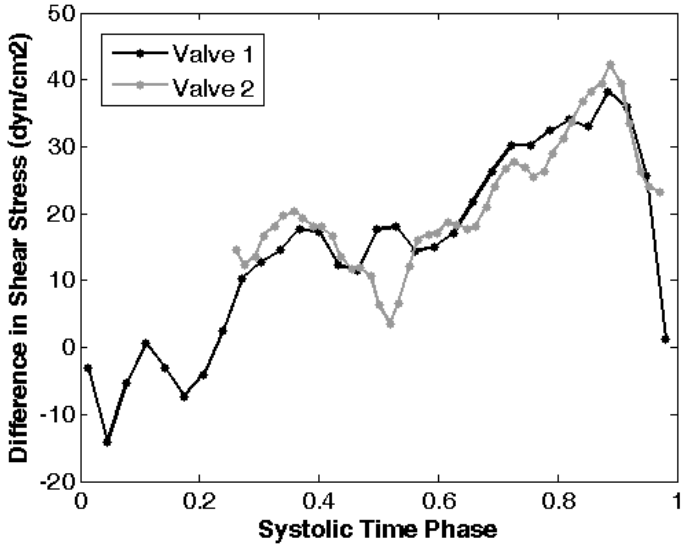

Figure 6-20. *Shear stresses measured in the polymeric valves in vitro less the shear stresses calculated with the simulation assuming the same volumetric flow rates and the same channel dimension. This deviation between the two data sets can be explained by the taper angle in the actual valves leaflets during systole, which contrasts with the lack of taper angle in the simulations.*

6.2.1.2.2 Modeling Based on In Vivo Hemodynamics

Figure 6-21 shows the ascending aortic volumetric flow rates acquired through PC-MRI obtained from the literature. These volumetric flow rates were used as inputs in

the theoretical modeling to obtain shear stresses, which are shown in same figure. Modeling results showed that the peak ventricular surface shear stresses were approximately 92 dyn/cm^2 and 77 dyn/cm^2 for data from Powell et al. and Langerak et al., respectively. The shear stress rose rapidly to its peak during early systole, and then gradually reduced to a negative value over the remaining systolic time. In both *in vivo* data sets, shear stress reversed in direction during late systole for a substantial amount of time (110 ms for Powell et. al., and 108 ms for Langerak et al.). Peak negative shear stresses were calculated to be 35 dyn/cm^2 and 38 dyn/cm^2 for Powell et al. and Langerak et al., respectively.

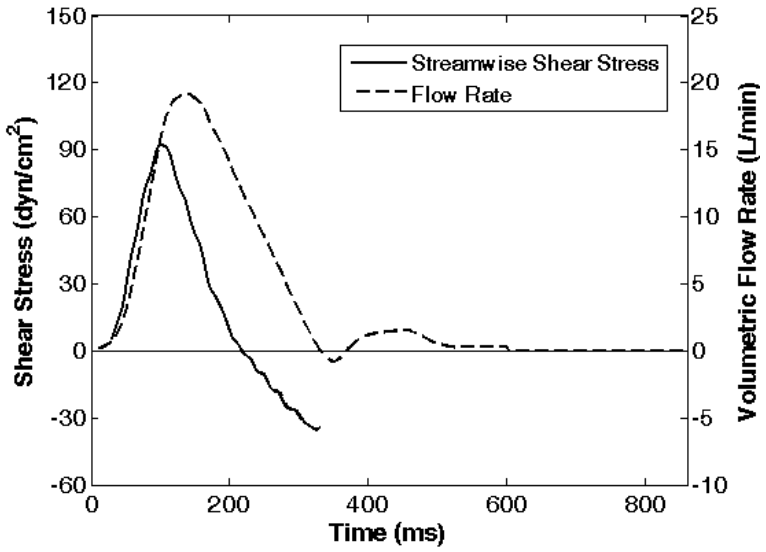

Figure 6-21a. *In vivo flow curve acquired with PC-MRI, obtained from Powell et al. [112] and the ventricular surface shear stress on the aortic valve, calculated with theoretical simulations.*

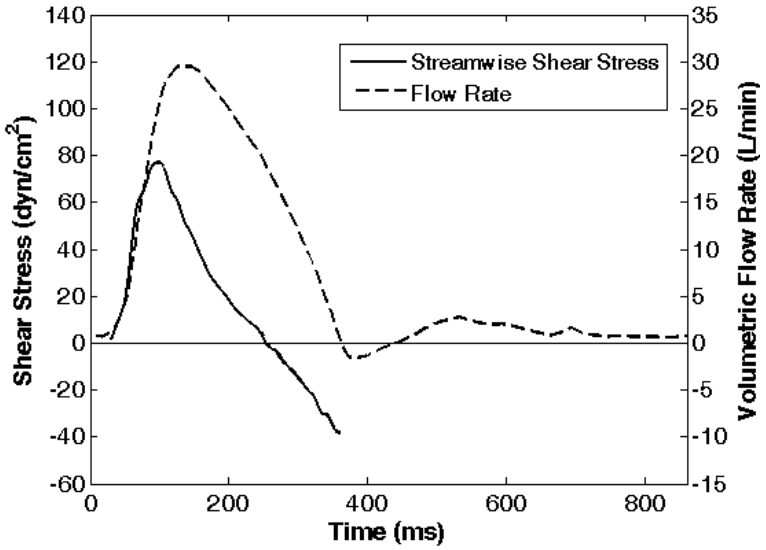

Figure 6-21b. *In vivo flow curve acquired with PC-MRI, obtained from Langerak et al. [113] and the ventricular surface shear stress on the aortic valve, calculated with theoretical simulations.*

The flow profiles computed from the theoretical modeling are shown in figure 6-22. Results showed similar characteristics as the *in vitro* measurements in the following aspects: (1) throughout the systolic duration, flow continuously developed, leading to redistribution of velocity profile; (2) reverse flow was observed first in the fluid closest to the leaflet during late systole.

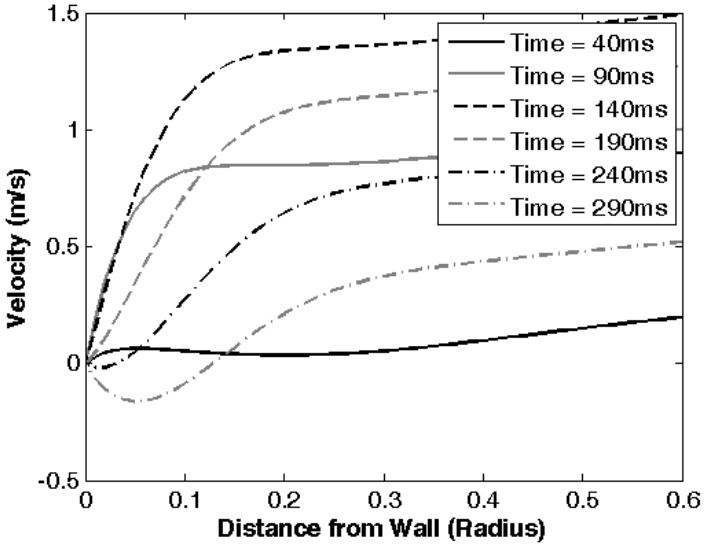

Figure 6-22a. *Flow profiles near the ventricular surface of the aortic valve for in vivo flow curves from Powell et al. [112], calculated with the theoretical modeling.*

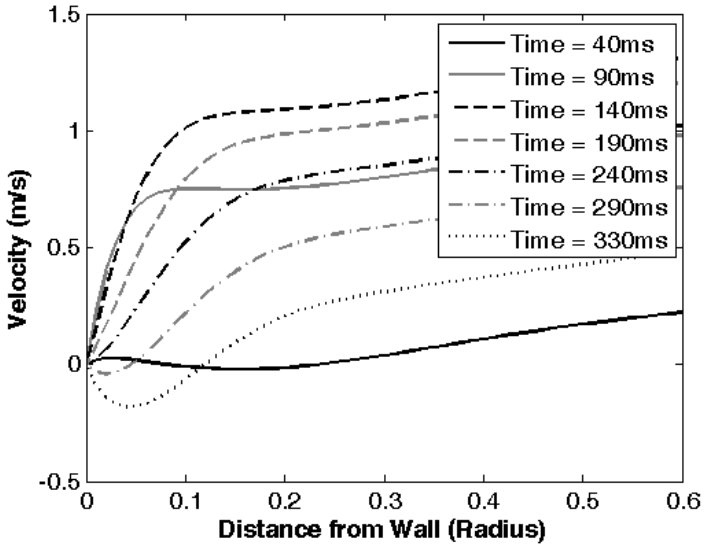

Figure 6-22b. *Flow profiles near the ventricular surface of the aortic valve for in vivo flow curves from Langerak et al. [113], calculated with the theoretical modeling.*

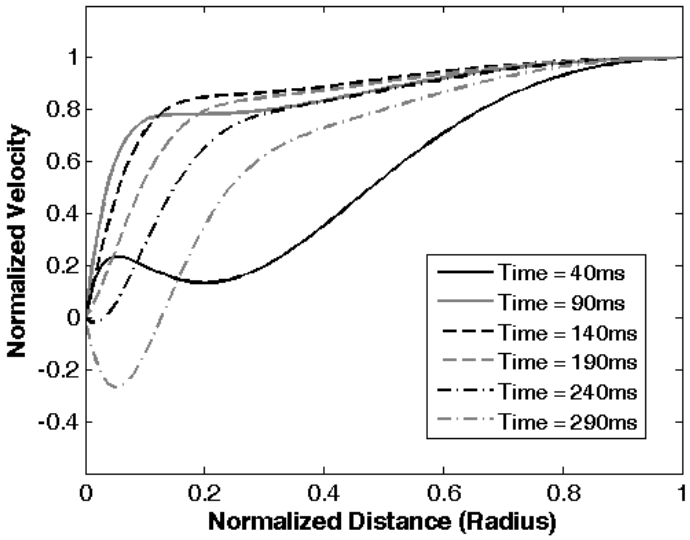

Figure 6-22c. *Flow profiles near the ventricular surface of the aortic valve for in vivo flow curves from Powell et al.[112], normalized by centerline velocities.*

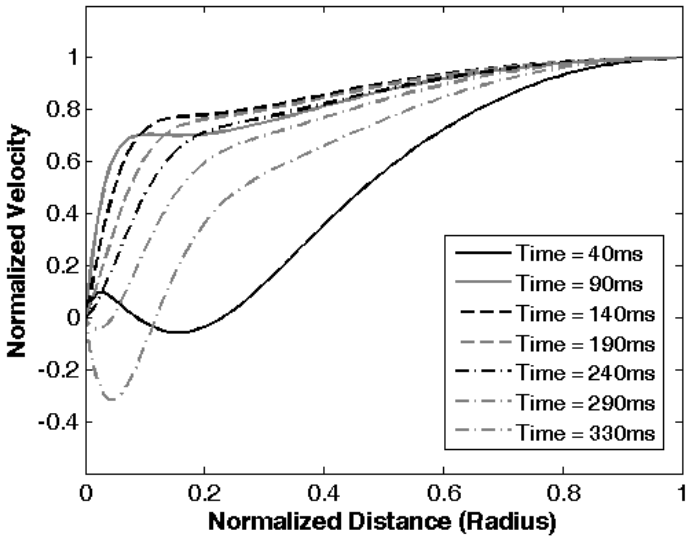

Figure 6-22d. *Flow profiles near the ventricular surface of the aortic valve for in vivo flow curves from Langerak et al. [113], normalized by centerline velocities.*

Compared to *in vivo* flow curves, flow curves obtained from the *in vitro* LDV work had similar accelerating phase. However, the *in vitro* flow curve peaks later than the

in vivo flow curve, and had a steeper deceleration phase than the *in vivo* flow curve. As opposed to the *in vitro* shear stress results, *in vivo* data showed only one single shear stress peak, which occurred during an earlier time point in systole. Further, *in vivo* data showed longer duration but smaller magnitudes of negative shear stresses. Differences in shear stress between the *in vitro* and *in vivo* cases could be explained by differences in the flow waveforms: the some theoretical modeling algorithm yielded slightly different shear stress waveforms for these two cases, when the only difference in the input was the volumetric flow waveform.

6.2.2 Quantification of Aortic Surface Shear Stresses

Shear stresses measured with the *in vitro* native tri-leaflet aortic valve model are presented here. Two dimensional shear stresses over the entire cardiac cycle are presented and preliminaries associated with it are presented. In the next subsection, section 6.2.3, the variation of systolic streamwise shear stresses with stroke volume and heart rate are presented.

6.2.2.1 Flow Loop Hemodynamics

The imposed flow and pressure waveforms are presented in figure 6-23. Aortic pressure was carefully controlled to be between 80 mmHg and 120 mmHg, and the cardiac output was 4.0 L/min. Ventricular pressure was 127 mmHg at its maximum. The maximum systolic transvalvular pressure gradient was 20 mmHg, while the mean was 12 mmHg. The peak flow rate was 20 L/min, and the valve had an effective orifice area of

1.42 cm2. These moderate values were associated with the small size of the valve (21mm).

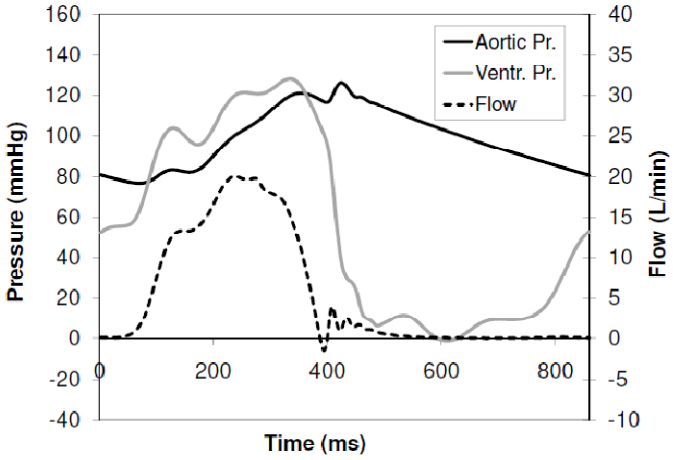

Figure 6-23. *Hemodynamics of the in vitro normal aortic valve model simulated at normal adult resting condition.*

6.2.2.2 Leaflet Dynamics

The back-scattered light intensity technique provided a description of the location of the valve leaflet along the scan line over the entire cardiac cycle. The back-scattered light intensity map is shown in figure 6-24, from which the segmented leaflet location was obtained, as show in figure 6-24b. The position axis for these plots was set to be 0 mm at the average diastolic leaflet position. The results showed that significant valve leaflet opening and closing motion were observed during the 56 – 94 ms time points and the 356 – 370 ms durations, corresponding to early systole and late systole. Maximum velocity of the valve leaflet was approximately 2.1 m/s during the opening phase (at the 74 ms time point) and 2.6 m/s during the closing phase (at the 368 ms time point), as resolved by the current data acquisition temporal resolution of 500 Hz. Before and after the peak velocity, the leaflet accelerated and decelerated, driven by the pressure gradient across it as well as leaflet membrane tension. During the closing motion, the deceleration

of the valve leaflet after closure was too rapid to be captured by the measurements. However, the leaflets appeared to be well damped against oscillations after closure, exhibiting no oscillations in this position.

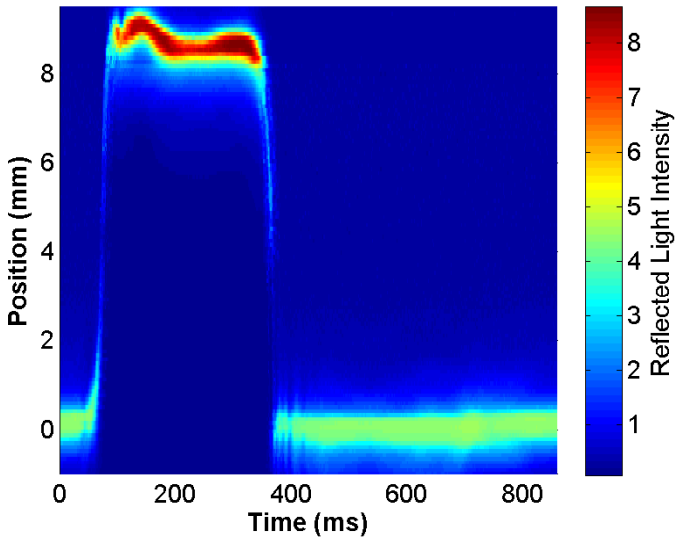

Figure 6-24a. *Backscattered light intensity map: intensity of the reflected light at various velocity-measurement locations (vertical axis) and at various time points in the cardiac cycle (horizontal axis).*

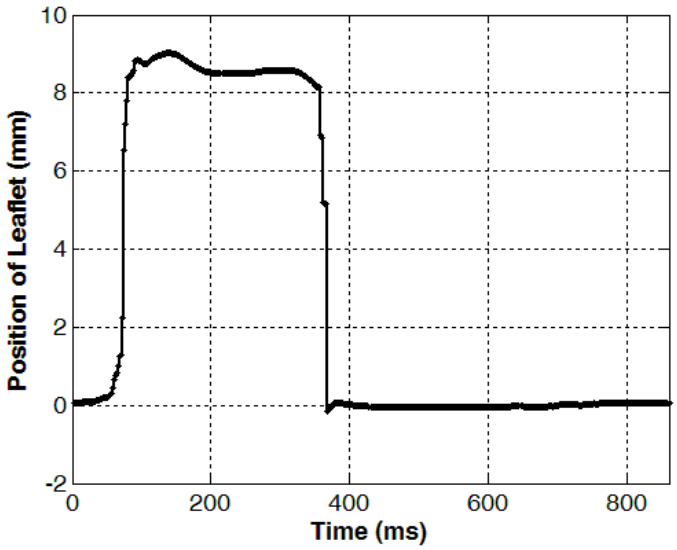

Figure 6-24b. *Position of the valve leaflet over the cardiac cycle, segmented from the backscattered light intensity (figure 6-24a).*

During systole, not considering the moments when the leaflet was rapidly opening and closing, the leaflet was stable and stayed within 0.44 mm of the average systolic position. The out-of-plane velocities, which were calculated from the leaflet position data, were between -0.026 m/s and 0.020 m/s, and the average of the absolute value of these velocities was 0.006 m/s. The out-of-plane accelerations were between -1.8 m/s^2 and 3.3 m/s^2, with a mean magnitude of 0.45 m/s^2. These values were small in magnitude, further demonstrating the stability of the leaflet. Since the aortic valve leaflet acted similarly to a lever hinged to the annulus, radial motion of the leaflet (i.e. rotation about the hinge) would have associated stream-wise or axial displacement perpendicular to the LDV line of measurement. This axial velocity of the leaflet were quantified and accounted for during shear stress computations: the frame of reference were set to follow the valve leaflet, and fluid velocities were quantified as quantities relative to the velocity of the valve leaflet (through simple arithmetic). In order to quantify the leaflet axial velocity, it was assumed that the no-slip flow boundary condition applied at the leaflet surface. The velocity of the leaflet in the in-plane directions were then estimated by using LDV measurement of velocities close to the leaflet surface. Within the same time window, leaflet velocity in the stream-wise direction was between -0.034 m/s and 0.016 m/s with an average of absolute value of 0.008 m/s, and leaflet velocity in the non-stream-wise direction was between -0.032 m/s and 0.002 m/s, with an average absolute value of 0.009 m/s. In the streamwise directions, leaflet surface acceleration was between than -1.1 m/s^2 and 1.2 m/s^2 at all times when shear stress was measured, with an average absolute value of 0.4m/s^2. In the non-streamwise direction, leaflet surface acceleration was between -0.9

m/s^2 to 1.0 m/s^2, with an mean absolute value of 0.2 m/s^2. These velocities were low, again indicating that the valve leaflet was relatively stationary.

For diastole, within the time window of shear stress quantification, out-of-plane leaflet velocity and acceleration were similarly small. Velocity was between -0.017 m/s and 0.020 m/s, with an average absolute value of 0.012 m/s. Acceleration was between 1.4 m/s^2 and -1.4 m/s^2, with an average absolute value of 0.3m/s^2. Leaflet stream-wise velocity was between -0.016 m/s and 0.002 m/s with an average absolute value of 0.002 m/s, while leaflet non-streamwise velocity was between -0.007 m/s and 0.000 m/s with an average absolute value of 0.002 m/s. In the streamwise directions, leaflet surface acceleration was between than -0.2 m/s^2 and 0.2 m/s^2 at all times when shear stress was measured, with an average absolute value of 0.05 m/s^2. In the non-streamwise direction, leaflet surface acceleration was between -0.2 m/s^2 and 0.3 m/s^2, with a mean absolute value of 0.08 m/s^2. The leaflet motion was shown to be stable for LDV measurements near it.

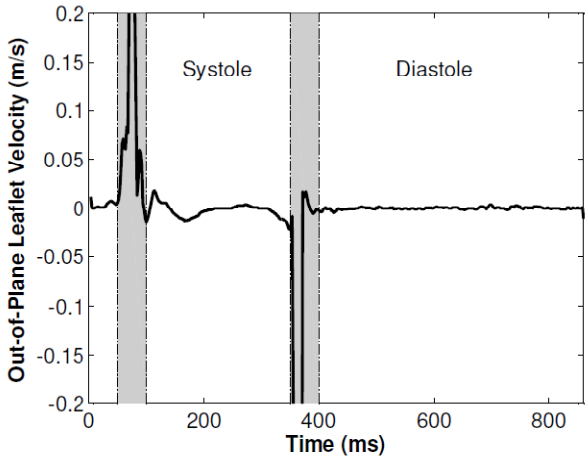

Figure 6-25. *The out-of-plane velocity of the valve leaflet, calculated from the leaflet position data (figure 6.24b). The valve leaflet had low out-of-plane velocities except during the opening and closing phases (shaded regions).*

6.2.2.3 Leaflet Orientation

From the measurements of leaflet position at adjacent points on the leaflet, the orientation of the leaflet over time with respect to the LDV probe was determined. Within the time window of LDV measurements over the entire cardiac cycle, the orientation of the leaflet in the stream-wise direction was between -0.15 and 0.04 radians, while in the non-stream-wise direction, the orientation was between -0.008 and 0.12 radians. The squared cosine corrections were small in value, ranging from 0.2% to 3%. Since orientation was not greater than 0.15 radians, errors in shear stress magnitude due to out-of-plane flow could be expected to be less than 3% of relevant shear stress magnitudes, as discussed in section 6.1.6.

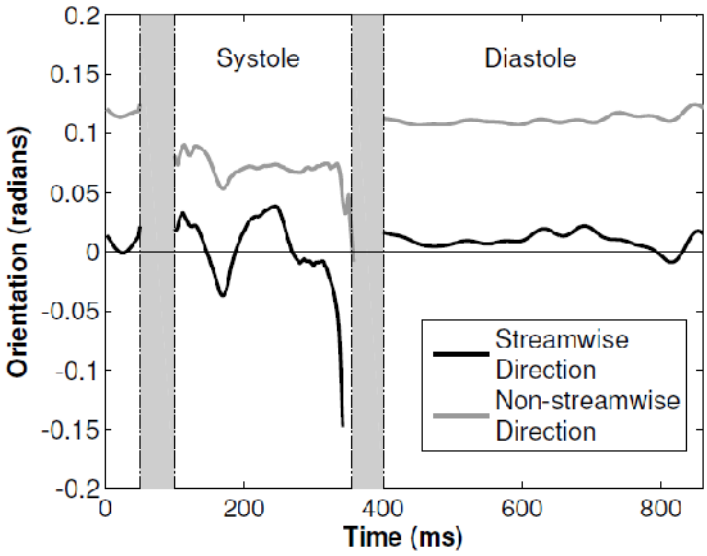

Figure 6-26. *The orientation of the leaflet with regards to the LDV probe alignment. The LDV probe was positioned such that this orientation difference between the leaflet surface and the LDV probe is limited to less than 0.15 radians.*

6.2.2.4 Flow Fields

Figure 6-27 shows the ensemble averaged velocity measurement at various positions along the interrogation line (vertical axis) over the cardiac cycle (time is the horizontal axis). Measurements showed that the valve opening phase was associated with high stream-wise velocity towards the aorta, but low velocities in the non-stream-wise direction, as was expected due to the reduction of the volume of fluid in the sinus space due to the valve leaflet moving in, causing flow fields to be dominated by fluid leaving the sinus towards the aorta. Immediately after opening, fluid velocities near the valve were low. At about 90 ms after the rapid leaflet opening phase, higher velocities developed near the leaflet in the stream-wise direction. At about 200 ms, a vortex formed in the sinus, as could be observed by adjacent columns of fluid with stream-wise velocities of opposite direction. In the non-stream-wise direction, higher velocities developed about 140 ms after the rapid leaflet opening phase. Vortex formation was also observed from the non-stream-wise velocity measurements: flow closer to the leaflet moved in the negative direction, but beyond about 11mm from closed leaflet position, fluid moved in the positive direction.

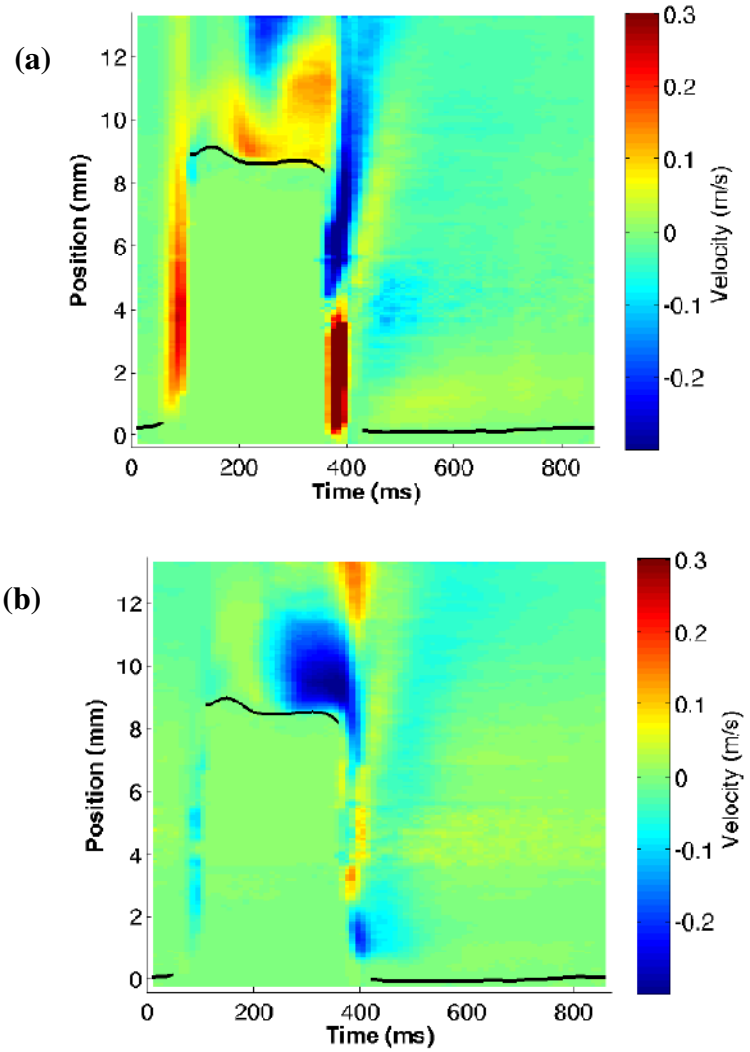

Figure 6-27. *Ensemble average velocity at various measurement locations (vertical axis) at various times over the cardiac cycle (horizontal axis) in the (a) streamwise and (b) non-streamwise direction. The black line indicates the valve leaflet aortic surface location.*

Within the time window of LDV measurements, the standard deviation of the ensemble averaged velocities at measurement locations used for shear stress computations varied from 0.01 m/s to 0.13 m/s, with a mean of 0.04 m/s, which was of the same order of magnitude as those in the steady flow loops, demonstrating the same quality of data acquisition. The standard deviation of velocity measurements could also

serve as indicators of instability or variability in flow. Figure 6-28a shows the standard deviation of measured velocity over time at a measurement location approximately 0.9 mm away from the average leaflet systolic location, while figure 6-28b shows the measured velocity at the same location over time. At this location, variability of velocities in the two directions followed the same trends despite having different velocity magnitudes. Velocity variability was low during early systole, but was elevated during mid-to-late systole. Immediately after valve closure, velocity variability increased even more and peaked, before coming down, quickly at first, and then gradually over the remaining duration of diastole. High variability in flow was not necessarily associated with high ensemble-averaged velocity. For example, stream-wise velocity was high at the 200 ms time point, but the standard deviation was low, and the converse is true at the 300 ms time point.

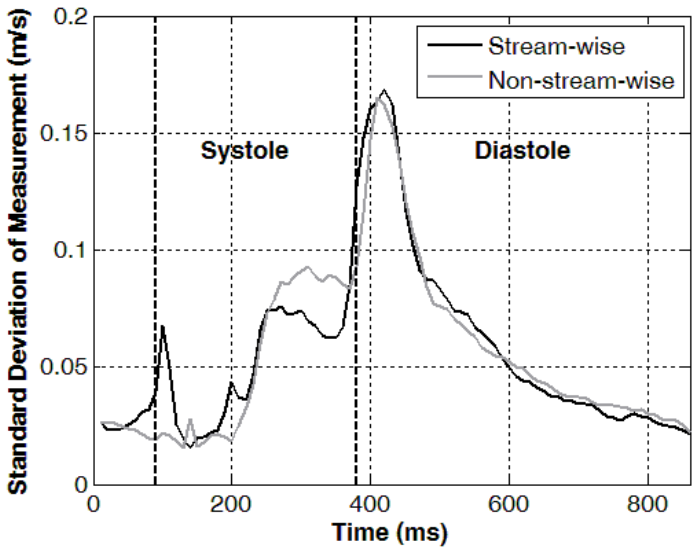

Figure 6-28a. *Ensemble standard deviation of velocities measured at a location 0.9mm away from the systolic valve leaflet location.*

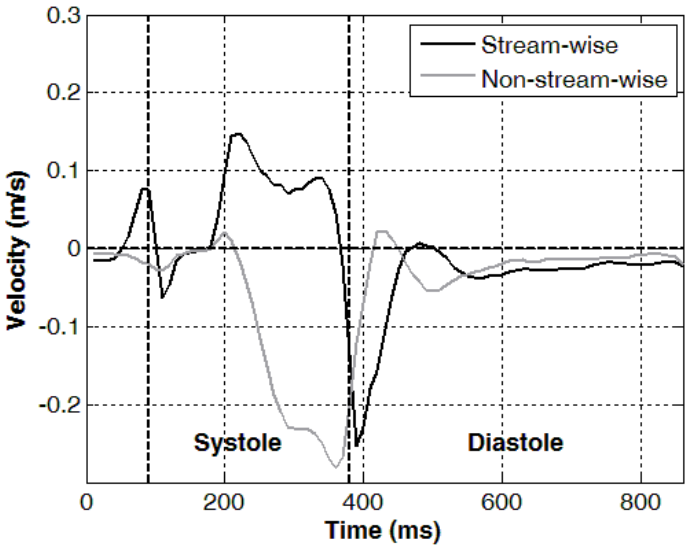

Figure 6-28b. *Velocities measured at a location 0.9mm away from the systolic valve leaflet location.*

6.2.2.5 Shear stress Computation

The same shear stress terminology convention as adopted in section 6.2.1.1.5 will be used here.

The computation of shear stress required the determination of the two terms in equation 5-3. An order of magnitude analysis showed that the first term in equation 5-3 (the radial gradient of stream-wise or non-stream-wise velocities) was two orders of magnitude higher than the second term (the stream-wise or non-stream-wise gradient of radial velocities). In the stream-wise direction, the average magnitude of the first term was 8.45 dyn/cm^2 during systole and 1.38 dyn/cm^2 during diastole, while that of the second term was 0.11 dyn/cm^2 during systole and 0.01 dyn/cm^2 during diastole (Radial velocities or out-of-plane velocities were calculated as the rate of change of the leaflet radial position, which was measured with the back-scattered intensity method). The

relative magnitude of the two terms over the cardiac cycle is shown in figure 6-29. The second term was thus neglected in subsequent calculations.

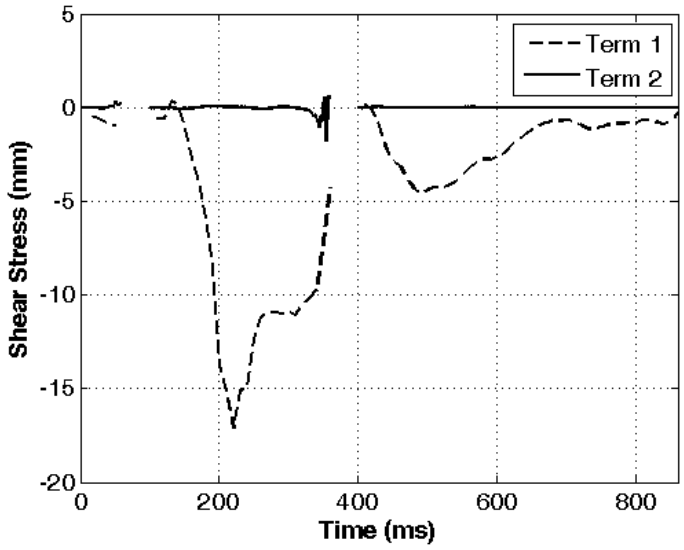

Figure 6-29. *Comparison of the magnitudes of shear stresses due to the two terms in shear rate (shear stress due to term 1 =* $\mu \frac{\delta u_i}{\delta x_j}$*; shear stress due to term 2 =* $\mu \frac{\delta u_j}{\delta x_i}$ *)*

Shear stress results are shown in figure 6-30. The measured shear stress results showed that shear stress had greater variations and had higher magnitudes during systole than diastole. Systolic shear stress, however, did not elevate until mid systole; it was low during early systole, being lower than 5 dyn/cm^2 in both stream-wise and non-stream-wise directions. These low early systolic shear stresses coincided with the time period of quiescent flow in the sinus. Thereafter, shear stresses decreased slightly in magnitude and then elevated to its peak value, which was during mid- to end-systole. This large elevation of shear stress magnitude coincided with the formation of the vortical flow in the sinus in the respective plane of measurements. During early diastole, remnant sinus flow after valve closure increased shear stresses to 3.3 dyn/cm^2 and 2 dyn/cm^2. Subsequently, shear stresses dissipated as flow in the sinus dissipated over the remaining

duration of diastole. The data further revealed that significant shear stress levels in the non-stream-wise direction existed, with non-streamwise peak shear stress (15.3 dyn/cm^2) similar to the order of magnitude of the peak shear stress in the stream-wise direction (18.6 dyn/cm^2). Streamwise shear stress elevated and peaked earlier than non-streamwise shear stress, but had substantial magnitude when the non-stream-wise shear stress peaked.

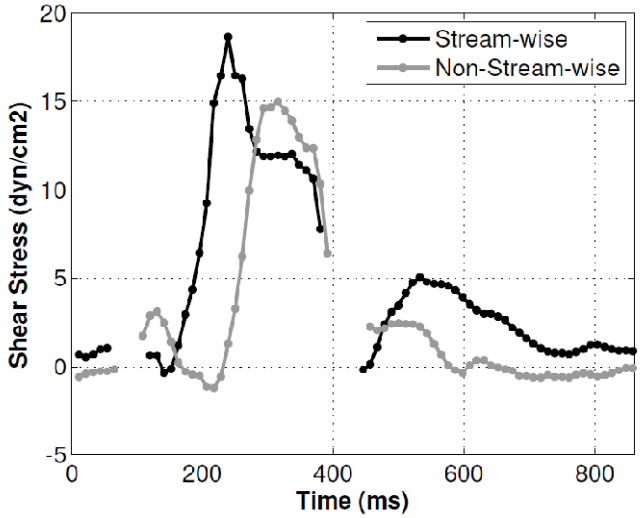

Figure 6-30. *Shear stress on the aortic surface of the valve leaflet over the cardiac cycle.*

6.2.3 Effects of Stroke Volume and Heart Rate on Streamwise Shear Stresses on the Aortic Surface of the Aortic Valve

In this subsection, the effects of heart rate and stroke volume on systolic streamwise shear stress are illustrated.

6.2.3.1 Flow Loop Hemodynamics

The trileaflet native valve model was exposed to various hemodynamic conditions with a range of heart rates (50, 70, 90 beats/min) and stroke volumes (27, 43, 62, 68 ml).

Pressures, however, were fixed at 80/120 mmHg. The representative pressure waveforms over the cardiac cycle are shown in figure 6-31a, taken from the 70 beats/min heart rate and 62 ml stroke volume case. The shapes of the pressure curves were similar for the other conditions. Due to its small size (21mm), the valve was observed to have a maximum systolic pressure gradient of 16.3 mmHg, average systolic gradient of 10.1 mmHg, and an EOA of approximately 1.22 cm^2 at this hemodynamic condition. The systolic flow waveforms for different stroke volumes at 70 beats/min are shown in figure 6-31b, and for different heart rates at 55 ml stroke volume are shown in figure 6-20c. As expected, the volumetric flow rate increased with increasing stroke volume, and systolic duration decreased with increasing heart rate.

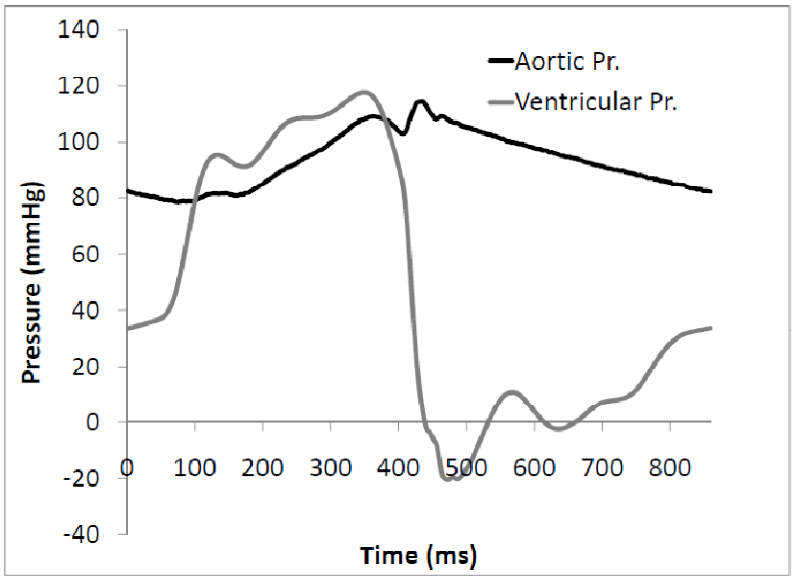

Figure 6-31a. *Typical pressure waveform simulated for the valve model. Aortic pressure is controlled to be between 80 mmHg and 120 mmHg.*

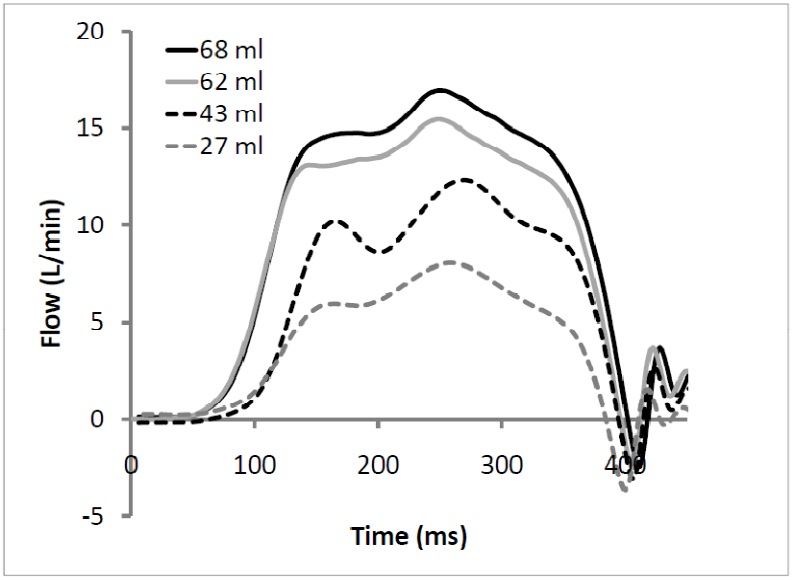

Figure 6-31b. *Systolic bulk flow waveform through the valve model for the various stroke volume conditions investigated at the same heart rate of 70 beats/min.*

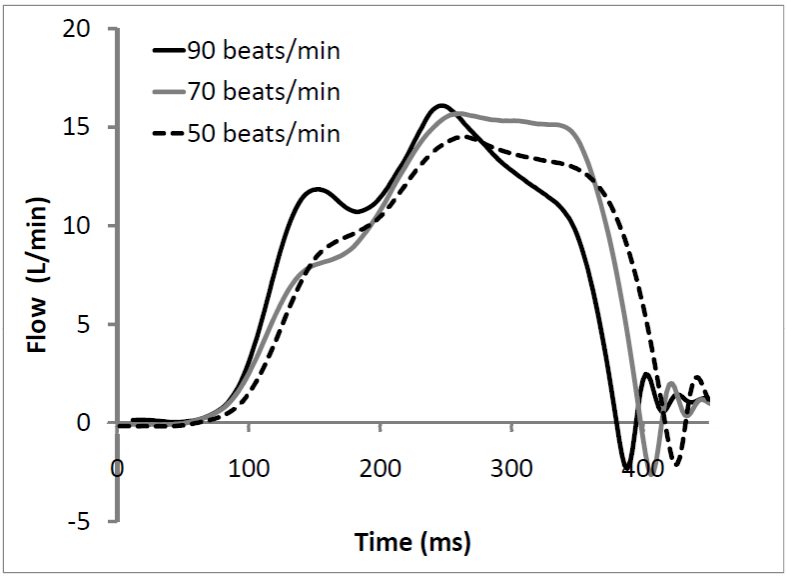

Figure 6-31c. *Systolic bulk flow rate waveform for the various heart rate conditions at the same stroke volume of 55 ml.*

6.2.3.2 Leaflet Dynamics

The reflected light intensity technique provided a description of the valve leaflet location along the scan line. Figure 6-32a shows the raw back-scattered light intensity

map, demonstrating that the signals had little noise. Systolic positions of the leaflets are shown in figure 6-32b for the various stroke volume cases, and figure 6-32c for the various heart rate cases. The systolic position of the valve leaflet was similar across all the conditions, where the leaflet was opened further during early systole than late systole. Across different stroke volumes, systolic leaflet positions were less than 1mm different from each other, and no obvious trend of dependency of leaflet position on stroke volume was observed. At the lower stroke volumes, however, valve leaflets tended to close earlier due to slightly shorter systolic durations. At the higher heart rates, the valve leaflets started to move towards closure earlier, due to a decrease in systolic duration at higher heart rates. Systolic positions of the valve leaflet were very similar for the 50 beats/min and the 70 beats/min cases, and were less than 0.1 mm apart. For the 90 beats/min case, the valve leaflet was slightly further away from the sinus than the other two heart rate cases.

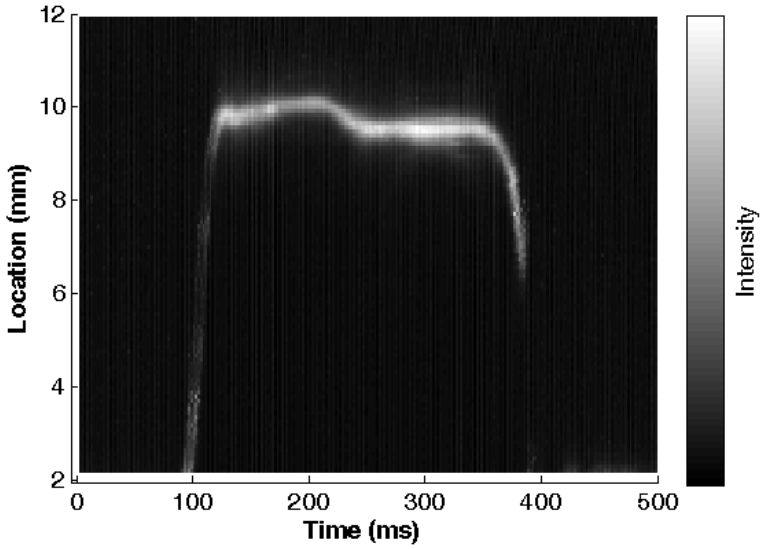

Figure 6-32a. *Sample back-scattered light intensity map, demonstrating that little noise were recorded, and the ensemble averaged location of the valve leaflet could be clearly traced.*

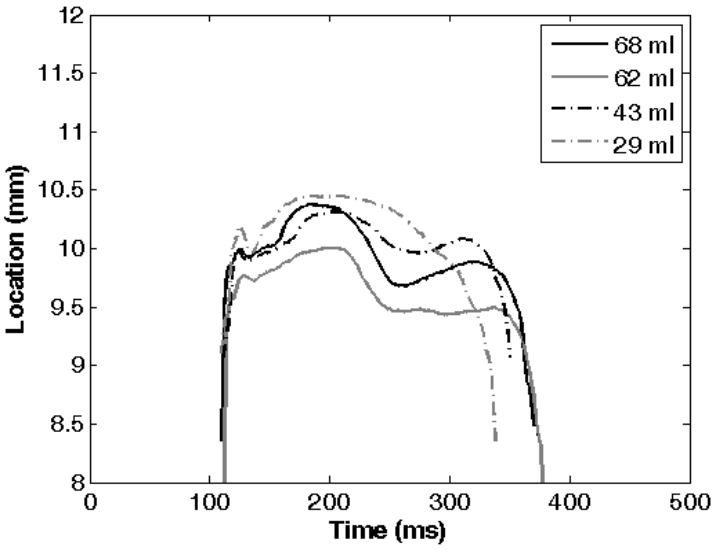

Figure 6-32b. *Leaflet positions over systole for the various stroke volume conditions at the same heart rate of 70 beats/min.*

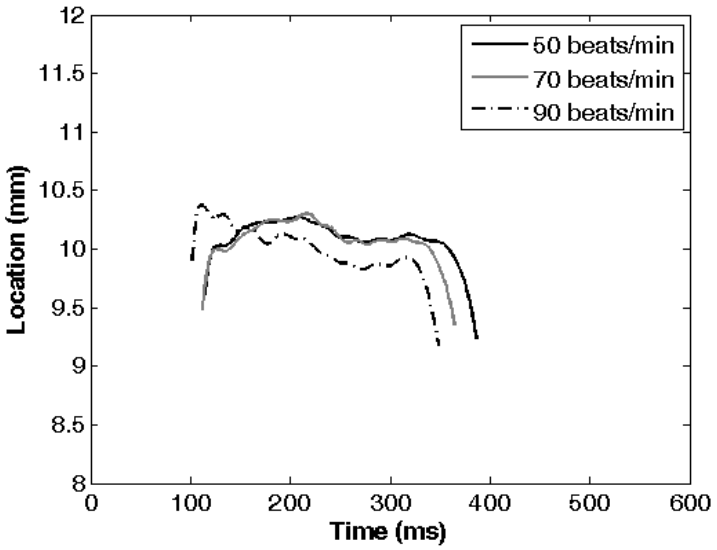

Figure 6-32c. *Leaflet positions over systole for the various heart rate conditions at the same stroke volume of 55 ml.*

6.2.3.3 Shear Stress across Different Stroke Volume Conditions

Viscous shear stress measurements are shown in figure 6-33a. The initial measurements indicated that the significant viscous shear stress was observed only during

systole, and diastolic viscous shear stress was small, and took the predictable shape of a monotonic decrease to zero. Thus, subsequent measurements where stroke volume and heart hate were varied focused on systolic shear stresses only. Figure 6-33 shows the fluid shear stress waveforms experienced during systole at the same point on the valve leaflet under different stroke volume conditions. The general characteristics of systolic shear stresses were preserved across different stroke volume conditions. Shear stresses were low during early systole and elevated during later parts of systole. During early systole, immediately after valve opening, a low negative peak was observed in all the conditions. Thereafter, shear stresses were close to zero for the higher stroke volume cases and were slightly negative in the lower stroke volume cases. Shear stresses increased rapidly to a peak value at approximately the 275 ms time point, and declined rapidly after that, getting close to zero at approximately the 350 ms time point. The measurements revealed that peak shear stress magnitude increased with increasing stroke volume. Late systolic peak shear stresses ranged from 1.1 dyn/cm^2 at 29 ml stroke volume to 15.0 dyn/cm^2 at 68 ml stroke volume, as displayed in table 6-3.

Table 6-3. *Peak viscous shear stresses measured in the different stroke volume cases at the same heart rate.*

Heart Rate	Stroke Volume	Peak Shear Stress
70 beats/min	68 ml	15.0 dyn/cm^2
70 beats/min	62 ml	13.4 dyn/cm^2
70 beats/min	43 ml	6.4 dyn/cm^2
70 beats/min	29 ml	1.1 dyn/cm^2

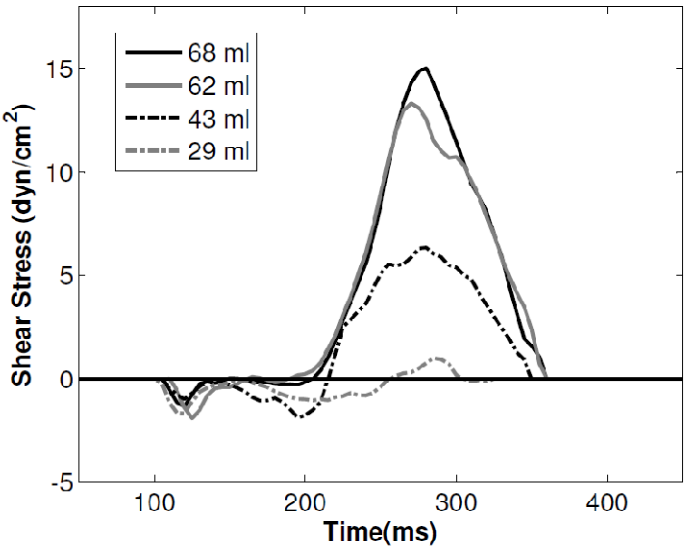

Figure 6-33a. *Streamwise direction shear stress waveforms over systole for the various stroke volume cases at the same heart rate of 70 beats/min.*

The Reynolds shear stresses were estimated and are shown in figure 6-33b. Unsteadiness of flow was only observed during late systole, early diastole period at around the 400 ms time point, most likely due to adverse pressure gradient and flow reversal and mixing. This unsteadiness resulted in excessive Reynolds shear stress during this period of time. During the majority of systole, however, Reynolds shear stress was less than 10 dyn/cm^2.

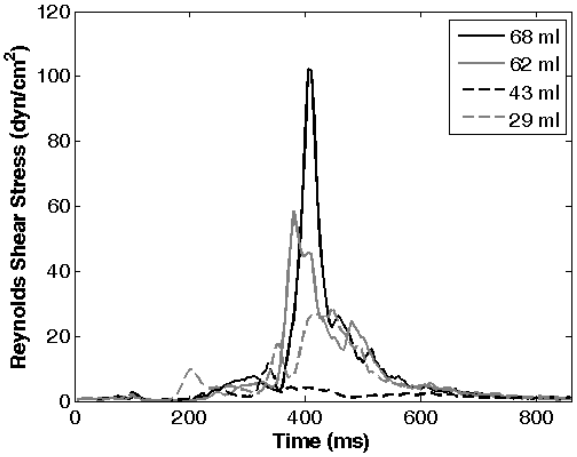

Figure 6-33b. *Reynolds shear stress estimation for the various stroke volume cases at the same heart rate of 70 beats/min.*

6.2.3.4 Shear Stress across Different Heart Rate Conditions

Figure 6-34a shows the viscous fluid shear stresses at the same point on the valve leaflet at different heart rates. At all heart rates, shear stresses were negative at early systole. Subsequently, the lower heart rates cases demonstrated the general characteristics such as low shear during early systole and the half sinusoid shear stress peak during late systole. At 90 beats/min however, the initial low shear stress characteristic was not observed, but was replaced by a rapid increase in shear stresses to the early systolic peak of approximately 5 dyn/cm^2. This was possibly due to the difference in valve leaflet dynamics at 90 beats/min compared to the other two heart rates. Thereafter, shear stress decreased slightly before growing to the late systolic peak of approximately 7.8 dyn/cm^2. Between 50 beats/min and 70 beats/min cases, slight differences were observed: the 70 beats/min case had a lower late systolic peak shear stress of 10.2 dyn/cm^2 while the 50 beats/min case had 11.4 dyn/cm^2. In the 50 beats/min case, late systolic shear stress

decline occurred later than in the 70 beats/min case. As tabulated in table 6-4, the results showed that increased heart rate led to a reduction in the late systolic peak shear stress.

Table 6-4. *Peak shear stresses measured in the different heart rate cases at the same heart rate.*

Heart Rate	Stroke Volume	Peak Shear Stress
50 beats/min	55 ml	11.4 dyn/cm^2
70 beats/min	55 ml	10.2 dyn/cm^2
90 beats/min	55 ml	7.8 dyn/cm^2

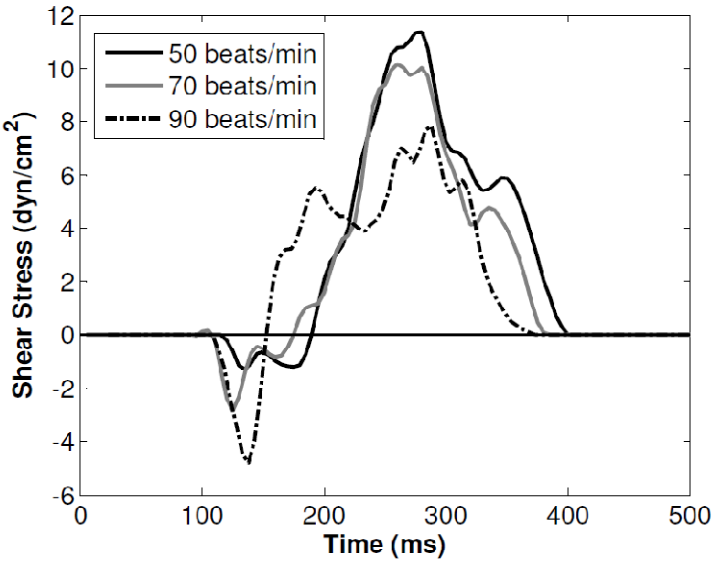

Figure 6-34a. *Streamwise direction shear stress waveforms over systole for the various heart rate cases at the same stroke volume of 55 beats/min.*

Reynolds normal stresses were estimated in figure 6-34b. Reynolds stress peaks at between 76 dyn/cm^2 and 101 dyn/cm^2 during late systole. There was no specific trend of differences between the various heart rate cases, but stresses were generally higher during late systole period for all these cases.

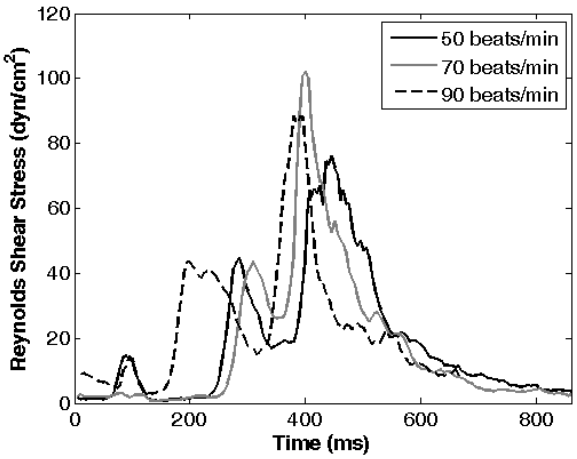

Figure 6-34a. *Reynolds shear stress estimation for the various heart rate cases at the same stroke volume of 55 beats/min.*

6.2.3.5 One-Standard Deviation Range of Measured Shear Stresses

Using methods described in section 5.2.5.2, the one standard deviation bound for the shear stresses measured under different stroke volumes and heart rates were calculated. The results are shown in Figure 6-35a-f. Shear stresses appear to be more variable during mid- to late-systole. At the higher stroke volume and lower heart rate cases, shear stresses were more variable during the decreasing arm, or the deceleration phase. For the lower stroke volume and the highest heart rate cases, shear stresses were more variable during mid-systole than end-systole. With increasing stroke volume and heart rate, shear stress variability appears to increase.

(a)

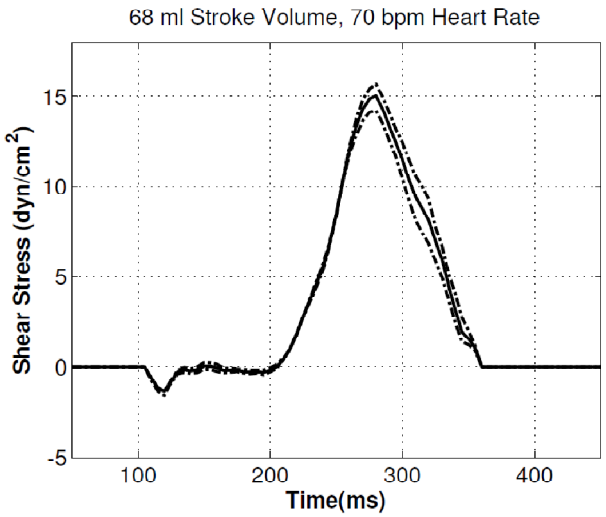

(b)

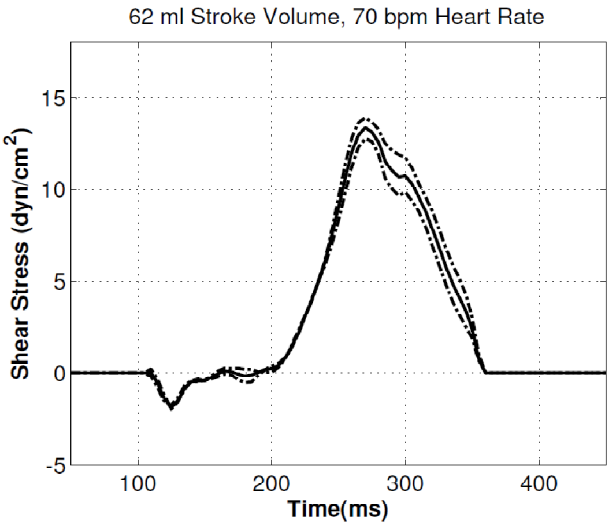

c)

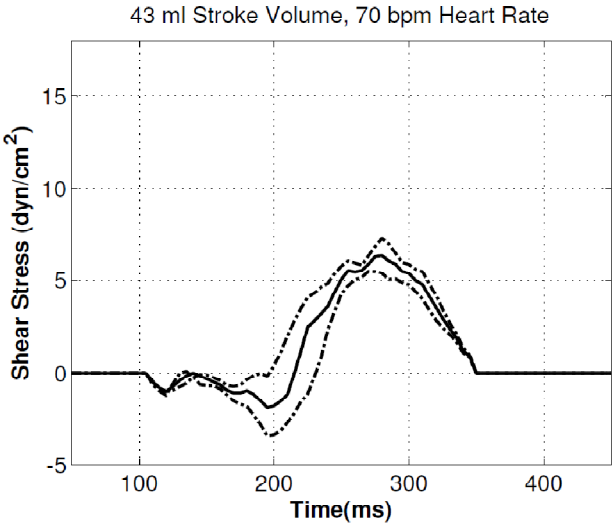

(d)

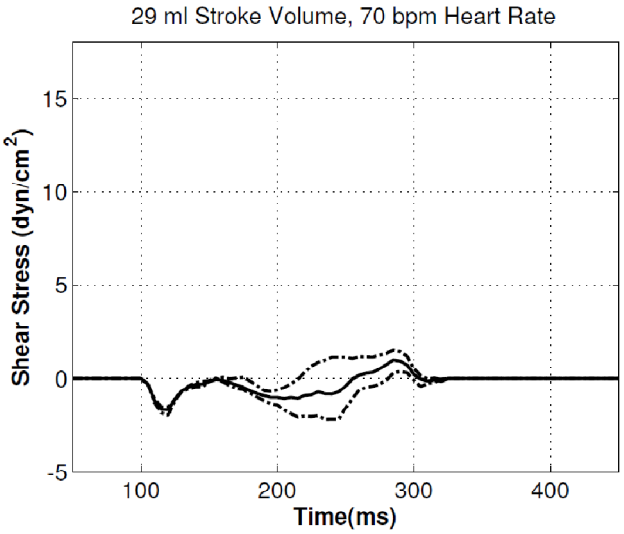

(e)

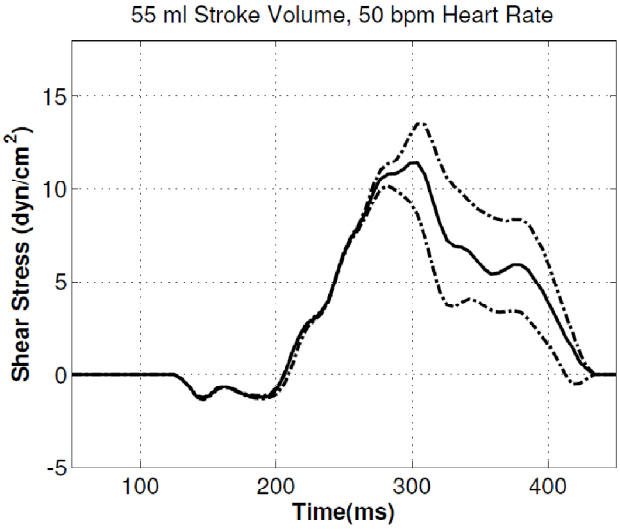

(f)

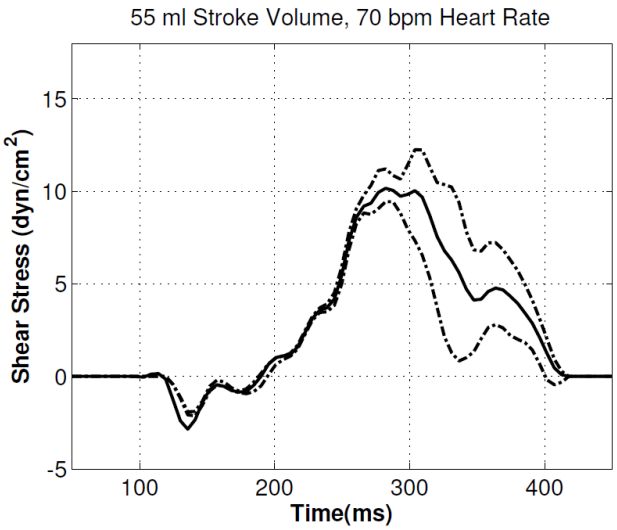

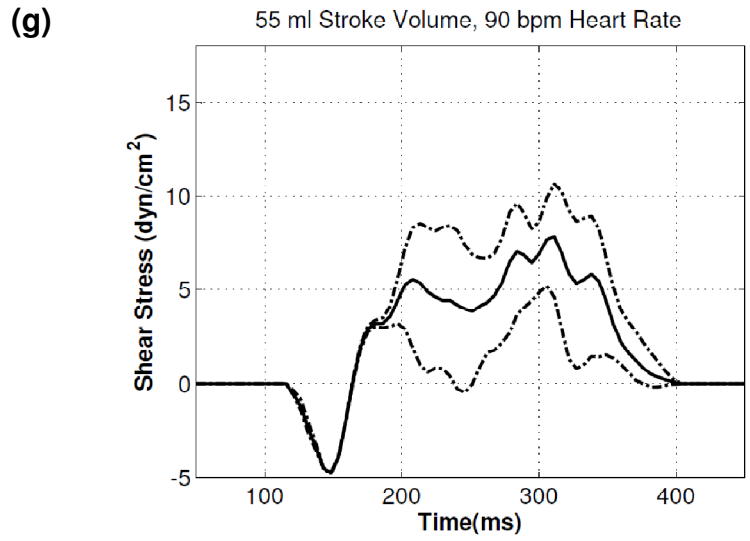

Figure 6-35. *Shear stress waveforms over systole and the standard deviation of shear stresses for (a-d) different stroke volume conditions at the same heart rate of 70 beats/min; and (e-g) different heart rate conditions at the same stroke volume of 55 ml.*

6.2.4 Error Associated with LDV Shear Stress Measurement Technique

The results presented in this thesis are composed of shear stress calculations based on the ensemble mean velocity profiles, measured from LDV. During the acquisition of data, however, it was noted that there was a significant spread of velocity values at various time points and spatial points. With the current data, it was uncertain whether the ensemble average velocity profile reflected the instantaneous velocity profile, or whether there was a stochastic relationship between the two. The interpretation shear stress results in the current thesis must be approached with some caution. This uncertainty is consequent to the choice of using LDV as the measurement technique for calculating shear stress due to lack of a better method. LDV, being a point-by-point measurement technique, could not provide instantaneous velocity profile gradients or instantaneous leaflet locations, and any interpretation of shear stresses must be performed using the

ensemble average and standard deviation of velocities and leaflet locations. This section presents analysis of the errors with the variability of velocity and leaflet location measurements, based on methods described in 5.2.5. It should be noted that the variability of velocity and leaflet locations could reflect physical phenomenon actually occurring in the in vitro heart valves models, due to cycle-to-cycle variations in flow in the experimental loop and cycle-to-cycle variations in the valve leaflet dynamics. There could also be similar natural variations in native heart valves. Future work is needed to devise more advanced methods to study this variability and its effect on shear stress.

6.2.4.1 Estimating Error in Shear Stress from Maximum and Minimum Bounds of Velocity and Leaflet Location

Using the maximum and minimum bounds of leaflet locations and the closest velocity data point, the maximum and minimum bounds of shear stresses were estimated for the various valve leaflet cases investigated: aortic surface shear stress measured in the native tissue trileaflet valve under 70 beats/min and 68 ml stroke volume, ventricular surface shear stress measured in the polymeric valve, and aortic shear stress measured on both leaflets of the bicuspid aortic valve. The results are presented in figure 6-36. Velocity measurements are shown in blue dots, the leaflet locations shown as the horizontal error bar to delineate the maximum and minimum locations, while the pink dotted lines indicate the flow profiles calculated for assessment of shear stress uncertainty. Four velocity profiles were obtained for each case: (1) max velocity and min distance from leaflet; (2) max velocity and max distance from leaflet; (3) min velocity and min distance from leaflet; (4) min velocity and max distance from leaflet. The highest and lowest shear

stress obtained from these 4 velocity profiles were documented in the table next to the figure 6-36. This investigation was performed for 4 time points spread out over systole.

In general, wide variations of shear stresses were observed, which could sometimes range from positive to negative directions. This analysis presents the worst case scenario because, instantaneously, the maximum velocity might not match with the minimum leaflet location and vice versa. Nonetheless, it demonstrated the limitation of the LDV method as a shear stress measuring tool, given that the LDV could only perform point by point measurements, and could not measure both leaflet location and velocities at the same time, and there was no way to tell which velocity data point corresponded to which leaflet location measurement.

The high variability of shear stresses, however, could be a physical phenomenon: flow in the aortic valve sinus was indirectly induced, and could be physically displaying high variability. Further, the bicuspid valve showed more shear stress variability than the trileaflet valve, corroborating with the observation that the bicuspid valve had a smaller flow orifice and thus had a higher stenosis, which can lead to unsteady flow.

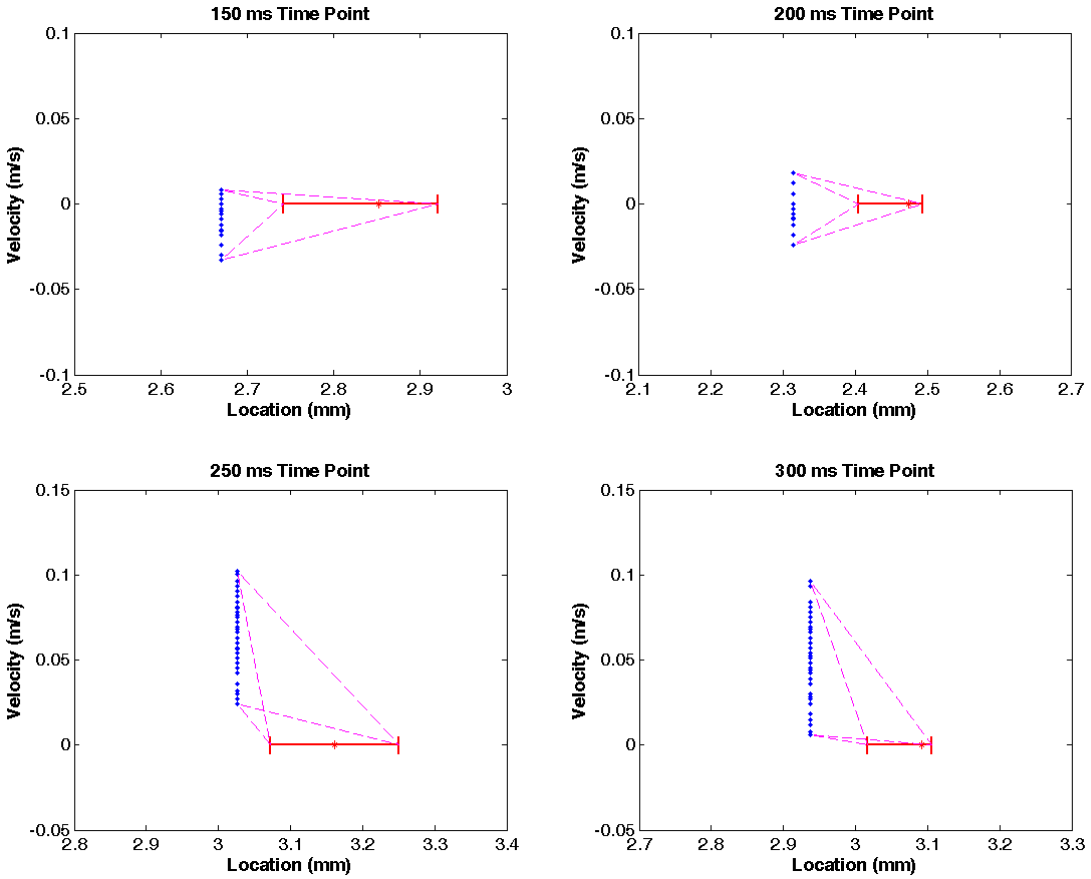

Time Point	150 ms	200 ms	250 ms	300 ms
Max. shear stress (dyn/cm^2)	4.23	7.56	84.35	45.87
Min. shear stress (dyn/cm^2)	-17.44	-10.08	4.08	1.35

Figure 6-36a. *Error analysis of shear stress computation for aortic surface shear stress on the trileaflet native tissue valve, taking into account the variability of the leaflet location and the velocity measured closest the leaflet location, and the tabulation of the maximum and minimum shear stress computed from this analysis. Blue: velocity measurements; red: leaflet location maximum and minimum bounds; pink: flow profiles considered when calculating shear stress maximum and minimum bounds*

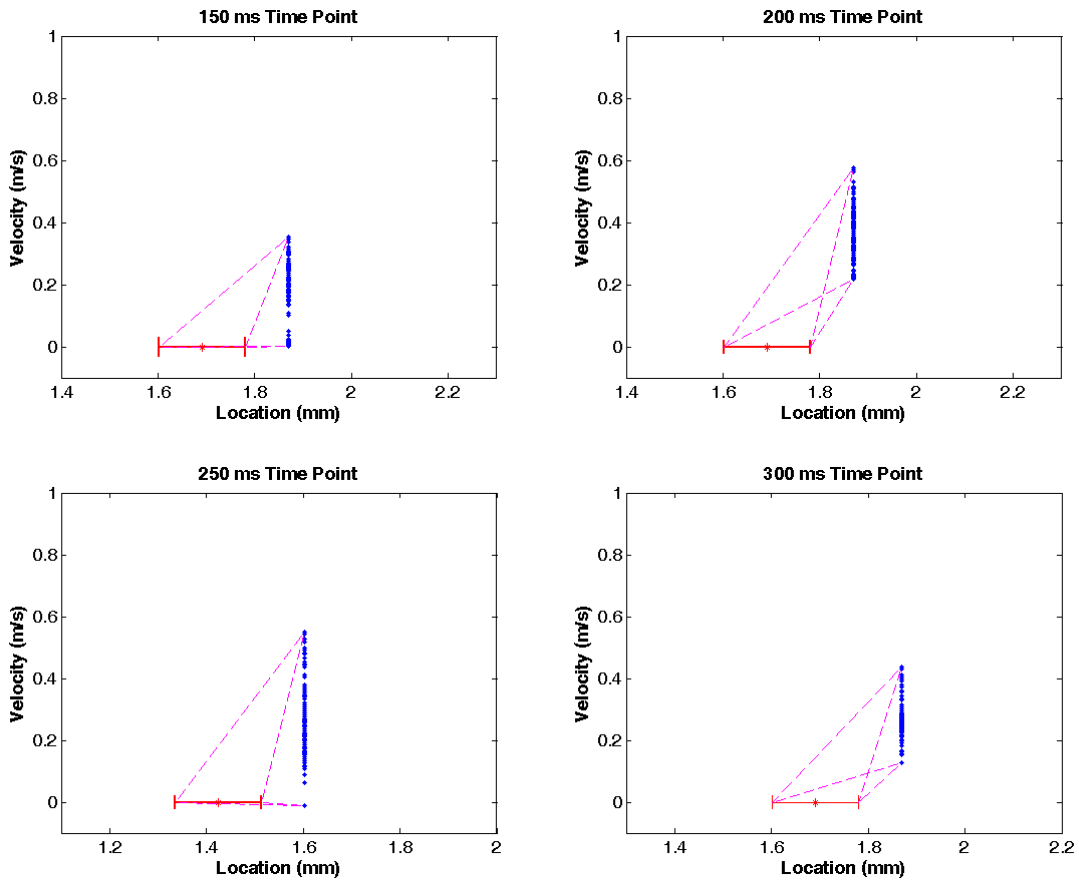

Time Point	150 ms	200 ms	250 ms	300 ms
Max. shear stress (dyn/cm^2)	150.41	246.12	235.18	185.96
Min. shear stress (dyn/cm^2)	0.46	39.99	-5.47	18.23

Figure 6-36b. *Error analysis of shear stress computation for ventricular surface shear stress on the polymeric valve, taking into account the variability of the leaflet location and the velocity measured closest the leaflet location, and the tabulation of the maximum and minimum shear stress computed from this analysis.Blue: velocity measurements; red: leaflet location maximum and minimum bounds; pink: flow profiles considered when calculating shear stress maximum and minimum bounds*

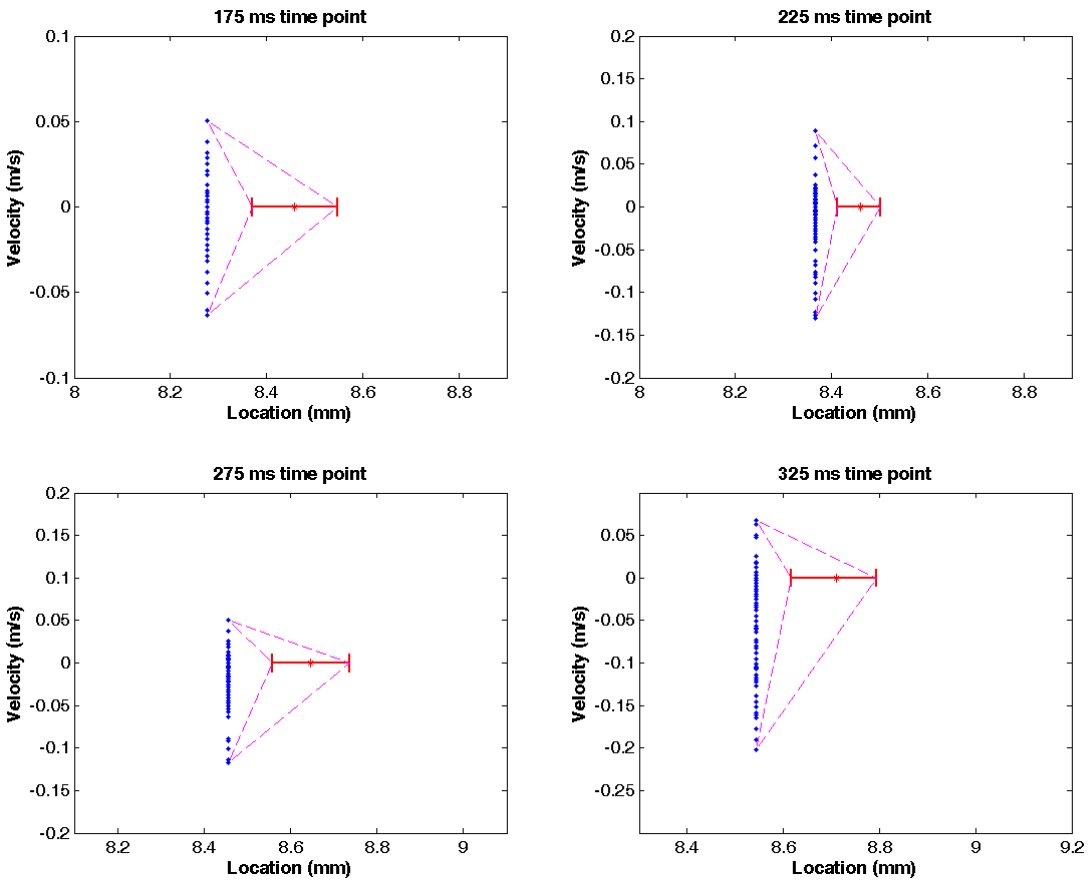

Time Point	175 ms	225 ms	275 ms	325 ms
Max. shear stress (dyn/cm^2)	20.72	71.13	42.74	35.87
Min. shear stress (dyn/cm^2)	-25.90	-104.16	-71.24	-107.62

Figure 6-36c.*Error analysis of shear stress computation for aortic surface shear stress on the bicuspid aortic valve fused leaflet, taking into account the variability of the leaflet location and the velocity measured closest the leaflet location, and the tabulation of the maximum and minimum shear stress computed from this analysis.Blue: velocity measurements; red: leaflet location maximum and minimum bounds; pink: flow profiles considered when calculating shear stress maximum and minimum bounds*

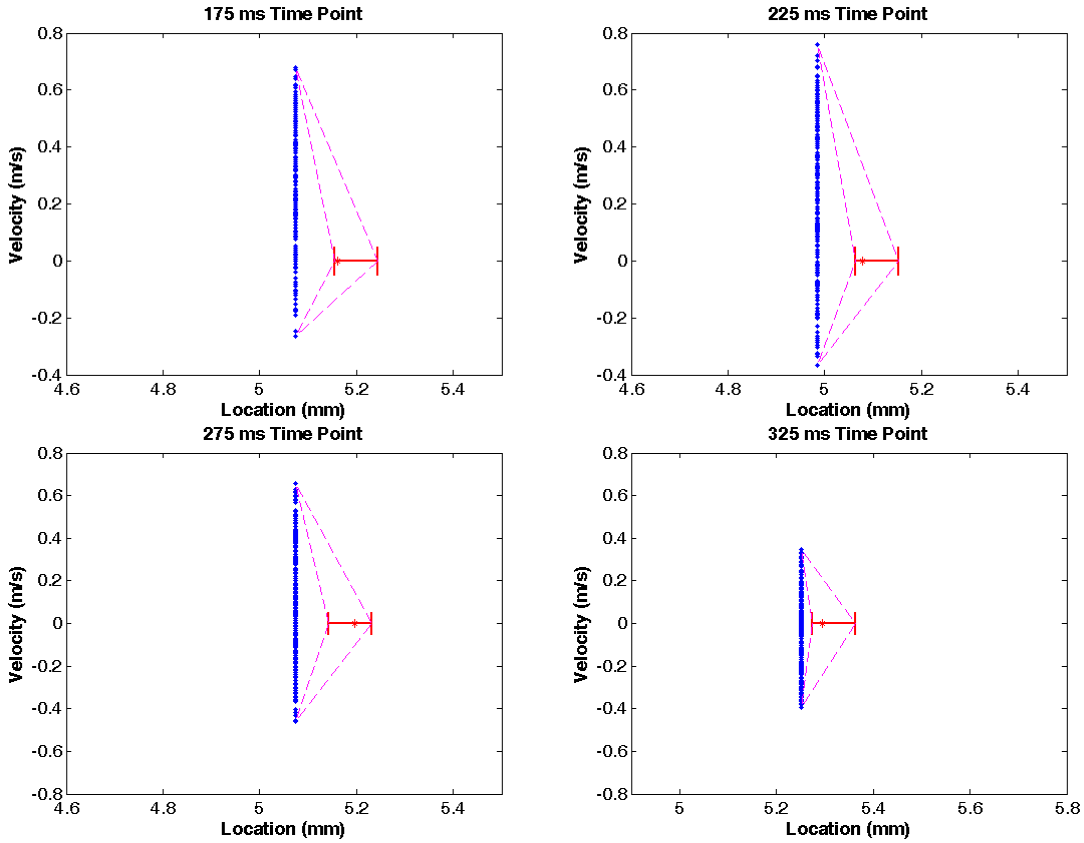

Time Point	175 ms	225 ms	275 ms	325 ms
Max. shear stress (dyn/cm^2)	316.58	363.97	365.54	574.21
Min. shear stress (dyn/cm^2)	-124.26	-175.92	-256.58	-658.50

Figure 6-36d. *Error analysis of shear stress computation for aortic surface shear stress on the bicuspid aortic valve non-fused leaflet, taking into account the variability of the leaflet location and the velocity measured closest the leaflet location, and the tabulation of the maximum and minimum shear stress computed from this analysis.Blue: velocity measurements; red: leaflet location maximum and minimum bounds; pink: flow profiles considered in calculating shear stress maximum and minimum bounds*

6.2.4.2 Displaying Variability of Measured Velocities and Leaflet Location as Indications of Errors in Shear Stress Measurement

To guide the reader, the variability of measured velocities before the calculation of ensemble average velocity profiles is documented. These raw velocity measurement data are presented in figure 6-37 for two cases: (1) velocities near the aortic surface of the

native tissue tri-leaflet aortic valve model (figure 6-37a) using data presented in section 6.2.3 on the 68 ml stroke volume, 70 beats/min case; and (2) velocities near the ventricular surface of the polymeric valve model (figure 6-37b) using data presented in section 6.2.1 on measurements near the leaflet of the polymeric valve model #2.

Velocity variability changes with time phase and measurement location. On the aortic side, within the sinus volume, velocities were more variable during late systole as compared to early systole. During late systole, velocities were more variable further away from the leaflet surface, as could be seen in the comparison between velocities measured at 1.96 mm from the mean systolic leaflet location with those measured at 0.089 mm from the mean systolic leaflet location. The standard deviation of measured velocity was 0.049 m/s on the average during late systole at the 1.96 mm location, but was only 0.028 m/s at the 0.089 mm location. During diastole, velocities were more variable during the early diastolic phase. During the first 100 ms of diastole, standard deviation of measured velocities was about 0.10 m/s, while the standard deviation during the last 100 ms of diastole was 0.015 m/s. Early diastole is the period when the valve is either rapidly closing or has just closed. Flow in the sinus space during this period is unsteady, due to adverse pressure gradients leading to flow reversals and extensive fluid mixing, which leads to excessive variability of velocities.

On the ventricular side (measured with the polymeric valve), within the valve orifice, velocities were more variable nearer to the valve leaflet than further out in the valve orifice. Standard deviation of measured velocities was 0.073 m/s when averaged over the systolic duration at 0.089 mm away from the mean systolic leaflet location, but was 0.046 m/s at 1.2 mm away from the mean systolic leaflet location. Further, velocities were more

variable during mid systole as compared to early or late systole, as can be observed in figure 6-37b. After the valve closes, similar excessive velocity variable was observed, most likely due to the same flow phenomenon as discussed above. The standard deviation of measured velocities was about 0.11 m/s during the first 100 ms of diastole and about 0.016 m/s during the last 100 ms of diastole, similar to that observed in the native tissue aortic valve. It should be noted that diastolic measurements could have been performed in the sinus space instead of valve orifice space, since the valve leaflet location changes between systole and diastole.

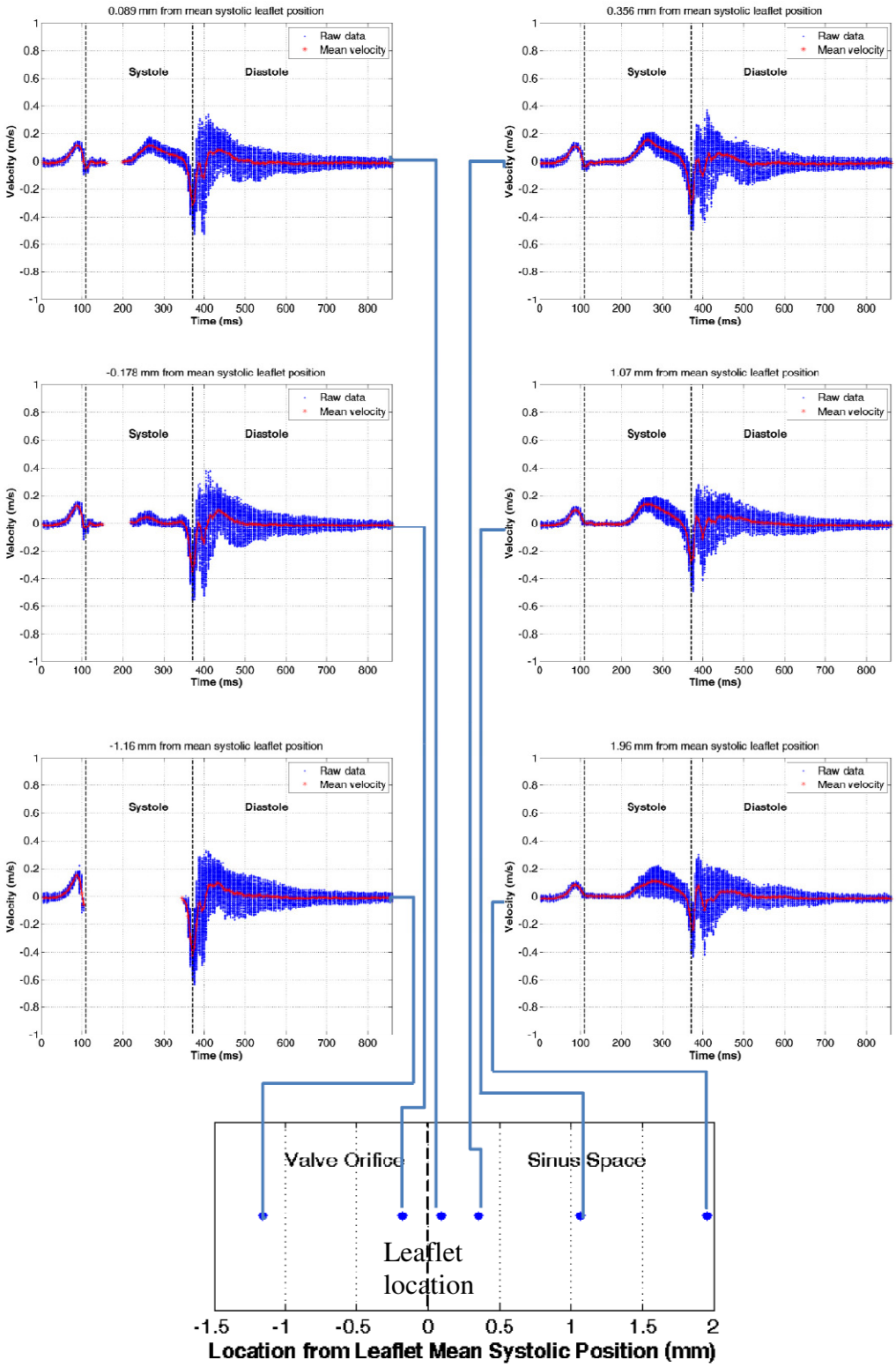

Figure 6-37a. *Plots of raw velocity measurements (blue) and the ensemble mean velocity values over all time phases within the cardiac cycle, at multiple locations near the native tissue valve leaflet for the case of 68 ml stroke volume and 70 beats/min heart rate.*

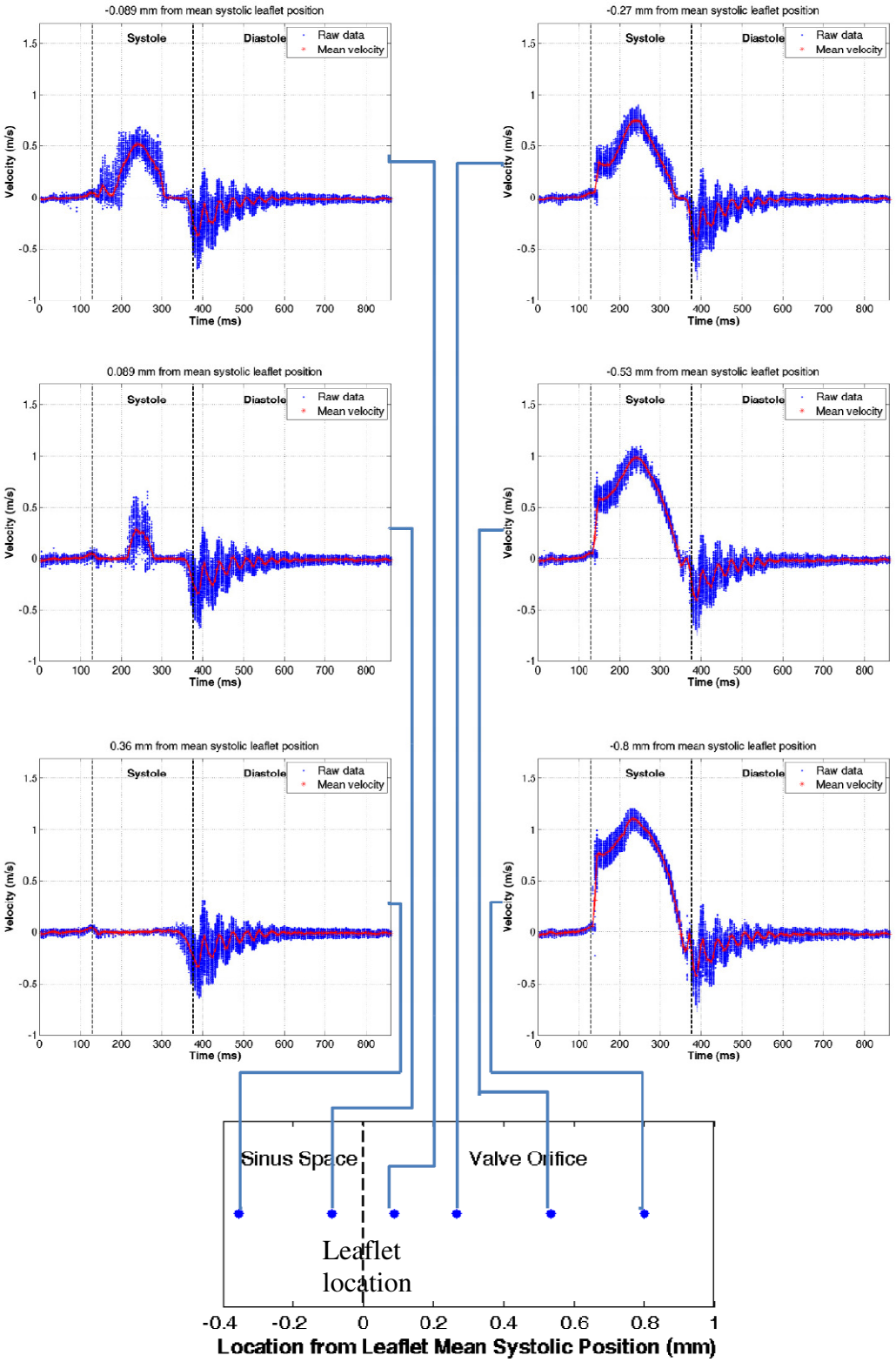

Figure 6-37b. *Plots of raw velocity measurements (blue) and the ensemble mean velocity values over all time phases within the cardiac cycle, at multiple locations near the polymeric valve (#2) leaflet.*

The shear stress measurement technique employed in the current thesis uses both the ensemble average velocity profile and the ensemble averaged leaflet location to calculate shear stresses and assumes ensemble average values to be equivalent to instantaneous values. Since the variability in the location of the valve leaflet can also contribute to errors, this section documents the variability of the measured valve leaflet locations using the back-scattered light intensity technique. Backscattered intensity values over 3 cycles were averaged to get rid of intensity spikes caused by particles in the fluid and were taken as one single measurement. Leaflet location was computed for seven to fifteen cycles were computed to give the mean and standard deviation of the measurements, and are plotted in figure 6-38. The standard deviation of the leaflet location measurement, averaged over systole, was 0.54 of a measurement spatial step or 48 microns for the 68 ml stroke volume case, and 0.46 of a measurement step or 41 microns for the 43 ml stroke volume case. This indicated that in 96% of cases, the leaflet was within 1 spatial step or about 89 microns of the ensemble average location. Together, this data show that the leaflet location was repeatable between cardiac cycles in the valve models.

a)

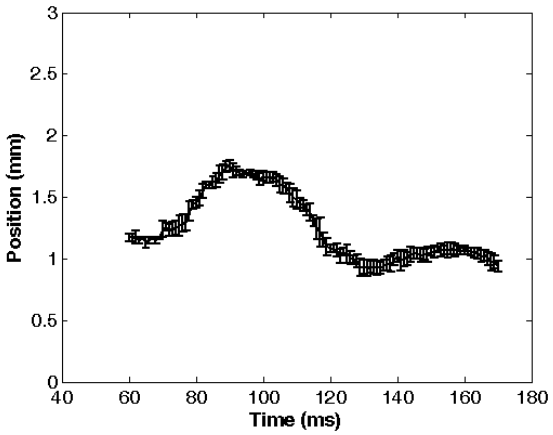

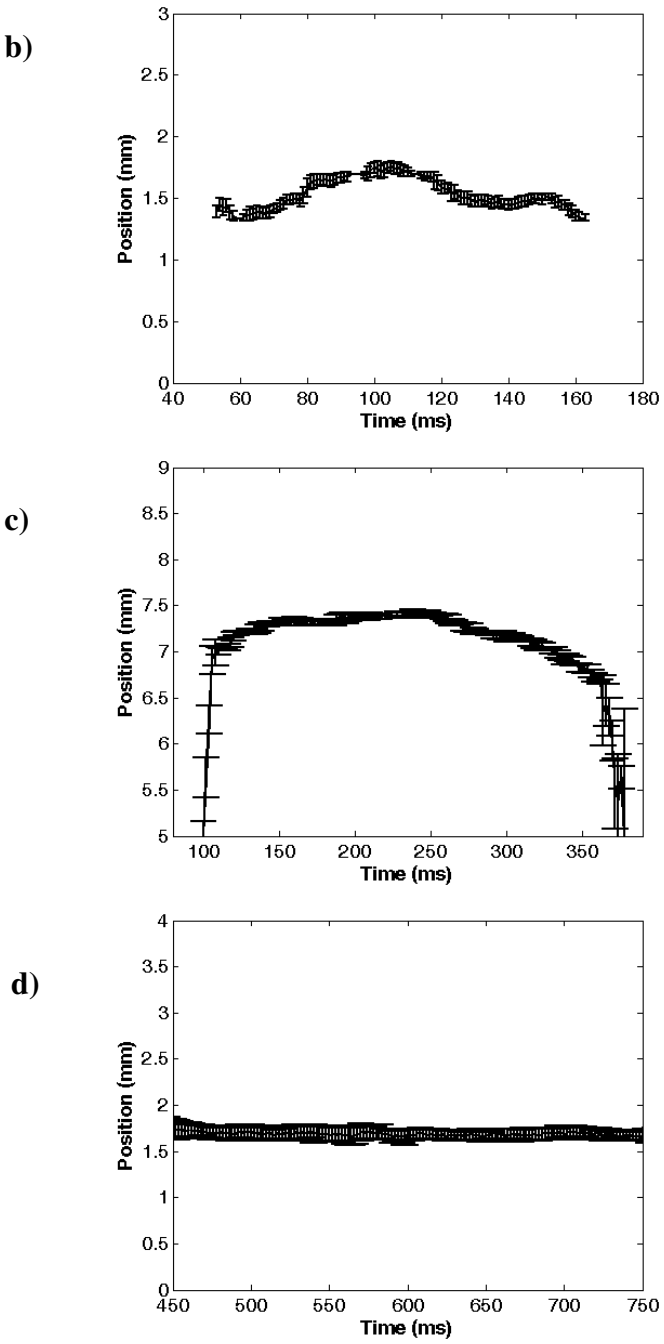

Figure 6-38. *Plot of location of native tissue tri-leaflet aortic valve leaflet during systole for (a) the case of 68 ml stroke volume and 70 beats/min heart rate and (b) the case of 43 ml stroke volume and 70 beats/min heart rate; and of the location of the native tissue bicuspid aortic valve leaflet during (c) systole and (d) diastole, illustrating both the mean values at each time phase and the standard deviation at that time phase.*

6.2.4.3 Performing Stochastic Analysis of Individual Velocity Data Points to Calculate the Variability of Shear Stress to Assess Errors in Shear Stress Measurements

As preliminary work towards determining the statistics of fluid shear stresses based statistics of individual velocities measured with LDV, Monte Carlo simulations were performed. The probability distribution function of shear stresses on the valve leaflet was generated based on the probability distribution function of velocities at each measurement point and time phase. The simulation generated probability distribution functions of shear stresses for measurements on the aortic surface of the native tissue trileaflet valve, and are shown in figure 6-39. These showed that the currently presented measurement technique could lead to substantial standard deviations of shear stress measurements. At 250 ms, 275 ms, and 300 ms time points, the standard deviation of shear stresses were 3.38, 3.89, and 3.42 dyn/cm^2 respectively, which were 54%, 35% and 39% of the mean shear stress magnitude respectively. These substantial variations in shear stresses could indicate a realistic phenomenon, and could be occurring in native aortic valves. However, more advanced methods to study the variations of shear stresses, and the effects of these variations on mechanobiology are needed.

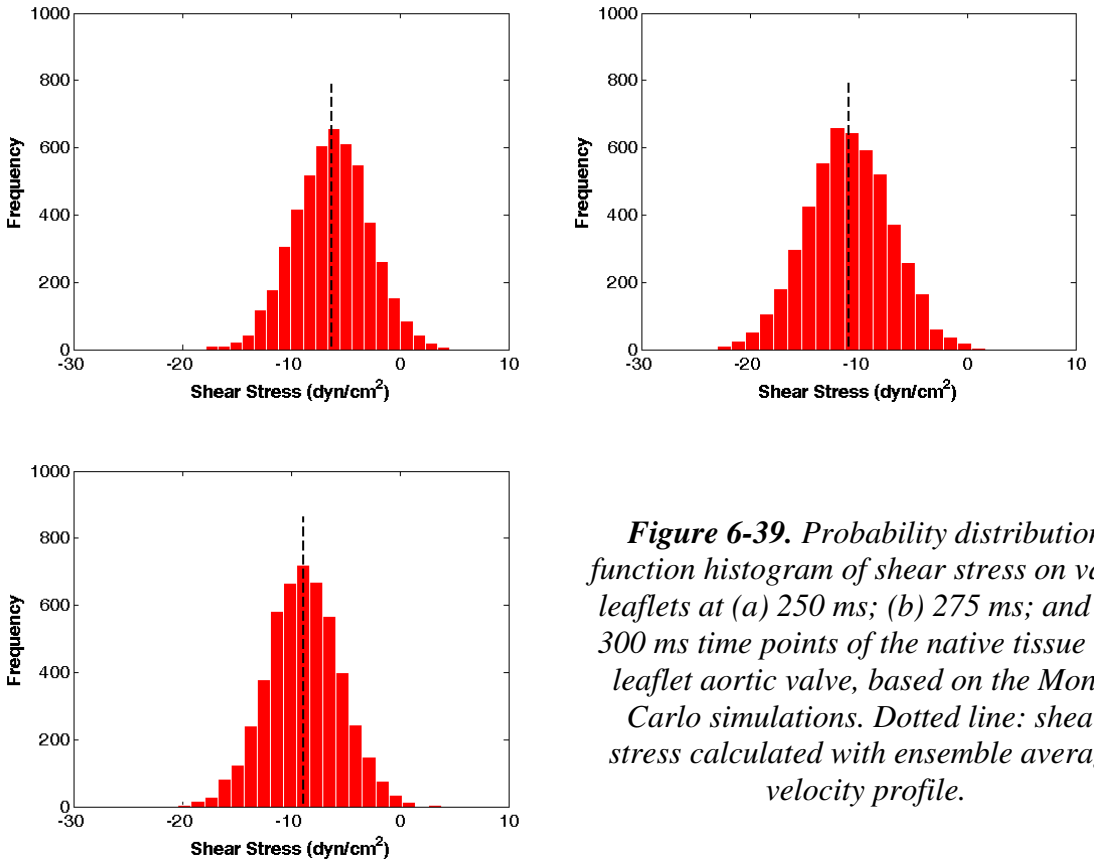

Figure 6-39. *Probability distribution function histogram of shear stress on valve leaflets at (a) 250 ms; (b) 275 ms; and (c) 300 ms time points of the native tissue tri-leaflet aortic valve, based on the Monte Carlo simulations. Dotted line: shear stress calculated with ensemble average velocity profile.*

6.3 Specific Aim 3: Shear Stresses on the Aortic Surface of the Congenital Bicuspid Aortic Valve

In this specific aim, results for shear stresses on the aortic surface of the bicuspid aortic valve model are presented, and are compared to those from the normal tricuspid aortic valve model.

6.3.1 Experimental Hemodynamics

The hemodynamic conditions simulated for both the BAV model and the trileaflet valve model are shown in figure 6-40. While the flow channel up and downstream of the

valve had an inner diameter of 25mm, the BAV model had an effective orifice area of 1.0 cm^2 and the mean and peak systolic pressure gradient was 24 mmHg and 40 mmHg respectively, and can be classified as a mildly to moderately stenotic valve.

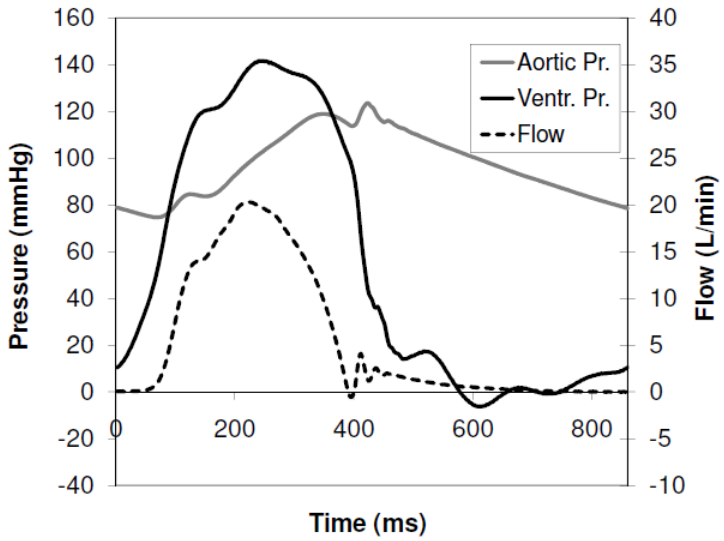

Figure 6-40. *Flow and pressure waveforms simulated in the pulsatile flow loop for the bicuspid aortic valve model.*

6.3.2 Valve Model Characteristics

Figure 6-41 shows the ventricular view of the valve in the flow loop, recorded with a camera through an en face viewing window in the ventricular chamber. After valve closure, the fused leaflet and normal leaflet of the valve had projected areas over the channel area in the ratio of approximately 40%:60%, corresponding to the most common clinical BAV morphology [65]. When the valve was open, the fused leaflet demonstrated impaired mobility and tended to obstruct flow. Analysis of the downstream flow field using Particle Image Velocimetry showed that the forward flow jet was skewed

towards the normal leaflet, as will be discussed in section 5.1.1.1. These characteristics are common features of the clinical BAV [76]. Figure 6-42 shows the B-mode and Doppler ultrasound images of the BAV model in the *in vitro* flow loop. Once again, the fused leaflet was observed to be less mobile, opening incompletely and obstructing flow. Doppler signals demonstrated that forward flow was skewed away from the fused leaflet. These images had some similarities with clinical Doppler echocardiography images of clinical BAV shown in figure 6-42d.

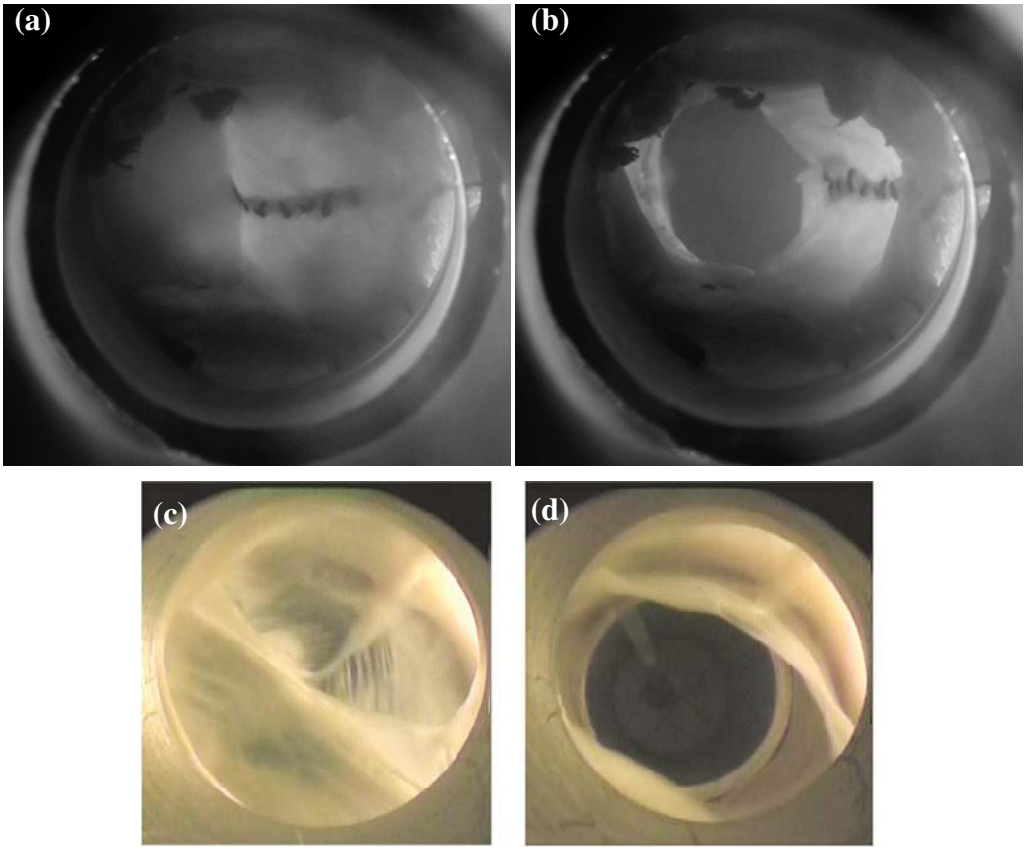

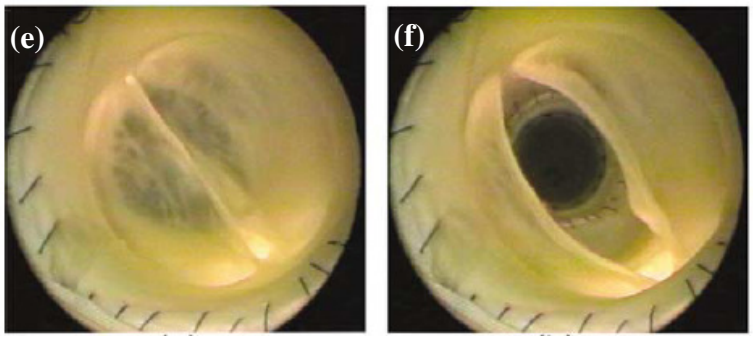

Figure 6-41. *Ventricular view of the BAV model in the flow loop in the closed (a) and open (b) configurations. The fused leaflet dominates approximately 60% of the channel cross sectional area, has impaired mobility, and obstructs flow. The valve appear similar to human BAV, shown in (c-f) [76].*

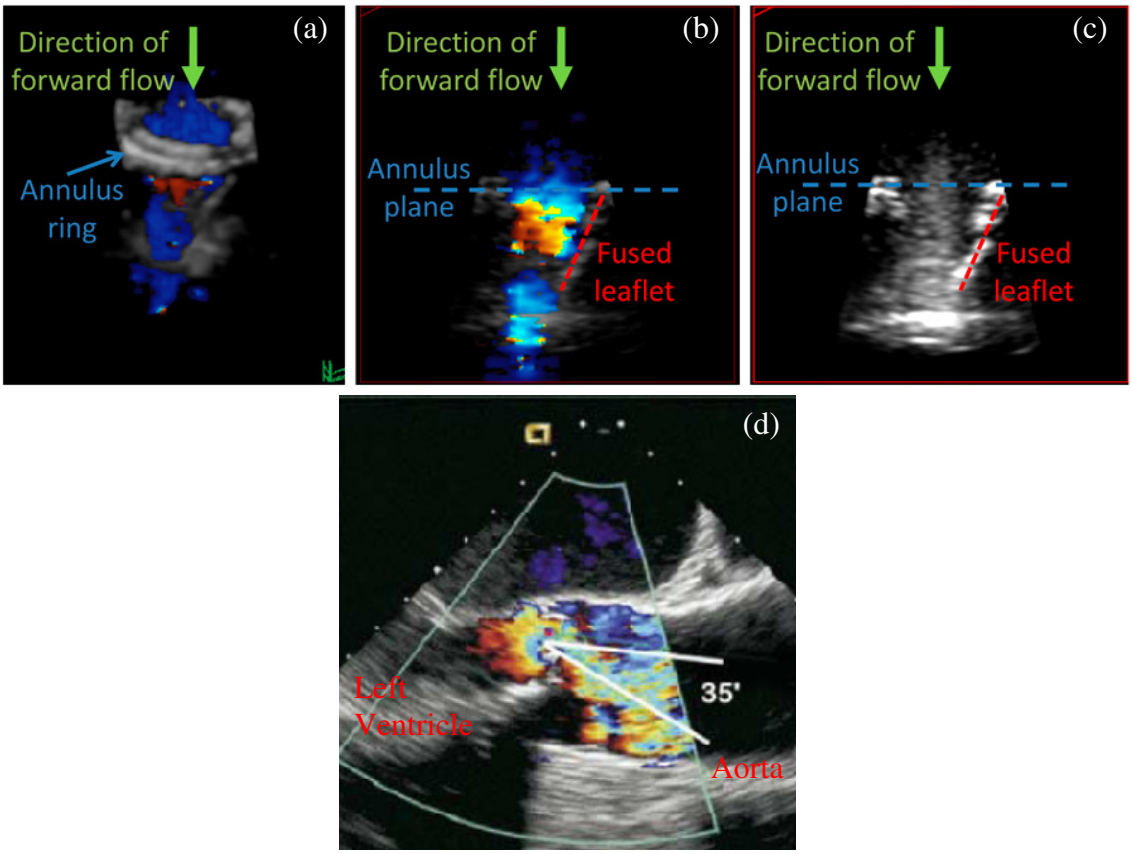

Figure 6-42. *(a-c): Ultrasound images of the BAV model in the in vitro flow loop. (a) 3D B-mode and Color Doppler ultrasound of the valve; (b) 2D B-mode and Color Doppler ultrasound of the valve; (c): 2D B-mode ultrasound of the valve. The fused leaflet is visible in these images, but the non-fused leaflet had faint signals. Color Doppler signals showed that the flow is skewed away from the fused leaflet. (d) Clinical Color Doppler echocardiogram of a stenotic human BAV with eccentric forward flow [119].*

6.3.3 PIV Measurements of General Flow Features

PIV provided a description of the flow fields downstream of the BAV and the normal valve models, as shown in figure 6-43, and provided data on the interaction between the forward flow and the sinus flows. In the normal AV, a central forward flow jet was observed while in the BAV, the forward flow jet was skewed to the non-fused leaflet sinus. Velocities in the BAV were observed to be higher than that in the normal AV, since the BAV has a small effective orifice area.

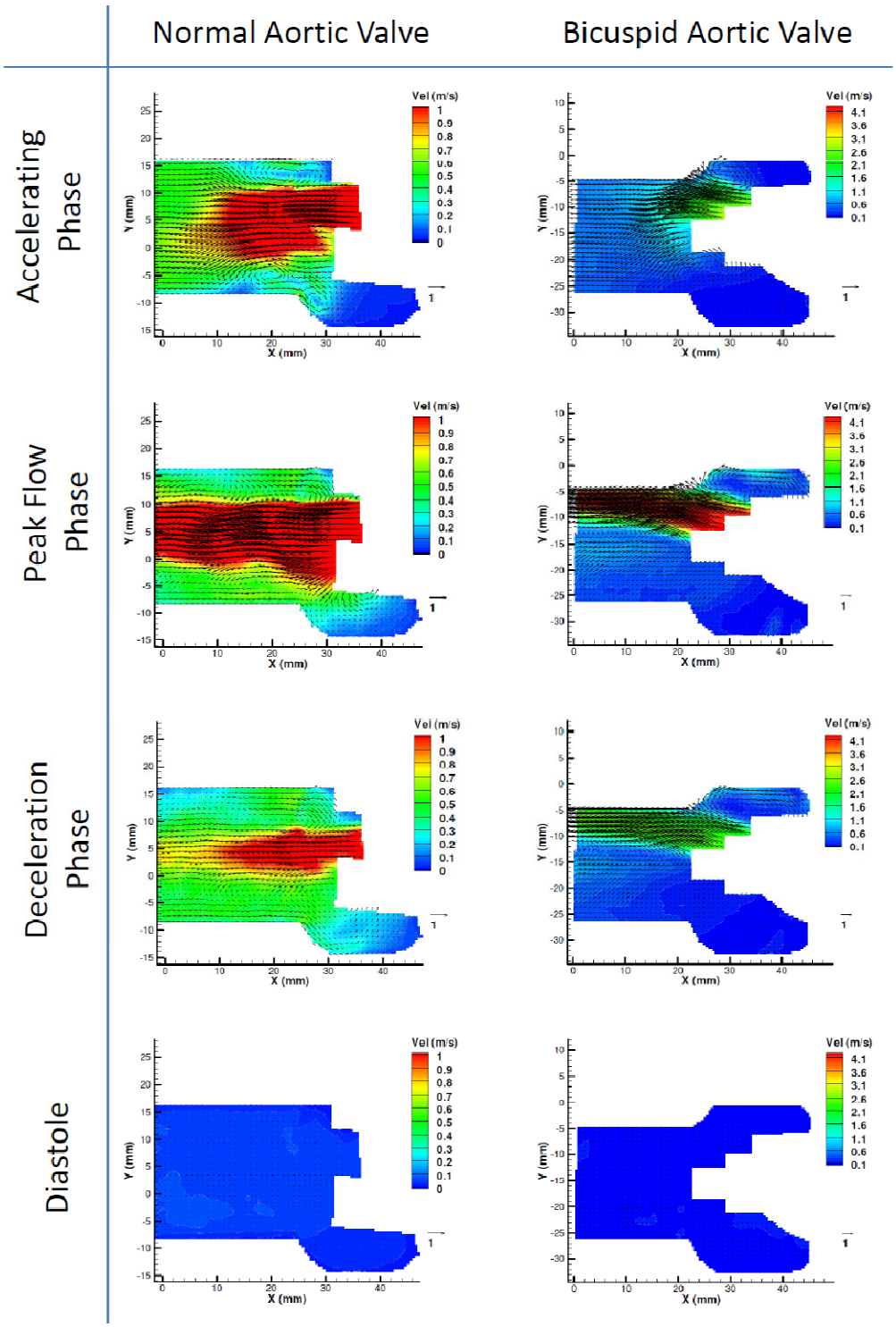

Figure 6-43. *Ensemble averaged flow fields in directly downstream and in the sinuses of the normal aortic valve and the bicuspid aortic valve models, measured with PIV. Arrows indicate velocity direction, while color indicates velocity magnitude. Note that the velocity scales for the two valves are different.*

Peak forward flow velocity in the BAV was slightly in excess of 4.0 m/s, indicating a stenosis severity of borderline between moderate and severe stenosis [120]. Peak forward flow velocity in the normal AV was slightly in excess of 2.0 m/s, representing a mild stenosis [120], which was most likely caused by the small size of the valve.

In the normal AV, sinus vortex flow was brought about because of shear/drag forces induced on the fluid in the sinus by the fast-moving central forward flow jet. In the BAV, since the forward flow collided with the aorta wall near the sinotubular junction of the non-fused leaflet sinus, part of the forward flow was directed into the non-fused sinus. This resulted in the forward flow directly driving the vortical flow in the non-fused leaflet sinus by entering the sinus, instead of inducing it through shear/drag interaction. On the other side, nearer to the fused leaflet sinus, the forward flow caused a vortex directly lateral to it, which in turn induced the sinus vortex in the fused leaflet sinus. Velocities in the non-fused leaflet sinus were thus higher than those in the fused-leaflet sinus.

6.3.4 LDV Measurements

6.3.4.1 Leaflet Dynamics

The back-scattered light intensity map in the fused-leaflet sinus is shown in figure 6-44a, from which the path of the fused leaflet could be clearly traced, as shown in figure 6-44b. Measurements indicated that valve leaflet had stable positions for the majority of systole and diastole, and was mostly free from disturbed fluttering or oscillatory motions. Between systole and diastole, the leaflet moved quickly between the open and closed positions, and disturbed motions occurred only for approximately 20-30ms after valve closure. Shear stress computations were omitted for these time periods.

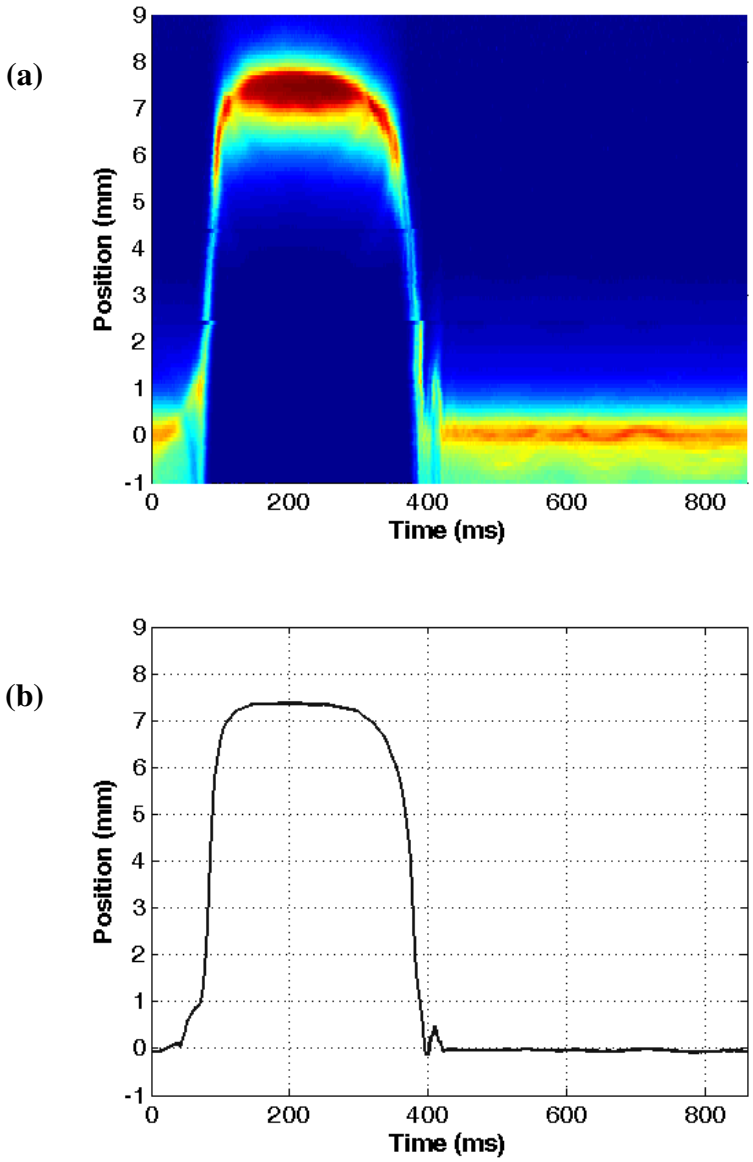

Figure 6-44. ***(a)*** *Back-scattered light intensity map (light intensity along the radial line of velocity measurement over the cardiac cycle) in the fused-leaflet sinus. (b) Actual path of the valve leaflet segmented from the back-scattered light intensity map.*

6.3.4.2 Measured Velocities

The sample velocity maps, combined with the leaflet locations are shown in figure 6-45. These maps were plotted for both leaflets of the BAV. The maximum velocity

magnitudes within the fused-leaflet sinus was -0.4 m/s to 0.4 m/s for both the streamwise and non-streamwise velocities, and -0.6 m/s to 0.3 m/s for the streamwise velocities in the non-fused leaflet sinus.

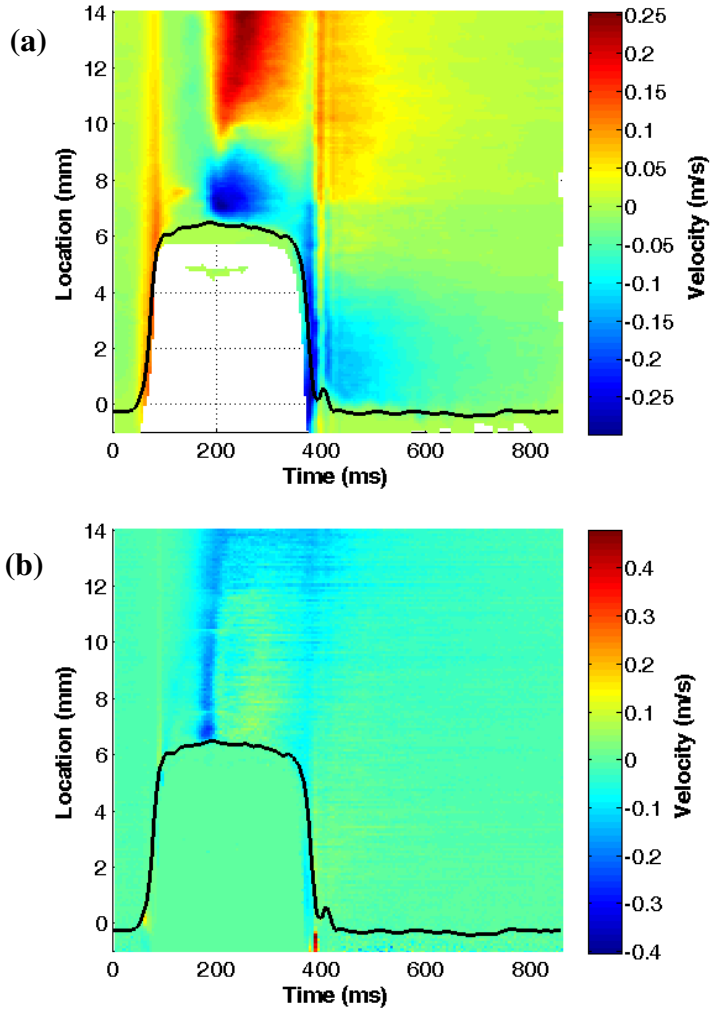

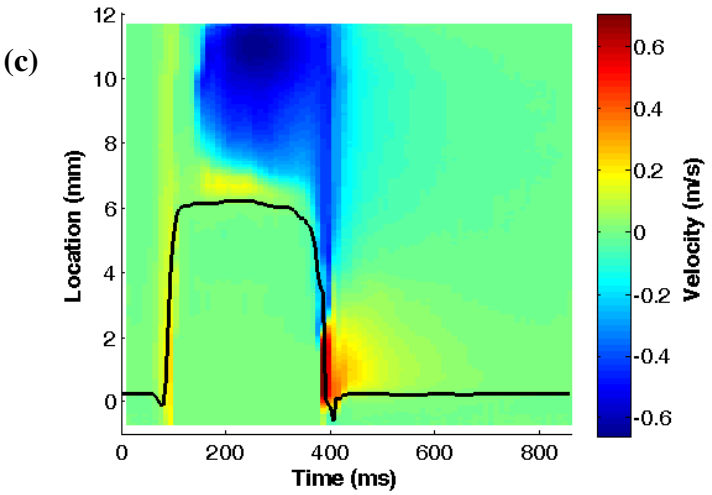

Figure 6-45. *Velocity maps in the vicinity of the BAV fused leaflet over the cardiac cycle for the (a) streamwise, and (b) non-streamwise directions; and (c) the velocity map in the vicinity of the BAV non-fused leaflet over the cardiac cycle for the streamwise direction. The black lines indicate the location of the valve leaflet at this measurement location.*

6.3.4.3 Measured Shear Stresses

The same terminology convention for shear stress are used here as in 6.2.1.1.5. The computed shear stresses are plotted in figure 6-46 for both the fused leaflet and the normal leaflet in the stream-wise direction, and also in non-stream-wise directions for the fused leaflet.

In the streamwise direction, shear stresses were elevated for both leaflets during systole, when flow in the sinus gathered velocity to form the sinus vortex. While systolic shear stress resembled that of a sinusoid, peaking at about 210 ms time point, diastolic shear stress started at a high magnitude during early diastole and reduced to zero during late diastole, before elevating again during the transients before valve opening.

Systolic shear stresses on the fused leaflet were opposite in direction as that on the normal leaflet, which was related to the opposite direction of vortices in the two sinuses.

Peak systolic shear stress magnitude was lower on the normal leaflet than that on the fused leaflet: 18 dyn/cm^2 versus 33 dyn/cm^2. The same went for peak diastolic shear stress: 3 dyn/cm^2 versus 17 dyn/cm^2.

In the non-streamwise direction for the fused leaflet, shear stresses peaked at 12 dyn/cm^2 during early systole, at about the 180ms time point. Subsequently, non-streamwise shear stress reduced and stayed near to zero for the rest of systole. During diastole, shear stresses were low, staying less than 2 dyn/cm^2 all the time.

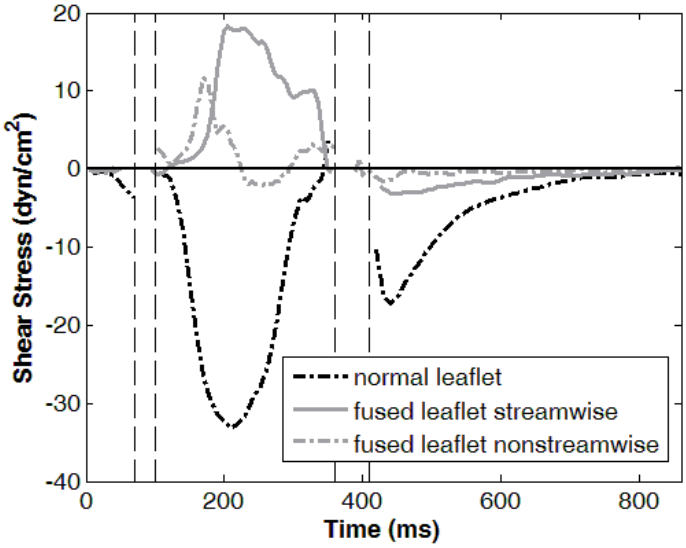

Figure 6-46. *Shear stress on the central portion of the fused leaflet and normal leaflet of the bicuspid aortic valve model.*

6.3.4.4 Shear Stress Variability Compared to Normal Valve

Shear stress waveforms measured in the BAV had largely similar shape as those measured from the normal tricuspid aortic valve model: systolic shear stress was sinusoidal, and diastolic shear stress had a shape of a gradual decrease to zero from the

early diastolic magnitude. However, the variability of measured shear stresses was observed to be different, especially during systole.

6.3.4.4.1 Variability in Velocities Near the Valve Leaflet

Figure 6-47a and 6-47b show the standard deviation of velocities for velocities measured at approximately 1mm lateral (nearer to the sinus wall) of the valve leaflets, in their open-valve systolic position (figure 6-47a) and the close-valve diastolic position (figure 6-47b), for 3 different leaflets: the BAV fused leaflet, the BAV normal leaflet, and the leaflet of a normal tri-leaflet valve. The standard deviation is a measure for the variability of measured velocities. Figure 6-47a shows that, when the valves were open, velocities 1mm away from the BAV fused and BAV normal leaflets were especially variable, especially during mid-systole, which was distinctly different velocities 1mm away from the leaflet of the normal valve, which showed only minor variability throughout systole. For the normal tri-leaflet valve, there was elevation of variability during late systole / early diastole period, most likely due to fluid mixing from adverse pressure gradient and flow reversal associated with valve closure. The amount of variability in the velocities was the same for all three types of valve leaflets.

During diastole, this location was far away from the leaflet and was well into the sinus. Variability of flow at this location during diastole showed little differences between the three cases.

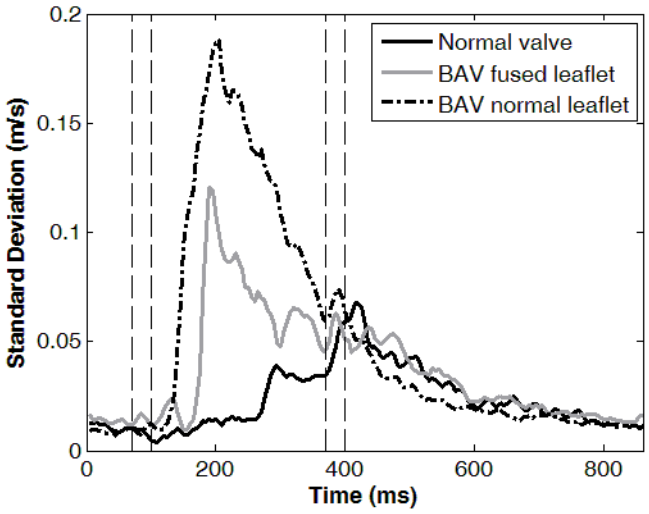

Figure 6-47a. *Variability of velocity measured at the location 1mm away from the leaflet when the leaflet is at the systolic position, plotted over time.*

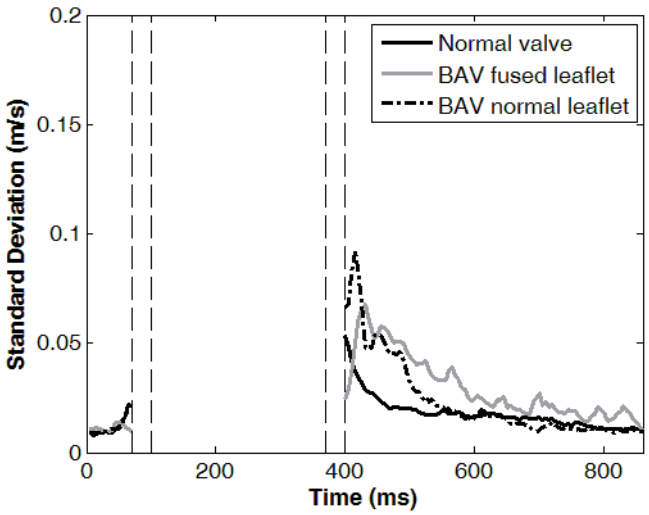

Figure 6-47b. *Variability of velocity measured at the location 1mm away from the leaflet when the leaflet is at the diastolic position, plotted over time.*

Figure 6-47b shows that, when the valve is closed, velocities at the location 1mm away from the valve leaflet demonstrated variability which gradually decreased from an initial high to a low value, coinciding with the dissipation of fluid motion in the sinuses.

Variability of flow was higher near the BAV fused leaflet and BAV normal leaflet than that on the normal valve leaflet during early diastole. However, from mid-diastole onwards, the variability of flow near all three leaflets was similar.

6.3.4.4.2 Power Spectral Analysis of Velocities Near Valve Leaflet

Since it was unclear if the higher shear stress variability on the BAV leaflets was due to magnitude differences between different cycles or high frequency fluctuating unsteadiness within each cycle, a power spectrum analysis was performed on time-sequenced velocity acquisitions very near (about 1 mm away from) the systolic leaflet positions. The inputs into the power spectral analysis were instantaneous velocities less their ensemble velocities, or the deviation of each velocity from the ensemble mean velocity. The measurements were analyzed in their original time sequence, with both systolic and diastolic velocities included. The resulting power spectrum for a range of relevant frequencies is shown in figure 6-48. The plot in figure 6-48a was obtained using the sample-and -hold method described by Adrian et al. [109], while the plot in figure 6-48b was obtained using the sample-and-hold method with refinement to account for the bias due to non-uniform velocity sampling, described by Moreau [110].

Both results plots showed that velocities near the BAV leaflets had greater tendency to deviate from their ensemble mean over a range of frequencies. The difference between velocities near the BAV and those near the normal tricuspid AV were especially wide for the lower frequencies, indicating that most of the additional variability in the BAV could be accounted for by magnitude variations from one cycle to the next. However, differences were also observed for frequencies as high as 10-30 Hz. This

indicated that there were some tendencies for velocities near the BAV to fluctuate about their ensemble average waveform in a high frequency nature.

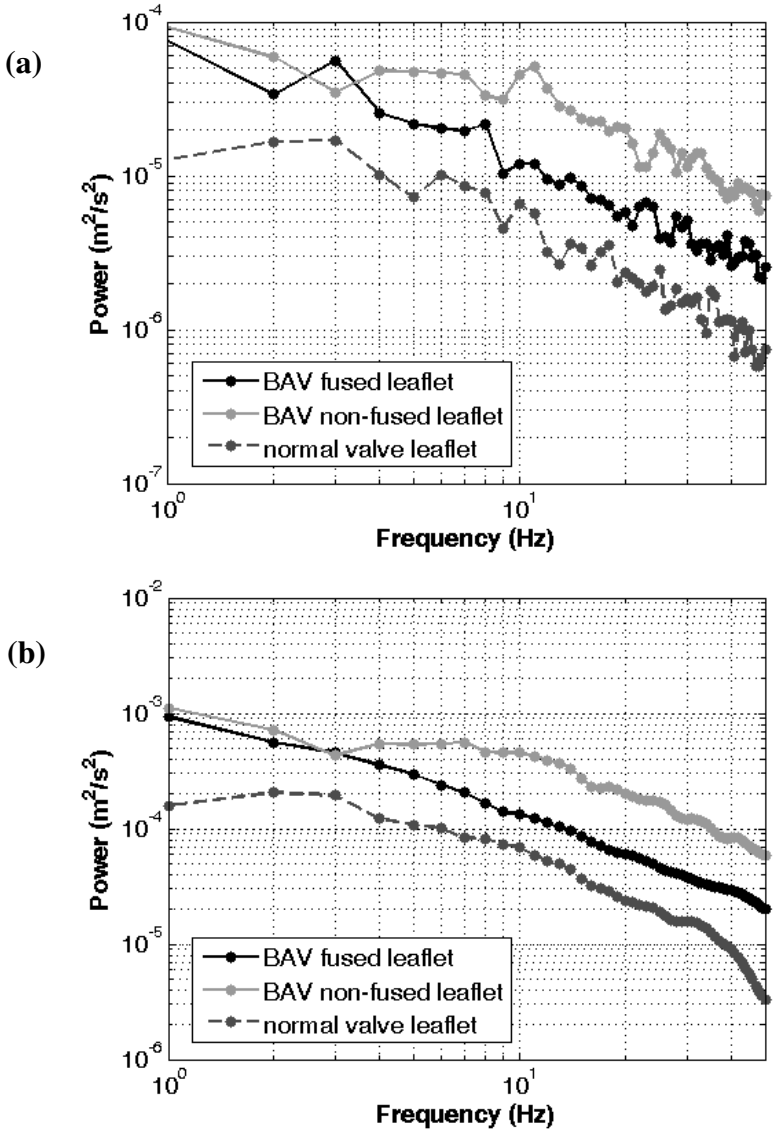

Figure 6-48. *Power spectral breakdown of the frequency components of the velocities measured 1mm away from the valve leaflets during systole: a comparison between the fused leaflet of the BAV, the normal leaflet of the BAV and a leaflet of the normal tricuspid aortic valve. Power Spectrum were obtained with (a) the sample and hold method [109] and (b) the sample and hold method with refinement [110].*

6.3.4.4.3 *One Standard Deviation Bounds of Shear Stresses*

Using methods described in 5.2.5.2, the one-standard-deviation range of stream-wise shear stress at all time points in the cardiac cycle could be calculated for the fused-leaflet of the BAV. Shear stresses with its bounds are shown in figure 6-49. As discussed, the standard deviation of shear stresses is a measure of shear stress variability. Shear stress variability was low throughout diastole and early systole, but saw a large increase during mid-systole, when average shear stress was peaking. The peak of the upper bound shear stress was about twice the peak of the average shear stress, while the lower bound shear stress reversed in direction for the first half of systole.

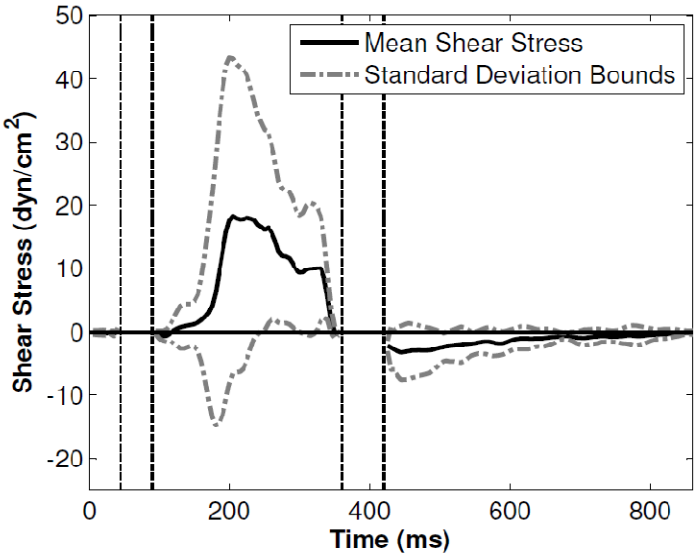

Figure 6-49. *Ensemble average shear stress waveform for the BAV fused leaflet, and the one standard deviation bounds for the shear stress, calculated by adding or subtracting one the ensemble standard deviation to the ensemble average.*

6.4 Specific Aim 4: Ex Vivo Studies of the Effects of Fluid Shear Stresses on Porcine Aortic Valve Leaflet Biology

In this specific aim, preliminary *ex vivo* mechanobiology experiments were performed to investigate the effects of the above measured shear stresses on the biology of the native aortic valve, with relevance to aortic valve calcification disease. These experiments demonstrated that the aortic valve leaflets were sensitive differences in fluid shear stress that they were exposed to, such as shear stress magnitude, shear stress frequency and variability in shear stresses. These preliminary results identified specific shear stress conditions which are pro-calcific, and can now be used in further investigations into the biological pathways of shear-induced calcification.

Porcine aortic valve leaflets were incubated in the cone and plate bioreactor under various shear stress waveforms to determine the biological response of aortic valve leaflets. The shear stress characteristics investigated were (1) magnitude of shear stress; (2) frequency of shear stress; and (3) variability of shear stress. These characteristics were investigated because they were observed to be primary nature of variations in the native aortic valve mechanical environment when hemodynamics were varied or when the valve was bicuspid: changes in stroke volume and heart rate resulted in changes in magnitude and frequency of shear stresses; and the bicuspid aortic valve geometry resulted in shear stresses being unstable, with variations in shear stress magnitudes in consecutive cycles, and could result in high frequency fluctuations of shear stresses.

6.4.1 Routine Hematoxyin and Eosin Stain

H&E staining was done routinely to ensure that there was no tissue damage or other abnormality to the samples after culture in the cone and plate bioreactor. Sample images are shown in figure 6-50, showing that the tissue structure was mostly intact, as were the endothelial layers, the cell nuclei were round instead of smeared out, indicating that that the cells were most likely alive.

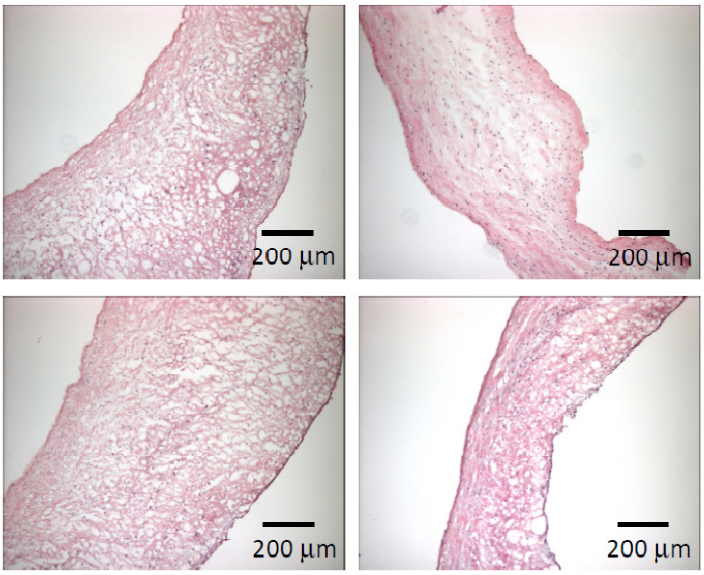

***Figure 6-50**. H&E stained samples after culture from the cone and plate bioreactor.*

6.4.2 Sinusoidal Shear Stress Waveform Experiments

Results are presented in this section on responses of native porcine aortic valve leaflets to sine waveforms of shear stresses at various magnitudes and frequencies. Sinusoidal waveforms were used as shear stress inputs as a means of deconstructing the complicated measured waveforms to simpler, manageable ones, such that specific characteristics of shear stresses could be tested. This way, we can isolate biological responses specific to these shear stress characteristics, and be sure that the observed

responses were not a result of the more complex confounding characteristics blended into the shear stress waveforms. The rationale for the magnitudes and frequencies of shear stress tested are discussed in section 5.5.2.

6.4.2.1 Arsenazo Assay Results

The Arsenazo assay quantified the amount of calcium within the tissues from the culture experiments. The results are shown in figure 6-51. The low shear stress magnitude condition (5 dyn/cm^2, 1Hz) and the high frequency condition (10 dyn/cm^2, 4 Hz) had significantly more calcium accumulation than the other conditions. There were no differences in the amount of calcium for all the other shear stress conditions and the fresh controls. It was noteworthy that the normal valve pulsatile shear stress waveform did not show differences with fresh controls, higher magnitude sine wave shear stresses, and lower frequency sine wave shear stresses.

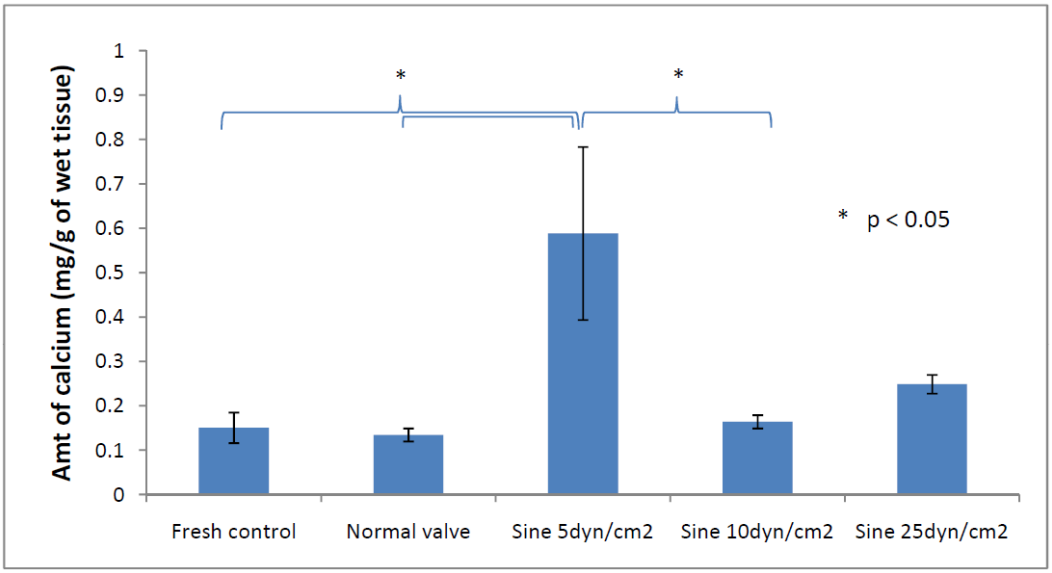

Figure 6-51a. *Amount of calcium in valve tissue samples after the 72h culture exposed to sinusoidal shear stress of various magnitudes at 1 Hz frequency, compared to fresh controls and normal aortic valve shear stress waveform, obtained with the Arsenazo assay.*

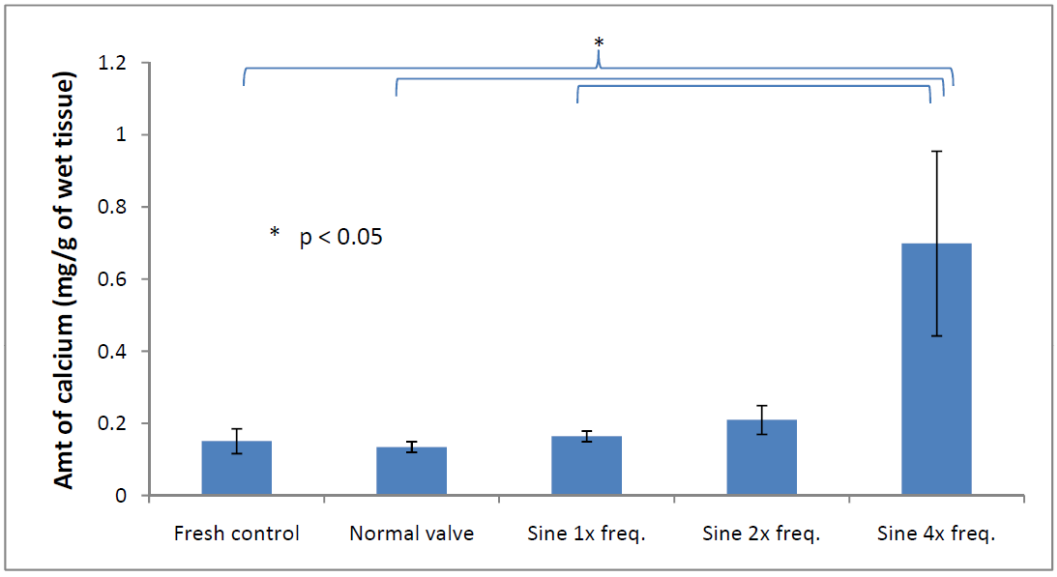

Figure 6-51b. *Amount of calcium in valve tissue samples after 72h culture exposed to sinusoidal shear stresses of various frequencies at 10 dyn/cm^2 magnitude, compared to fresh controls and normal valve shear stress waveforms, obtained with the Arsenazo assay.*

6.4.2.2 Von Kossa Assay Results

Von Kossa stains are shown in figure 6-52. These stains showed that the fresh porcine valve leaflet had little calcium nodules, while the leaflet samples cultured in the cone and plate bioreactor showed varying levels of calcification, depending on the shear stress condition the sample was exposed to. Calcification occurred as distributed spots of mineralization distributed throughout the leaflet and as concentrated region of mineralization just under the endothelial surface. The 10 dyn/cm^2 4 Hz condition appeared to have developed the most calcification nodules, followed by the 5 dyn/cm^2 1 Hz, the 25 dyn/cm^2 1 Hz, and the 10 dyn/cm^2 1 Hz conditions. The 10 dyn/cm^2 2 Hz condition appeared to have the least amount of calcification nodules. These results qualitatively agreed with the Arzenaso assay results.

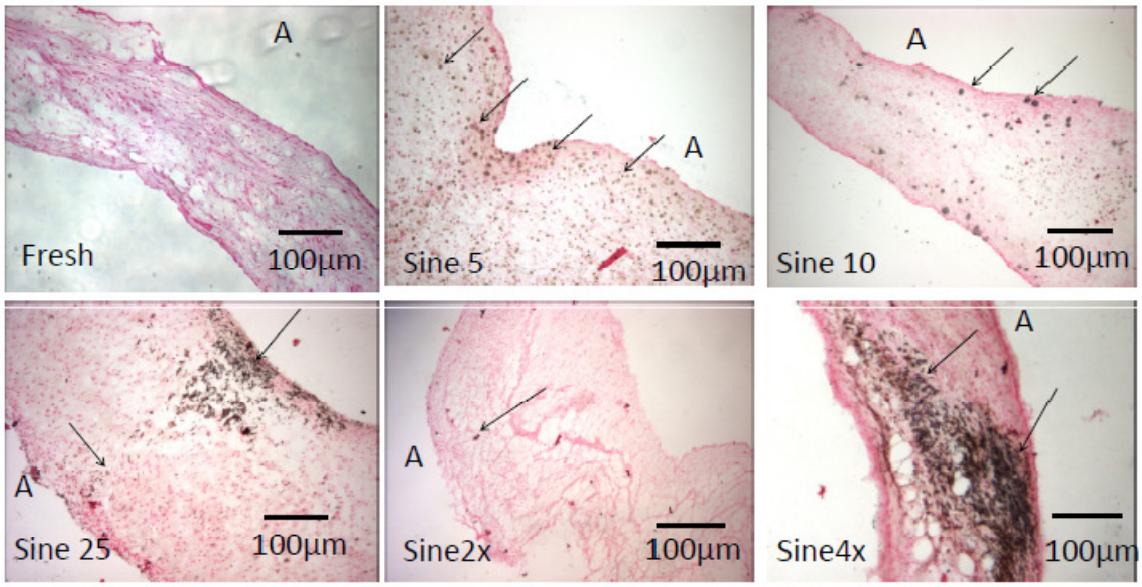

Figure 6-52. *von Kossa stains on sections of valve leaflets incubated under the various sinusoidal shear stress waveforms, showing the development of calcium nodules. The results supported the Arsenazo assay qualitatively. Sine 5: 5 dyn/cm^2 magnitude at 1 Hz; Sine 10: 10 dyn/cm^2 magnitude at 1 Hz; Sine 25: 25 dyn/cm^2 magnitude at 1 Hz; Sine 2x: 10 dyn/cm^2 magnitude at 2 Hz; Sine 4x: 10 dyn/cm^2 magnitude at 4 Hz; A: aortic surface of the valve leaflet.*

6.4.2.3 Alizarin Red Assay Results

Alizarin Red results showed that calcium nodules developed in the valve leaflets, manifesting as either distributed spots or a continuous strip of calcification (figure 6-53). These calcification regions were mostly concentrated just under the surface of the valve leaflet. There was significant amount of variability in the size of calcification area observed in each section. Qualitatively, however, it was not discernable which condition resulted in higher amounts of calcification.

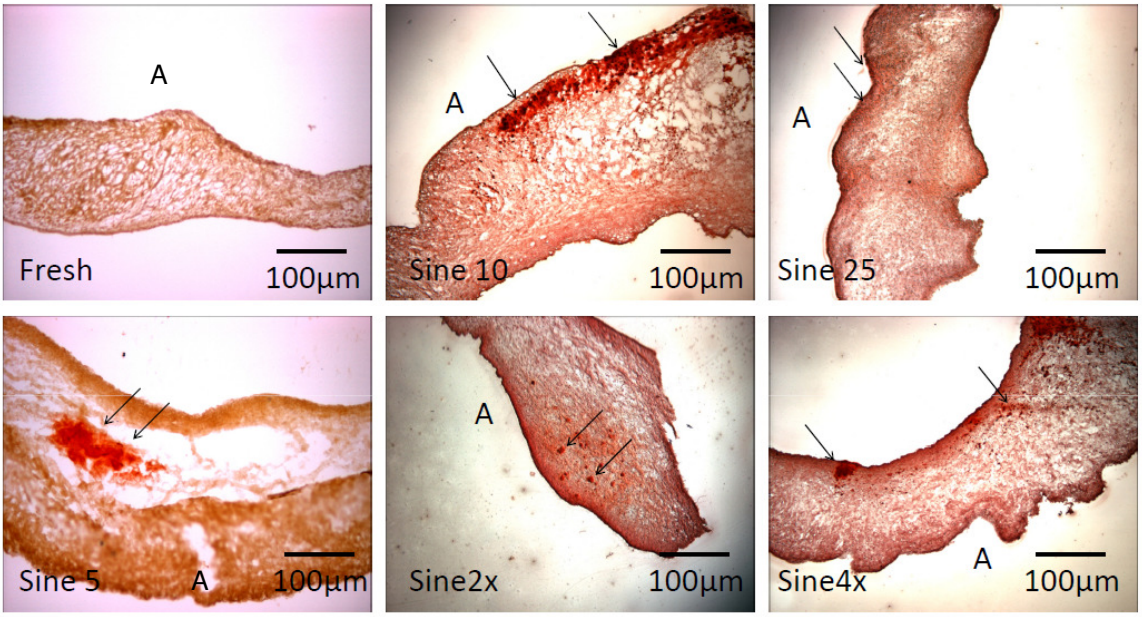

Figure 6-53. *Alizarin Red stains on sections of valve leaflets incubated under the various sinusoidal shear stress waveforms, showing the development of calcium nodules. Fresh: fresh control samples; Sine 5: 5 dyn/cm^2 magnitude at 1 Hz; Sine 10: 10 dyn/cm^2 magnitude at 1 Hz; Sine 25: 25 dyn/cm^2 magnitude at 1 Hz; Sine 2x: 10 dyn/cm^2 magnitude at 2 Hz; Sine 4x: 10 dyn/cm^2 magnitude at 4 Hz; A: aortic surface of the valve leaflet.*

6.4.3 BAV Shear Stress Waveforms Experiments

6.4.3.1 Shear Stress Waveforms Inputs to the Bioreactor

From the LDV measurements of shear stresses, excessive systolic shear stress variability on the BAV leaflets was found. This specific characteristic was investigated to see if it impacts the overall biological response of valve leaflets. Fresh porcine valve leaflets were exposed to shear stress shown in figure 5-10 for this purpose. These waveforms were constructed based on measurements from the BAV fused leaflet. The waveform in figure 5-10a was the ensemble averaged shear stress on the BAV fused leaflet, which is devoid of all shear stress unsteadiness. The waveform in figure 5-10b was derived by alternating between the ensemble averaged shear stress with the upper

bound and lower bound shear stress waveforms, representing a shear stress waveform which had exaggerated variations in magnitude from one cycle to another. The waveform in figure 5-10c was derived by superimposing a 20 Hz sinusoidal (oscillatory) waveform with an amplitude of half of the standard deviation of shear stress onto the ensemble averaged shear stress waveform. This represented a waveform with high frequency fluctuations during systole. The 20 Hz frequency was chosen as a speculation of what might occur in real valves. While it embodied some of the high frequency fluctuations observed in shear stress measurements from the BAV, it did not have direct basis from the measurements. It could be noted, however, that 20 Hz was within the frequency range of the power spectral analysis presented in section 6.3.4.4.2. There were differences in 20 Hz power spectra of velocities close to the leaflets of the BAV and that of the normal valve. Further, measurements by other authors indicated that turbulent flow downstream of the aortic valve had power spectra with a range of frequencies that included 20 Hz [115, 116]. As a normal valve control, the shear stress waveform measured in the normal tricuspid aortic valve was also used in the bioreactor and compared to the above waveforms.

To avoid exposing the fresh leaflet samples to excessively high shear stresses, so that only the effects of variability of shear stresses could be discerned and not the effects of the magnitude of shear stresses, all waveforms were normalized by a factor of 0.56, such that the ensemble average shear stress waveform had a peak of 10 dyn/cm^2, while the upper bound waveform had a peak of 23 dyn/cm^2. This especially applied in the case of the 2nd and 3rd waveforms. Since the objective was to study effects of systolic shear

stress variability on valve biology, the diastolic shear stress waveforms were kept constant for all three waveforms.

6.4.3.2 Arsenazo Assay Results

The results from the Arsenazo assay are shown in figure 6-54. There was no statistical significance between the ensemble averaged BAV shear stress waveform group, the fresh control group, and the normal valve shear stress waveform group. The two shear stress waveform which included shear stress variability (the BAV inter-cycle magnitude variability group; and the BAV fluctuating variability group) had significantly more calcification than the fresh control group and the normal valve shear stress group. This indicated, first, that shear stress variability increased calcification response; and second, that the lack of shear stress variability resulted in no significant increase in calcification from fresh control samples. The BAV fluctuating variability shear stress waveform group showed the most calcium accumulation.

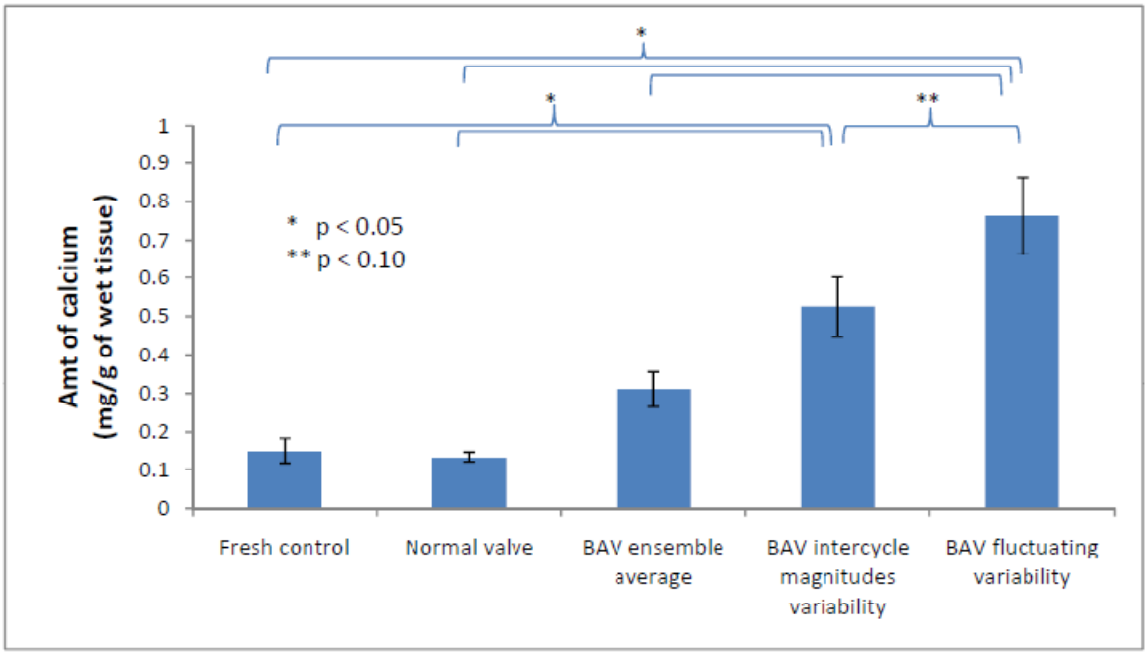

Figure 6-54. *Amount of calcium in valve tissue samples after 72h culture exposed to shear stresses with various characteristics obtained from measurements in the BAV valve model in specific aim 4.*

6.4.3.3 Von Kossa Assay Results

Von Kossa stains are shown in figure 6-55. These stains showed that the fresh porcine valve leaflet had little calcium nodule, while the leaflet samples cultured in the cone and plate bioreactor showed varying levels of calcification. Calcification occurred as distributed spots distributed throughout the leaflet and as concentrated region of mineralization just under the endothelial surface. Qualitatively, it was not discernable which shear stress waveform led to high amounts of calcification.

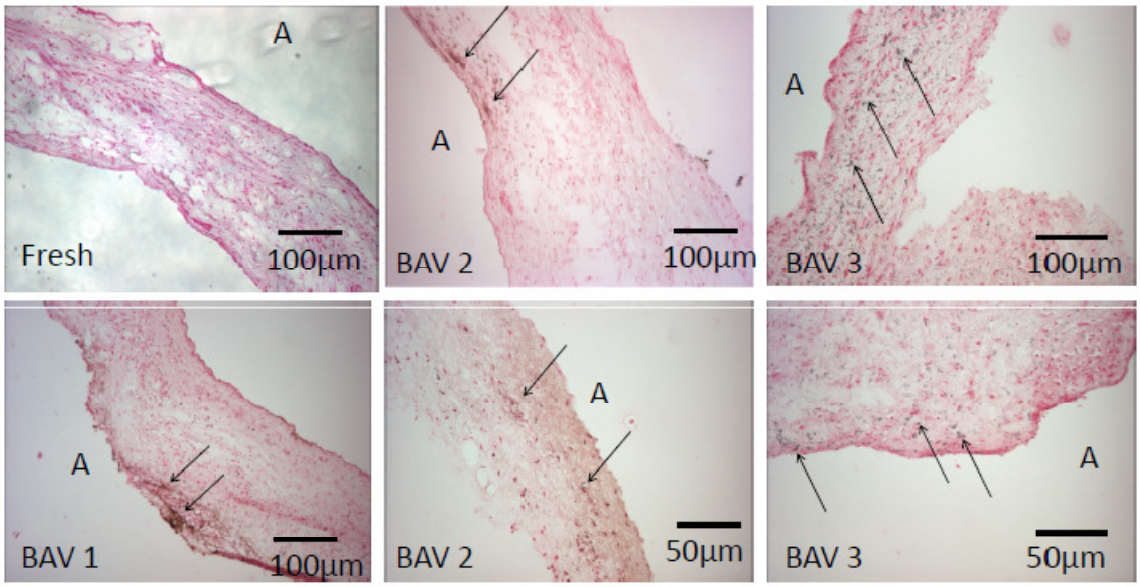

Figure 6-55. *Von Kossa stains on sections of valve leaflets incubated under the various BAV shear stress waveforms, showing the development of calcium nodules. BAV 1: ensemble averaged shear stresses (figure 5-10a); BAV 2: shear stress waveform with inter-cycle magnitude variability (figure 5-10b); BAV 3: BAV shear stress waveform with fluctuating intra-cycle magnitude variability (figure 5-10c); A: aortic surface of the valve leaflet.*

6.4.3.4 Alizarin Red Assay Results

Alizarin Red stain results are shown in figure 6-56. The stains showed mild amounts of calcification, mostly on or just under the aortic surface endothelium, for all the shear stress waveforms tested. Qualitatively, it was not discernable which condition resulted in higher amounts of calcification.

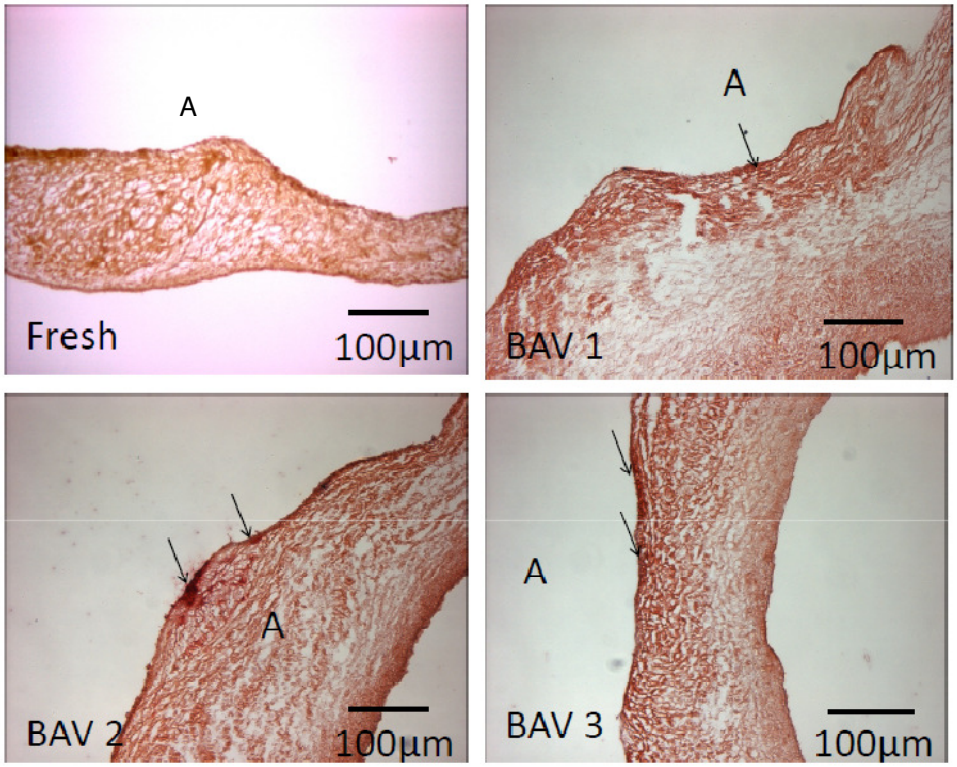

Figure 6-56. *Alizarin Red stains on sections of valve leaflets incubated under the various BAV shear stress waveforms, showing the development of calcium nodules. Fresh: fresh control samples; BAV 1: ensemble averaged shear stresses (figure 5-10a); BAV 2: shear stress waveform with inter-cycle magnitude variability (figure 5-10b); BAV 3: BAV shear stress waveform with fluctuating intra-cycle magnitude variability (figure 5-10c); A: aortic surface of the valve leaflet.*

CHAPTER 7

DISCUSSION

7.1 The Use of LDV Method for Shear Stress Measurements

In specific aim 1, the method to measure shear stresses on the surface AV leaflets was devised, and was chosen to be an *in vitro* approach. Validation work showed that the approach was feasible. It was shown that LDV can be used to make measurements very close to a native tissue and that the surface of the valve leaflet could be tracked with the back-scattered light intensity method.

7.1.1 Error Associated with LDV Shear Stress Measurement Technique

The results presented in this thesis are composed of shear stress calculations based on the ensemble mean velocity profiles, measured from LDV. During the acquisition of data, however, it was noted that there was a significant spread of velocity values at various time points and spatial points. With the current data, it was uncertain whether the ensemble average velocity profile reflected the instantaneous velocity profile. The interpretation shear stress results in the current thesis must be approached with some caution. This uncertainty is consequent to the choice of using LDV as the measurement technique for calculating shear stress due to lack of a better method. LDV, being a point-by-point measurement technique, could not provide instantaneous velocity profile gradients or instantaneous leaflet locations, and any interpretation of shear stresses must be performed using the ensemble average and standard deviation of velocities and leaflet locations. Specifics of the analysis of the errors with the variability of velocity and leaflet location measurements are presented in section 6.2.4.1, based on methods described in

5.2.5. It should be noted that the variability of velocity and leaflet locations could be the result of physical phenomenon actually occurring in the in vitro heart valve models, which was faithfully captured by the LDV measurements. Such variations could also be occuring in native heart valves. Future work is needed to devise more advanced methods to study this variability and its effect on shear stress, and to study the effects of shear stress variability on the biology of heart valves.

Despite the uncertainty of whether the ensemble average velocity profile would represent the instantaneous velocity profiles, the currently presented data represent the closest study to obtaining high resolution time-varying shear stress measurements on aortic valve leaflets. Although the LDV technique has shortcomings as a measurement technique for fluid shear stress measurements, it was more effective than other techniques, such as PIV, ultrasound or MRI.

The variability of velocities measured at any one point within one time phase can be due to three factors: (1) the natural unsteady flow physics occurring in the valve, leading to a significant spread of measured velocities; (2) cycle-to-cycle variability in the experimental flow loop setup (3) the variability of valve leaflet location with respect to the LDV probe, which leads to slightly different measured velocities at different cardiac cycles; and (4) the fact that the LDV measurement volume was focused at a location with high shear rate, such that one end of the 126 micron length measurement volume, velocities are much lower than those at the other end, thus resulting in a spread of measured velocity magnitudes.

Since the leaflet location variability study showed that the valve leaflets had repeatable locations from one cycle to the next, the variability in the location of the valve

leaflet is unlikely to be the main cause of the spread in the measured velocities. On the aortic side of the valve leaflet, within the sinus space, PIV measurements have shown that velocities can vary significantly from one cycle to the next, most likely because the sinus vortex is a secondary flow feature induced by the forward flow. Thus the measured velocity variability most likely caused by the physical phenomenon of significant velocity variability occurring in the AV sinuses. Finally, the high variability of velocities measured near the ventricular surface of the valve leaflet was most likely due to the high shear rate of fluid near the surface.

The variability of velocities measured at any one point within one time phase can be due to three factors: (1) the natural unsteady flow physics occurring in the valve, leading to a significant spread of measured velocities; (2) the variability of valve leaflet location with respect to the LDV probe, which leads to slightly different measured velocities at different cardiac cycles; and (3) the fact that the LDV measurement volume was focused at a location with high shear rate, such that one end of the 126 micron length measurement volume, velocities are much lower than those at the other end, thus resulting in a spread of measured velocity magnitudes.

Since the leaflet location variability study showed that the valve leaflets had repeatable locations from one cycle to the next, the variability in the location of the valve leaflet is unlikely to be the main cause of the spread in the measured velocities. On the aortic side of the valve leaflet, within the sinus space, PIV measurements have shown that velocities can vary significantly from one cycle to the next, most likely because the sinus vortex is a secondary flow feature induced by the forward flow. Thus the measured velocity variability most likely caused by the physical phenomenon of significant

velocity variability occurring in the AV sinuses. Finally, the high variability of velocities measured near the ventricular surface of the valve leaflet was most likely due to the high shear rate of fluid near the surface.

7.1.2 Advantages of *In Vitro* Shear Stress Measurement

The shear stress methodology design solution was chosen to be an *in vitro* one, associated with the use of appropriate *in vitro* valve models and *in vitro* flow loop. The decision for such an approach is partially explained in the introduction sections 2.3.2 and 2.3.3. The alternative methods of using non-invasive *in vivo* scans with MRI and echocardiography to estimate AV shear stresses cannot be established, due to the low temporal and spatial resolution of these techniques. Even though some authors have presented data on wall shear stress of vessels, the lack of sufficient resolution brings up the question of whether these measurements provided sufficient accuracy. The typical spatial resolution of echocardiography is 0.5 – 1.5 mm, and the typical temporal resolution is 50 Hz, or even lower in the 3D mode. The typical spatial resolution of MRI is 0.5 - 1 mm. From the experimental work performed in this thesis, it can be shown that these resolutions will have extensive errors. This can be demonstrated with a typical flow profile near the aortic surface of the valve leaflet surface during mid-late systole, shown in figure 7-1a. With a resolution of 89 microns, shear rate was 312 s^{-1}. With the resolution of 500 microns, however, shear rate would have been measured to be 214 s^{-1} (figure 7-1b), which would have been an error of 31%. For errors to be within 5%, a spatial resolution of 250 microns or better would be necessary.

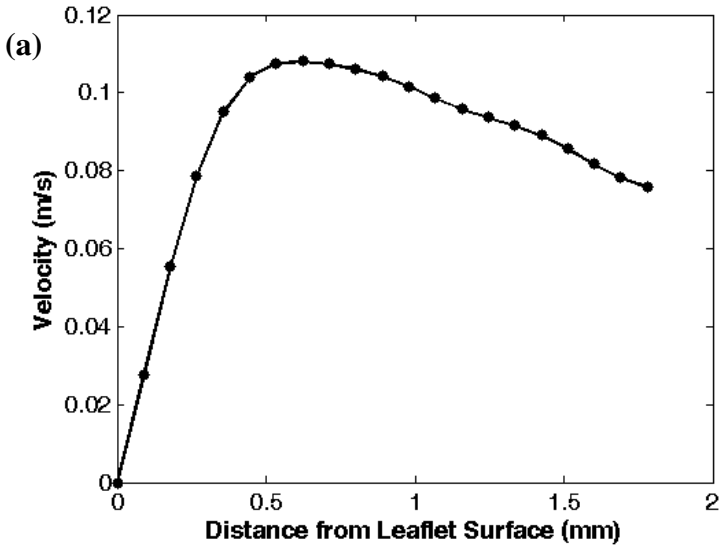

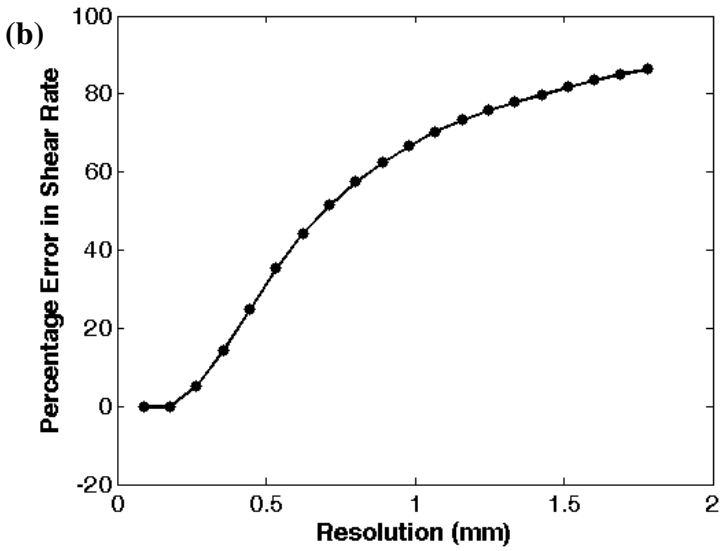

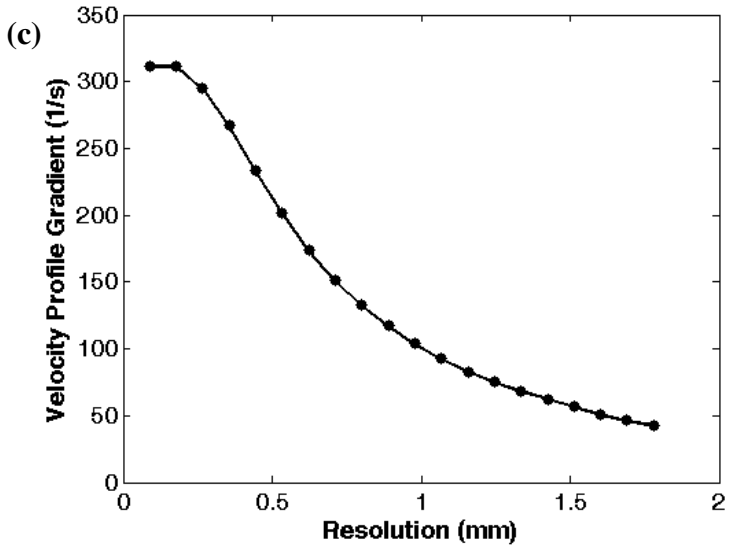

Figure 7-1. *(a) a typical streamwise velocity profile near the surface of the aortic surface of the AV leaflet; (b) shear stresses that would have been measured with the adoption of the various spatial resolution in the x-axis, based on the flow profile in (a); and (c) the percentage error that would have resulted at these various spatial resolution.*

In terms of temporal resolution, the chosen *in vitro* approach allowed a superior temporal resolution of 200 Hz or even higher, and allowed the evolution of shear stress over time to be elucidated.

With the MRI, difficulties can exist in locating the valve leaflet, due to high noise to signal ratio, providing an additional level of problems. In echocardiography, a similar noise problem exists for Color Doppler measurements, making the quantification of velocity gradient difficult. Further, Color Doppler measurements only yield one-component velocities, and with probe-misalignment, can yield large errors.

The choice of the *in vitro* approach to obtaining shear stress data was made also due to the lack of data in the literature in this regards. As discussed in section 2.3.2, although hot film anemometry and LDV has been well used to elucidate large scale biological

flows, there has been no data on the dynamic fluid shear stresses experienced by the AV leaflets. The only study performed in this regards by Weston et al. [42] did not provide sufficiently realistic data since experiments were performed with steady flows, and did not provide shear stresses on the aortic surface. Data provided by the current study can complement the existing body of literature on simulation work investigating shear stresses on the AV leaflet.

7.1.3 Stability of Leaflet Motions of Valve Models

Consequent to the *in vitro* approach, the use of valves models were necessary. These valve models have physiologic leaflet dynamics. In the leaflet tracking results (figure 6-24, 6-32 and 6-44), leaflet dynamics data indicated that in the native valve modes (both tricuspid and bicuspid), the leaflets remained mostly non-dynamic when fully opened or fully closed, but have high velocities during the closing and openings phases. Leyh et al. [35] provided *in vivo* echocardiographic evidence that the AV leaflets behaved similar to these valve models, with rapid opening and closing motions but mostly slow-moving during most of systole, as shown in figure 7-2. The stability of the leaflets motion of the valve models was important because it enabled the *in vitro* shear stress measurement by minimizing measurement errors. In the current study, at all times when shear stresses were measured and calculated, the valve model leaflets were slow-moving. For the polymeric valve, leaflet motions exhibited some oscillations immediately after valve closure, due to the design of the valve. However, since only systolic shear stresses were measured using these valves, the leaflet unsteadiness after valve closure did not affect the shear stress measurements.

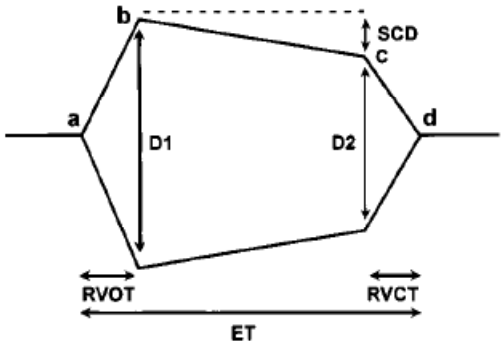

Figure 7-2. *Schematic drawing of measured aortic valve opening and closing characteristics of 3 distinct phases: a-b, rapid valve opening; b-c, slow systolic closure; and c-d, rapid valve closing movement. RVOT indicates rapid valve opening time; ET, ejection time; SCD, slow closing displacement; and D2, leaflet displacement before rapid valve closing. Adapted from [35].*

7.1.4 Validation of the Leaflet Position Tracking Method

The position tracking method was validated in two different experiments, and results were described in section 6.1.2. The first experiment, which involved the measurement of back-scattered light intensity in the close vicinity of the valve leaflet surface, was a demonstration that back-scattered light intensity varied with position around the valve leaflet. It was thus possible to distinguish locations with respect to the valve leaflet using the back-scattered light intensity alone. Since this experiment cannot prove that the same method will work in the dynamic environment, the second experiment, which involved the measurement of the position of a sinusoidally moving piston head, was performed. In the second experiment, the excellent match between the piston head location as measured by the back-scattered light position tracking method and by the position sensor of the

piston pump showed that the back-scattered light method worked even in the dynamic environment. A small delay was observed between the two outputs: the position sensor output was about 4 ms delayed from the back-scattered light method output, and as demonstrated, the errors between the two output was drastically reduced when the 4 ms delay was corrected. One possible explanation for the existence of this delay was that filtering electronics in the position sensor system delayed its output. None-the-less, the piston head position waveform outputs from the two methods matched very well in terms of their shapes and magnitudes.

The back scattered light intensity technique could effectively measure the location of the valve leaflet because of the repeated nature of the motion of the valve leaflet. The technique provided ensemble average reflected light intensity, which would have good signals only if the motion of the valve leaflet was repeated. Random noise of back-scattered light intensity spikes were observed frequently in the back-scattered light data, due to the presence of particles within the flow. However, the averaging over a number of cardiac cycles removed these noise spikes.

7.1.5 Validation of Velocity Measurements Near the Valve Leaflet

Measurements in the first and second flow loops, which were steady flow loops, showed that the use of LDV near a biological tissue would not lead to errors, such that the velocities measured near the valve leaflet would be reliable and could be used for shear stress computations.

Measurements in the first flow loop had good agreement with Poiseuille's law, having a parabolic profile in the near wall region, and obeying the no-slip boundary condition. This suggested that the reflection of the laser light off the surface of the valve

leaflet did not affect measurements, as was evident in the velocities matching theoretical ones. Also, the location of the highest back-scattered light intensity matched that of no-slip point. Since the highest back-scattered light intensity was validated to be the location of the valve leaflet surface, this observation provided further confidence that the correct velocities were measured. These observations were corroborated by measurements in the second flow loop, which also showed that the no-slip boundary condition could be observed at the point of the highest back-scattered light intensity.

The tabulation of standard deviation of velocity measurements provided an estimation of the variability of velocity measurements. The occurrence of variations in velocity measurements could be explained by variations associated with noise recorded by the LDV measurement technique as well as actual variations in the true velocities. Variations encountered in the first and second flow loops with the steady flow were attributable mostly to noise recorded by the LDV technique and system, since care was taken to keep velocities variations in this loop to the minimal. The baseline variability of flow measurements due to noise was found to be 0.014 m/s to 0.026 m/s in the steady flow loops.

In the pulsatile loop, a range of measured velocity variability was observed, indicating that on top of the baseline variability due to the LDV system, variability in flow was also present, in addition to the baseline variability. The minimum variability observed in the pulsatile experiments was approximately 0.2 m/s, and which occurred during early systole and late diastole. This minimum variability was similar in order of magnitude to the baseline variability observed in the steady flow loops. Indicating that the baseline noise level of the LDV system had not changed between these experiments,

and further suggesting that variability observed in excess of this baseline level were due to variability of flow. Between different measurement locations and between different hemodynamic conditions, similar patterns of the levels of velocity variability could be consistently observed, for example, variability of flow increased from early systole to mid systole, most likely due to the unsteadiness of flow during the induction of the sinus vortex; and for example, variability of flow tended to be higher during late systole and early diastole. This could be explained as such: adverse pressure gradient decelerated flow during this period, resulting in flow reversal, fluid mixing, and fluid hammer against the closing valve, thus causing excessive variability in flow.

Close inspection would yield the observation that high standard deviations were not necessarily associated with high velocity, and this further showed that this variability is not due to the noise generated by the measurement system, and can be interpreted as a flow unsteadiness measure. Given this understanding, we can properly characterize variability of flow measured by subtracting the observed variability of velocities with the baseline variability of measurements established using a stable, steady flow loop.

The squared cosine correction of shear stresses to be in the orientation of the leaflet from the orientation of the LDV probe was demonstrated to be feasible, yielding errors of less than 3%, with the analysis in section 6.1.6. The analysis showed that in cases where the radial velocity component (or the velocity component impinging onto the leaflet surface) was small, the percentage errors in measurements due to the orientation misalignment were small. In the aortic valve, it is qualitatively conceivable that the flow near the center of the valve leaflet aortic surface would be approximately parallel to the leaflet surface, having small impinging velocity component. This is because flow in the

sinus has been observed to take the form of a single vortex in each sinus in previous *in vitro* [31] and *in vivo* work [34], and not as wall-impinging jets. Further, the results in the current study had shown that the out-of-plane leaflet motions were small compared to in-plane fluid velocities, and thus flows very near to the surface of the valve should be dominated by in-plane velocity components and had small out-of-plane velocity components. It could thus be argued that there were minimal wall impinging / radial velocity components in flows near the valve leaflet, and that the squared cosine angle correction algorithm to measured shear stresses would have small errors. This was especially so because the angle difference between leaflet surface and the probe alignment was kept small whenever shear stress was computed: less than 0.15 radians or 4.3 degrees.

7.1.6 The Use of LDV as Opposed to Other *In Vitro* Techniques

The use of LDV in the current study stems from difficulties with using other *in vitro* techniques for these measurements. A very popular alternative to LDV is PIV, which involves illuminating a plane of interest with a laser sheet within the flow body, and photo-imaging particles illuminated by the laser to track their motion. PIV allows measurement of velocities in an entire field of view within an instance, distinguishing it from LDV's ability to measure only one velocity at one point within the same instance. However, LDV enjoyed superior spatial resolution than conventional PIV and is thus more suitable for measurements of shear stresses, where a high resolution is demanded. Also, scattering of laser light from the tissue makes surface velocity measurements using PIV very challenging, because the regions close to the valve leaflet on PIV images will

be saturated with light, making velocity computation difficult. Further, this scattering of light can result in particles outside the laser sheet layer being illuminated, causing errors in velocity computations.

The other *in vitro* alternative to LDV is the use of hot film anemometry, where a hot film is attached to the leaflet surface, and the rate of heat transferred from the film to flow moving past the surface of the leaflet can be calibrated to measure shear stresses. This technique holds the promise of measuring shear stresses during rapid valve motion, which is impossible with the LDV technique in the current study. However, hot film anemometry requires in situ calibration to be accurate, which is difficult to achieve with the complex aortic valve geometry. Further, the wires attached to the hot film may alter flow fields and alter valve motion.

The proposed experimental measurement technique of fluid shear stresses experienced by the aortic valve leaflet can supplement computational modeling work to achieve comprehensive understanding of the shear stress environment of the aortic valve leaflets, and can act as a validation tool for simulations.

7.2 Aortic Surface Shear Stress Characteristics

In specific aim 2, general shear stress characteristics on the aortic surface of the valve leaflet, as well as the effects of flow rate and heart rate on the shear stresses were measured.

7.2.1 The Role of the Sinus Vortex in Aortic Surface Shear Stress

The general aortic surface shear stress characteristics described in the section 6.2 can be explained by the interaction between sinus flow and valve leaflets. Sinus vortices are induced by the interaction between forward flow and fluid in the sinus volume. Once induced, the sinus vortices appeared to be the main cause of aortic surface shear stresses elevation during systole. These vortices were first described by Bellhouse et al. [31] using experimental data and theoretical modeling. It has also been studied in a number of *in vitro* investigations [121, 122], and more recently, was measured in humans using phase contrast magnetic resonance imaging [34].

In the current study, sinus vortex flow was detected in the form of adjacent columns of fluid moving in opposite directions, developing during mid to late systole. Vortices could be detected in both the streamwise direction and the non-streamwise direction. For example, in figure 6-27a, fluid near to the 10 mm radial location were positive, but fluid at the 12 mm radial location were negative between the 200-300 ms time period, demonstrating a vortex with streamwise velocity components. In figure 6.27b, negative fluid velocities were found near to 10mm location but positive fluid velocities were found near the 12 mm radial location, during the 300-400 ms time period. It could be speculated that the vortical flow in the sinus evolved in direction through the course of systole, most likely depending on the geometry of the valve. The LDV measurements in the current study, however, were only in two directions, and did not include radial velocity components. Thus the elucidation of the true nature of the vortices that may be found in the sinuses could not be performed. Results shown with PIV, as shown in figure 6-43, however, could demonstrate the presence of vortical flow in the sinus in both the normal

tricuspid aortic valve and the bicuspid aortic valve. The enlarged figures of flow vector field at the late systole time point is shown here again (figure 7-3). Given that the geometry of the sinus was that of an ellipsoid, flows in the sinus would most likely be vortical in nature. Further, it is interesting to note that these vortical flows evolved over time, and is a worthy subject of a separate, more detailed fluid mechanics investigation.

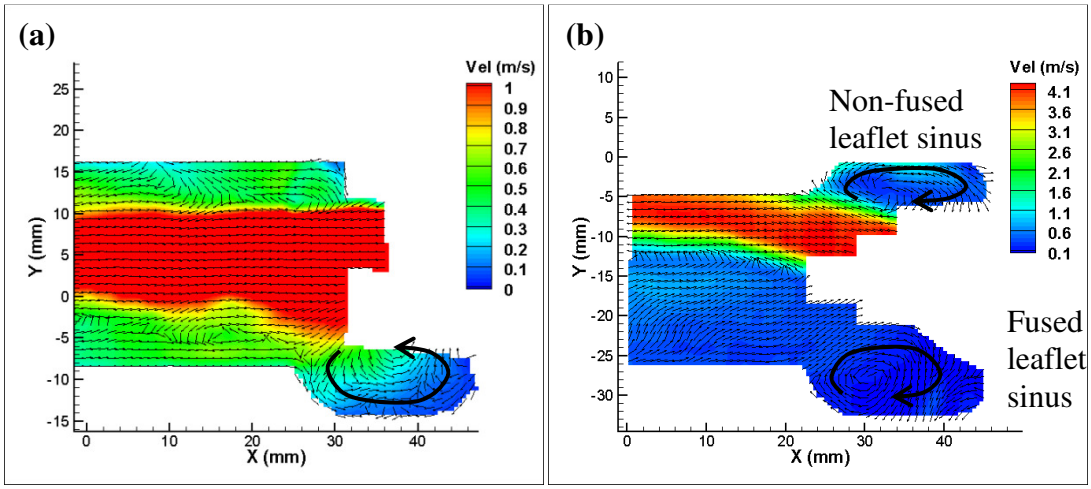

Figure 7-3. *Velocity vector fields within the sinus and downstream of (a) the normal tricuspid aortic valve and (b) the bicuspid aortic valve. The BAV fused leaflet sinus is at the bottom, while the non-fused leaflet sinus is at the top. Vortical flow could be observed in the sinus, as indicated by the schematic curved arrows.*

The interaction between the forward flow and fluid in the sinus can vary based on the opening angle of the valve. If the leaflet at peak systole opens into the sinus region, a portion of the forward jet directly enters the sinus, forming a sinus vortex due to the curvature of the sinus walls (figure 7-4b). In this case, there will be little delay between the peak flow and peak aortic shear stress. On the other hand, if the leaflet opening angle is smaller than 90°, the sinus vortex is formed due to entrainment of the quiescent sinus flow by the stronger forward jet, where the forward flow jet induces sinus flow by drag

forces (figure 7-4a). This results in a larger delay in peak shear stresses after the peak flow.

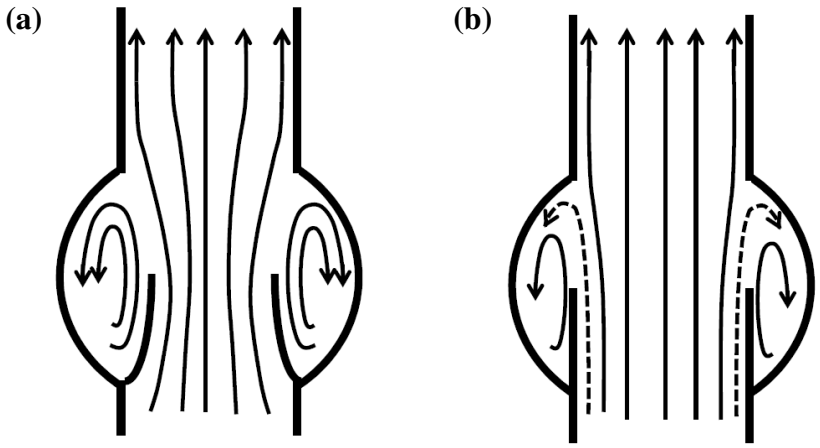

Figure 7-4. *Schematic of possible mechanism of sinus vortex induction. (A) Sinus vortex is induced by shear forces of the adjacent forward flow jet. (B) Sinus vortex is induced by part of the forward flow entering the sinus after encountering the sinotubular junction.*

The 90 beats/min, 55 ml stroke volume case most likely represented the case in figure 7-4a during early systole. Leaflet tracking (figure 6-32c) showed that the valve leaflet moved further out towards the sinus wall than the other heart rate conditions during early systole (between 100 ms to 150 ms time period in figure 6-32c). For the remaining duration of systole, the valve leaflet was closer to the center of the valve. Shear stresses results showed that there were differences in the shear stress waveform of this 90 beats/min high heart rate condition from that of the other slower heart rate conditions, as will be discussed in details in the following sections. It could be speculated the difference in shear stress waveform was due to the aberrant leaflet dynamics. Thus, in the current study, the sinus vortex characteristics could be said to be a function of leaflet dynamics.

Data in the current study also suggested that the sinus flows were strongly influenced by valve hemodynamics, and by valve and sinus geometries, as will be explained in the coming sections.

For all the other hemodynamic cases tested in this study (shear stresses shown in figure 6-30, 6-33 and 6-34), the sinus flow were most likely induced with the mechanism described by figure 7-4a. This is because the systolic shear stress elevation was delayed from the onset of systole, indicating that forward flow was not directly entering the sinus to drive flow, but is inducing sinus flow through drag forces, resulting in a delayed formation of sinus vortex causing the delay in shear stress elevation.

After peak flow during mid systole, the driving force for the sinus vortex decreased as forward flow decelerated. Flow in the sinus most likely decreased in magnitude due to viscous dissipative forces, thus leading to smaller velocities and thus weaker shear stresses, leading to shear stresses decreasing to zero at the end of systole.

7.2.2 Aortic Surface Shear Stress Over the Cardiac Cycle

Shear stresses result in figure 6-30 demonstrated the general aortic shear stress characteristics over the cardiac cycle. The slight elevation in shear stress during early systole was most likely the result of flow in the sinus caused by the leaflet opening motion. This elevation was observed immediately after the end of the rapid leaflet opening motion. Thereafter, shear stress magnitude decreased as the sinus flow that was excited by leaflet opening motion was dissipated. At mid-systole, the formation of the sinus vortical flow in the stream-wise direction resulted in elevation of stream-wise shear stress to its peak. Thus the shear stresses shown in figure 6-30 belonged to the case (a) of

figure 7-4. This elevation in shear stress occurred only during mid-systole because it took substantial amount of time for the forward flow to induce the sinus vortical flow, which exhibited sufficient velocity only during mid-systole. The vortex, however, shifted in orientation during late systole, most likely due to the geometry of the valve leaflet, which caused a substantial elevation in non-stream-wise shear stress as well as a reduction in stream-wise shear stress on the leaflet. During late systole, as the leaflet started to move towards the centerline of the valve, shear stresses in both directions decreased.

Flow reversed under the adverse pressure gradient during late systole, resulting in fluid mixing. Subsequently, rapid closing motion of valve and fluid hammer on the valve causes further fluid mixing. These phenomena resulted in remnant fluid motion distal to the valve, which dissipated over the diastolic duration through viscous interactions. This could explain the characteristics of diastolic shear stress demonstrated in figure 6-30: a gradual decrease to zero. Nearing end diastole, however, ventricular contraction brought about reduction in transvalvular pressure, leading to minor motion of the valve before rapid valve opening, which led to small elevation of shear stresses. Diastolic shear stresses were observed to be small compared to systolic shear stresses.

The results showed that shear stresses on the surface of the valve had a significant non-streamwise component. The measurements showed that flow in the sinus could have significant non-streamwise components. This could be due to the non-symmetric geometry of the valve, which resulted in lateral bias to the sinus vortex. With the natural variations of geometries *in vivo*, aortic valves are unlikely to be perfectly symmetric, and as such, lateral biases similar to those observed in the current study would be expected. It is noteworthy that the peak shear stresses found in the current study were in vicinity of 18

– 20 dyn/cm2, which had a general order of magnitude match with the results from a previous simulation study by Ge et al. [43].

Discrepancies, however, can be found between the current study and that of Weinberg et al.'s study [46]. Weinberg et al reported, through their simulations that the magnitude of shear stresses on the aortic to be approximately between +2 dyn/cm^2 and -2 dyn/cm^2, which is about one order of magnitude smaller than that observed in the current study. The difference could be attributed to the length of the valve leaflet with regards to the aortic sinus height. In Weinberg et al.'s simulation, the valve leaflet appeared to be sufficiently long such that during the opened phase, it covered the entire entry to the sinus volumes. Without the interaction between forward flow and the sinus volume, shear stresses resulting from the simulation would naturally be very small. This differed from the current study, where sufficient space was allowed for this interaction. The geometry used by Weinberg's simulation thus did not exactly agreed with Swanson's measurements of aortic valve dimensions, where the distance between the tip of the aortic valve leaflet when opened and the sinotubular junction was measured to be about 0.2 times the annulus diameter. Further, it appeared that sinus vortices were not observable in Weinberg's simulations, indicating a discrepancy between their simulations and clinical measurements performed by Markl et al. [34], who reported sinus vortex flow from MRI measurements.

7.2.3 Effects of Heart Rate and Stroke Volume and Leaflet Dynamics

From the results of section 6.2.2, shear stress characteristics were observed to be a function of heart rate, stroke volume, and leaflet dynamics. Increased stroke volume was observed to increase systolic shear stresses. This is expected because a larger stroke

volume will result in increased bulk forward flow rate, which will induce stronger sinus vortices, resulting in higher shear stresses. Indeed a review of the velocity magnitudes measured in the sinuses for the different stroke volume conditions showed that with higher stroke volume, higher sinus flow velocities were found ().

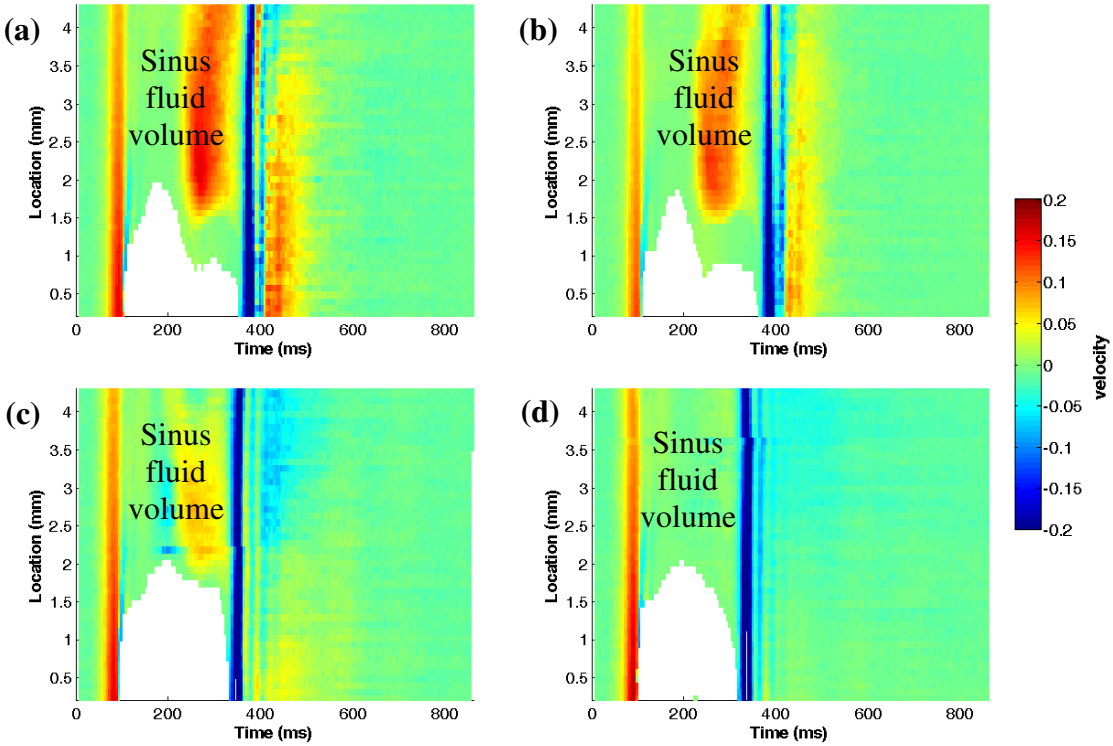

Figure 7-5. *Streamwise velocity magnitudes in the vicinity of the tricuspid aortic valve leaflet systolic position, for the various stroke volume cases (a, 68 ml; b, 62ml; c, 43ml; d, 27ml) at the same heart rate of 70 beats/min. Systole was between 100 and 380 ms. The location axis indicate radial distance along the measurement line, with the smaller number being nearer to the center of the valve. These plots demonstrate that sinus flow velocities increases with stroke volume.*

On the other hand, increased heart rate led to decrease in average systolic shear stress. This can be explained by the reduction in systolic duration with higher heart rate, resulting in insufficient time for high velocities to be induced in the sinus by bulk forward flow, and consequently reduced shear stress on the valve leaflet. Increased heart

rate at the same stroke volume implied that bulk forward flow rates are higher, since the same amount of fluid must move through the valve within a shorter period of time. This increase in forward flow rate was favorable to shear stress magnitude, but overall, shear stresses still decreased due to reduced systolic duration.

At 90 beats/min, the valve leaflet was observed to have slightly different dynamics than the cases with lower heart rates: the valve leaflet opened further during early systole (between 100 ms and 160 ms) than the other heart rate cases, but was nearer to the center of the valve for the rest of systole (figure 6-32c). Further, bulk forward flow was higher than the other heart rates during early systole (between 100 ms and 220 ms) but lower in late systole. This initial wider leaflet opening and higher bulk forward flow rate during early systole are most likely the reason for early systolic elevation of shear stress magnitudes (both in the positive and negative direction) compared to those observed in the other heart rate cases, as explained in section 7.3.2. The valve leaflet could have allowed fluid from the forward flow to move directly into the sinus space by opening wider, according to the mechanism described by figure 7-4b, thus providing higher driving force for flow in the sinus, as opposed to relying on the mechanism described by figure 7-4a, which would have taken time for forward flow to induce sinus flow through drag interaction.

The narrower leaflet opening and lower bulk forward flow rates during late systole (between 220 ms and 370 ms time points) are most likely the reason for the late systolic reduction of shear stresses compared to those observed at the other heart rates. Immediately after leaflet opening, a small negative shear stress peak was observed for all the heart rate and flow rate conditions. This is mostly likely associated with the inertia of

valve opening. At the 90 beats/min condition, the valve leaflet was more dynamic during the opening phase, so the initial negative shear stress peak was more prominent.

7.2.4 Variability of Shear Stresses over Systole

In the current study, the variability of shear stresses experienced by the AV can be presented as the standard deviation of shear stresses measured on the AV. Figure 6-35 demonstrate the output from such a calculation. From these results, it could be observed that the variability of shear stress was different at different time points during systole. In general, higher shear stress variability was observed during mid- to late-systole. This is likely because peak flow occurred during about mid systole, and this increased flow velocities were associated with increased unsteadiness. During late systole, adverse pressure gradient occurred across the valve as the ventricle is at the end of its contraction stroke. This adverse pressure gradient act to decelerate forward flow during end-systole, and can result in excessive mixing of fluid downstream of the valve and in the sinus volume, which can result in unsteadiness, leading to increased variability in the shear stress experienced by the valve leaflets. At adult resting hemodynamics, the variability of shear stresses in the tricuspid aortic valve was small, with a two-standard-deviation width of about 2.5 dyn/cm^2. This indicates that there was high repeatability in the shear stress waveform from one cardiac cycle to the next.

The levels of shear stress variability across different hemodynamic conditions could also be investigated. Comparing the width of shear stress standard deviation bounds in figures 6-35 across different hemodynamic conditions, we can observe that increasing stroke volume appeared to reduce variability of shear stresses. This could be because

increased stroke volume led to more stable sinus vortex flows. Increasing heart rate, on the other hand, appears to increase variability of shear stresses. At the highest heart rate condition, shear stress unsteadiness was no longer confined to late systole, but also mid systole and the later periods of early systole. This unsteadiness could be a result of altered leaflets dynamics in the higher heart rate conditions.

7.3 Ventricular Surface Shear Stress Characteristics

7.3.1 General Characteristics

In the measured and simulated results of the ventricular surface shear stresses in section 6.2.1.1.5 and section 6.2.1.2.1 (figure 6-18), systolic shear stresses were observed to have a "single-hump" shape or half-sinusoid shape. These shear stresses were observed to peak between 64 dyn/cm^2 to 91 dyn/cm^2. The order of magnitude of these measurements agree with those in the simulations performed by Ge et al. [43], and Weinberg et al [46], who observed peak ventricular shear stresses of approximately 70 dyn/cm^2 and 38 dyn/cm^2. The shape of the shear stress waveforms have a resemblance to the volumetric flow curve, which is not surprising, since ventricular surface shear stress was directly caused by forward flow, and since a theoretical relationship between the volumetric flow curve and shear stresses could be derived, as presented in section 6.2.1.2. The deviations between the shape of the volumetric flow waveform and the shear stress waveform can be explained by flow development and is discussed in section 7.4.3.

In the shear stress waveform measured with the *in vitro* valve models (figure 6-18), a shear stress spike was observed during early systole, shortly after the period of rapid valve opening motion. This shear stress spike peaked at about 50-60 dyn/cm^2, which has peak shear stress magnitude at mid-systole. This shear stress spike peak was most likely

caused by the snapping motion of the valve leaflet upon fully opening, which caused a temporarily disturbance in the flow. The flow curve reflected a similar disturbance during this time point, as can be observed from the interruption in the smoothly increasing flow curve during early systole.

In both measured and simulated results, reverse shear stresses were observed during late systole, even before the volumetric flow rate decreased to zero. Flow profile results (figures 6-17 and 6-19) showed that this was caused by reversal of flow immediate adjacent to the valve leaflet ventricular surface while overall forward flow was still positive. This observation is consistent with the Womersley solution of pulsatile pipe flow [123]. Thus, we are compelled to conclude that *in vivo* ventricular surface shear stress most likely exhibited the same reversal in direction during late systole, instead of having the conventionally accepted half-sinusoid shape.

7.3.2 Theoretical Solution for Ventricular Surface Shear Stress

The lack of satisfactory techniques to measure ventricular surface shear stresses dictates the need for theoretical or empirical solutions for these quantities. A theoretical framework based on the Womersley solution for pulsatile flow is described in specific aim 2 (section 6.2.1.2), and was validated using LDV measurements in an optically clear polymeric valve. This theoretical framework allows one to reasonably estimate ventricular surface shear stresses based on volumetric flow rates, allowing its application to clinical scenario, where volumetric flow rates can be obtained by non-invasive scans. We demonstrate this based on two clinical datasets obtained from the literature in section 6.2.1.2.2.

The theoretical model of ventricular surface shear stress requires inputs in the form of valve size, and volumetric flow waveform over the cardiac cycle, and corrections to computed shear stresses can be made if the valve opening angle deviates from 90^{o}. Values of AV opening angles can be obtained with echocardiography, which is routinely performed as standard of care. Information on the systolic AV orifice dimension can also be obtained through the same means, or from MRI scans. Bulk flow rates through the valve can be obtained through PC-MRI evaluation of the ascending aorta, or through echocardiographic evaluation of ventricular volumes. Thus the method of calculating the ventricular surface shear stress using the Womersley solution is highly feasible on human subjects. This method holds the advantage of being much less computationally intensive than full Fluid-Structure-Interaction simulations, and shear stresses can be calculated with relative ease.

However, it must be noted that several assumptions were made in the formulation of the theoretical model, such as sufficient development length for similarity of profiles along axial direction, and such as the round shape of the open valve geometry, and the absence of the sinus space. The calculations using the theoretical model must thus be limited to an order of magnitude analysis for in vivo ventricular surface shear stress, and to be a back-of-the-envelope analysis of the characteristics expected in the in vivo conditions.

7.3.3 Determinants of Ventricular Surface Shear Stress

The ventricular surface shear stress results from specific aim 2 demonstrate that flow on the ventricular surface of the AV leaflet is constantly developing, since the out-of-

plane gradient of the normalized streamwise velocity profile decreases and the boundary layer thickness increases over systole. In the ventricular surface shear stress results presented in section 6.2.1, the instantaneous shear stress (τ) through systole is dictated by two opposing forces. On one hand, an increase in Q results in increased τ due to an increase in velocity gradient at the wall. Conversely, flow development reduces the velocity gradient at the wall and thus reduces τ. It is noted that the fully developed parabolic flow profile was never observed, indicating that forward flow was never fully developed within the short systolic duration. Thus steady flow experiments [42] or fully developed numerical models cannot capture these unsteady changes in flow, and are incapable of accurately predicting instantaneous shear stresses τ.

The observed ventricular surface shear stress was a combination of these two effects and was demonstrated in the experimental and numerical results from the theoretical simulation. This was particularly demonstrated in two situations (with reference to figure 6-18a): (1) during early systole, the rate of change of shear stress ($d\tau/dt$) matches the rate of change of volumetric flow rate (dQ/dt). At peak systole, ($d\tau/dt$) lagged (dQ/dt) due to flow development. Since flow development occurred over time, it led to the accumulation of shear stress deficit over time, ensuring that shear stress gradually became less responsive to bulk flow rate increases; (2) peak shear stress occurred 30-55 ms before peak flow rate, which can be explained by flow development, which caused more shear stress reduction than increasing bulk flow could cause shear stress elevation within the 30-55 ms interval.

A comparison of the experimentally measured shear stresses to results from the theoretical modeling showed the effect of the opening angle of the valve. The two

polymeric valves used in the current study had slightly convergent opening angles, whereas the numerical simulations were conducted in straight tubes. A more convergent leaflet opening angle provided a more favorable pressure gradient, which led to thinner boundary layers and reduced flow development. The time lag between peak shear stress and peak volumetric flow rate was shorter in the experimental results than in the simulation results, indicating that the taper of the leaflet opening angle in the experiments reduced flow development. Further, during late systole, favorable pressure gradient due to the taper in the valves resulted in delayed flow reversal near the leaflet surface, leading to delayed reversal of shear stress. This could also explain the lower magnitude of negative shear stresses found in the experimental results than in the shear stress results calculated with the theoretical model using the same *in vitro* flow curves.

The effects of a convergent opening angle on shear stress was more clearly presented in figure 6-20, which showed the differences in shear stresses between the experiments (tapered valves) and the corresponding simulations (straight tube). During early systole, this difference was near zero, and it gradually increased to the end systolic value of approximately 40 dyn/cm^2. The curves for the two valves look similar to each other. Native valves have natural variations in valve opening angles ranging from 75^o (convergent) to 110^o (divergent) [124]. The polymeric valves used in the current study were on the convergent extreme of this spectrum, having opening angles of 72.1^o and 77.4^o. The small difference in opening angle between the two valves most likely explained the difficulty in discerning a difference in the two curves in figure 6-20. However, these results illustrated the effect of opening angle on the actual shear stresses, and can be used to provide a correction to Womersley solutions calculated using *in vivo*

flow rates. Shear stresses obtained from *in vivo* flow rates will be underestimated if the valves have opening angle less than 90^o, and overestimated if the valves have opening angle greater than 90^o. Most valves, however, were reported to be parallel or close to parallel, thus the Womersley solutions are likely close to the true shear stresses and need minimal correction.

7.4 Comparison of Shear Stresses on the Two Surfaces

The comparison of shear stresses on the two surfaces of the aortic valve leaflet is of interest because of the clinical observation that aortic valve calcification nodules are found exclusively on the aortic surface, leading to hypothesis that the differential shear stress environment on both sides has led to pathological responses on the aortic surface that led to calcification. The data from the results section showed that the ventricular surface shear stress differed from the aortic surface shear stresses in the following ways:

(1) Ventricular surface shear stresses were about 3-4 times higher in magnitude than those on the aortic surface. Peak ventricular shear stresses were measured or calculated to be 64 to 91 dyn/cm2, but the maximum shear stress on the tricuspid aortic valve leaflet was 19 dyn/cm2. In cases of lower stroke volume or higher heart rate, aortic surface shear stresses were even slower.

(2) Ventricular surface shear stress reversed in direction to a significant magnitude for a significant duration, while that on the aortic surface did not. If flow reversal was present on the aortic surface, it was usually during diastole, and the shear stress magnitudes were small.

(3) During systole, the aortic surface shear stress waveform was skewed towards late systole in most cases, whereas ventricular surface shear stress waveform was skewed towards early systole. The reason for the skewedness in the aortic surface shear stresses was because of the delay in the development of the sinus vortex from the onset of systole. Aortic surface shear stress was elevated only when the sinus vortex formed. As for the ventricular surface shear stresses, gradual flow development over the entire duration of systole resulted in some gradual reduction in shear stress, resulting in late systolic shear stress being lower than early systolic shear stress, and creating a shape that skewed towards early systole.

In both the aortic and ventricular surface shear stresses, however, one commonality was that both shear stresses were higher during systole than diastole. Forward flow was the driving force for shear stresses on both sides of the valve leaflet.

The current study has shown that there are distinct differences in the shear stress waveforms experienced by both sides of the valve leaflet, substantiating the possibility that the preferential development of calcification nodules on the aortic surface might be because of different mechanical environment on both sides. There is, however, literature on alternative explanations. Simmons et al. [98] described differences in the phonotype of endothelial cells found on the two surfaces of the aortic valve leaflet, and speculated that this phenotype difference could be contributing to this specific localization pattern of calcium nodules. Nonetheless, Simmons et al. acknowledged that the aortic valve endothelium is subjected to distinctly different fluid dynamics on either side of the leaflet, which may be contributing to the differential endothelial phenotype on either side to define sidedness. This notion tied back to the importance of the biomechanical

environment of both sides of the valve leaflet. Guerraty et al. [125], on the hand, found that only the aortic surface (and not the ventricular surface) expressed ALCAM surface proteins when exposed to hypercholesterolemia, adding to the literature of differences between cellular phenotype on both sides of the leaflet.

The question of whether shear stress environment or biological factors are responsible for this calcium localization pattern is an important one, to answer to which might inspire new therapies for AV disease. Further studies on this topic are warranted.

7.5 Shear Stresses in the Bicuspid Aortic Valve

7.5.1 The Bicuspid Aortic Valve Model

The current BAV model was modeled to be representative of the most common BAV morphology: the fused leaflet covered between two thirds and half of the valve area [65]; the fused leaflet had restricted motion, and blocked flow even in the fully open position [76], and forward flow was skewed away from the fused leaflet sinus [69]. The BAV valve model had a peak flow Reynolds number of 12,400, while that of the normal aortic valve model had a peak flow Reynolds number of 7800. This indicated that the downstream flow fields of the valves were most likely turbulent, and thus the velocity and pressure field in these flow fields had high variability. The turbulence intensity was most likely a function of the valve area. A smaller valve area would lead to higher velocities to maintain the same cardiac output and thus increased the chance for turbulence or increased the intensity of the turbulence. The turbulence intensity was most likely higher in the BAV model due to higher Reynolds number, and because the flow in the BAV impinged on the aortic wall.

Patients with BAVs and severe stenosis undergo balloon valvuloplasty during a young age, followed by surgical valvuloplasty in some cases, and thus BAVs with high pressure gradients are rarely left alone (without intervention) to reach older ages. Clinically observed calcified BAVs at advanced ages would thus most likely come from the lower gradient cohort of BAV patients. Since the focus of the current study is on the calcification of the BAV in response to its mechanical environment, which would occur during older ages, a low gradient valve model would be more relevant than high gradient valve models. The current valve model had a peak systolic gradient of less than 50 mmHg, and if encountered clinically, would be recommended by AHA guidelines not to undergo valvuloplasty treatment [120], which is suitable for the current study, and which is clinically realistic: it is possible to find patients at a similar level of stenosis who did not have intervention during childhood, and whose valve has calcification lesions.

In the current study, only one BAV model and one BAV geometry was studied. Clinically, BAV comes in a wide range of geometries, including those with three-lobed sinus instead of the two-lobed sinus assumed in the current study [67], and those with central valve orifice and non-eccentric forward flow, instead of the eccentric one in the current study [69]. This one valve model, however, provided important information on how the BAV fluid mechanics could differ from that of a normal tricuspid aortic valve. To truly comprehensively understand the fluid mechanics of the BAV, future works that include a sweep of all possible BAV geometry variations must be performed.

7.5.2 Characteristics of Sinus Flows and Measured Shear Stress

Similar to results from specific aim 2, the shear stresses data obtained in specific aim 3 on the BAV model indicated that aortic surface shear stresses were the outcome of the sinus vortex flow. In both cases, the sinus vortex developed during systole, and dissipated away during diastole after valve closure, due to viscous dissipation. Thus similar to the aortic surface shear stresses in the tricuspid aortic valve, aortic surface shear stresses on the BAV were higher in magnitude during systole than diastole, and peaked at about 200 ms (figure 6-46 and 6-48), approximately the same time as the peak forward flow.

Examination of the velocities measured along a radial line by LDV indicated that the vortices in the two sinuses were of opposite direction. In the normal leaflet sinus, velocities near the sinus wall pointed upstream while velocities near the leaflet pointed downstream. In the fused leaflet sinus, velocities near the sinus wall pointed downstream while velocities near the leaflet pointed upstream. This was the result of a skewed forward flow, which pointed towards the non-fused leaflet sinus, away from the fused sinus. Part of the forward flow, upon colliding with the sinotubular junction of the non-fused leaflet sinus, diverged into the non-fused leaflet sinus, directly fueling the vortex there (figure 7-4b). On the other hand, the vortex in the fused leaflet sinus was a secondary vortex. The forward flow jet drove a primary vortex adjacent to the jet directly downstream of the fused leaflet sinus, which in turns drove the vortex in the fused leaflet sinus, which is in the opposite direction as the first vortex. The result was that the vortex in the fused leaflet sinus was in the opposite direction to that expected in a normal valve, and the fluid shear stresses on this leaflet were opposite in direction (figure 7-3). These observations were supported by the PIV measurements conducted with the same valve,

shown in figure 6-40 and figure 7-3. Further, since the sinus vortex in the fused leaflet sinus was indirectly driven by the forward flow, it took a longer time to form when compared to the sinus in the non-fused leaflet sinus. This explains the delay in the elevation of shear stress on the fused leaflet during systole, as opposed to that in the non-fused leaflet (as can be observed in figure 6-46).

7.5.3 Variability of Shear Stresses

As discussed previously, flow directly downstream of the BAV orifice was most likely turbulent, and impinged onto the aortic wall, resulting in unsteadiness in velocities and pressures. This unsteadiness would be passed on to flow in the sinuses, since the forward flow was the driving force for flow in the sinus. Thus even though flow in the sinuses did not have sufficient velocity to reach turbulence (as demonstrated in figure 6-45), it was very unsteady, as shown in the extensive analysis in section 6.3.4.4. Unsteadiness in flow was most significant during mid-systole as can be observed from the high variability of velocity measurements during this period in both sinuses of the BAV, in comparison with that of the normal tricuspid aortic valve sinus. Being directly driven by the strong and unsteady forward flow jet, velocities in the BAV non-fused leaflet sinus were not only higher than that in the fused leaflet sinus, but also had higher variability.

The one-standard deviation bound analysis (figure 6-49) showed that there was variability in the magnitude of shear stresses during systole. However, it was difficult to discern if this were caused by magnitude variations of shear stress waveform which were smooth over time, or if this were caused by shear stress waveforms which were

fluctuating at high frequency within each cardiac cycle. The power spectrum analysis (figure 6-48) was utilized to discern this. Since the power spectral analysis required temporally sequential data, it could not use shear stresses as inputs, because shear stresses could only be obtained through ensemble averaging. Power spectral analysis was performed, however, on velocities measured very close to the valve leaflets' surface, and thus would have appropriate indication of the characteristics of shear stresses experienced by the valve leaflet surface.

For all cases investigated with the power spectral analysis, the results showed that velocity deviation from ensemble mean had broad band characteristics without any distinctive features at specific frequencies. Nonetheless, power spectrum of fluctuating velocities near the BAV leaflets had higher magnitudes than those near the TAV leaflet, indicating higher levels of velocity unsteadiness near the BAV leaflets, and thus higher levels of unsteadiness of fluid shear stresses experienced by the BAV leaflets. The difference in power spectrum between the BAV and the normal valve was also broad band.

Differences in the power spectra between the two valves were observed in the lower frequency ranges, indicating that unsteadiness of velocities near the BAV leaflet could be explained by cycle-to-cycle magnitude variations. However, there were differences in the power spectra at the higher frequencies (10-30 Hz) between the two valves as well, indicating that some of the velocity variability could be due to high frequency fluctuations about the ensemble mean waveform. Thus the shear stresses experienced by the BAV leaflets most likely had general magnitude variations from one cycle to the next, as well as high frequency fluctuations within each cycle (during systole).

It could be noted that the 10-30 Hz range agreed with studies by Stein et al. [115], who measured flow with hot wire anemometer in humans just distal of the aortic valve, and analyzed the measured velocities for the power spectrum. Stein et al observed that, in both normal and stenotic human aortic valves, there was significant magnitude in the power spectrum at the frequencies of between 10-30 Hz, and there were observable differences between the power spectrum of the normal human valve and the stenotic human valve within this range. This motivated the design of the shear stress waveform shown in figure 5-10c for investigation with the cone and plate in the current thesis, where a 20 Hz oscillation was superimposed onto the ensemble average shear stress waveform of the BAV. This waveform was designed to investigate the effects of high frequency fluctuations in shear stress on aortic valve biology.

In summary, a result of turbulence of the forward flow caused by the stenosis of the BAV, and the skewed forward flow caused by eccentric valve geometry, the flow in the sinus region became much more unsteady than that in the normal tricuspid aortic valve, resulting in both cycle-to-cycle shear stress magnitude variability in shear stresses as well as intra-cycle fluctuating shear stress magnitude variability.

7.6 Mechanobiology Responses of Aortic Valve Leaflet Tissues

Mechanobiology experiments were performed with the cone and plate bioreactor in specific aim 4. This bioreactor was a validated device for exposing aortic valve samples to uniaxial shear stresses [100], and has been previously used to study the responses of porcine aortic valve leaflet tissues to varying shear stress patterns, and it was found that non-native shear stresses can lead to tissue inflammation [5]. The osteogenic media

culture of valve leaflet samples was a validated approach to simulating aortic valve calcification within acute periods by accelerating calcification responses [89]. Whole valve leaflet tissues were found to develop inflammation and form calcium nodules after this osteogenic media culture, similar to early calcification lesion morphology. This was again demonstrated in the Von Kossa and Alizarin Red stains of the porcine aortic valve samples cultured in the cone and plate bioreactor in the current study, shown in figures 6-51, 6-52, 6-54 and 6-55. Further, in the previous validation work of the cone and plate system, it was shown that the endothelial layer was not damaged after long culture duration [100]. This was again demonstrated in the current study in the H&E stains in section 6.4.1. The current study utilized both the cone and plate bioreactor and the osteogenic media culture to investigate effects of specific shear stress waveform characteristics: (1) the magnitude of shear stress waveforms; (2) the frequency of shear stress waveforms; and (3) the unsteadiness of shear stress caused (observed in the BAV).

7.6.1 Construction of Waveforms for Tests in the Cone and Plate Bioreactor

In the current study, specific shear stress waveforms were designed for use in the cone and plate bioreactor. These waveforms included both simplified waveforms designed for isolating specific shear stress characteristics, and realistic waveforms which were measured from specific aims 2 and 3.

The simplified waveforms were designed to be perfectly sinusoidal, devoid of the details of shear stress magnitude changes over time demonstrated in specific aims 2 and 3. Through such a simplification process, complicated characteristics of shear stresses, such as sudden changes in magnitudes were eliminated, and basic characteristics such as shear

stress amplitude and frequency, can be tested for their effects of valve calcification. The current study was preliminary in nature and was by no means a comprehensive investigation of all possible shear stress waveforms, but with the understanding obtained through the current studies, experiments with more complicated and realistic shear stress waveforms can now be performed.

The simplified shear stress waveforms chosen included three characteristics potentially important for valve biology: (1) shear stress amplitude; (2) shear stress frequency; and (3) rate of change of shear stress (temporally). Shear stress frequency and the rate of change of shear stress were invariably associated with each other. In the group of waveforms with the same amplitude but different frequencies, increased frequency also had increased rate of change of shear stress, and thus the results could be interpreted to be caused by either factor. In the group of waveforms with the same frequency but different shear stress amplitude, however, the waveforms with higher amplitude had both increased amplitude and increased rate of change of shear stress, and had to be interpreted with caution.

Realistic shear stress waveforms tested in the current study included the normal tricuspid aortic valve shear stress waveform (figure 5-6), the ensemble averaged BAV fused-leaflet shear stress waveform (figure 5-10a), and the two waveforms constructed to represent unsteady shear stresses found in the BAV fused leaflet (figure 5-10b and figure 5-10c). These shear stress waveforms meant to test the hypothesis that the native shear stresses experienced by the normal tricuspid aortic valve were not pro-calcific, but certain altered shear stress waveforms were. In other words, the normal tricuspid aortic valve shear stress waveform served as the normal valve control. The ensemble average BAV

shear stress waveform designed to be another control waveform, one which had no unsteadiness in it, so that its effects can be compared to the two waveforms designed to represent unsteadiness.

The first unsteady shear stress waveform (figure 5-10b) was constructed to test the effect of cycle-to-cycle magnitude changes in shear stress waveform. Thus this waveform was constructed to be smooth over time within each cycle, but had great magnitude differences from one cycle to the next. This waveform is an idealization. Realistically, the shear stress magnitude can be at any magnitude, accordingly to the probability described by the ensemble mean and the standard deviation bounds. Since it was not possible to make the cone and plate motor execute probabilistic random waveforms, the idealization was necessary. The second unsteady shear stress waveform (figure 5-10c) was constructed to test the effects of high frequency fluctuating shear stresses within the cardiac cycle. The 20 Hz oscillation chosen for super-imposition with the ensemble average waveform was chosen because it falls within the range of frequencies where differences in power spectral density was observed (figure 6-48), and was sufficiently high frequency to produce significant differences in the shear stress waveform. Again this waveform was chosen as an idealization. Actual shear stress fluctuations would, again follow some definable probability rules, which was, again, difficult to input into the cone and plate system. The choice of 20 Hz was an idealization chosen to embody some of the high frequency fluctuations observed in measurements in the BAV valve model, and did not have any direct basis from the measurements. Its purpose was to test if the high frequency fluctuations would cause differences.

7.6.2 Implications of the *Ex Vivo* Experiments Results

The results from the Arsenazo assay showed that there was quantifiable increase in the amount of calcium accumulation in the leaflet tissue samples when exposed to (1) consistently low magnitude shear stress; (2) high frequency shear stress or high rate of shear (temporal); and (3) unsteady shear stresses.

The 5 dyn/cm^2 sinusoidal shear stress waveform was found to accumulate the most calcium at the end of the 3 day culture, as opposed to fresh control, normal valve waveform, and other sinusoidal shear stress waveform of higher magnitudes. This suggested that if shear stress was consistently low, the leaflets would have a higher tendency to calcify. This observation corroborated results from earlier studies by Butcher et al. [4], who found that the absence of shear stress (static culture) up-regulated oxidative and inflammatory expressions of aortic valve endothelial cells which were hypothesized to be pathways leading to calcification [96]. The lack of sufficient magnitudes of shear stress appeared to elicit pathological response from the valve tissues in both cases which were relevant to calcification. Applying this concept to the clinical scenario, it would be prudent to ensure the presence of aortic sinuses during valve-sparing operations (the reconstruction of the aortic root due to aneurysm) [126], such that there would be sufficient sinus space for the vortex formation, which would impose higher magnitude shear stresses on the aortic surface of the aortic valve leaflets.

In terms of frequency of the shear stress waveform, it was found that neither the 1 Hz sinusoidal waveform nor the 2 Hz waveform had significantly increased amount of calcium from the normal tricuspid valve shear stress waveform or from the fresh control. This result suggested that increase shear stress frequency due to increase in heart rate

would not cause calcification tendency in the valve leaflet tissue. Since increased frequency of shear stress due to increased heart rate would not go much beyond 2 Hz. The Arzenaso results also suggested that at sufficiently high frequency of 4 Hz, calcium accumulation significantly increased. This frequency of heart beat represented unsteadiness in shear stress rather than increased heart rate, which could be brought about by unsteady forward flow due to turbulence, or by leaflet fluttering. The 4 Hz high frequency shear stress case could also represent the case when the temporal rate of change of shear stress was high. Such an analysis is important because endothelial cells were hypothesized to be able to detect difference in the temporal rate of change of shear stresses [127, 128]. Thus high temporal gradient of shear stress was also observed in the above experiment to induced greater amount of calcium accumulation.

The peak temporal gradient of shear of the various conditions can be summarized in table 7-1 and illustrated in figure 7-6. We could observe, here, that the effects of shear stress magnitude may override that of the temporal gradient of shear. For example, although the 25 dyn/cm^2 1 Hz waveform had fairly high temporal gradient of shear, it did not result in significant calcium accumulation. Further, although the 5 dyn/cm^2 1 Hz waveform had low temporal gradient of shear, it resulted in significant calcium accumulation. These suggested that the high amplitude of shear stress in the 25 dyn/cm^2 case could be preventing calcium accumulation despite having a high temporal gradient of shear, and the consistently low amplitude of shear stress in the 5 dyn/cm^2 case could be the cause for calcium accumulation, despite having a low temporal gradient of shear.

Table 7-1. Peak temporal gradient of simplified sinusoidal shear stress waveforms

Condition	Peak temporal gradient of shear stress
Sin 5 dyn/cm^2, 1 Hz	5 dyn/cm^2/s
Sin 10 dyn/cm^2, 1 Hz	10 dyn/cm^2/s
Sin 25 dyn/cm^2, 1 Hz	25 dyn/cm^2/s
Sin 10 dyn/cm^2, 2 Hz	20 dyn/cm^2/s
Sin 10 dyn/cm^2, 4 Hz	40 dyn/cm^2/s

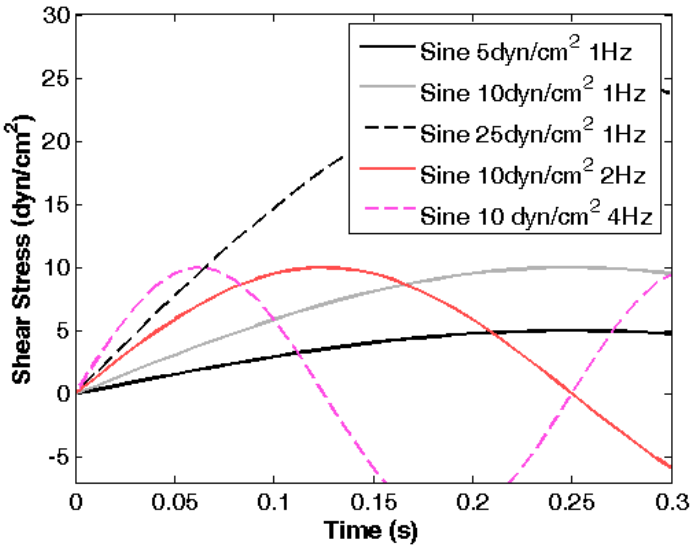

Figure 7-6. *The comparison of the temporal gradient of various idealized sinusoidal shear stress waveforms. The 4 Hz waveform had the highest temporal gradient, followed by the 25 dyn/cm^2 waveform, 2 Hz waveform, the 10 dyn/cm^2 waveform, and finally the 5 dyn/cm^2 waveform.*

In the results obtained from using the BAV shear stress waveforms, it was found that both the waveform exhibiting high frequency fluctuating patterns and waveform exhibiting alternating cycle-to-cycle magnitudes caused higher calcium accumulation than waveform with fixed pattern every cycle (both the BAV ensemble average waveform and the normal tricuspid valve waveform). This interesting observation could be used to draw a parallel to the mechanobiology of arterial endothelium. In arteries, low and oscillatory wall shear stress from blood flow tended to develop atherosclerosis [129], as demonstrated by the correlation between sites of such a shear stress environment and sites of atherosclerosis. This was similar to how fluctuating or unsteady shear stresses up-

regulated calcification response in the current study. This suggested that the aortic valve tissues and arterial wall tissues may have some similarity in their mechanobiology response.

Unsteadiness in shear stress observed in the BAV model in the current study was likely due to the stenotic geometry of the BAV, which resulted in higher turbulence intensity than in the normal aortic valve. This notion implied that shear stress unsteadiness would not be confined to the BAV cases, but also to other forms of stenotic aortic valve leaflets, such as the stenotic uni-cuspid aortic valve, or the stenotic calcified aortic valve. Whether shear stress unsteadiness played a role in these valves to accelerate calcification is current unknown, and should be investigated further.

7.7 Physiological Implications of Findings

7.7.1 Implications of Shear Stress Data

A detailed description of the time-varying shear stress waveforms on the aortic valve leaflets is crucial to the complete characterization of the mechanical environment of the aortic valve. On top of being useful for shear stress mechanobiology experiments, shear stress data can be used to support mass transport studies, such as lipid transport on native valve leaflets [130] or calcium transport in prosthetic valve leaflets. It can be use to understand systolic stretch mechanics of the valve, since forward flow will impart drag forces on leaflets to stretch them in the radial direction [18], and systolic stretch may have implications on stretch-mediated biological responses.

The characterization of shear stress environment of the aortic valve is incomplete to date, even though multiple studies investigating shear stress mechanobiology of the aortic

valve depend on it. In the absence of dynamic fluid shear stress data, investigators resorted to idealized shear stress waveforms for mechanobiology experiments, such as steady shear and sine waveforms [4, 5, 87, 131]. The data contained in this thesis are thus important to enable mechanobiology experiments with more physiologic shear stress waveform inputs.

As discussed in section 7.2, aortic surface shear stresses elevated only during systole, and only when the sinus vortex developed. Considered together with evidence that low magnitude or absence of fluid shear stresses are pro-inflammatory to the endothelium [4, 132, 133], this result suggests that the presence of the sinus may be important to the health of the valve. The pouch geometry of the sinus ensures that there are sufficient spaces between the leaflets the aortic root walls to allow vortical flow to develop within the sinuses, induced by interaction with the forward flow through the valve, to expose the aortic surface of the valve to periodic higher shear stresses during systole, and protect the leaflets from sclerosis. In conditions where the sinus vortex does not develop, shear stresses on the aortic surface of the leaflet will remain low all the time, and may be harmful to the biology of the valve. For example, in patients who have undergone the valve-sparing procedure to treat ascending aortic aneurysms [126], if the Dacron graft replacement aorta were straight tubes without sinus bulges, MRI scans have shown that no sinus vortex will develop during systole [33]. This will imply that aortic surface of the valve will be exposed to non-physiologic shear stresses, and may result in pathological degeneration of the aortic valve, since the aortic valve is mechano-sensitive to fluid shear stresses. Further, studies showed that in valve-sparing procedures where grafts had no sinus bulges, the leaflet motion during opening and closing are altered from the native

state [35, 134], which may again alter shear stress patterns on the leaflet, and hold implications for future valve degeneration.

The results from specific aim 2 showed that, contrary to past intuition [5, 96], ventricular surface shear stresses should reverse during late systole to a significant magnitude and for a significant duration, and aortic surface shear stress should not reverse in direction significantly. Significant magnitudes of shear stress were observed only during systole attributable to the formation of sinus vortices. While this vortex could evolve to have a significant non-stream-wise component, it is unlikely that the vortex will completely reverse in direction to have significant reversed shear stress. Further, shear stresses during diastole are generally low fluid velocities which remained after the closure of the valve was usually small in magnitude. The physiological implications of these findings to valve biology are currently unclear, and warrant further investigations.

The observation that aortic valve tissues can respond pathologically to low and unsteady shear stresses in the current thesis suggested a similarity between aortic valve endothelium and arterial endothelium as discussed in the previous section. Since both types of tissues are part of the arterial side of the cardiovascular system, it is conceivable that there would be similarities between them. Butcher et al. [4] however, showed, through the genetic profiling of both arterial endothelial cells and aortic valve endothelial cells after exposure to shear stresses, that there are differences in the genetic expressions of these two types of cells. This suggested that the cellular phenotype of these two kinds of cells may not be the same.

7.7.2 Implications of Dependency of Aortic Surface Shear Stresses on Hemodynamics

Results in section 6.2.3 in specific aim 2 showed that aortic surface shear stress was strongly influenced by hemodynamic parameters. This indicated that any disease conditions with altered hemodynamics have the potential of affecting aortic surface shear stresses, such as tachycardia or outflow impairment. Since mechanobiology results shown in the current thesis were preliminary, how these specific alterations in shear stresses from its normal state can affect the aortic valve biology is unknown, and warrant further investigation. However, it is widely accepted that low and oscillatory shear stresses will lead to vascular endothelium sclerosis [133, 135]. If we assume a similar reaction of aortic valve endothelium to shear stress as vascular endothelium, we can conclude that higher heart rates will reduce shear stress magnitude and potentially elicit sclerotic responses from the aortic valve, while higher stroke volumes will increase shear stress magnitude and decrease sclerotic responses from the aortic valve. Thus tachycardia would be harmful to the heart valve tissues while exercise would be beneficial. This notion corroborates with epidemiological findings that tachycardia is associated with increased risk for heart diseases [136, 137], and that exercise can prevent the formation of AV calcification [138].

Further, in the case of hypertension, which was found to be associated with increased risk of aortic valve calcification [97, 139], studies have shown that the stroke volume and heart rate of the patient could be altered [140-142]. It can be speculated that this increase in calcification risk is caused by altered fluid shear stress on the aortic valve leaflet surface due to alterations in hemodynamics. Hypertension could also later the aortic

valve annulus dynamics, which would affect the valve leaflet dynamics, again leading to potentially harmful changes in the fluid shear stress waveform shape.

7.7.3 The Possibility that BAV Calcification may be Related to Fluid Shear Stress Environment of its Leaflets

The traditional view on BAV leaflet calcification is that genetic factors are the cause of the calcification. This view is substantiated by epidemiological evidence that the BAV is associated with the NOTCH1 gene defect [143], and NOTCH1 signaling disruption has been shown to increase aortic valve calcification in the mouse model as well as *in vitro* [144]. NOTCH1 has also been implicated in aorta dilatation in BAV patients, where dilatation was observed to continue even after prosthetic valve replacement which returned hemodynamics to the normal state [79, 145]. This has led to beliefs that this co-morbidity of BAV is not dependent on the mechanical environment, but is due to a tissue defect.

However, results from the current study suggested that on top of genetic factors, the mechanical environment of the aortic valve also play a role in calcification. The current study proposed a possible pathway for BAV calcification due to its mechanical environment by first demonstrating that the BAV leaflets could experience altered fluid shear stress characteristics, such as the excessive unsteadiness in fluid shear stresses on the leaflets due to turbulent and eccentric forward flow; and, second, that these shear stress characteristics could elicit pathological biological responses related to valve calcification in ex vivo culture experiments.

The current study, however, had not investigated all possible scenarios. For example, it is possible that BAVs to be non-stenotic and non-eccentric, such that forward flows will not be turbulent or skewed, and thus not have unsteadiness fluid shear stress on the valve leaflets. However, there is evidence in the literature that the fluid mechanical environment can be drastically altered in the BAV. Robicsek et al. [76] investigated human BAV explants in an *in vitro* flow loop and commented that these valves exhibited unsteady valve kinematics, and speculated that turbulence would be present in these valves. Brummer et al. showed that a range of forward flow eccentricities can be found in various human BAV patients using MRI [69], and showed that a correlation between the aortic dilatation and forward flow eccentricity could be established.

Further, there is evidence that endothelial cells respond to turbulent flows. Davies et al [146] investigated with effects of turbulent flows on arterial endothelial cells, and found altered cellular turnover, alterations in cell orientation. Davies et al, however, experimented with arterial endothelial cells, and not aortic valve endothelial cells. Nonetheless, similarities between these two endothelial cell types are possible. This suggests that the turbulence in the BAV valve model may be physiologically relevant to the biology of valve.

To fully investigate this notion, further work is required. Clinical studies can be performed to investigate whether there is correlation between levels of aortic valve calcification and the mechanical environment of the valve. The presentation of such data will involve the determination of the mechanical environment of both BAV and normal aortic valves to a patient specific level, and then the determination of the level of calcification in specific patients.

7.8 Limitations

7.8.1 Errors Associated with Velocity Variability

The most important limitation of the technique developed for fluid shear stress estimation in this thesis was the inability of the measuring system to make instantaneous velocity measurements at multiple points in order to give instantaneous velocity profiles. Consequently, it was uncertain if the ensemble average velocity profile sufficiently represented the instantaneous velocity profiles or what the deviation was from ensemble average to instantaneous values, as discussed numerous times in the methods, results and discussion chapters (sections 5.2.5, section 6.2.4, section 7.1.1 etc).

Due to a lack of a better analysis method, this LDV method was still performed using the ensemble average velocity profiles to obtain fluid shear stresses. Data such as the variability of velocities, leaflet locations and shear stress measurements were presented as well, as well as analysis of possible errors due to this variability (section 6.2.4). Future work is required to better account for the effects of this variability on shear stress values.

7.8.2 Validations of Methods only in Systems with Static Surfaces

The key limitation of this thesis is the lack of validation of the shear stress measurement methods on a dynamic surface. Validations were only performed for the following: (1) validation for back-scattered surface position tracking method on a static surface as well as a dynamic surface, and (2) LDV velocity measurements near a static surface, and shear stress measurements on the static surface. To fully validate the proposed shear stress measurement methods, however, a system with a dynamic surface

should be used to generate additional validation data. For validation to be feasible in this system, either a theoretical solution for the flow and shear stress must exist, or an alternative "gold-standard" method of measuring shear stress must exist to provide the true shear stress values. Shear stress measured in the proposed methods in this thesis can then be compared to the true shear stress values for full validation. The design of such a system, however, is non-trivial, and has not been achieved in this thesis.

In the current thesis, however, whenever shear stresses were measured, the valve leaflets surfaces were almost stationary, having velocities of less than 0.034 m/s in any direction, and accelerations of less than 1.0 m/s2 in any direction. Thus, stable leaflet position allowed the proposed methods, which were validated in a system with static surfaces, to measure shear stresses.

7.8.3 *In Vitro* Nature of Study

Another limitation of this thesis was the *in vitro* nature of the study with valve models. Consequently, it suffered from the limitations of any *in vitro* model – it could not completely replicate exact *in vivo* conditions, such as *in vivo* volumetric flow waveforms, compliance of the native aortic root, and person-specific AV and aortic root geometry. The *in vitro* approach, however, is the only currently achievable method of experimentally measuring shear stresses, given resolution limitations of non-invasive scanning modalities, and allows absolute control over the hemodynamics. Further, the conditions simulated were sufficiently close to native conditions to allow an estimation of the *in vivo* shear stress characteristics.

Due to the *in vitro* approach, minor differences exist between *in vitro* test conditions and *in vivo* conditions. For example, in specific aim 2 (section 6.2.1), as demonstrated in figures 6-12 and 6-21, *in vivo* flow waveforms peaked during early systole, while the *in vitro* flow waveforms peaked during mid-systole, and the *in vivo* flow waveforms had a smaller gradient than *in vitro* flow waveforms during the deceleration phase. Shear stress results from the *in vitro* studies consequently differed slightly from *in vivo*: *in vitro* results demonstrated an additional shear stress peak during early systole due to flow disturbances related to snapping motion of leaflet opening, and *in vitro* results show shorter periods of reversed shear stresses.

7.8.4 Limitations of the Valve Models

Secondly, the use of the valve models is another weakness of the study. For specific aims 2 and 3, the fixation of the valve so that experiments could be performed over extended period of time resulted in changes in material properties of the valve [50, 147], which might have altered leaflet dynamics to be closer to those of bioprosthetic valve rather than fresh aortic valves. For example, during systole, it was shown that the valve leaflets would stretch in the streamwise or radial direction due to drag forces from forward flow [18]. In the valve models, since they were fixed, such a deformation will be greatly reduced. However, we expect this effect to be minimal in the measurement of shear stresses. In specific aim 2, Geometric differences exist between these polymeric valves and the native valves. The polymeric valves used are stented valves, which might slightly alter the dynamics of motion of the leaflets. However, since the ventricular surface shear stresses were desired in this aim, there is a need to use a valve model that

has transparent leaflets to gain optical access to the ventricular side, despite its differences with a native aortic valve.

For specific aim 3, the BAV model was a surgical modification from a normal aortic valve, and even though the geometry was controlled as much as possible, the BAV model might have differences with actual clinical BAV geometry. The model might also have different material property from the clinical BAV. Validation experiments, however, showed that the BAV valve model was sufficiently similar to the clinical human BAV, as discussed in sections 6.3.2 and 6.3.3. Further, there is a wide range of different geometries in clinically observed BAV. For example, some BAV have two-lobed sinuses while others have three-lobed geometries [67], and different BAV have different valve orifice eccentricities [69]. In the current study, only one type of BAV was studied, and there was no systematic sweep of the space of possible of various BAV geometries and characteristics, which is indeed necessary for a comprehensive understanding of the BAV fluid mechanics. Nonetheless, the model studied provided important information of how a BAV could differ from a normal valve.

7.8.5 Lack of Coronary Flow

The lack of coronary modeling in the current study rendered the diastolic shear stress results for the aortic surface (in specific aims 2 and 3) more applicable to the non-coronary leaflet than the left or right coronary leaflets. We note, however, that the diastolic coronary flow has a low average velocity of 25 cm/s [148], and total flow per cycle of about 10% of the volume of a sinus, and thus may not have very strong influence on diastolic sinus flow.

7.8.6 Idealized Sinus Geometry

Although the sinus chamber was machined to match the radial width and axial height of human aortic sinuses as measured by previous investigators, the shape of the sinus may have differences with that of human aortic sinuses. In the sinus chamber, the sinuses took the shape of regular elongated sphere, while that of a human aortic sinus may be rounder and skewed towards the annulus. This difference in shape may lead to differences in the sinus vortex flow, which may lead to differences in shear stresses.

7.8.7 Lack of the Third Velocity Component

The current study presents velocity measurements in two directions (streamwise and non-streamwise directions) instead of all three directions because the measurement of the radial direction fluid velocity is technically challenging very close to the valve leaflet. For example, close the valve leaflet surface, the measurement of the radial velocity component require that one of the laser beam pair crosses the valve leaflet, which, for the native tissue valve models, is impossible, because the valve tissue will block the laser light (figure 7-7).

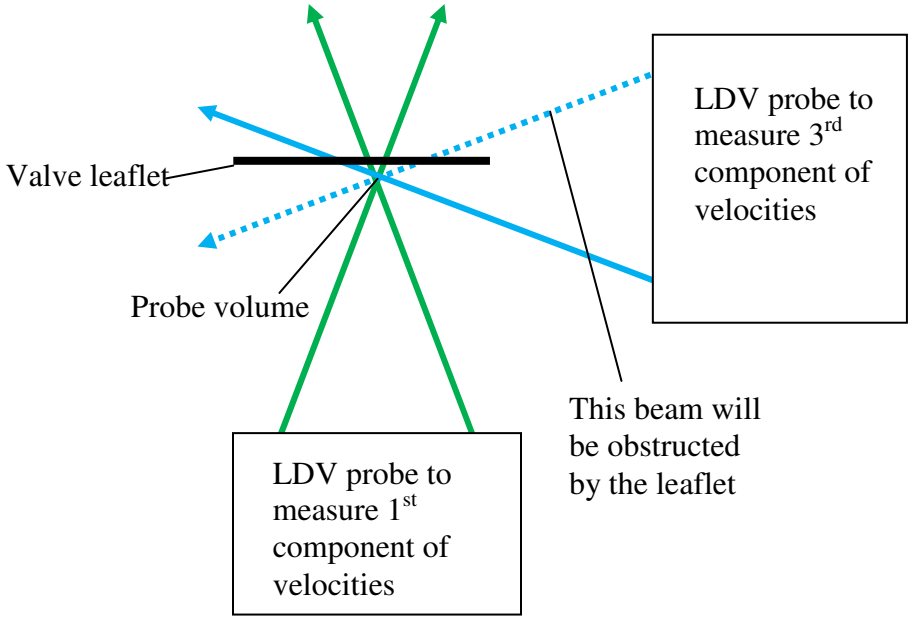

Figure 7-7. *Schematic of the LDV laser beam paths in an attempt to make velocity measurements in all 3 directions, showing that, when making measurements very close to the valve leaflet, the opacity of the leaflet will block one of the two laser beams required for measuring radial velocities.*

The lack of data on the third component might have resulted in errors since the leaflet surface was not perfectly aligned with the LDV probe. However, the misalignment angle was kept at less than 0.15 radians, and errors caused by the misalignment between the leaflet surface and the probe were estimated to be less than 3% as shown in section 6.1.6.

7.8.8 Lack of Measurements During Valve Opening and Closing

The LDV technique was able to measure velocities over the entire cardiac cycle, but cannot be applied to obtain measurements during the time periods when valve leaflets were rapidly opening or closing. This was because the valve leaflets were moving too fast for shear stress computation to be accurate, and because the orientation of the valve leaflet was greater than 0.15 radians. A more advanced surface mounted measurement

technique might be needed to achieve this. However, these rapid motions are restricted to a small portion of the cardiac cycle, and it is expected that a linear trend in shear stress exists between the points where measurements have been made. A more advanced surface mounted measurement technique might be needed to achieve this.

7.8.9 Limitations of the Womersley Solution for Estimation of Ventricular Surface Shear Stress

The theoretical modeling for the ventricular surface shear stress using the Womersley solution was intended as an order of magnitude analysis to obtain general features of ventricular surface shear stresses. The assumption of a straight tube geometry was an idealization from the native valve in its opened configuration, and so was the assumption that there was sufficient entrance length. Even though the results of the modeling showed agreements with the measurements in the polymeric valve model, it must be noted that significant simplification assumptions were made.

7.8.10 Limitations of *Ex Vivo* Culture Experiments

The mechanobiology results shown in the current thesis are preliminary in nature. Further work are required to confirm that the calcium accumulation in the tissues were indeed the result of active cellular process, instead of passive calcium accumulation. For example, assays on the inflammatory and apoptosis response of the tissues can be performed to confirm changes in cellular responses. Nonetheless, the fact that the AV tissues accumulate calcium to different extent in different mechanical conditions provides some support for the notion that active cellular processes were involved, because the rate

of passive calcium accumulation should be uniform for all samples since the same culture media was used.

In the ex vivo culture work, the use of porcine leaflets might not exactly replicate human aortic valve biology. Porcine genes, however, were shown to be highly similar to human genes, and porcine tissue is a more practical substitute. Also, the calcification results are based on observations from normal healthy leaflet tissues. BAV leaflets may have genetic defects and might have different biological response. Finally, the technique of osteogenic culture of tissues, which was used as a simulation of accelerated calcification, may hold differences with clinical BAV leaflet calcification, even though there are morphological similarities.

CHAPTER 8

CONCLUSIONS

In this thesis, it was demonstrated that shear stresses on the surface of the aortic valve can be measured using suitable aortic valve models with the LDV technique under controlled hemodynamics. The method for measuring this was developed and validated. The method was then applied to multiple aortic valve models were used, demonstrating its versatility. In future, this method can be applied to other dynamic cardiovascular parts, such as the mitral valve.

The current thesis provided experimental data on the shear stress environment of the normal native aortic valve, as well as the bicuspid aortic valve. Such information was previously was not found in the literature. Shear stress on the ventricular surface of the leaflet was demonstrated to be the result of a developing flow, which led to the shear stress waveform shape being skewed towards early systole. Peak ventricular surface shear stresses were shown in the range of 64 – 91 dyn/cm^2, which was about 3-4 times higher in magnitude than peak aortic surface shear stresses, which were in the range of 13 - 19 dyn/cm^2, under normal adult resting hemodynamics. Further, systolic ventricular shear stress was found to reverse in direction during end systole to a significant magnitude and for a significant duration of time. A theoretical framework for estimating ventricular surface shear stresses has been developed and *in vivo* shear stresses using bulk flow rates have been estimated. The results were similar to the *in vitro* shear stress measurement results, with similar peak shear stress order of magnitudes and shear stress reversal during late systole.

In contrast, shear stress on the aortic surface of the leaflet was demonstrated not to reverse in direction, except if the reversed shear stress were small in magnitude. Aortic surface shear stress was higher during systole than diastole. Systolic aortic surface shear stress was found to be elevated only with the formation of the forward flow sinus vortex, and since it took time for forward flow to induce sinus flow, systolic aortic surface shear stress waveform had a shape that was skewed towards late systole. Further, systolic aortic surface shear stresses increased with higher stroke volume and with wider valve leaflet opening, but decreased with higher heart rate.

Shear stresses experienced by the BAV was also investigated in the current thesis, showing that the BAV valve geometry could lead to altered fluid shear stresses on the valve leaflets, in the form of increased shear stress unsteadiness. This unsteadiness was found to be in the form cycle-to-cycle magnitude variability, and in the form of high frequency fluctuations about the ensemble mean shear stresses.

Finally, the current thesis provided also preliminary insights of the effects of various relevant fluid shear stresses characteristics on the calcification pathology of the aortic valve leaflets. It was found that (1) consistently low magnitude shear stresses; (2) high frequency shear stresses; and (3) unsteady shear stresses increased tendency of aortic valve leaflet to accumulate calcium, using a ex vivo culture bioreactor, and porcine aortic valve samples. The identification of these conditions will enable future studies in to the biological pathways of disease expressions in these specific conditions.

CHAPTER 9

RECOMMENDATIONS AND FUTURE DIRECTIONS

9.1 Future Studies

9.1.1 More Physiologic Shear Stress Measurements

Even with the data presented in this thesis, the understanding of shear stress environment on the aortic valve is not complete. The current thesis represents the initial steps taken to experimentally measure shear stresses on heart valves. Future studies should include the measurements of shear stresses in more physiological conditions, such as more realistic aortic root geometries, or *in vivo* measurements. One possible means of obtaining shear stresses in locations without optical access is the use of hot film anemometer, which will be discussed in section 10.2.1.

9.1.2 Measurements in Different Aortic Valve Geometries or Hemodynamic Conditions

The LDV shear stress measurement techniques developed in this thesis can be further used to characterize shear stresses in different aortic valve geometries / hemodynamic conditions, since only limited number of valve models were used in this thesis, which cannot represent all possible scenarios. For example, valves of different levels of stenosis can be studied to investigate the effects of stenosis on shear stresses, or valves of different orifice sizes can be used to investigate the effects of effective orifice area on shear stresses. Such studies may be especially important for BAVs. Clinically, multiple

different BAV morphologies exist, but the current thesis only touched on one commonly encountered morphology. Thus further investigations are required.

The construction of valve models using native tissues involves challenging craftwork, and it may be difficult to achieve very specific desired outcome such as level of stenosis or eccentricity of forward flow. It may be possible to develop methodologies to 3D print flexible valve models using stereo-lithography. This way, valve models of controlled characteristics can be manufactured and tested. Further, echocardiography scans of aortic valves of normal adults and valve patients can be used to prototype highly anatomic valve geometries for shear stress studies.

9.1.3 Further *Ex Vivo* Investigation of Effects of Shear Stresses on Aortic Valve Biology

With the detailed measurements in the current thesis, more realistic shear stress waveforms can be used for *ex vivo* mechanobiology experiments, instead of using idealized shear stress waveforms.

Further, the current thesis does not dwell deep into the biological pathways leading to calcification, and this should be a topic of further investigation.

9.2 Recommendations for Improving Specific Methods

9.2.1 Alternative Method for Measuring Shear Stresses on Aortic Valve Leaflets: Hot Film Anemometry

Although the current thesis demonstrated that the use of LDV can be used to measure shear stresses using *in vitro* valve models, there are limitations to method, which are

discussed thoroughly in Chapter 8. One alternative to using the LDV is to use hot film anemometry, where a hot film is attached to the leaflet surface, and the rate of heat transferred from the film to flow moving past the surface of the leaflet can be calibrated to measure shear stresses. The advantage of the hot film anemometry is that it allows the shear stress during all time points to be measured, including the time periods where the valve leaflets are moving rapidly. Shear stresses during these time periods are not measured in the current thesis due to limitations of the methods. While it is envisioned that the shear stresses during these time periods will not deviate far from the interpolation of shear stresses before and after these periods, hot film anemometry allow this notion to be confirmed. Further, the hot film can be used in locations without optical access, such as *in vivo*, or in an *in vitro* valve model without optical access.

The hot film anemometer can be calibrated by applying the LDV techniques in the current thesis: by concurrently making measurements with both the hot film and the LDV. Calibration can be performed in situ, or post-data collection, when the valve leaflet can be cut out together with the probe and placed in a calibration device.

Models of hot film anemometers suitable for shear stress measurements are available commercially. These come in miniature sizes of a few millimeters in dimension, and have probes which are mountable in locations remote from the rest of the anemometer, connected by wires. Chemical methods to glue the probe onto native aortic valve leaflet and detaching it can be developed so that the same probe can be re-used multiple times.

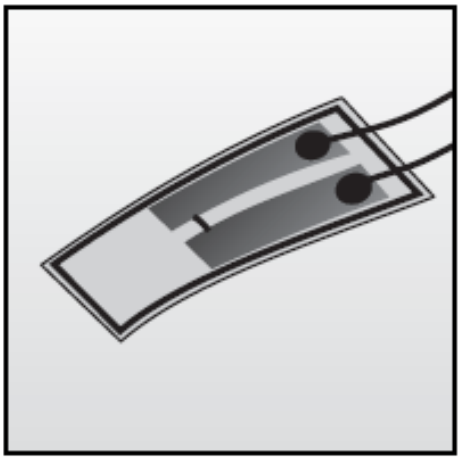

Figure 10-1. *Sketch of a miniature hot-film anemometry probe that can potentially be used for measuring shear stresses on the aortic valve leaflet, in vivo or in vitro.*

9.2.2 Improvements to Theoretical Modeling of Ventricular Shear Stresses

The theoretical model discussed in section 6.3.2 assumes that the valve leaflets are opened such that they are parallel to the axial direction, with the leaflet opening angle at 90 degrees. This is clearly an idealization to enable the calculations. However, the current theoretical model can be improved to include effects of valve taper angle. Theories of pulsatile flow in a converging or diverging tube are available in literature, such as those by Cerny et al. [149], Ren-Jing et al. [150] and Rao et al. [151]. Both studies were intended to model blood flow in blood vessels, but can be adapted for blood flow in the AV. Incorporation of these theories will allow closer approximation of ventricular surface shear stresses. However, at present, the explicit form of the solution in the tapered tube which is directly applicable to valves has not been developed, and warrants further study.

APPENDIX A

MECHANICAL DRAWINGS

A1.1. Normal Aortic Valve Tri-Lobed Sinus Chamber

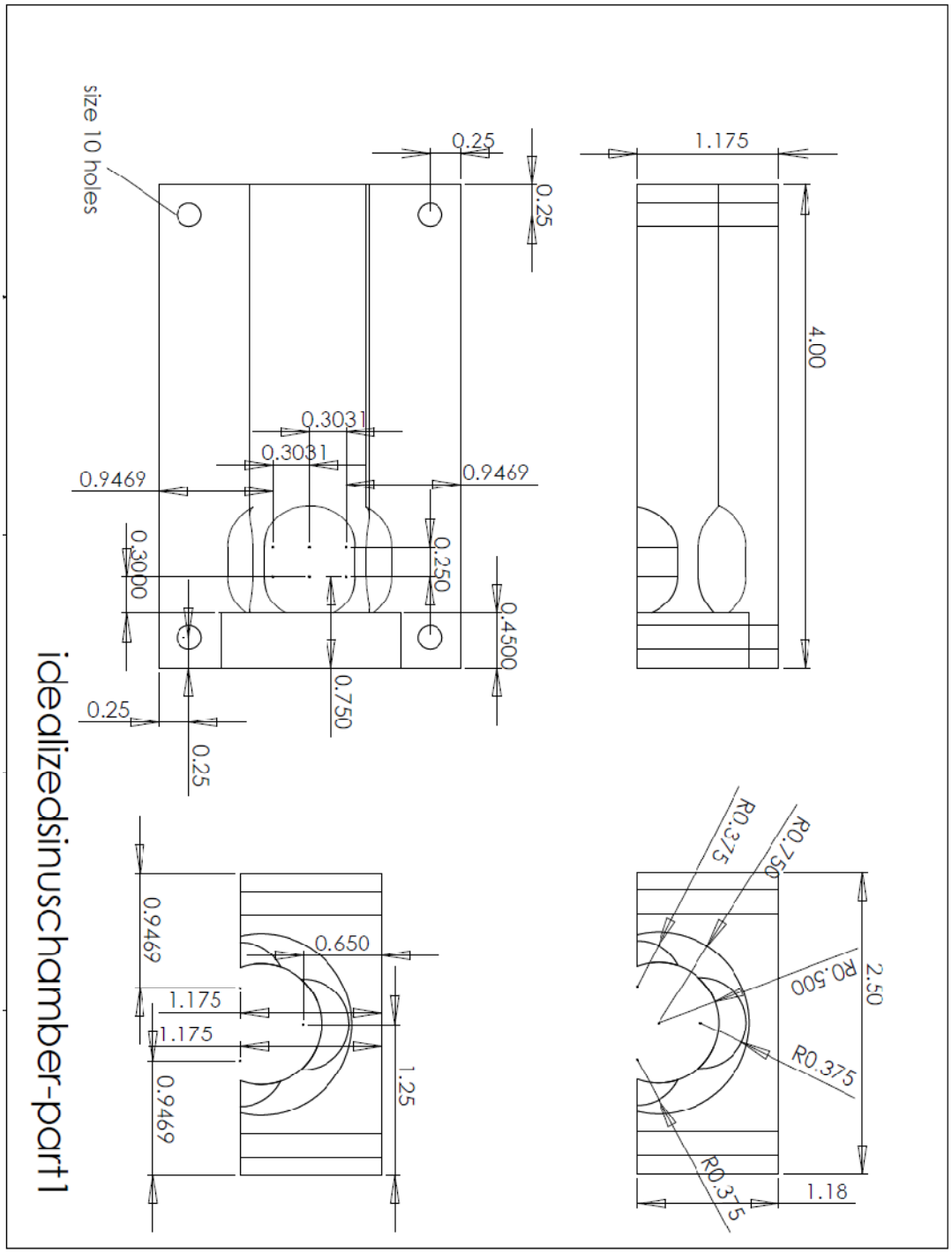

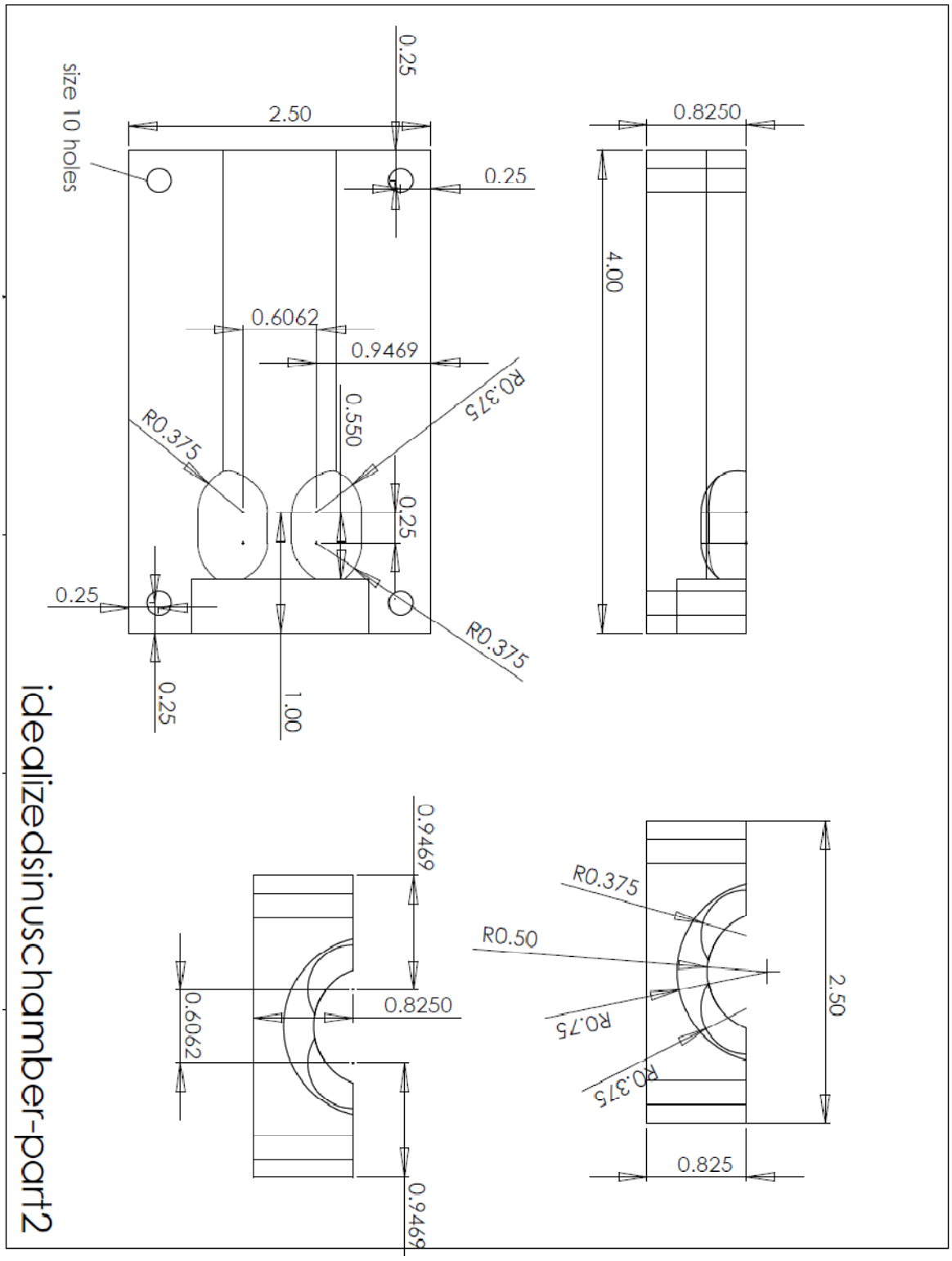

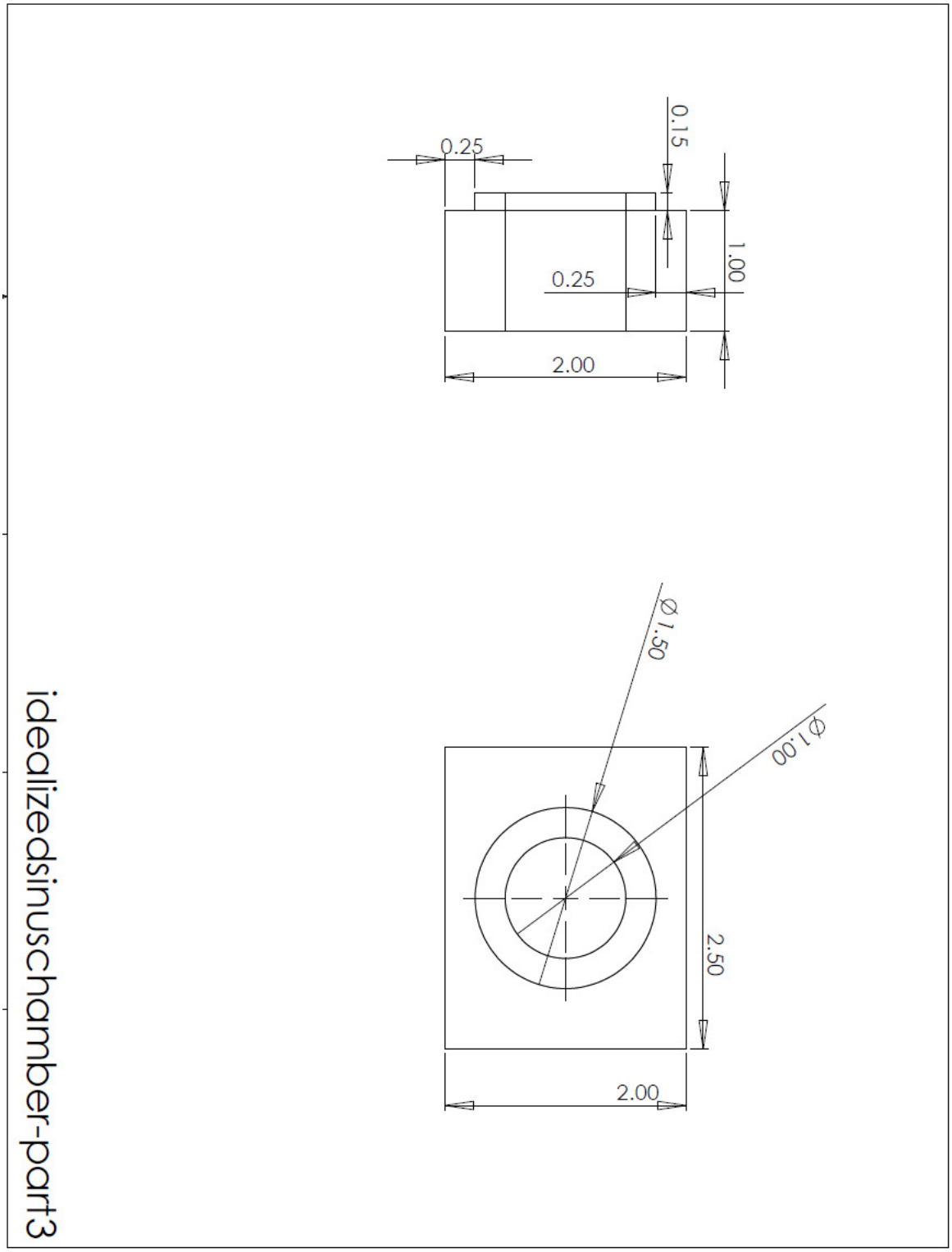

A1.2. Bicuspid Aortic Valve Bi-Lobed Sinus Chamber

Part 1

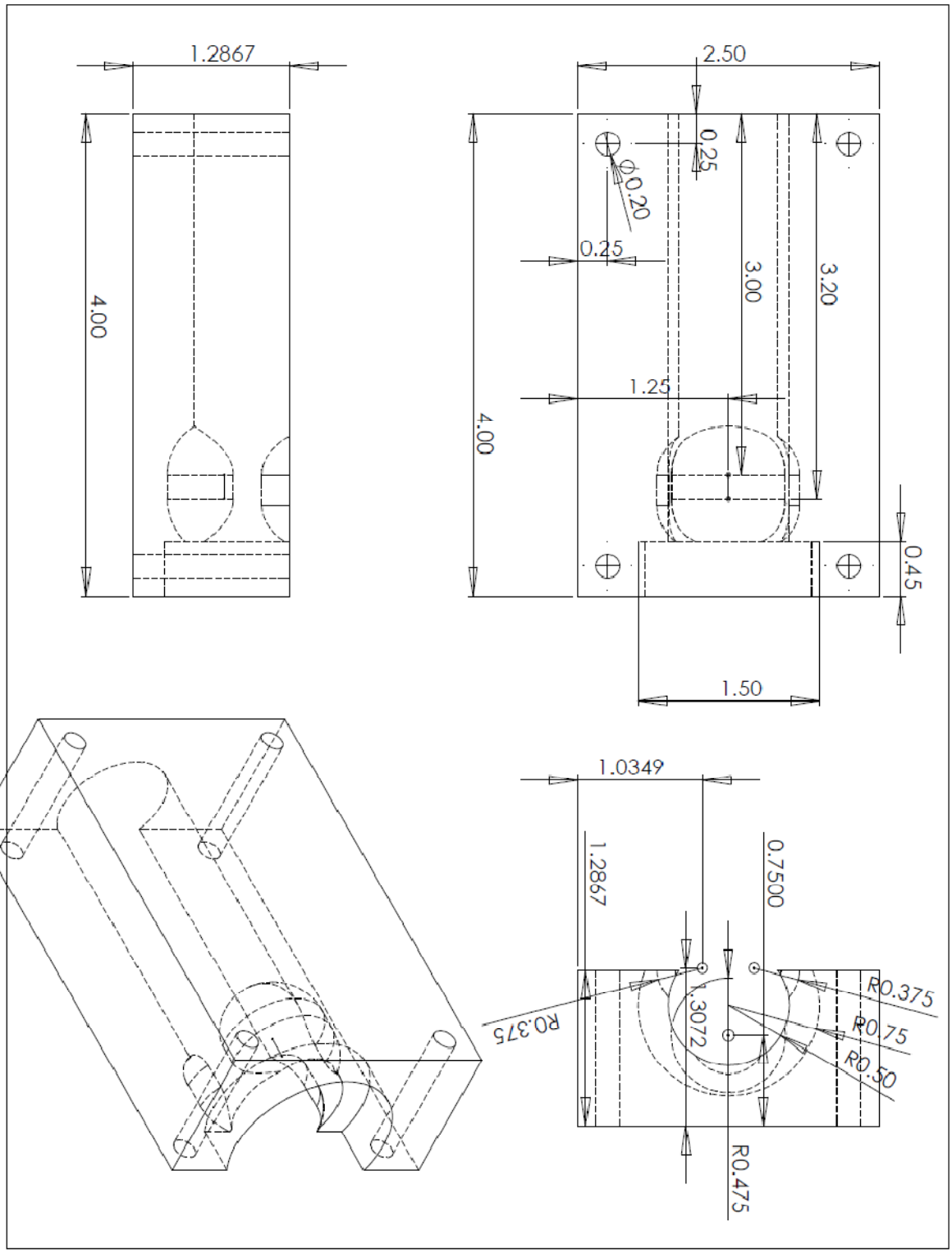

Part 2

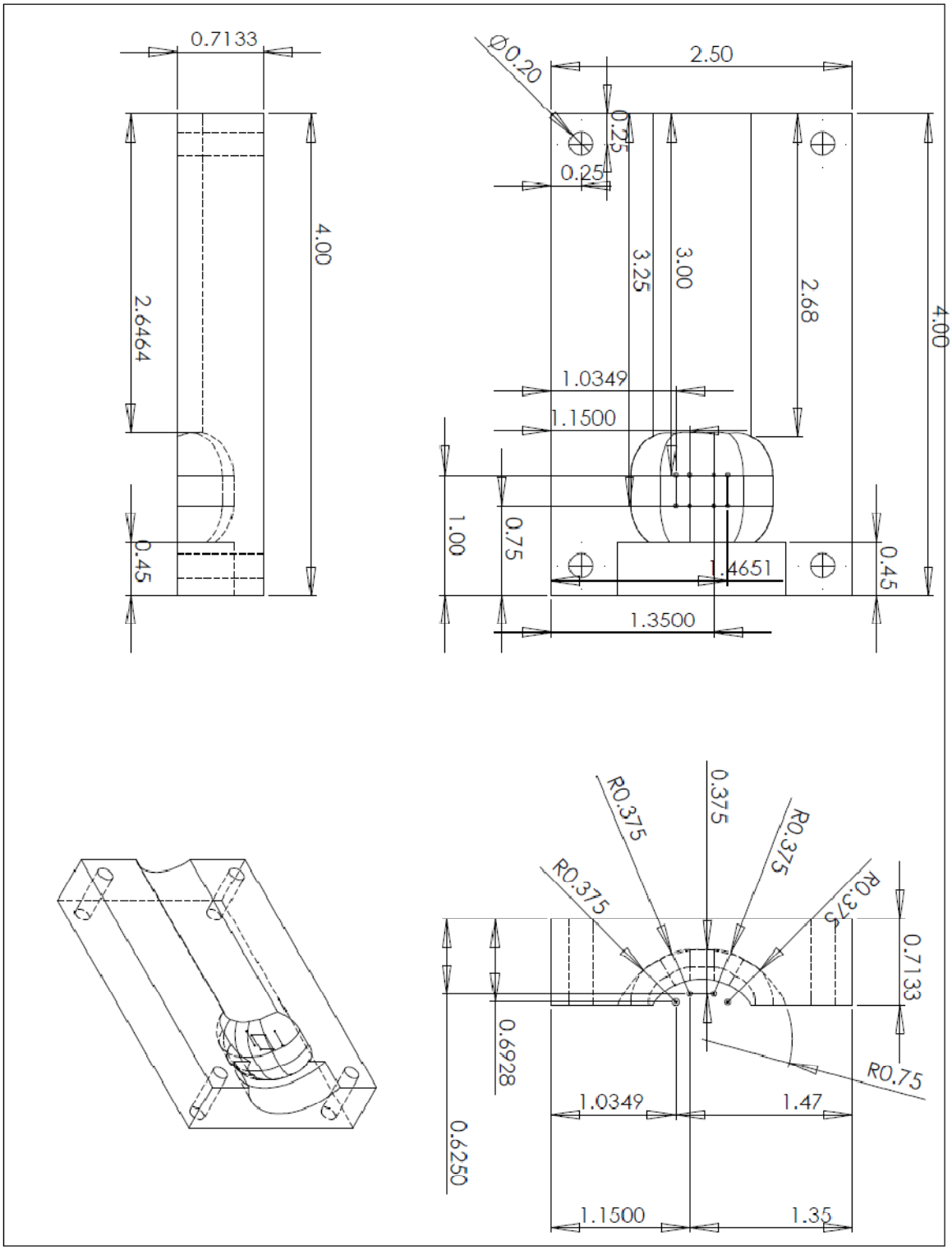

Part 3

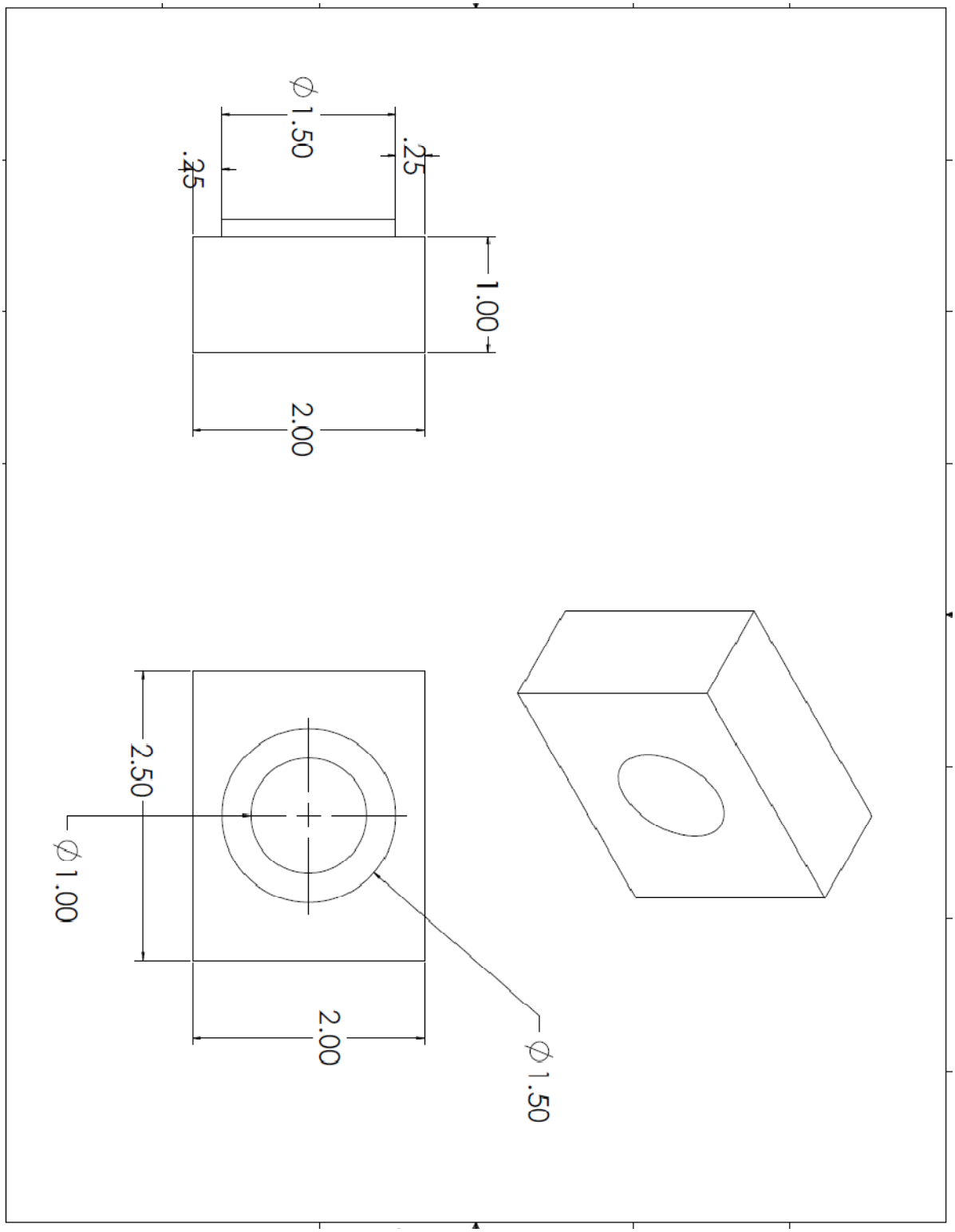

A1.3. Ring Stent

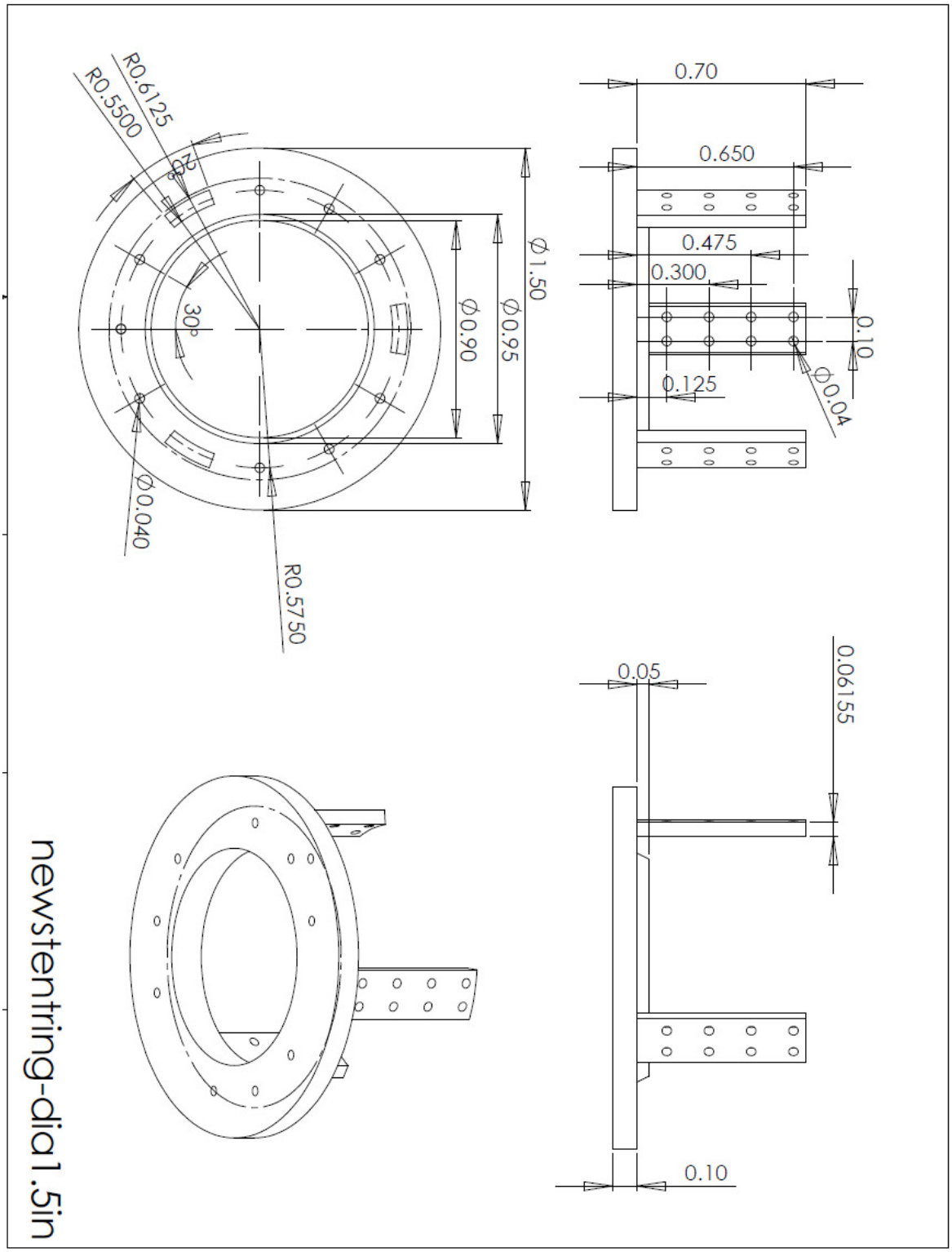

A1.4. The Cone and Plate Apparatus

A4.1. Overall Bioreactor Assembly

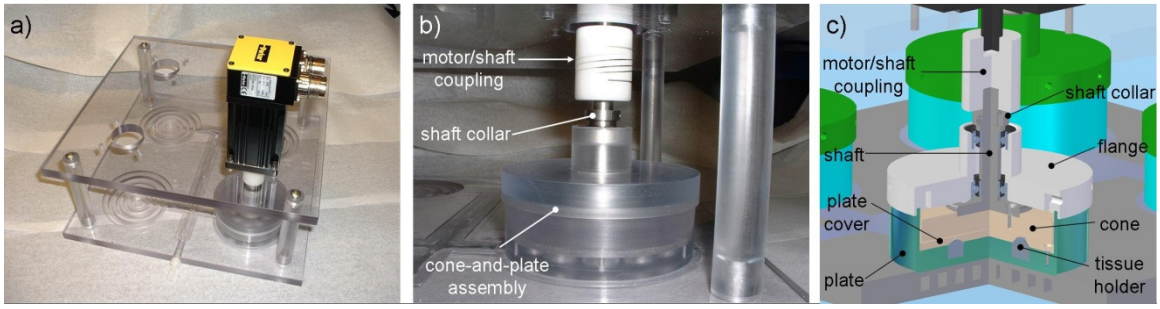

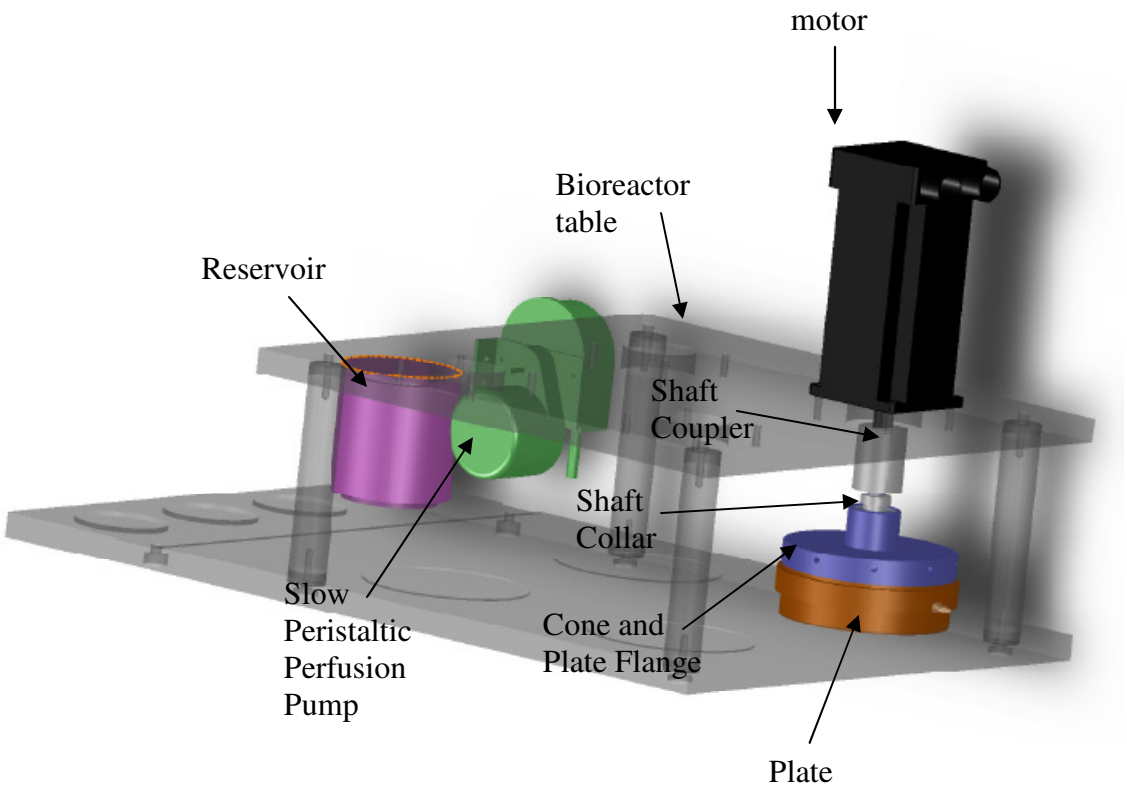

A4.2. Cone

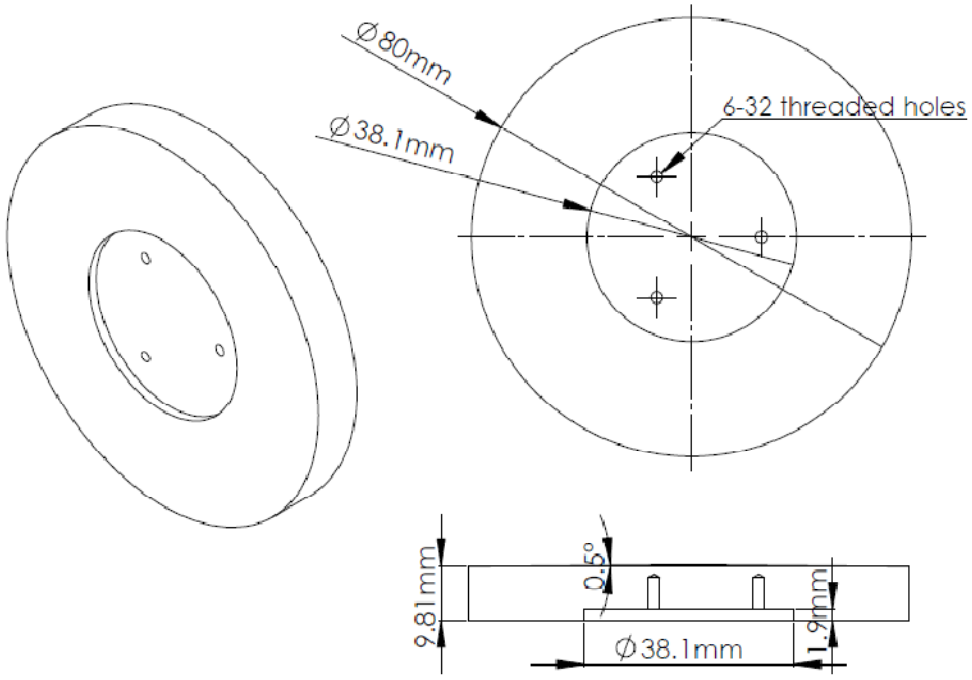

A4.3. Shaft and Shaft Collar

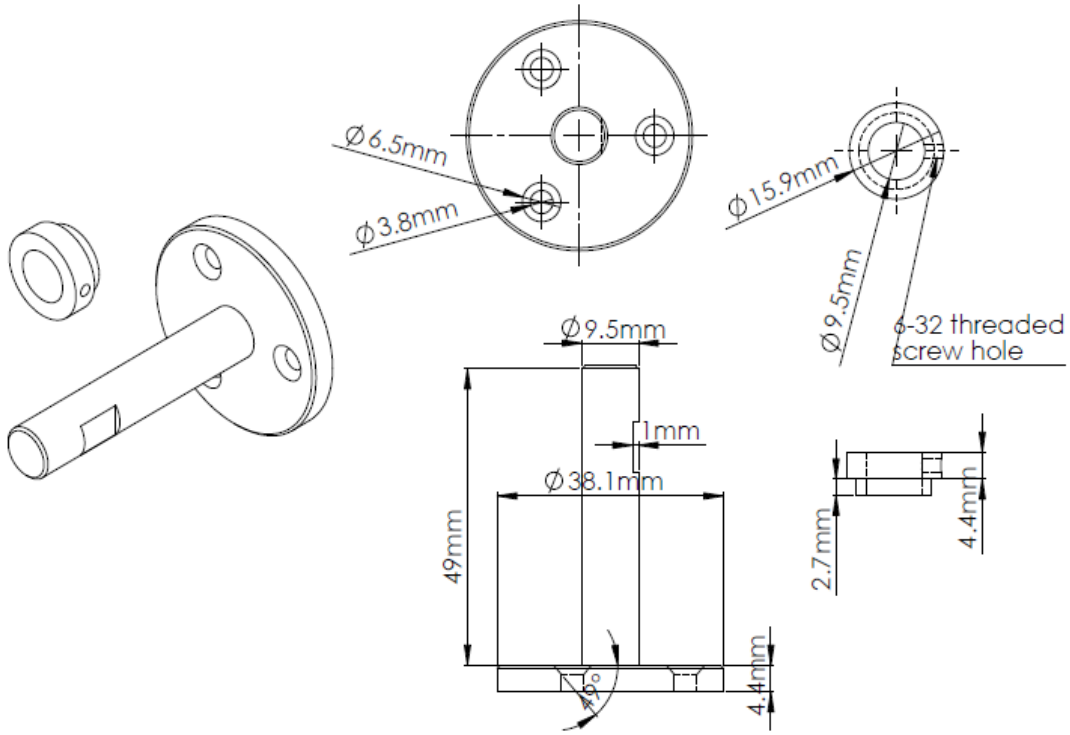

A4.4. Cone Flange

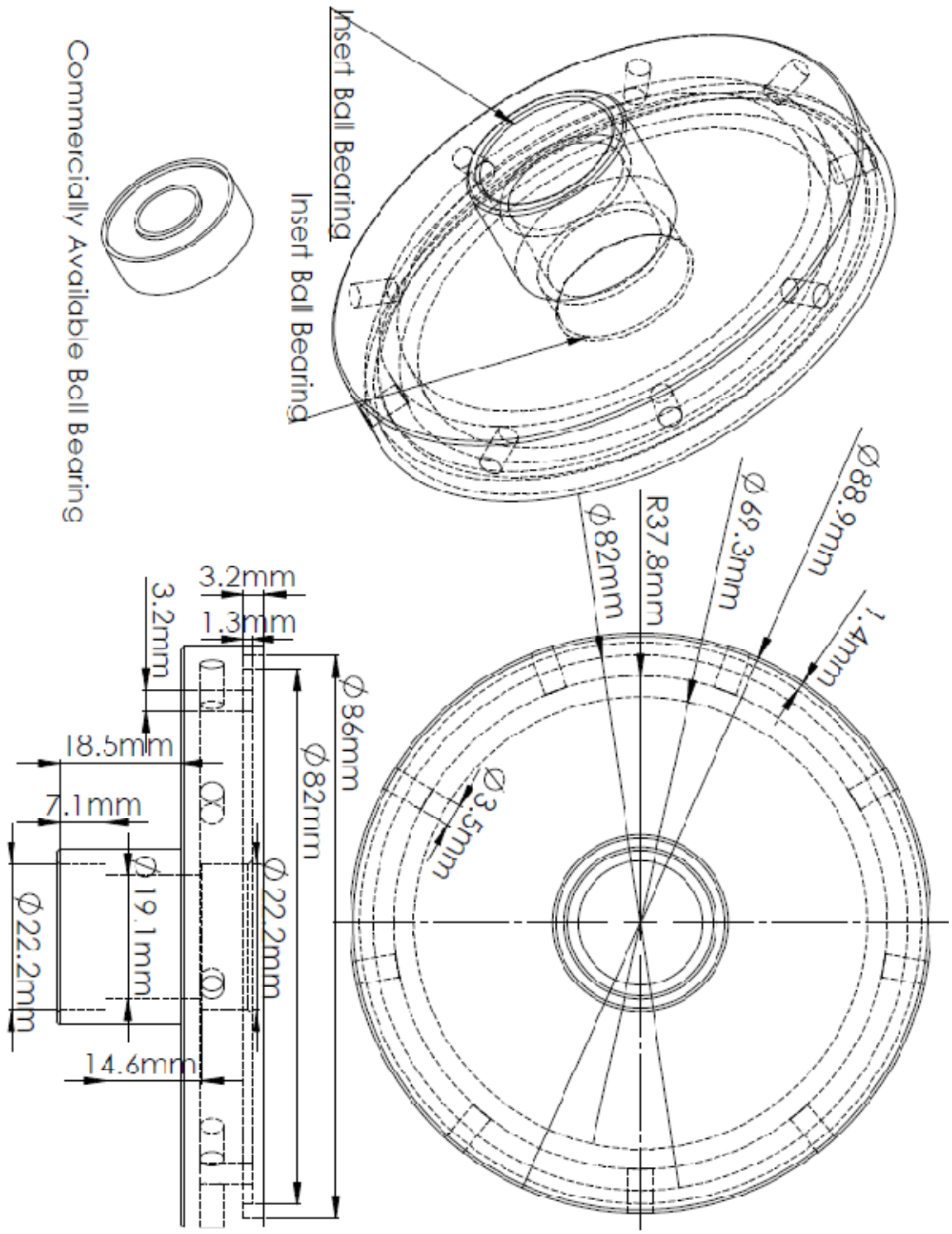

A4.5. Plate

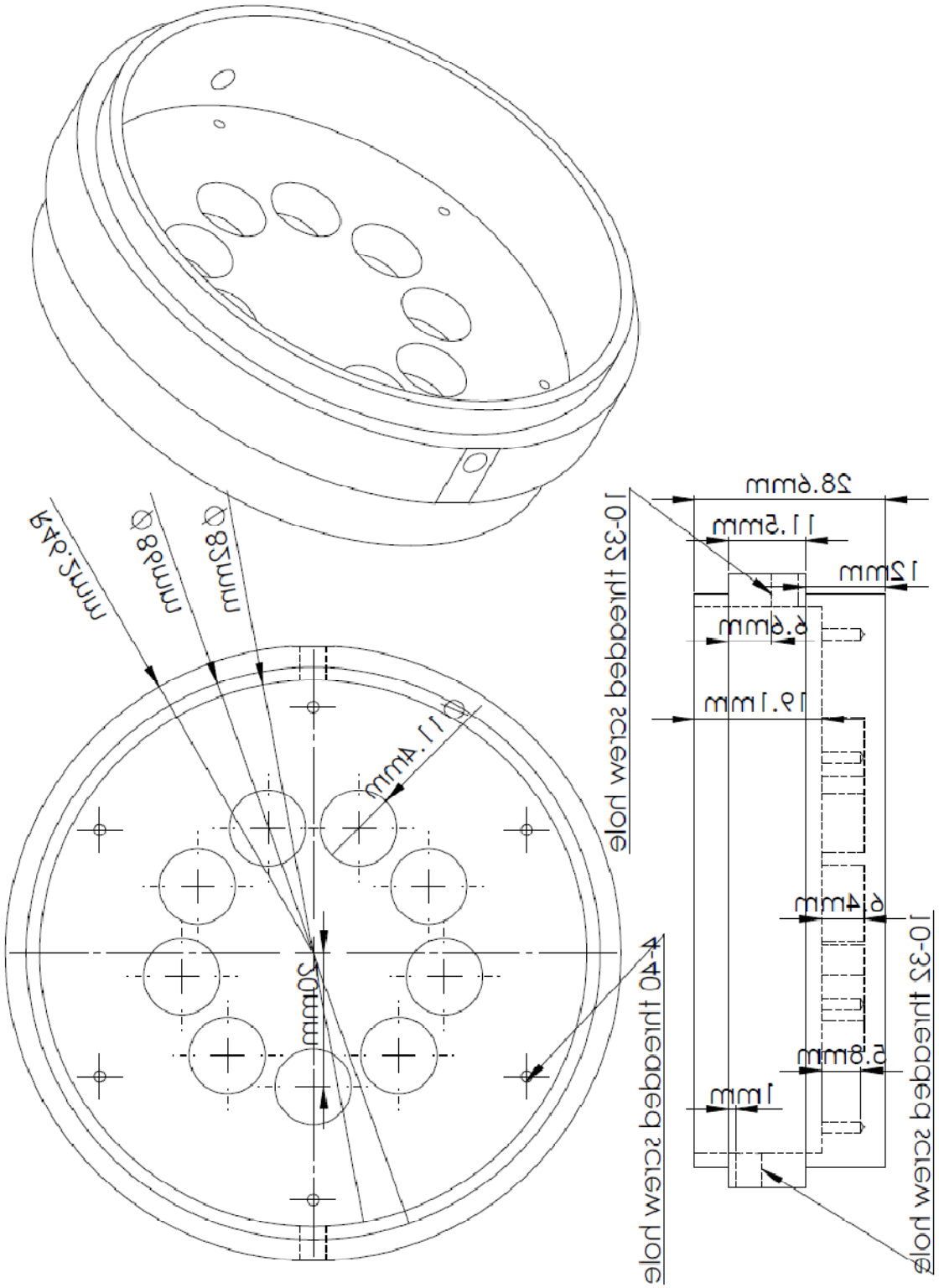

A4.6. Plate Cover

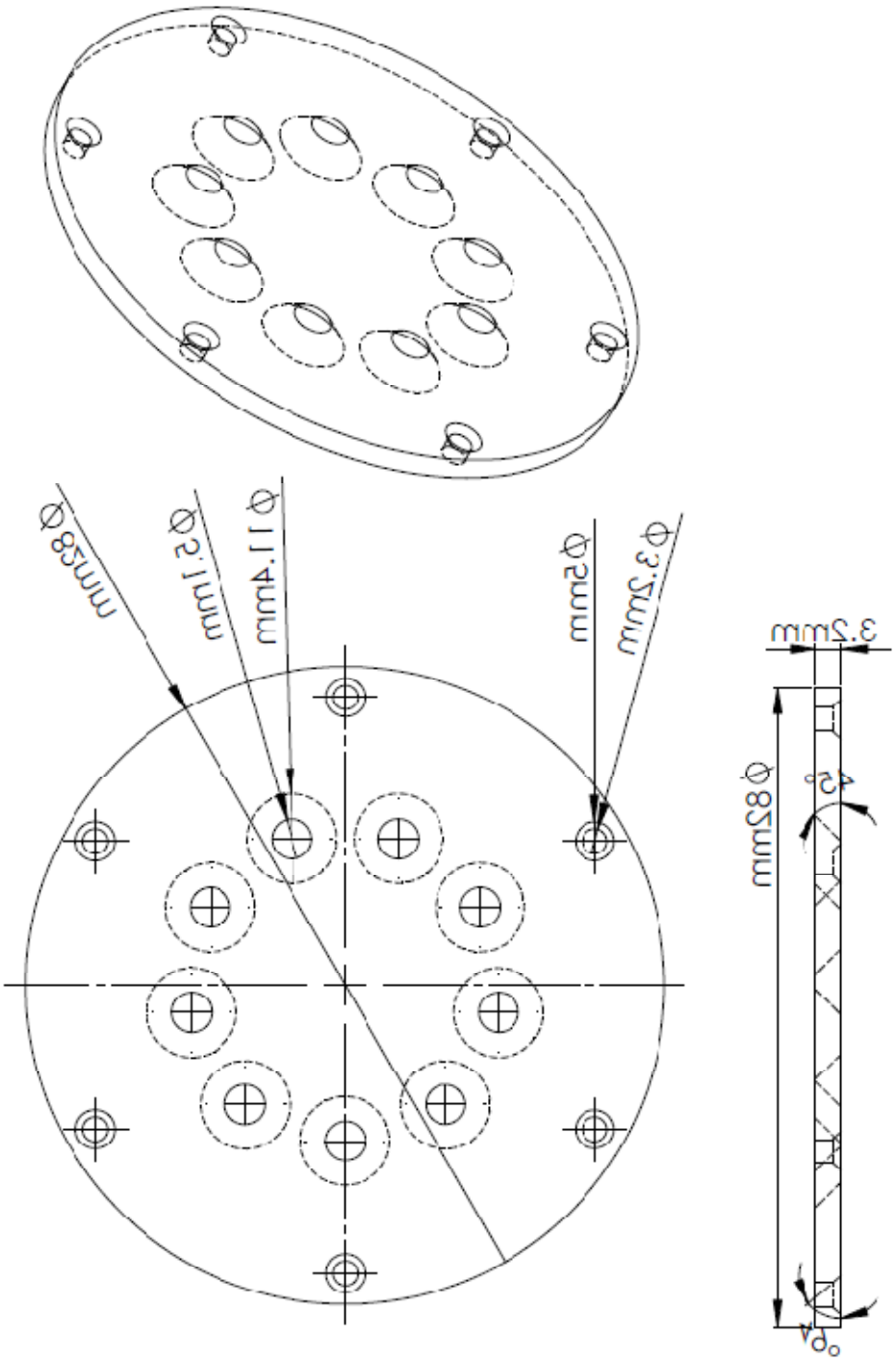

A4.7. Bioreactor Supporting Frame

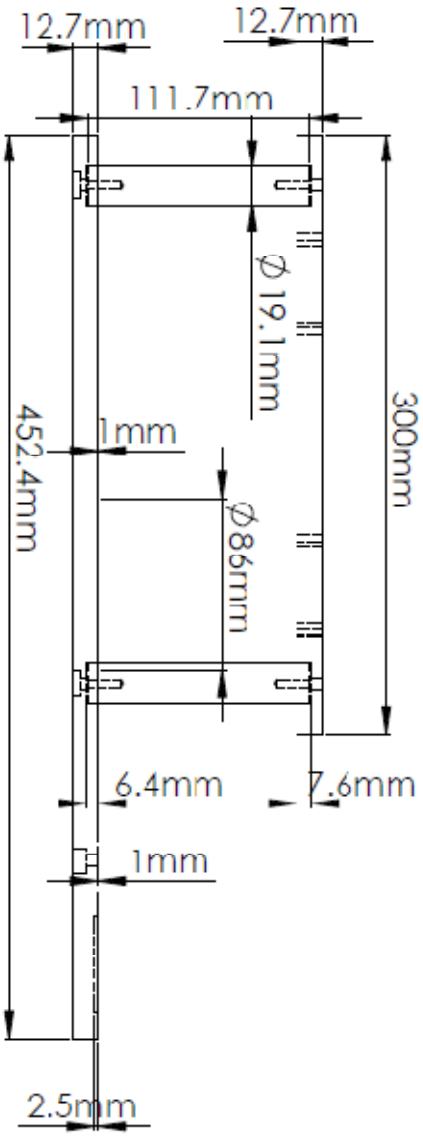

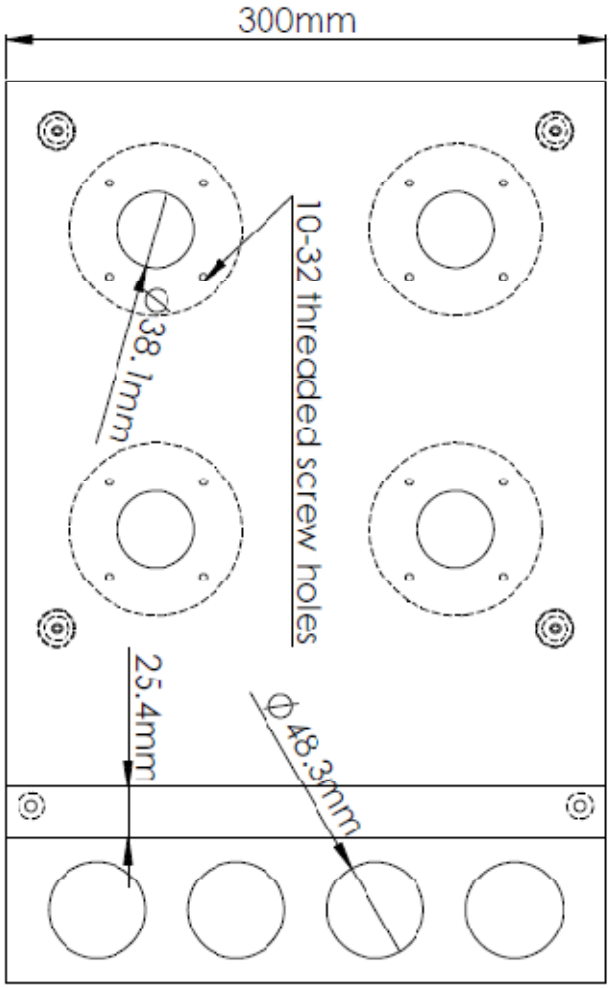

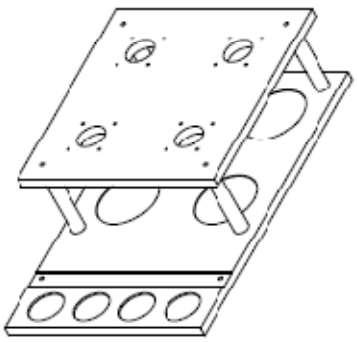

A4.8. Perfusion Reservoir

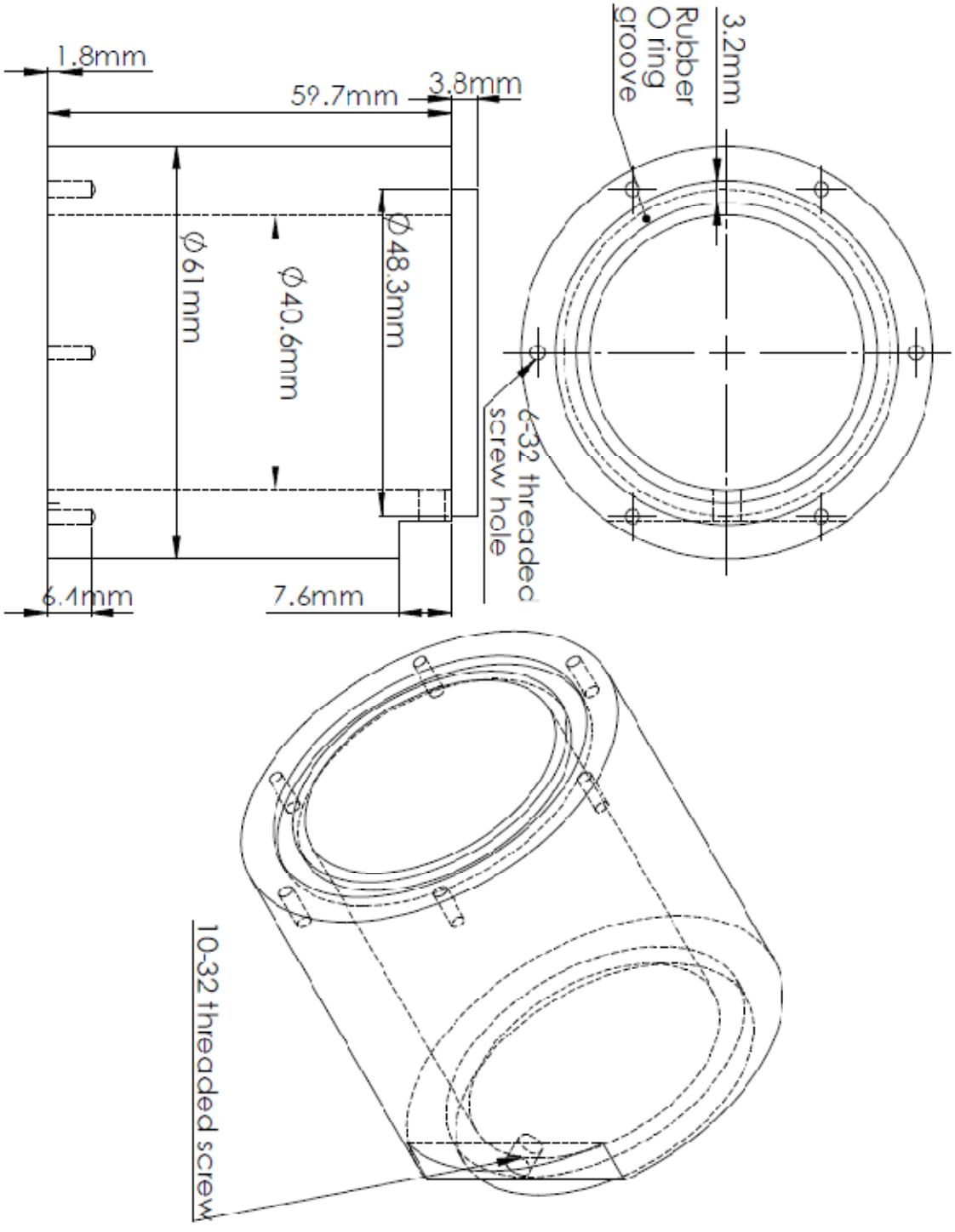

A4.9. Perfusion Reservoir Lid

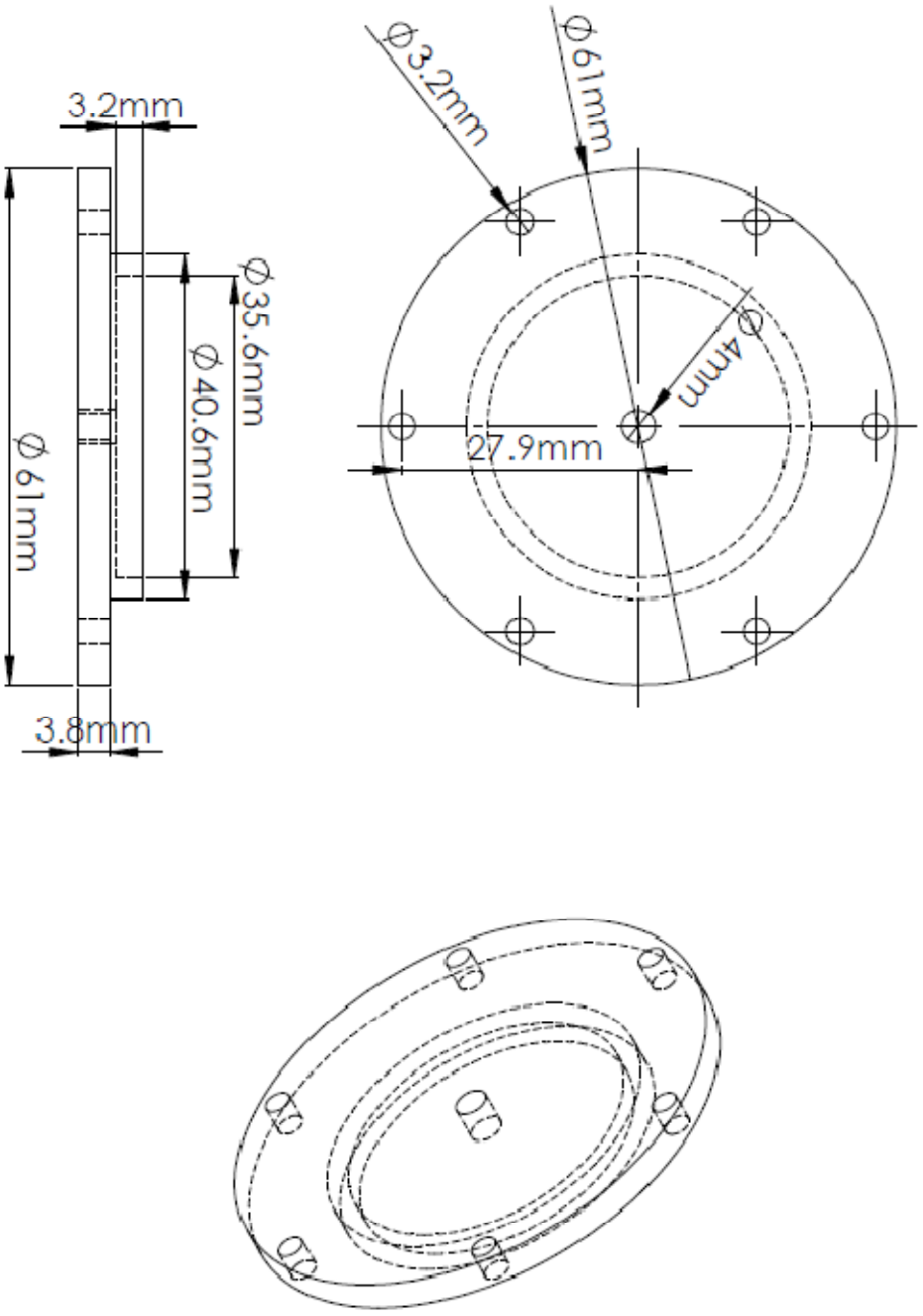

APPENDIX B

MATLAB CODES

B1. Generating Flows for Validating Order of Magnitude of Errors Associated with Probe – Leaflet Misalignment (Described in Section 5.2.3.5)

The following codes generate various flow fields of classical solutions of Navier-Stokes, and estimates the errors associated with the misalignment of the LDV probe and valve leaflet surface. Section 5.2.3.5 discusses the need for this validation.

B1.1 Cylindrical Couette Flow Simulation

This code generates the 2D Cylindrical Couette flow field, to test errors associated with a 0.15 radians LDV probe misalignment with the valve leaflet surface.

```
function couetteflow

%first generate the flow field of the theoretical Couette Flow
%then compare shear stress if LDV probe is directly perpendicular to
the
%surface versus the probe is slightly misalinged with the surface (0.15
%radians misalignment)

xrange=linspace(-0.005,0.005,200);
yrange=linspace(-0.01,-0.005,100);
[x,y]=meshgrid(xrange,yrange);
tau=100;

r=sqrt(x.^2+y.^2);
x(find(r>0.01 | r<0.007 | y==0))=NaN;
y(find(r>0.01 | r<0.007 | y==0))=NaN;
v=tau*(0.01-r);
theta=atan(x./y);
vx=v.*cos(theta);
vy=-v.*sin(theta);


alpha=0.15;
```

```
rs=linspace(0.000089,0.0018,20);
xs=rs*sin(alpha);
ys=rs*cos(alpha)-0.01;

for i=1:length(rs)
    result=interpolatehiemenz(xrange,yrange,vx,vy,xs(i),ys(i));
    vs(i)=dot(result,[cos(alpha) sin(alpha)]);
end

r0=linspace(0.000089,0.0018,20);
x0=r0*sin(0);
y0=r0*cos(0)-0.01;

for i=1:length(r0)
    result=interpolatehiemenz(xrange,yrange,vx,vy,x0(i),y0(i));
    v0(i)=result(1);
end


rs(1)=0;vs(1)=0;r0(1)=0;v0(1)=0;
figure(2)
plot([0 r0]*1000,[0 v0],'k.-','markersize',20,'linewidth',1.5)
hold on
plot([0,rs]*1000,[0,vs],'k^-','markersize',6,'markerfacecolor',[1 1
1]*0.6,'linewidth',1.5,'color',[1 1 1]*0.6)
hold off
set(gca,'fontsize',14)
H=legend('wall normal line','0.15 radians slanted line');
xlabel('Distance from wall (mm)','FontSize',14,'FontWeight','Bold')
ylabel('Measured Velocity (mm)','FontSize',14,'FontWeight','Bold')
set(H,'position',[0.4086    0.1829    0.4518    0.1238]);


taus=mean(rs(2:end)./vs(2:end));
tau0=mean(r0(2:end)./v0(2:end));
tauscorr=mean(rs(2:end)./vs(2:end)*cos(alpha)^2);
taudiff=taus-tau0;
taudiffcorr=tauscorr-tau0;
taudiffp=taudiff/tau0;
taudiffpcorr=taudiffcorr/tau0;
[taus tau0 taudiff taudiffp]
[tauscorr tau0 taudiffcorr taudiffpcorr]


plot(x0*1000,y0*1000,'k-','linewidth',2)
hold on
plot(xs*1000,ys*1000,'k--','linewidth',2)
quiver(x(:,2:5:end)*1000,y(:,2:5:end)*1000,vx(:,2:5:end),vy(:,2:5:end),
2,'showarrowhead','on','autoscale','on','color',[1 1 1]*0.6);
axis equal
angle=linspace(-3/2*pi,-1/2*pi,100);
wallx=sin(angle)*0.01*1000;
wally=cos(angle)*0.01*1000;
plot(wallx,wally,'k-','linewidth',1.5)
plot(0,-10,'k.','markersize',20)
```

```
plot(xs*1000,ys*1000,'k--','linewidth',2)
plot(x0*1000,y0*1000,'k-','linewidth',2)
hold off
set(gca,'fontsize',14);
xlabel('x-coordinate (mm)','FontSize',14,'FontWeight','Bold')
ylabel('y-coordinate (mm)','FontSize',14,'FontWeight','Bold')
axis([-3 3 -11 -6])
text(0,-10.3,sprintf('Point of shear \nstress
measurement'),'fontsize',13)
legend('wall normal line','0.15 radians slanted line')
```

B1.2 Hiemenz Flow Simulation

This code generates the 2D Himenz flow field, where flow impinges onto a wall at (0,0) coordinates. Near to this point along the wall, the velocity component impinging onto the wall is large, compared to the velocity component parallel to the wall. Further away from this point, the velocity component parallel to the wall is larger than that impinging onto the wall. Errors associated with a 0.15 radians LDV probe misalignment with the valve leaflet surface are tested at various points along the wall.

```
function hiemenzinpinge

%first generate the flow field of the theoretical Hiemenz Flow
%then compare shear stress if LDV probe is directly perpendicular to
the
%surface versus the probe is slightly misalinged with the surface (0.15
%radians misalignment)


%first get the flow fields as described by Hiemenz in impinging fows
ro=1000;
mu=3.5 *10^-6; %dynamic viscosity m2/s
B= 0.5 / 0.01; %U0/L, U0 is approaching velocity, L is length scale
numax=0.0012*sqrt(B/mu);

options = odeset('RelTol',1e-4,'AbsTol',[1e-4 1e-4 1e-5]);
[nu,F]=ode45(@dF,[0 numax],[0 0 1.23259],'options');
plot(nu,F)
y=nu/sqrt(B/mu);

numxstep=200;
x=linspace(-0.004,0.004,numxstep);
```

```
u=B*F(:,2)*x; %wall is at the top
v=-F(:,1)*sqrt(B*mu)*ones(1,numxstep);


[XX YY]=meshgrid(x,y);
plot([-0.6 -0.6],[0 0.7],'k-','linewidth',2)
hold on
plot([-0.6 -0.495],[0 0.7],'k--','linewidth',2)
quiver(XX(2:2:end)*1000,YY(2:2:end)*1000,u(2:2:end),v(2:2:end),5,'color
',[1 1 1]*0.6)
plot([-0.6 -0.6],[0 0.7],'k-','linewidth',2)
plot([-0.6 -0.495],[0 0.7],'k--','linewidth',2)
plot([-3 3],[0 0],'k-','linewidth',2)
%plot([0 0],[0 5],'k-.','linewidth',2)
plot([-3 3],[0 0],'k-','linewidth',2)
plot(0,0,'k.','markersize',20)
hold off
axis equal
axis([-1.1 1.1 -0.3 1.5])
set(gca,'fontsize',14)
xlabel('Distance from stagnation point
(mm)','FontSize',14,'FontWeight','Bold')
ylabel('Distance from Wall (mm)','FontSize',14,'FontWeight','Bold')
text(0,-0.12,sprintf('Stagnation\nPoint'),'fontsize',14)
text(-0.5, -0.05,'Wall','fontsize',14)
legend('wall normal line','0.15 radians slanted line')

mag=(u.^2+v.^2).^0.5;
figure()
surf(XX,YY,mag,'edgecolor','none');
axis equal
view([0 0 1])

%next get shears at different x locations
%assuming perfectly orthogonal to x axis

nyi=12;
xi=linspace(-0.003,0.003,90);
yi=linspace(0,0.001,nyi);

uvel=zeros(length(xi),length(yi));
for i=1:length(xi)
    for j=1:length(yi)
        result=interpolatehiemenz(XX(1,:),YY(:,1),u,v,xi(i),yi(j));
        uvel(i,j)=result(1);
        %vvel(i,j)=result(2);
    end
end

xshift=sqrt(((yi(2)-yi(1))^2)*9/409)*[0:nyi-1];
yishifted=sqrt(((yi(2)-yi(1))^2)*400/409)*[0:nyi-1];
unitvec=[20,-3]/norm([20,-3]);

uvelslant=zeros(length(xi),length(yi));
```

```
for i=1:length(xi)
    for j=1:length(yi)
        result=interpolatehiemenz(XX(1,:),YY(:,1),u,v,xi(i)-
xshift(j),yishifted(j));
        uvelslant(i,j)=result(1);
        vvelslant(i,j)=result(2);
        mvel(i,j)=dot([uvelslant(i,j),vvelslant(i,j)],unitvec);
    end
end

for i=1:length(xi)
    plot(yi,uvel(i,:),'.')
    hold on
    plot(yi,mvel(i,:),'r.')
    hold off
    input(num2str(i));
end

for i=1:length(xi)
    grad(i)=uvel(i,2)/yi(2);
    gradslant(i)=mvel(i,2)/yi(2);
    gradslantcorr(i)=gradslant(i)/cos(atan(0.1))^2;
end
plot(xi,grad/100)
hold on
plot(xi,gradslant/100,'r')
plot(xi,gradslantcorr/100,'k')
hold off

mudynamic=0.001;
figure()
plot(xi*1000,(grad)*mudynamic*10,'k.')
hold on
plot([-0.17 -0.17],[-10 10],'k-.','linewidth',0.9)
plot([0.3 0.3],[-10 10],'k-.','linewidth',0.9)
plot([-3 3],[0 0],'k-','linewidth',0.9)
plot([0 0],[-10 10],'k-','linewidth',0.9)
surf([-0.17 0.3;-0.17 0.3],[10 10;-10 -10],ones(2)*-
1,'edgecolor','none')
colormap(gray)
caxis([-5 0])
hold off
set(gca,'fontsize',14)
axis([-3 3 -10 10])
xlabel('Distance from stagnation point
(mm)','FontSize',14,'FontWeight','Bold')
ylabel('Shear Stress (dyn/cm^2)','FontSize',14,'FontWeight','Bold')

figure()
plot(xi*1000,(gradslantcorr-grad)*mudynamic*10,'k.')
hold on
plot([-0.17 -0.17],[-0.1 0.1],'k-.','linewidth',0.9)
plot([0.3 0.3],[-0.1 0.1],'k-.','linewidth',0.9)
plot([-3 3],[0 0],'k-','linewidth',0.9)
plot([0 0],[-0.1 0.1],'k-','linewidth',0.9)
```

```
surf([-0.17 0.3;-0.17 0.3],[0.1 0.1;-0.1 -0.1],ones(2)*-
1,'edgecolor','none')
colormap(gray)
caxis([-5 0])
hold off
set(gca,'fontsize',14)
axis([-3 3 -0.1 0.1])
xlabel('Distance from stagnation point
(mm)','FontSize',14,'FontWeight','Bold')
ylabel('Absolute Error (dyn/cm^2)','FontSize',14,'FontWeight','Bold')

figure()
plot(xi*1000,(gradslantcorr-grad)./(grad)*100,'k.')
hold on
plot([-0.17 -0.17],[-50 50],'k-.','linewidth',0.9)
plot([0.3 0.3],[-50 50],'k-.','linewidth',0.9)
plot([-3 3],[0 0],'k-','linewidth',0.9)
plot([0 0],[-50 50],'k-','linewidth',0.9)
surf([-0.17 0.3;-0.17 0.3],[50 50;-50 -50],ones(2)*-
1,'edgecolor','none')
colormap(gray)
caxis([-5 0])
hold off
set(gca,'fontsize',14)
axis([-3 3 -25 25])
xlabel('Distance from stagnation point
(mm)','FontSize',14,'FontWeight','Bold')
ylabel('Percentage Error (%)','FontSize',14,'FontWeight','Bold')
```

B1.3 Subroutine to codes in B1.1 and B1.2

```
function result=interpolatehiemenz(XX,YY,u,v,xi,yi)

%subroutine

nx=find(XX>xi,1,'first');
XXupper=XX(nx);
XXlower=XX(nx-1);

ny=find(YY>yi,1,'first');
YYupper=YY(ny);
YYlower=YY(ny-1);

u1=u(ny-1,nx-1);
u2=u(ny-1,nx);
u3=u(ny,nx-1);
u4=u(ny,nx);
v1=v(ny-1,nx-1);
v2=v(ny-1,nx);
v3=v(ny,nx-1);
v4=v(ny,nx);

r=(xi-XXlower)/(XXupper-XXlower)*2-1;
```

```
s=(yi-YYlower)/(YYupper-YYlower)*2-1;

N1=(1-r)*(1-s)/4;
N2=(1+r)*(1-s)/4;
N3=(1-r)*(1+s)/4;
N4=(1+r)*(1+s)/4;

ui=N1*u1+N2*u2+N3*u3+N4*u4;
vi=N1*v1+N2*v2+N3*v3+N4*v4;

result=[ui,vi];
```

B2. Back-Scattered Light Position Tracking Code (Described in Section 5.2.3)

This code tracks surface of dynamic objects using the back-scattered light intensity method described in section 5.2.3. This code can be used for the validation experiment for the method. The first part of the code tracks the position of the pump head of a piston pump, and the second part of the code calculates the output from the position sensor of the piston pump. The first part of the code can also be used for tracking aortic valve leaflets in actual shear stress measurement experiments.

```
function dynleaflettrack

%this code is used to track the location of the piston pump head
%which is set to move in a perfectly sinusoidal motion of 2mm amplitude
by
%the signal generator
%the piston pump head was tracked with the back-scattered LDV laser
light
%intensity method
%This code however, is directly applicable to valve leaflets

path ='C:\ LDV work\2011jan13-dynamic leaflet tracking validation';
pathout='C:\LDV work\2011jan13-dynamic leaflet tracking validation';
file='PMT-';
file2='sensor-';

B=[];
loc=[];
time=[2:2:1000]';

for i=6500:25:8750
```

```
    i
    loc=[loc i];

    A=dlmread([path '\' file sprintf('%4.4d',i) '.txt']);
    [s1 s2]=size(A);
    A=A(:,2:s2);

    G=mean(A')';
    B=[B G];
end

XX=ones(length(time),1)*(loc*0.0892/25-27.6506);
YY=time*ones(1,length(loc));
figure(1)
mesh(XX,YY,B);
view([0,0,1])

figure(2)

[ss1 ss2]=size(B);
t=1:ss2;
for i=1:ss1
    if i==1
        C=mean([B(i:i+2,:); B(end-1:end,:)])';
    elseif i==2
        C=mean([B(i-1:i+2,:); B(end,:)])';
    elseif i==ss1-1
        C=mean([B(1,:); B(i-2:end,:)])';
    elseif i==ss1
        C=mean([B(1:2,:); B(i-2:end,:)])';
    else
        C=mean(B(i-2:i+2,:))';
    end

    C2=fouriersmooth4(C,20,2000)';
    loc2=linspace(loc(1),loc(end),2000);
    location(i)=loc2(find(C2==max(C2)));

    plot([location(i) location(i)],[0 1],'r');
    hold on;
    plot(loc,C','g');
    plot(loc2,C2','k');
    hold off;
    input(''); %use this line if you want to observe peak finding
end

plot(location)
location2=location/25*0.0635;
dlmwrite([pathout '\PMTtrackout.txt'],location2', 'delimiter',
'','newline', 'pc','precision','%15.10f');


%This portion of the code is for analyzing the signals from the
position tracker
```

```
%of the piston pump head motion, to be compared to the back-scattered
light
%tracking method results. This section is not normally used when
applied to the
%actual valve leaflets
DD=[];
for i=6500:25:8750
    i
    loc=[loc i];

    A=dlmread([path '\' file2 sprintf('%4.4d',i) '.txt']);
    [s1 s2]=size(A);
    A=A(:,2:s2);

    G=mean(A')';
    DD=[DD G];
end

DDm=mean(DD,2);
plot(DDm)
dlmwrite([pathout '\sensortrackout.txt'],DDm, 'delimiter', '','newline',
'pc','precision','%15.10f');


%review it
L=dlmread([pathout '\PMTtrackout.txt']);
S=dlmread([pathout '\sensortrackout.txt']);
%manual calibration: calibration for position sensor is that the
waveform
% should be +- 2mm from mean position.

S2=S-mean(S);
S2=S2/max(abs(S2));
S2=S2*2; %mm

L2=L-mean(L); %mm

plot([2:2:1000],S2,'k-','linewidth',2)
hold on
plot([2:2:1000],L2(1:1:end),'k-.','color',[1 1
1]*0.5,'linewidth',2,'markersize',15)
hold off
legend(sprintf('Position sensor\noutput') ,sprintf('Backscattered
light\ntracking method output'))
set(gca,'fontsize',14)
axis([0 1000 -2.5 2.5])
grid on
xlabel('Cycle Time (ms)','FontSize',14,'FontWeight','Bold')
ylabel('Position of Piston Head (mm)','FontSize',14,'FontWeight','Bold')
```

B3. Codes for Obtaining Ventricular Shear Stresses From the Polymeric Valves

B3.1 Overall Code for Plotting All results (Described in section 5.2.4)

This code plots all ventricular shear stress data measured from the polymeric valves (methods are described in section 5.2.4), as well as the output from the theoretical modeling of ventricular shear stress (described in section 5.4). It also plots the comparison of measured data and output from the theoretical modeling.

```
function analyze_valve_model1

%plot ventricular shear stresses for valve model 1 compared to flow
curve,
%measured flow profiles;
%Womersley shear stress solution for valve model 1;
%and Womersley solution flow profiles.


flow=dlmread('C:\Users\Yap\Desktop\PIV lab\LDV work\May09-
polymericLDV\polymeric LDV hemo\flow.txt');
s1=dlmread('C:\Users\Yap\Desktop\PIV lab\LDV work\May09-
polymericLDV\c\shearstress_corrected.txt');
s2=dlmread('C:\Users\Yap\Desktop\PIV lab\LDV work\May09-
polymericLDV\e\shearstress_corrected.txt');
s3=dlmread('C:\Users\Yap\Desktop\PIV lab\LDV work\May09-
polymericLDV\f\shearstress_corrected.txt');
Wom=modifiedwomersley4(1);

figure(2)
[AX,H1,H2]=plotyy(s2(9:37,1)+25,s2(9:37,2),[2:2:860],flow);
hold on
plot(s1(9:37,1)+25,s1(9:37,2),'-','LineWidth',2,'Color',[1 1 1]*0.3)
plot(Wom(:,1),Wom(:,2),'-.','Color',[1 1 1]*0.7, 'LineWidth',2)
hold off
set(AX(1),'Ycolor','k','FontSize',14)
set(AX(2),'Ycolor','k','FontSize',14)
set(H1,'LineStyle','-','Color',[1 1 1]*0,'LineWidth',2)
set(H2,'Color',[1 1 1]*0.5,'LineWidth',2,'LineStyle','--')
set(AX(1),'XLim',[0 860])
set(AX(2),'XLim',[0 860])
set(AX(2),'YLim',[-25 25])
set(AX(1),'YLim',[-100 100])
set(get((AX(1)),'Ylabel'),'String','Shear Stress
(dyn/cm^2)','FontSize',14,'FontWeight','Bold')
```

```
set(get((AX(2)),'Ylabel'),'String','Volumetric Flow Rate
(L/min)','FontSize',14,'FontWeight','Bold')
xlabel('Time (ms)','FontSize',14,'FontWeight','Bold')
set(AX(1),'YTick',[-100:20:100])
set(AX(2),'YTick',[-25:5:25])
H=Legend('Shear stress pt 1','Shear stress pt 2','Simulation','Flow');
hold on
plot([0 860],[0 0],'k','LineWidth',1)
hold off

A=dlmread('C:\Users\Yap\Desktop\PIV lab\LDV work\May09-
polymericLDV\poly1g\1gleafletlocation.txt');
d=0.088458405;
A=A/25*d;
figure()
plot([2:2:860],A-min(A),'-.','LineWidth',2)
set(gca,'FontSize',14);
xlabel('Time (ms)','FontSize',14,'FontWeight','Bold')
ylabel('Position from Closed Position
(mm)','FontSize',14,'FontWeight','Bold')
axis([0 860 -1 8])

%plot non-streamwise
sld=dlmread('C:\Users\Yap\Desktop\PIV lab\LDV work\May09-
polymericLDV\d\P1d-V-shearstress.txt');
[AX,H1,H2]=plotyy(s1(9:37,1)+25,s1(9:37,2),[2:2:860],flow);
hold on
plot([9:37]*10+25,sld(9:37),'-.','LineWidth',2,'Color',[1 1 1]*0.3)
hold off
set(AX(1),'Ycolor','k','FontSize',14)
set(AX(2),'Ycolor','k','FontSize',14)
set(H1,'LineStyle','-','Color',[1 1 1]*0,'LineWidth',2)
set(H2,'Color',[1 1 1]*0.5,'LineWidth',2,'LineStyle','--')
set(AX(1),'XLim',[0 860])
set(AX(2),'XLim',[0 860])
set(AX(2),'YLim',[-15 25])
set(AX(1),'YLim',[-60 100])
set(get((AX(1)),'Ylabel'),'String','Shear Stress
(dyn/cm^2)','FontSize',14,'FontWeight','Bold')
set(get((AX(2)),'Ylabel'),'String','Volumetric Flow Rate
(L/min)','FontSize',14,'FontWeight','Bold')
xlabel('Time (ms)','FontSize',14,'FontWeight','Bold')
set(AX(1),'YTick',[-60:20:100])
set(AX(2),'YTick',[-15:5:25])
H=Legend('Streamwise shear stress','Non-streamwise shear
stress','Flow');
set(H,'FontSize',11)
hold on
plot([0 860],[0 0],'k','LineWidth',1)
hold off

%compare with Wom
n=find(s1(:,2)~=0);
for i=1:length(n)
    m=find(Wom(:,1)>s1(n(i),1),1,'first')
    if Wom(m,1)~=s1(n(i),1)
```

```
        w=(Wom(m,2)+Wom(m-1,2))/2;
    else
        w=Wom(m,2);
    end
    comp(n(i))=s1(n(i),2)/Wom(m,2);
end


%this is to get the difference between the average shear stress of the
%2 points and the Womersley solution
sa=(s1+s2)/2;
sa(:,1)=sa(:,1)+24;
W=[0 0; Wom; 0 0];
diff=[];
for i=1:86
    n=find(W(:,1)==sa(i,1));
    if ~isempty(n)
        temp=mean(W(n-1:n+1,2));
        diff=[diff; sa(i,1) sa(i,2)-temp];
    end
end

%plot all again
sld=dlmread('C:\Users\Yap\Desktop\PIV lab\LDV work\May09-
polymericLDV\d\P1d-V-shearstress.txt');
figure(1)
[AX,H1,H2]=plotyy(s2(9:37,1)+25,s2(9:37,2),[2:2:860],flow);
hold on
plot(s1(9:37,1)+25,s1(9:37,2),'-','LineWidth',2,'Color',[1 1 1]*0.4)
plot(Wom(:,1),Wom(:,2),'-.','Color',[1 1 1]*0.7, 'LineWidth',2)
plot([9:37]*10+25,sld(9:37),'-.','LineWidth',2,'Color',[1 1 1]*0.3)
hold off
set(AX(1),'Ycolor','k','FontSize',14)
set(AX(2),'Ycolor','k','FontSize',14)
set(H1,'LineStyle','-','Color',[1 1 1]*0,'LineWidth',2)
set(H2,'Color',[1 1 1]*0.5,'LineWidth',2,'LineStyle','--')
set(AX(1),'XLim',[0 860])
set(AX(2),'XLim',[0 860])
set(AX(2),'YLim',[-25 25])
set(AX(1),'YLim',[-100 100])
set(get((AX(1)),'Ylabel'),'String','Shear Stress
(dyn/cm^2)','FontSize',14,'FontWeight','Bold')
set(get((AX(2)),'Ylabel'),'String','Volumetric Flow Rate
(L/min)','FontSize',14,'FontWeight','Bold')
xlabel('Time (ms)','FontSize',14,'FontWeight','Bold')
set(AX(1),'YTick',[-100:20:100])
set(AX(2),'YTick',[-25:5:25])
H=Legend('Shear stress pt 1','Shear stress pt 2','Simulation','Non-
stream-wise shear stress pt 2','Flow');
set(H,'fontsize',11)
hold on
plot([0 860],[0 0],'k','LineWidth',1)
hold off
```

B3.2 Code for Calculating Ventricular Surface Shear Stresses Based on the Theoretical Womersley Solution for Pipe Flow (Described in Section 5.4)

This program calculates the ventricular surface shear stresses based on the theoretical Womersley Solution described in section 5.4. It acts as a subroutine to code B3.1.

```
function results=modifiedwomersley4(num,flowfile)

%this program divides a bulk flow Q(t) into frequency components
%seeks the Wormersley solution for all freq components
%and combines them together to yield the flow profile v(t,r)
%and then provide wall shear

%cutoff freq
freq=50;
%flow profile resolution
spp=200;

if nargin==0
    num==2;
    flowfile='';
end

if nargin==1
    flowfile='';
end

if num==1
    flow=dlmread('ventrshearstressflow.txt');
elseif num==2
    flow=dlmread('flow.txt');
elseif num>2
    flow=flowfile;
end

%flow(220:end)=0;
flow=(flow)/1000/60; %change L/min to m3/s
Nt=length(flow);
Q0=mean(flow);
Q=flow-Q0;
dt=0.002;
T=0.86;
```

```
t=[1:Nt]*dt;
w=2*pi/T;

for i=1:freq %freq
    %a(i)=0;
    %b(i)=0;
    c(i)=0;
    for j=1:Nt %timestep
        %a(i)=a(i)+Q(j)*cos(i*w*t(j));
        %b(i)=b(i)+Q(j)*sin(i*w*t(j));
        c(i)=c(i)+Q(j)*exp(-i*w*t(j)*sqrt(-1));
    end
end
%a=a*dt*2/T;
%b=b*dt*2/T;
c=c*dt*2/T;


%------check if DFT was done properly
for i=1:Nt %timestep
   Qr(i)=0;
   Qrr(i)=0;
   for j=1:freq %freq
       %Qr(i)=Qr(i)+a(j)*cos(j*w*t(i))+b(j)*sin(j*w*t(i));
       Qrr(i)=Qrr(i)+c(j)*exp(j*w*t(i)*sqrt(-1));
   end
end
% figure(1)
% plot(Qr,'r*-')
% hold on
% plot(real(Qrr)+Q0,'k^-')
% plot(Q+Q0)
% hold off
% input(' ');


%-----------------

if num==1 | num==2
    R=10/1000; %m
elseif num==3
    R=9/1000; %m
elseif num==4
    R=12/1000; %m
end
ro=1000; %kg/m3
mu=3.5/1000000; %m2/s
umu=3.5/1000; %kinematic
r=linspace(0,R,100);

Ta0=Q0/R^3/pi*4*umu;
v0=Q0*2/pi/R^2*(1-r.^2/R^2);
P0=Q0*8*umu/pi/R^4;
for i=1:freq
    aa(i)=R*sqrt(i*w/mu);
```

```
    term1(i)=1-2*besselj(1,sqrt(-1)^1.5*aa(i))/sqrt(-
1)^1.5/besselj(0,sqrt(-1)^1.5*aa(i))/aa(i);
    dP(i)=c(i)*sqrt(-1)*umu*aa(i)^2/pi/R^4/term1(i);
    %term2(i)=(1-term1(i))/2/aa(i);
    term2(i)=besselj(1,sqrt(-1)^1.5*aa(i))/sqrt(-
1)^1.5/aa(i)/besselj(0,sqrt(-1)^1.5*aa(i));
    term3(i,:)=1-besselj(0,sqrt(-1)^1.5*aa(i)*r/R)/besselj(0,sqrt(-
1)^1.5*aa(i));
end
for i=1:Nt
    Shear(i)=0;
    QQ(i)=0;
    vv(i,:)=v0;
    P(i)=0;
    for j=1:freq
        Shear(i)=Shear(i)+R*dP(j)*term2(j)*exp(j*w*t(i)*sqrt(-1));
        QQ(i)=QQ(i)+pi*R^4*dP(j)/sqrt(-
1)/umu/aa(j)^2*term1(j)*exp(j*w*t(i)*sqrt(-1));
        vv(i,:)=vv(i,:)+R^2*dP(j)/sqrt(-
1)/umu/aa(j)^2*term3(j,:)*exp(j*w*t(i)*sqrt(-1));
        P(i)=P(i)+dP(j)*exp(j*w*t(i)*sqrt(-1));
    end
end
QQ=QQ+Q0;
Shear=Shear+Ta0;
P=P+P0;

%plot
figure()
time3=[2:2:860];
if num==1
    results=[time3(45:219)' real(Shear(45:219)')*10];

[AX,H1,H2]=plotyy(time3(45:219),real(Shear(45:219))*10,time3,real(flow)
*1000*60);
elseif num==2
    results=[time3(30:207)' real(Shear(30:207)')*10];

[AX,H1,H2]=plotyy(time3(30:207),real(Shear(30:207))*10,time3,real(flow)
*1000*60);
elseif num==3
    results=[time3(15:165)' real(Shear(15:165)')*10];

[AX,H1,H2]=plotyy(time3(15:165),real(Shear(15:165))*10,time3,real(flow)
*1000*60);
elseif num==4
    results=[time3(15:180)' real(Shear(15:180)')*10];

[AX,H1,H2]=plotyy(time3(15:180),real(Shear(15:180))*10,time3,real(flow)
*1000*60);
end
set(AX(1),'Ycolor','k','FontSize',14)
set(AX(2),'Ycolor','k','FontSize',14)
set(H1,'Color','k','LineWidth',2)
set(H2,'Color','k','LineWidth',2,'LineStyle','--')
set(AX(1),'XLim',[0 860])
set(AX(2),'XLim',[0 860])
```

```
if num==4
    set(AX(2),'YLim',[-15 35])
    set(AX(1),'YLim',[-60 140])
elseif num==3
    set(AX(2),'YLim',[-10 25])
    set(AX(1),'YLim',[-60 150])
else
    set(AX(2),'YLim',[-15 25])
    set(AX(1),'YLim',[-90 150])
end
% set(AX(2),'YLim',[-1 3])
set(get((AX(1)),'Ylabel'),'String','Shear Stress
(dyn/cm^2)','FontSize',14,'FontWeight','Bold')
set(get((AX(2)),'Ylabel'),'String','Volumetric Flow Rate
(L/min)','FontSize',14,'FontWeight','Bold')
xlabel('Time (ms)','FontSize',14,'FontWeight','Bold')
LL=legend('Streamwise Shear Stress','Flow Rate');
set(LL,'Position',[0.4454    0.7400    0.4407    0.1526],'FontSize',12)
if num==4
    set(AX(1),'YTick',[-60:20:140])
    set(AX(2),'YTick',[-20:5:35])
elseif num==3
    set(AX(1),'YTick',[-90:30:150])
    set(AX(2),'YTick',[-15:5:25])
else
    set(AX(1),'YTick',[-90:30:150])
    set(AX(2),'YTick',[-15:5:25])
end
hold on
plot([0 860],[0 0],'k-','LineWidth',1)
hold off


%compare flow profiles
figure()
if num==1 | num==2
    mvv=(max(real(vv)'));
    for i=1:430
        vv2(i,:)=real(vv(i,:))/mvv(i);
    end
    plot([99:-1:0]/100,vv2(75,:)','Color',[1 1 1]*0,'LineStyle','-
','LineWidth',1.5)
    hold on
    plot([99:-1:0]/100,vv2(100,:)','Color',[1 1 1]*0.5,'LineStyle','-
','LineWidth',1.5)
    plot([99:-1:0]/100,vv2(125,:)','Color',[1 1 1]*0,'LineStyle','--
','LineWidth',1.5)
    plot([99:-1:0]/100,vv2(150,:)','Color',[1 1 1]*0.5,'LineStyle','--
','LineWidth',1.5)
    plot([99:-1:0]/100,vv2(175,:)','Color',[1 1 1]*0,'LineStyle','-
.','LineWidth',1.5)
    plot([99:-1:0]/100,vv2(190,:)','Color',[1 1 1]*0.5,'LineStyle','-
.','LineWidth',1.5)
    if num==1
        plot([99:-1:0]/100,vv2(200,:)','Color',[1 1
1]*0,'LineStyle',':','LineWidth',1.5)
```

```
    end
    hold off
    H=legend('Time = 150ms','Time = 200ms','Time = 250ms','Time =
300ms','Time = 350ms','Time = 380ms','Time = 400ms');
    set(gca,'FontSize',14)
    xlabel('Normalized Distance','FontSize',14,'FontWeight','Bold')
    ylabel('Normalized Velocity','FontSize',14,'FontWeight','Bold')
    set(H,'Position',[ 0.5345 0.1794 0.3232 0.4222],'FontSize',12);
    axis([0 1 -0.8 1.2])
end

if num==3
    mvv=(max(real(vv)'));
    for i=1:430
        vv2(i,:)=real(vv(i,:))/mvv(i);
    end
    plot([99:-1:0]/100,vv2(20,:)','Color',[1 1 1]*0,'LineStyle','-
','LineWidth',1.5)
    hold on
    plot([99:-1:0]/100,vv2(45,:)','Color',[1 1 1]*0.5,'LineStyle','-
','LineWidth',1.5)
    plot([99:-1:0]/100,vv2(70,:)','Color',[1 1 1]*0,'LineStyle','--
','LineWidth',1.5)
    plot([99:-1:0]/100,vv2(95,:)','Color',[1 1 1]*0.5,'LineStyle','--
','LineWidth',1.5)
    plot([99:-1:0]/100,vv2(120,:)','Color',[1 1 1]*0,'LineStyle','-
.','LineWidth',1.5)
    plot([99:-1:0]/100,vv2(145,:)','Color',[1 1 1]*0.5,'LineStyle','-
.','LineWidth',1.5)
    hold off
    H=legend('Time = 40ms','Time = 90ms','Time = 140ms','Time =
190ms','Time = 240ms','Time = 290ms');
    set(gca,'FontSize',14)
    xlabel('Normalized Distance
(Radius)','FontSize',14,'FontWeight','Bold')
    ylabel('Normalized Velocity','FontSize',14,'FontWeight','Bold')
    set(H,'Position',[ 0.5345 0.1794 0.3232 0.4222],'FontSize',12);
    axis([0 1 -0.6 1.2])
end

if num==4
    mvv=(max(real(vv)'));
    for i=1:430
        vv2(i,:)=real(vv(i,:))/mvv(i);
    end
    plot([99:-1:0]/100,vv2(20,:)','Color',[1 1 1]*0,'LineStyle','-
','LineWidth',1.5)
    hold on
    plot([99:-1:0]/100,vv2(45,:)','Color',[1 1 1]*0.5,'LineStyle','-
','LineWidth',1.5)
    plot([99:-1:0]/100,vv2(70,:)','Color',[1 1 1]*0,'LineStyle','--
','LineWidth',1.5)
    plot([99:-1:0]/100,vv2(95,:)','Color',[1 1 1]*0.5,'LineStyle','--
','LineWidth',1.5)
    plot([99:-1:0]/100,vv2(120,:)','Color',[1 1 1]*0,'LineStyle','-
.','LineWidth',1.5)
```

```
    plot([99:-1:0]/100,vv2(145,:)','Color',[1 1 1]*0.5,'LineStyle','-
.','LineWidth',1.5)
    plot([99:-1:0]/100,vv2(165,:)','Color',[1 1 1]*0.5,'LineStyle','-
.','LineWidth',1.5)
    hold off
    H=legend('Time = 40ms','Time = 90ms','Time = 140ms','Time =
190ms','Time = 240ms','Time = 290ms','Time = 330ms');
    set(gca,'FontSize',14)
    xlabel('Normalized Distance
(Radius)','FontSize',14,'FontWeight','Bold')
    ylabel('Normalized Velocity','FontSize',14,'FontWeight','Bold')
    set(H,'Position',[ 0.5345 0.1794 0.3232 0.4222],'FontSize',12);
    axis([0 1 -0.6 1.2])
end

%plot real unnormalized profile
if num==1 | num==2
    plot([99:-1:0]/100,real(vv(75,:))','Color',[1 1 1]*0,'LineStyle','-
','LineWidth',1.5)
    hold on
    plot([99:-1:0]/100,real(vv(100,:))','Color',[1 1
1]*0.5,'LineStyle','-','LineWidth',1.5)
    plot([99:-1:0]/100,real(vv(125,:))','Color',[1 1
1]*0,'LineStyle','--','LineWidth',1.5)
    plot([99:-1:0]/100,real(vv(150,:))','Color',[1 1
1]*0.5,'LineStyle','--','LineWidth',1.5)
    plot([99:-1:0]/100,real(vv(175,:))','Color',[1 1
1]*0,'LineStyle','-.','LineWidth',1.5)
    plot([99:-1:0]/100,real(vv(190,:))','Color',[1 1
1]*0.5,'LineStyle','-.','LineWidth',1.5)
    if num==1
        plot([99:-1:0]/100,real(vv(200,:))','Color',[1 1
1]*0,'LineStyle',':','LineWidth',1.5)
    end
    hold off
    H=legend('Time = 150ms','Time = 200ms','Time = 250ms','Time =
300ms','Time = 350ms','Time = 380ms','Time = 400ms');
    set(gca,'FontSize',14)
    xlabel('Distance from Wall
(Radius)','FontSize',14,'FontWeight','Bold')
    ylabel('Velocity (m/s)','FontSize',14,'FontWeight','Bold')
    if num==2
        set(H,'Position',[  0.6086  0.1342 0.2821
0.3063],'FontSize',12);
    elseif num==1
        set(H,'Position',[  0.6086  0.1215 0.2821
0.3063],'FontSize',12);
    end
    axis([0 0.5 -0.5 1.5])
end

if num==3
    plot([99:-1:0]/100,real(vv(20,:))','Color',[1 1 1]*0,'LineStyle','-
','LineWidth',1.5)
    hold on
```

```
    plot([99:-1:0]/100,real(vv(45,:))','Color',[1 1
1]*0.5,'LineStyle','-','LineWidth',1.5)
    plot([99:-1:0]/100,real(vv(70,:))','Color',[1 1 1]*0,'LineStyle','-
-','LineWidth',1.5)
    plot([99:-1:0]/100,real(vv(95,:))','Color',[1 1
1]*0.5,'LineStyle','--','LineWidth',1.5)
    plot([99:-1:0]/100,real(vv(120,:))','Color',[1 1
1]*0,'LineStyle','-.','LineWidth',1.5)
    plot([99:-1:0]/100,real(vv(145,:))','Color',[1 1
1]*0.5,'LineStyle','-.','LineWidth',1.5)
    hold off
    H=legend('Time = 40ms','Time = 90ms','Time = 140ms','Time =
190ms','Time = 240ms','Time = 290ms');
    set(gca,'FontSize',14)
    xlabel('Distance from Wall
(Radius)','FontSize',14,'FontWeight','Bold')
    ylabel('Velocity (m/s)','FontSize',14,'FontWeight','Bold')
    axis([0 0.5 -0.5 1.5])
end

if num==4
    plot([99:-1:0]/100,real(vv(20,:))','Color',[1 1 1]*0,'LineStyle','-
','LineWidth',1.5)
    hold on
    plot([99:-1:0]/100,real(vv(45,:))','Color',[1 1
1]*0.5,'LineStyle','-','LineWidth',1.5)
    plot([99:-1:0]/100,real(vv(70,:))','Color',[1 1 1]*0,'LineStyle','-
-','LineWidth',1.5)
    plot([99:-1:0]/100,real(vv(95,:))','Color',[1 1
1]*0.5,'LineStyle','--','LineWidth',1.5)
    plot([99:-1:0]/100,real(vv(120,:))','Color',[1 1
1]*0,'LineStyle','-.','LineWidth',1.5)
    plot([99:-1:0]/100,real(vv(145,:))','Color',[1 1
1]*0.5,'LineStyle','-.','LineWidth',1.5)
    plot([99:-1:0]/100,real(vv(165,:))','Color',[1 1
1]*0,'LineStyle',':','LineWidth',1.5)
    hold off
    H=legend('Time = 40ms','Time = 90ms','Time = 140ms','Time =
190ms','Time = 240ms','Time = 290ms','Time = 330ms');
    set(gca,'FontSize',14)
    xlabel('Distance from Wall
(Radius)','FontSize',14,'FontWeight','Bold')
    ylabel('Velocity (m/s)','FontSize',14,'FontWeight','Bold')
    axis([0 0.6 -0.5 1.5])
end
```

B3.3 Code For Calculating Shear Stresses from Experimental Measurements (Described in Section 5.4)

This code processes LDV outputs to obtain ventricular surface shear stresses for measurements in the polymeric valve model. The method is described in section 5.4.

```
function obtainshearAP6_1

%this code is to calculated the ventricular streamwise shear stresses
on the
%polymeric valve model 2; at location 1;
%after the mean and stdev of measured velocities as well as position of
%leaflet is determined

A=dlmread('C:\Users\Yap\Desktop\PIV lab\LDV work\Apr2010-
polym2\A6P1\mean.txt');
S=dlmread('C:\Users\Yap\Desktop\PIV lab\LDV work\Apr2010-
polym2\A6P1\stdev.txt');

AA=A;
d=0.088458405;

po=dlmread('C:\Users\Yap\Desktop\PIV lab\LDV work\Apr2010-
polym2\A6P1\position.txt');
intercept=po;
for i=1:84
    if po(i)~=0
        sprintf('%2.2d',i)
        nn=12;
        if i==75
            nn=8;
        end
        fit=A(i,po(i):po(i)+nn)';
        fit2=AA(i,po(i):po(i)+nn)';
        results2=leastsq([1:nn+1]',fit2,2);
        fit2para=results2{1};
        temp=results2{2};
        intercept1=(-temp(2)-sqrt(temp(2)^2-
4*temp(3)*temp(1)))/2/temp(3);
        intercept2=(-temp(2)+sqrt(temp(2)^2-
4*temp(3)*temp(1)))/2/temp(3);
        intercept(i)=min(intercept1,intercept2);
        intercept(i)
        gradatintr(i)=2*temp(3)*intercept(i)+temp(2);
        beta(i)=temp(3);

        SSerr(i)=sum((fit2para-fit).^2);
        SSmean=mean(fit);
        SStot(i)=sum((fit-SSmean).^2);
        Rsq(i)=1-SSerr(i)/SStot(i);
        err=S(i,po(i):po(i)+nn)';

        distt=(-intercept(i)+[1:nn+1])*d;
        errorbar(distt,fit,err,'b*','LineWidth',2)
        hold on
        if distt(1)>0
            plot([0 distt],[0;fit2para],'r-','LineWidth',2)
        else
            plot(distt,fit2para,'r-','LineWidth',2)
```

```
        end
        plot([0 2],[0 0],'k--','LineWidth',1.5)
        hold off
        set(gca,'FontSize',14)
        axis([0 1.2 -0.5 1.2])
        xlabel('Distance from Leaflet Surface
(mm)','FontSize',14,'FontWeight','Bold')
        ylabel('Velocity (m/s)','FontSize',14,'FontWeight','Bold')

        input('')
    end
end

shearrate=gradatintr/d*1000;
shearstress=shearrate*3.5/100; %(dyn/cm2)

plot(shearstress)

%plot properly
shearstress2=[shearstress zeros(1,172-length(shearstress))];
shearstress3=[ 0; movave3(shearstress2,3); 0];
plot([5:5:860],shearstress3,'-','LineWidth',2);

s1s=[[5:5:860]' shearstress2'];
s1s(29:74,2)=movave3(s1s(28:75,2),3);
dlmwrite('C:\Documents and Settings\CH\Desktop\PIV lab\LDV
work\Apr2010-polym2\A6P1\shearstress.txt',s1s, 'delimiter',
'','newline', 'pc','precision','%15.10f');

%use flow in run5
time=[10:10:860]+25;
n=find(time>860,1,'first');
time2=[time(n:end) time(1:n-1)];
time2=time2-double(time2>860)*860;
shear2=[shearstress3(n:end);shearstress3(1:n-1)];
[AX,H1,H2]=plotyy(time2,shear2*1.03,[2:2:860],flow);
set(AX(1),'Ycolor','k','FontSize',14)
set(AX(2),'Ycolor','k','FontSize',14)
set(H1,'Color','b','LineWidth',2)
set(H2,'Color','r','LineWidth',2,'LineStyle','--')
set(AX(1),'XLim',[0 860])
set(AX(2),'XLim',[0 860])
set(AX(2),'YLim',[-5 25])
set(AX(1),'YLim',[-20 100])
set(get((AX(1)),'Ylabel'),'String','Shear Stress
(dyn/s)','FontSize',14,'FontWeight','Bold')
set(get((AX(2)),'Ylabel'),'String','Volumetric Flow Rate
(L/min)','FontSize',14,'FontWeight','Bold')
xlabel('Time (ms)','FontSize',14,'FontWeight','Bold')
LL=legend('Streamwise Shear Stress','Non-Steamwise Shear Stress','Flow
Rate');
set(LL,'Position',[0.4454    0.7400    0.4407    0.1526],'FontSize',12)
set(AX(1),'YTick',[-20:20:100])
set(AX(2),'YTick',[-5:5:25])
```

```
%check on flow development
Ufree(29:68)=mean(A(29:68,end-5:end)');
for i=29:67
    A2(i,:)=A(i,po(i):po(i)+21)/Ufree(i);
end
A3=twodmovave(A2,1,1);
for i=29:67
    distt=(-intercept(i)+[1:21+1])*d;
    plot(distt,A2(i,:),'Color',[ (i-29)/(67-29)*[ 1 1 0] ] )
    axis([0 2.5 -0.2 1.2])
    hold on
    input(num2str(i))
end

%what is standard deviation
for i=29:73
    aa(i)=max(S(i,po(i):end));
end
aa=aa(find(aa~=0));
aa1=[max(aa) min(aa) mean(aa)]
```

B4. Codes for Obtaining Aortic Shear Stresses From the Native Valves

B4.1 Code for Plotting All results After Shear Stress Calcuations

This code plots all results from *in vitro* shear stress measurements on the aortic surface of the aortic valve leaflets, after the measurements have been processed into shear stress data.

```
function allshear_plotseverything

%Plots everything..!!
%native tissue normal aortic valve
%aortic surface shear stress over different heart rate / flow rate

%% ---
N2=dlmread('C:\Users\Yap\Desktop\PIV lab\LDV work\Tami work summer
2010\NV2\NV2-shearstress.txt');
N3=dlmread('C:\Users\Yap\Desktop\PIV lab\LDV work\Tami work summer
2010\NV3\NV3-shearstress.txt');
N4=dlmread('C:\Users\Yap\Desktop\PIV lab\LDV work\Tami work summer
2010\NV4\NV4-shearstress.txt');
N5=dlmread('C:\Users\Yap\Desktop\PIV lab\LDV work\Tami work summer
2010\NV5\NV5-shearstress.txt');
N6=dlmread('C:\Users\Yap\Desktop\PIV lab\LDV work\Tami work summer
2010\NV6\NV6-shearstress.txt');
```

```
N7=dlmread('C:\Users\Yap\Desktop\PIV lab\LDV work\Tami work summer
2010\NV7\NV7-shearstress.txt');
N8=dlmread('C:\Users\Yap\Desktop\PIV lab\LDV work\Tami work summer
2010\NV8\NV8-shearstress.txt');
N9=dlmread('C:\Users\Yap\Desktop\PIV lab\LDV work\Tami work summer
2010\NV9\NV9-shearstress.txt');
A50=dlmread('C:\Users\Yap\Desktop\PIV lab\LDV work\Tami work summer
2010\50NVA\50A-shearstress.txt');
B50=dlmread('C:\Users\Yap\Desktop\PIV lab\LDV work\Tami work summer
2010\50NVB\50B-shearstress.txt');
A90=dlmread('C:\Users\Yap\Desktop\PIV lab\LDV work\Tami work summer
2010\90NVA\90A-shearstress.txt');
B90=dlmread('C:\Users\Yap\Desktop\PIV lab\LDV work\Tami work summer
2010\90NVB\90B-shearstress.txt');

%correct for viscosity from 3.5 to 3.8
N2=N2*3.8/3.5;
N3=N3*3.8/3.5;
N4=N4*3.8/3.5;
N5=N5*3.8/3.5;
N6=N6*3.8/3.5;
N7=N7*3.8/3.5;
N8=N8*3.8/3.5;
N9=N9*3.8/3.5;
A50=A50*3.8/3.5;
B50=B50*3.8/3.5;
A90=A90*3.8/3.5;
B90=B90*3.8/3.5;

figure()
plot([5:5:860],N8,'k','color',[1 1 1]*0)
hold on
plot([5:5:860],N9,'k','color',[1 1 1]*0)
plot([5:5:860],N2,'k','color',[1 1 1]*0.2)
plot([5:5:860],N3,'k','color',[1 1 1]*0.2)
plot([5:5:860],N4,'k','color',[1 1 1]*0.4)
plot([5:5:860],N5,'k','color',[1 1 1]*0.4)
plot([5:5:860],N6,'k','color',[1 1 1]*0.6)
plot([5:5:860],N7,'k','color',[1 1 1]*0.6)
hold off

plot([5:5:860],-mean([N8 N9],2),'k','color',[1 1 1]*0,'linewidth',2)
hold on
plot([5:5:860],-mean([N2 N3],2),'k','color',[1 1 1]*0.5,'linewidth',2)
plot([5:5:860],-mean([N4 N5],2),'k-.','color',[1 1 1]*0,'linewidth',2)
plot([5:5:860],-mean([N6 N7],2),'k-.','color',[1 1 1]*0.5,'linewidth',2)
plot([0 860],[0 0],'k','linewidth',1.4)
hold off
set(gca,'fontsize',14)
xlabel('Time(ms)','FontSize',14,'FontWeight','Bold')
ylabel('Shear Stress (dyn/cm^2)','FontSize',14,'FontWeight','Bold')
axis([50 450 -5 18])
H=legend('68 ml','62 ml','43 ml','29 ml')
set(H,'position',[ 0.1497    0.6440    0.2357    0.2365])

figure()
```

```
plot([5:5:860]/860*667+80,A90,'k','color',[1 1 1]*0.6)
hold on
plot([5:5:860]/860*667+80,B90,'k','color',[1 1 1]*0.6)
plot([5:5:860],N2,'k','color',[1 1 1]*0.3)
plot([5:5:860],N3,'k','color',[1 1 1]*0.3)
plot([5:5:860]/860*1200-80,A50,'k','color',[1 1 1]*0)
plot([5:5:860]/860*1200-80,B50,'k','color',[1 1 1]*0)
hold off

plot([5:5:860]+20,mean([A90 B90],2),'k','color',[1 1
1]*0.6,'linewidth',2)
hold on
plot([5:5:860],mean([N2 N3],2),'k','color',[1 1 1]*0.3,'linewidth',2)
plot([5:5:860],mean([A50 B50],2),'k','color',[1 1 1]*0,'linewidth',2)
plot([0 860],[0 0],'k','linewidth',1.4)
hold off
set(gca,'fontsize',14)
xlabel('Time(ms)','FontSize',14,'FontWeight','Bold')
ylabel('Shear Stress (dyn/cm^2)','FontSize',14,'FontWeight','Bold')
axis([50 500 -20 5])
H=legend('90 beats/min','70 beats/min','50 beats/min');
set(H,'position',[0.1595    0.1512    0.2875    0.2365])

figure()
plot([1:172]/172+0.02,mean([A90 B90],2),'k','color',[1 1
1]*0.6,'linewidth',2)
hold on
plot([1:172]/172,mean([N2 N3],2),'k','color',[1 1 1]*0.3,'linewidth',2)
plot([1:172]/172,mean([A50 B50],2),'k','color',[1 1 1]*0,'linewidth',2)
plot([0 1],[0 0],'k','linewidth',1.4)
hold off
set(gca,'fontsize',14)
xlabel('Cycle Time Phase','FontSize',14,'FontWeight','Bold')
ylabel('Shear Stress (dyn/cm^2)','FontSize',14,'FontWeight','Bold')
axis([0.05 0.5 -20 5])
H=legend('90 beats/min','70 beats/min','50 beats/min');
set(H,'position',[0.1595    0.1512    0.2875    0.2365])

%for frequency data 2010 oct
A=dlmread('C:\Users\Yap\Desktop\PIV lab\LDV work\Tami work summer
2010\oct2010 - frequency LDV -DAQ\50bpm-shearstress.txt');
B=dlmread('C:\Users\Yap\Desktop\PIV lab\LDV work\Tami work summer
2010\oct2010 - frequency LDV -DAQ\70bpm-shearstress.txt');
C=dlmread('C:\Users\Yap\Desktop\PIV lab\LDV work\Tami work summer
2010\oct2010 - frequency LDV -DAQ\90bpm-shearstress.txt');

%correct for viscosity from 3.5 to 3.8
A(:,2)=A(:,2)/3.5*3.8;
B(:,2)=B(:,2)/3.5*3.8;
C(:,2)=C(:,2)/3.5*3.8;

plot(A(:,1),-movave3([0;A(:,2);0],3),'k','linewidth',2)
hold on
plot(B(:,1),-movave3([0;B(:,2);0],3),'k','color',[0.5 0.5
0.5],'linewidth',2)
plot(C(:,1)+18,-C(:,2),'k-.','linewidth',2)
```

```
plot([0 860],[0 0],'k','linewidth',1.4)
hold off
set(gca,'fontsize',14)
axis([0 500 -6 12]);
xlabel('Time (ms)','FontSize',14,'FontWeight','Bold')
ylabel('Shear Stress (dyn/cm^2)','FontSize',14,'FontWeight','Bold')
legend('50 beats/min','70 beats/min','90 beats/min')

%% for plotting with standard deviations.
N2=dlmread('C:\Users\Yap\Desktop\PIV lab\LDV work\Tami work summer
2010\NV2\NV2-shearstress.txt')*3.8/3.5;
N3=dlmread('C:\Users\Yap\Desktop\PIV lab\LDV work\Tami work summer
2010\NV3\NV3-shearstress.txt')*3.8/3.5;
N4=dlmread('C:\Users\Yap\Desktop\PIV lab\LDV work\Tami work summer
2010\NV4\NV4-shearstress.txt')*3.8/3.5;
N5=dlmread('C:\Users\Yap\Desktop\PIV lab\LDV work\Tami work summer
2010\NV5\NV5-shearstress.txt')*3.8/3.5;
N6=dlmread('C:\Users\Yap\Desktop\PIV lab\LDV work\Tami work summer
2010\NV6\NV6-shearstress.txt')*3.8/3.5;
N7=dlmread('C:\Users\Yap\Desktop\PIV lab\LDV work\Tami work summer
2010\NV7\NV7-shearstress.txt')*3.8/3.5;
N8=dlmread('C:\Users\Yap\Desktop\PIV lab\LDV work\Tami work summer
2010\NV8\NV8-shearstress.txt')*3.8/3.5;
N9=dlmread('C:\Users\Yap\Desktop\PIV lab\LDV work\Tami work summer
2010\NV9\NV9-shearstress.txt')*3.8/3.5;
N2p=dlmread('C:\Users\Yap\Desktop\PIV lab\LDV work\Tami work summer
2010\NV2\NV2-shearstress-p1std.txt')*3.8/3.5;
N3p=dlmread('C:\Users\Yap\Desktop\PIV lab\LDV work\Tami work summer
2010\NV3\NV3-shearstress-p1std.txt')*3.8/3.5;
N4p=dlmread('C:\Users\Yap\Desktop\PIV lab\LDV work\Tami work summer
2010\NV4\NV4-shearstress-p1std.txt')*3.8/3.5;
N5p=dlmread('C:\Users\Yap\Desktop\PIV lab\LDV work\Tami work summer
2010\NV5\NV5-shearstress-p1std.txt')*3.8/3.5;
N6p=dlmread('C:\Users\Yap\Desktop\PIV lab\LDV work\Tami work summer
2010\NV6\NV6-shearstress-p1std.txt')*3.8/3.5;
N7p=dlmread('C:\Users\Yap\Desktop\PIV lab\LDV work\Tami work summer
2010\NV7\NV7-shearstress-p1std.txt')*3.8/3.5;
N8p=dlmread('C:\Users\Yap\Desktop\PIV lab\LDV work\Tami work summer
2010\NV8\NV8-shearstress-p1std.txt')*3.8/3.5;
N9p=dlmread('C:\Users\Yap\Desktop\PIV lab\LDV work\Tami work summer
2010\NV9\NV9-shearstress-p1std.txt')*3.8/3.5;
N2m=dlmread('C:\Users\Yap\Desktop\PIV lab\LDV work\Tami work summer
2010\NV2\NV2-shearstress-m1std.txt')*3.8/3.5;
N3m=dlmread('C:\Users\Yap\Desktop\PIV lab\LDV work\Tami work summer
2010\NV3\NV3-shearstress-m1std.txt')*3.8/3.5;
N4m=dlmread('C:\Users\Yap\Desktop\PIV lab\LDV work\Tami work summer
2010\NV4\NV4-shearstress-m1std.txt')*3.8/3.5;
N5m=dlmread('C:\Users\Yap\Desktop\PIV lab\LDV work\Tami work summer
2010\NV5\NV5-shearstress-m1std.txt')*3.8/3.5;
N6m=dlmread('C:\Users\Yap\Desktop\PIV lab\LDV work\Tami work summer
2010\NV6\NV6-shearstress-m1std.txt')*3.8/3.5;
N7m=dlmread('C:\Users\Yap\Desktop\PIV lab\LDV work\Tami work summer
2010\NV7\NV7-shearstress-m1std.txt')*3.8/3.5;
N8m=dlmread('C:\Users\Yap\Desktop\PIV lab\LDV work\Tami work summer
2010\NV8\NV8-shearstress-m1std.txt')*3.8/3.5;
N9m=dlmread('C:\Users\Yap\Desktop\PIV lab\LDV work\Tami work summer
2010\NV9\NV9-shearstress-m1std.txt')*3.8/3.5;
```

```
A=dlmread('C:\Users\Yap\Desktop\PIV lab\LDV work\Tami work summer
2010\oct2010 - frequency LDV -DAQ\50bpm-shearstress.txt')*3.8/3.5;
B=dlmread('C:\Users\Yap\Desktop\PIV lab\LDV work\Tami work summer
2010\oct2010 - frequency LDV -DAQ\70bpm-shearstress.txt')*3.8/3.5;
C=dlmread('C:\Users\Yap\Desktop\PIV lab\LDV work\Tami work summer
2010\oct2010 - frequency LDV -DAQ\90bpm-shearstress.txt')*3.8/3.5;
Ap=dlmread('C:\Users\Yap\Desktop\PIV lab\LDV work\Tami work summer
2010\oct2010 - frequency LDV -DAQ\50bpm-shearstress-p1std.txt')*3.8/3.5;
Bp=dlmread('C:\Users\Yap\Desktop\PIV lab\LDV work\Tami work summer
2010\oct2010 - frequency LDV -DAQ\70bpm-shearstress-p1std.txt')*3.8/3.5;
Cp=dlmread('C:\Users\Yap\Desktop\PIV lab\LDV work\Tami work summer
2010\oct2010 - frequency LDV -DAQ\90bpm-shearstress-p1std.txt')*3.8/3.5;
Am=dlmread('C:\Users\Yap\Desktop\PIV lab\LDV work\Tami work summer
2010\oct2010 - frequency LDV -DAQ\50bpm-shearstress-m1std.txt')*3.8/3.5;
Bm=dlmread('C:\Users\Yap\Desktop\PIV lab\LDV work\Tami work summer
2010\oct2010 - frequency LDV -DAQ\70bpm-shearstress-m1std.txt')*3.8/3.5;
Cm=dlmread('C:\Users\Yap\Desktop\PIV lab\LDV work\Tami work summer
2010\oct2010 - frequency LDV -DAQ\90bpm-shearstress-m1std.txt')*3.8/3.5;

figure(1)
plot([5:5:860],-mean([N8 N9],2),'k','linewidth',2)
hold on
plot([5:5:860],-mean([N8p N9p],2),'k-.','linewidth',2)
plot([5:5:860],-mean([N8m N9m],2),'k-.','linewidth',2)
hold off
set(gca,'fontsize',14)
xlabel('Time(ms)','FontSize',14,'FontWeight','Bold')
ylabel('Shear Stress (dyn/cm^2)','FontSize',14,'FontWeight','Bold')
title('68 ml Stroke Volume, 70 bpm Heart Rate')
axis([50 450 -5 18])
grid on

figure(2)
plot([5:5:860],-mean([N2 N3],2),'k','linewidth',2)
hold on
plot([5:5:860],-mean([N2p N3p],2),'k-.','linewidth',2)
plot([5:5:860],-mean([N2m N3m],2),'k-.','linewidth',2)
hold off
set(gca,'fontsize',14)
xlabel('Time(ms)','FontSize',14,'FontWeight','Bold')
ylabel('Shear Stress (dyn/cm^2)','FontSize',14,'FontWeight','Bold')
title('62 ml Stroke Volume, 70 bpm Heart Rate')
axis([50 450 -5 18])
grid on

figure(3)
plot([5:5:860],-mean([N4 N5],2),'k','linewidth',2)
hold on
plot([5:5:860],-mean([N4p N5p],2),'k-.','linewidth',2)
plot([5:5:860],-mean([N4m N5m],2),'k-.','linewidth',2)
hold off
set(gca,'fontsize',14)
xlabel('Time(ms)','FontSize',14,'FontWeight','Bold')
ylabel('Shear Stress (dyn/cm^2)','FontSize',14,'FontWeight','Bold')
title('43 ml Stroke Volume, 70 bpm Heart Rate')
axis([50 450 -5 18])
```

```
grid on

figure(4)
plot([5:5:860],-mean([N6 N7],2),'k','linewidth',2)
hold on
plot([5:5:860],-mean([N6p N7p],2),'k-.','linewidth',2)
plot([5:5:860],-mean([N6m N7m],2),'k-.','linewidth',2)
hold off
set(gca,'fontsize',14)
xlabel('Time(ms)','FontSize',14,'FontWeight','Bold')
ylabel('Shear Stress (dyn/cm^2)','FontSize',14,'FontWeight','Bold')
title('29 ml Stroke Volume, 70 bpm Heart Rate')
axis([50 450 -5 18])
grid on

Ap2=max(-[Ap(:,2) Am(:,2)]')';
Am2=min(-[Ap(:,2) Am(:,2)]')';
Bp2=max(-[Bp(:,2) Bm(:,2)]')';
Bm2=min(-[Bp(:,2) Bm(:,2)]')';

figure(5)
plot(A(:,1),-movave3([0;A(:,2);0],3),'k','linewidth',2)
hold on
plot(Ap(:,1),movave3([0;Ap2;0],3),'k-.','linewidth',2)
plot(Am(:,1),movave3([0;Am2;0],3),'k-.','linewidth',2)
hold off
set(gca,'fontsize',14)
xlabel('Time(ms)','FontSize',14,'FontWeight','Bold')
ylabel('Shear Stress (dyn/cm^2)','FontSize',14,'FontWeight','Bold')
title('55 ml Stroke Volume, 50 bpm Heart Rate')
axis([50 450 -5 18])
grid on

figure(6)
plot(B(:,1),-movave3([0;B(:,2);0],3),'k','linewidth',2)
hold on
plot(Bp(:,1),movave3([0;Bp2;0],3),'k-.','linewidth',2)
plot(Bm(:,1),movave3([0;Bm2;0],3),'k-.','linewidth',2)
hold off
set(gca,'fontsize',14)
xlabel('Time(ms)','FontSize',14,'FontWeight','Bold')
ylabel('Shear Stress (dyn/cm^2)','FontSize',14,'FontWeight','Bold')
title('55 ml Stroke Volume, 70 bpm Heart Rate')
axis([50 450 -5 18])
grid on

figure(7)
plot(C(:,1)+18,-C(:,2),'k','linewidth',2)
hold on
plot(Cp(:,1)+18,-Cp(:,2),'k-.','linewidth',2)
plot(Cm(:,1)+18,-Cm(:,2),'k-.','linewidth',2)
hold off
set(gca,'fontsize',14)
xlabel('Time(ms)','FontSize',14,'FontWeight','Bold')
ylabel('Shear Stress (dyn/cm^2)','FontSize',14,'FontWeight','Bold')
title('55 ml Stroke Volume, 90 bpm Heart Rate')
```

```
axis([50 450 -5 18])
grid on
```

B4.2 Code for Tracking Valve Leaflet Position from Experimental Measurements (Described in Section 5.2.3)

This code tracks the dynamic position of the aortic valve leaflet surface based on the back-scattered LDV laser light intensity method, described in section 5.2.3.

```
%obtain Leaflet Position for 4.5L/min case location 1

path='C:\Users\Yap\Desktop\PIV lab\LDV work\Tami work summer
2010\NV2\Daq-NV2';
pathout='C:\Users\Yap\Desktop\PIV lab\LDV work\Tami work summer
2010\NV2';
file='JunNV1-';

B=[];
loc=[];
time=[2:2:830]';

for i=4250:25:7000
    i
    loc=[loc i];

    A=dlmread([path '\' file sprintf('%d',i) '.txt']);
    [s1 s2]=size(A);
    A=A(:,2:s2);
    G=mean(A')';
    if i>4000
     G=G*5;
    end
    plot(G)
    B=[B G];
end

XX=ones(length(time),1)*loc;
YY=time*ones(1,length(loc));
figure(1)
mesh(XX,YY,B)
view([0,0,1])

figure(2)

loc2=linspace(loc(1),loc(end),2000);
```

```
[ss1 ss2]=size(B);
t=1:ss2;
for i=1:ss1
    i
    C=B(i,:)';

    %This amplifies weak signals
    stdC=std(C);
    meanC=mean(C);
    diffC=C-meanC;
    signC=sign(diffC);
    C=meanC+signC.*abs(diffC).^0.4;
    %this smoothes out the signal and increases spatial resolution
     C2=fouriersmooth5(C,30,2000)';
     stdC=std(C2);
     meanC=mean(C2);
    location(i)=loc2(find(C2==max(C2)));
    plot([location(i) location(i)],[0 1],'r');
    hold on;
    plot(loc2,C2','k');
    plot(loc,C','g');
    hold off;
   % input(''); %use this line if you want to observe peak finding
end

location(1:48)=NaN;
location(195:end)=NaN;
plot(location)
dlmwrite([pathout '\NV2-leaflet.txt'],location',
'delimiter','','newline', 'pc','precision','%15.10f');
```

B4.3 Overall Code for Obtaining the Gradient Orientation of the Valve Leaflet with Respect to the LDV Probe (Described in Section 5.2.3.4)

This code calculates the orientation of the valve leaflet surface with respect to the orientation of the LDV probe orientation.

```
function obtaingradients2

%calculate orientation gradient of the valve leaflet with respect to
the
%LDV probe alignment
%for various heart rate cases

A50=dlmread('C:\Users\Yap\Desktop\PIV lab\LDV work\Tami work summer
2010\oct2010 - frequency LDV -DAQ\freq50-leaflet.txt');
B50=dlmread('C:\Users\Yap\Desktop\PIV lab\LDV work\Tami work summer
2010\oct2010 - frequency LDV -DAQ\freq50-dstrm-leaflet.txt');
```

```
A70=dlmread('C:\Users\Yap\Desktop\PIV lab\LDV work\Tami work summer
2010\oct2010 - frequency LDV -DAQ\freq70-leaflet.txt');
B70=dlmread('C:\Users\Yap\Desktop\PIV lab\LDV work\Tami work summer
2010\oct2010 - frequency LDV -DAQ\freq70-dstrm-leaflet.txt');
A90=dlmread('C:\Users\Yap\Desktop\PIV lab\LDV work\Tami work summer
2010\oct2010 - frequency LDV -DAQ\freq90-leaflet.txt');
B90=dlmread('C:\Users\Yap\Desktop\PIV lab\LDV work\Tami work summer
2010\oct2010 - frequency LDV -DAQ\freq90-dstrm-leaflet.txt');

A50=A50/25*0.089;
B50=B50/25*0.089;
A70=A70/25*0.089;
B70=B70/25*0.089;
A90=A90/25*0.089;
B90=B90/25*0.089;

grad50=(A50-B50)/(0.1*25.4);
grad70=(A70-B70)/(0.1*25.4);
grad90=(A90-B70)/(0.1*25.4);

cos50=cos(atan(grad50));
cos70=cos(atan(grad70));
cos90=cos(atan(grad90));

%plot the three leaflet locations
figure(1)
plot([2:2:492*2],movave3(A50/25*0.089,9)-23,'k','linewidth',2)
hold on
plot([2:2:492*2],movave3(A70/25*0.089,9)-23,'k','color',[0.5 0.5
0.5],'linewidth',2)
plot([2:2:492*2]+10,movave3(A90/25*0.089,9)-23,'k-.','linewidth',2)
hold off
set(gca,'Fontsize',14)
axis([0 600 8 12])
xlabel('Time (ms)','FontSize',14,'FontWeight','Bold')
ylabel('Location (mm)','FontSize',14,'FontWeight','Bold')
legend('50 beats/min','70 beats/min','90 beats/min')
```

B4.4 Code for Binning LDV Velocity Measurements into Time Bins, and Calculating Ensemble Average or Standard Deviation (Described in Section 5.2.1)

This code categorizes LDV raw velocity measurements into a number of time bins (based on the time within each cardiac cycle), specified by the user, such that ensemble averaging can be performed.

```
function velocity_bin

%read in files processed with LDVreadfile.m
%bins LDV measurements into time bins

path1='C:\Users\Yap\Desktop\PIV lab\LDV work\Tami work summer 2010\oct
2010 frequency LDV';
pathout1='C:\Users\Yap\Desktop\PIV lab\LDV work\Tami work summer
2010\oct 2010 frequency LDV';
file1='FQ90-';

timebins=133;
time=665;

BBm1=[]; BBm2=[];
BBs1=[]; BBs2=[];
BBn1=[]; BBn2=[];

for j=1:1:41
    disp(j)
    fid=fopen([path1 '\' file1 sprintf('%2.2d',j) '.txt']);
    fgetl(fid);
    fgetl(fid);
    A=textscan(fid,'%64f,%64f');
    A1=[A{1}(:) A{2}(:)];
    timeU=A1(:,1)-floor(A1(:,1)/65536)*65536;
    timeU2=floor(timeU/64000*timebins*1000/time)+1;

    for i=1:timebins
        D1=find(timeU2==i);
        E1=A1(D1,2);

        Bm1(i)=mean(E1);
        Bs1(i)=std(E1);
        Bn1(i)=length(E1);

        E1=E1(find(abs(E1-Bm1(i))<Bs1(i)));

        Bm1(i)=mean(E1);
        Bs1(i)=std(E1);
        Bn1(i)=length(E1);

        if Bn1(i)<1 Bm1(i)=NaN; end
    end

    BBm1=[BBm1 Bm1'];
    BBs1=[BBs1 Bs1'];
    BBn1=[BBn1 Bn1'];
end

dlmwrite([pathout1 '\FQ90-Umean.txt'],BBm1, 'delimiter', '','newline',
'pc','precision','%15.10f');
dlmwrite([pathout1 '\FQ90-Unumdata.txt'],BBn1, 'delimiter',
'','newline', 'pc','precision','%15.10f');
```

```
dlmwrite([pathout1 '\FQ90-Ustd.txt'],BBs1, 'delimiter', '','newline',
'pc','precision','%15.10f');
```

B4.5 Code for Computing Aortic Surface Shear Stresses (Described in Section 5.2.4)

This code calculates the aortic surface shear stress based from the LDV raw measurements. It takes in data output from code B4.4.

```
%calculate shear stresses for the 4.5L/min case location 2
%after obtaining the binned velocities, leaflet location and leaflet
orientation.
%Shear stress is computed for the ensemble average velocities,
%the ensemble average + 1 standard deviation velocities
%and the ensemble average - 1 standard deviation velocities

%% ------
d=0.089;
NV3=dlmread('C:\Users\Yap\Desktop\PIV lab\LDV work\Tami work summer
2010\NV3\NV3-leaflet.txt');
for i=1:165
    n=i*2.5;
    temp=abs([1:430]-n);
    n=find(temp<1.5);
    leaf(i)=mean(NV3(n))/25*d;
end
leaf=leaf-21;


A=dlmread('C:\Users\Yap\Desktop\PIV lab\LDV work\Tami work summer
2010\NV3\LDV-NV3\mean.txt');
As=twodmovave(A,1,1);
[XX YY]=meshgrid([51:-1:1]*d,[5:5:860]);
mesh(XX,YY,As)
hold on
plot3(leaf,[5:5:825],ones(165,1))
hold off
view([0 0 1])

d=0.089; %distance between two points
nn=20; %number of pts

po=dlmread('C:\Users\Yap\Desktop\PIV lab\LDV work\Tami work summer
2010\NV3\LDV-NV3\pp3yap.txt');
%t=[-nn:nn]*d;

for i=24:70
    B=As(i,po(i,2)-nn:po(i,2));

    temp=B(end-3:end-1)-B(end);
    R=leastsq([1:3]',temp',1);
    R2=R{2};
```

```
    temp2=4+R2(1)/R2(2);

    if temp2<1 & temp2>0
        t=[[-nn:-1]+temp2, 0, [1:nn]-temp2]*d;

        B=B-B(end);
        n=length(B);
        B2=[B -fliplr(B(1:end-1))];
        B3=fouriersmooth7(t,B2,t(end)-t(1),20);
        B3=B3(:,1);
        shearrate(i)=(B3(n+1)-B3(n-1))/2/(d*(1-temp2)) *1000; %vel =
m/s, d = mm
    else
        t=[-nn:nn]*d;
        B=B-B(end);
        n=length(B);
        B2=[B -fliplr(B(1:end-1))];
        B3=fouriersmooth3(B2,10);
        shearrate(i)=(B3(n+1)-B3(n-1))/2/d *1000; %vel = m/s, d = mm
    end

    plot(t,B2,'.');
    hold on
    plot(t,B3,'r-');
    %plot(B3,'r')
    hold off
    axis([-2 2 -0.2 0.2])
    grid on
    input('')
end

shearstress=shearrate*3.5/100; %(dyn/cm2)
shearstress2=movave3([0 shearstress 0],3);
shearstress2(172)=0;
dlmwrite('C:\Users\Yap\Desktop\PIV lab\LDV work\Tami work summer
2010\NV3\NV3-shearstress.txt',shearstress2, 'delimiter', '','newline',
'pc','precision','%15.10f');


%plot to visualize
for i=20:75
    plot(A(i,:),'b.-')
    hold on
    plot(As(i,:),'r.-')
    plot(55-leaf(i)/d,0,'m^')
    hold off
    grid on
    axis([0 40 -0.1 0.2])
    input(num2str(i))
end


%% +1 standard deviation shear stresses
A=dlmread('C:\Users\Yap\Desktop\PIV lab\LDV work\Tami work summer
2010\NV3\LDV-NV3\mean.txt');
```

```
std=dlmread('C:\Users\Yap\Desktop\PIV lab\LDV work\Tami work summer
2010\NV3\LDV-NV3\stdev.txt');
Aplus=A+std;
As=twodmovave(Aplus,1,1);
[XX YY]=meshgrid([51:-1:1]*d,[5:5:860]);
mesh(XX,YY,As)
hold on
plot3(leaf,[5:5:825],ones(165,1))
hold off
view([0 0 1])

d=0.089; %distance between two points
nn=20; %number of pts

po=dlmread('C:\Users\Yap\Desktop\PIV lab\LDV work\Tami work summer
2010\NV3\LDV-NV3\pp3yap.txt');
%t=[-nn:nn]*d;

for i=24:70
    B=As(i,po(i,2)-nn:po(i,2));

    temp=B(end-3:end-1)-B(end);
    R=leastsq([1:3]',temp',1);
    R2=R{2};
    temp2=4+R2(1)/R2(2);

    if temp2<1 & temp2>0
        t=[[-nn:-1]+temp2, 0, [1:nn]-temp2]*d;

        B=B-B(end);
        n=length(B);
        B2=[B -fliplr(B(1:end-1))];
        B3=fouriersmooth7(t,B2,t(end)-t(1),20);
        B3=B3(:,1);
        shearrate(i)=(B3(n+1)-B3(n-1))/2/(d*(1-temp2)) *1000; %vel =
m/s, d = mm
    else
        t=[-nn:nn]*d;
        B=B-B(end);
        n=length(B);
        B2=[B -fliplr(B(1:end-1))];
        B3=fouriersmooth3(B2,10);
        shearrate(i)=(B3(n+1)-B3(n-1))/2/d *1000; %vel = m/s, d = mm
    end

    plot(t,B2,'.');
    hold on
    plot(t,B3,'r-');
    %plot(B3,'r')
    hold off
    axis([-2 2 -0.2 0.2])
    grid on
    input('')
end
```

```
shearstress=shearrate*3.5/100; %(dyn/cm2)
shearstress2=movave3([0 shearstress 0],3);
shearstress2(172)=0;
dlmwrite('C:\Users\Yap\Desktop\PIV lab\LDV work\Tami work summer
2010\NV3\NV3-shearstress_p1std.txt',shearstress2, 'delimiter',
'','newline', 'pc','precision','%15.10f');


%% -1 standard deviation shear stresses
A=dlmread('C:\Users\Yap\Desktop\PIV lab\LDV work\Tami work summer
2010\NV3\LDV-NV3\mean.txt');
std=dlmread('C:\Users\Yap\Desktop\PIV lab\LDV work\Tami work summer
2010\NV3\LDV-NV3\stdev.txt');
Aminus=A-std;
As=twodmovave(Aminus,1,1);
[XX YY]=meshgrid([51:-1:1]*d,[5:5:860]);
mesh(XX,YY,As)
hold on
plot3(leaf,[5:5:825],ones(165,1))
hold off
view([0 0 1])

d=0.089; %distance between two points
nn=20; %number of pts

po=dlmread('C:\Users\Yap\Desktop\PIV lab\LDV work\Tami work summer
2010\NV3\LDV-NV3\pp3yap.txt');
%t=[-nn:nn]*d;

for i=24:70
    B=As(i,po(i,2)-nn:po(i,2));

    temp=B(end-3:end-1)-B(end);
    R=leastsq([1:3]',temp',1);
    R2=R{2};
    temp2=4+R2(1)/R2(2);

    if temp2<1 & temp2>0
        t=[[-nn:-1]+temp2, 0, [1:nn]-temp2]*d;

        B=B-B(end);
        n=length(B);
        B2=[B -fliplr(B(1:end-1))];
        B3=fouriersmooth7(t,B2,t(end)-t(1),20);
        B3=B3(:,1);
        shearrate(i)=(B3(n+1)-B3(n-1))/2/(d*(1-temp2)) *1000; %vel =
m/s, d = mm
    else
        t=[-nn:nn]*d;
        B=B-B(end);
        n=length(B);
        B2=[B -fliplr(B(1:end-1))];
        B3=fouriersmooth3(B2,10);
        shearrate(i)=(B3(n+1)-B3(n-1))/2/d *1000; %vel = m/s, d = mm
    end
```

```
    plot(t,B2,'.');
    hold on
    plot(t,B3,'r-');
    %plot(B3,'r')
    hold off
    axis([-2 2 -0.2 0.2])
    grid on
    input('')
end

shearstress=shearrate*3.5/100; %(dyn/cm2)
shearstress2=movave3([0 shearstress 0],3);
shearstress2(172)=0;
dlmwrite('C:\Users\Yap\Desktop\PIV lab\LDV work\Tami work summer
2010\NV3\NV3-shearstress_m1std.txt',shearstress2, 'delimiter',
'','newline', 'pc','precision','%15.10f');
```

B5. Code to Calculate Power Spectral Density of Data with Non-Uniform Spacing (Described in Section 5.2.5.3)

These codes are based on methods described by Adrian et al. [109] and Moreau et al. [110]

```
%% For BAV fused leaflet
temp=dlmread('diffBAVwhole.txt');
time=temp(:,1);
signal=temp(:,2);

%create sample and hold re-sampled, uniformly spaced data
timeSH=round(time(5)):1:time(end-4);
signalSH=zeros(length(timeSH),1);
for i=timeSH(1):1:timeSH(end)
    disp(i)
    nl=find(time>i,1,'first')-1;
    signalSH(i-timeSH(1)+1)=signal(nl);
end
dlmwrite('BAVwholeSH',[timeSH' signalSH])

A=dlmread('BAVwholeSH');
time=A(:,1);
signal=A(:,2);
P=2000;

%calculate autocorrelation function according to Moreau et al.
meandatarate=length(time)/time(end)*1000; %s^-1
samplinginterval=1/1000; %s
a=meandatarate*samplinginterval;
```

```
ca=(1+exp(-2*a))/(1-exp(-a))^2;

Ry=zeros(P,1);
for i=1:P
    Ry(i)=mean(signal(1:end-P).*signal(1+i:end-P+i));
end
Ry0=mean(signal(1:end-P).*signal(1:end-P));

Rr0=Ry0;
Rr(1)=ca*Ry(1)+(1-ca)/2*(Ry0+Ry(2));
for k=2:P-1
    Rr(k)=ca*Ry(k)+(1-ca)/2*(Ry(k-1)+Ry(k+1));
end

%calculate powerspectrum according to Moreau et al.
kappa=5;
Fs=1000;
Te=samplinginterval;
for f=1:50
    term2(f)=0;
    for k=1:P-1
        if f*k/Fs<kappa
            dkf=0.5*(1+cos(pi*f*k/Fs/kappa));
        else
            dkf=0;
        end
        term2(f)=term2(f)+dkf*Rr(k)*cos(2*pi*f*k*Te);
        %term2(f)=term2(f)+Rr(k)*cos(2*pi*f*k*Te);
    end
    PSm(f)=2*Te*(Ry0+2*term2(f));
end
PSmBAV=PSm;

%calculate power spectrum according to Adrian et al (sample and hold
without refinement)
for i=1:2000
    R(i)=mean(signal(1:end-2000).*signal(1+i:end-2000+i));
end
R0=mean(signal(1:end-2000).*signal(1:end-2000));
for i=1:50
    S(i)=1/pi/1000*sum(R.*cos(2*pi*i*[1:length(R)]/1000));
end
S=S+R0/pi/1000;
plot(S)

SBAV=S;


%% normal valve

temp=dlmread('diffnormTAMINV9whole.txt');
time=temp(:,1);
signal=temp(:,2);

%create sample and hold re-sampled, uniformly spaced data
```

```
timeSH=round(time(5)):1:time(end-4);
signalSH=zeros(length(timeSH),1);
for i=timeSH(1):1:timeSH(end)
    disp(i)
    nl=find(time>i,1,'first')-1;
    signalSH(i-timeSH(1)+1)=signal(nl);
end
dlmwrite('normalwholeSH',[timeSH' signalSH])

A=dlmread('normalwholeSH');
time=A(:,1);
signal=A(:,2);
P=2000;

%calculate autocorrelation function according to Moreau et al.
meandatarate=length(time)/time(end)*1000;
samplinginterval=1/1000; %s
a=meandatarate*samplinginterval;
ca=(1+exp(-2*a))/(1-exp(-a))^2;

Ry=zeros(P,1);
for i=1:P
    Ry(i)=mean(signal(1:end-P).*signal(1+i:end-P+i));
end
Ry0=mean(signal(1:end-P).*signal(1:end-P));

Rr0=Ry0;
Rr(1)=ca*Ry(1)+(1-ca)/2*(Ry0+Ry(2));
for k=2:P-1
    Rr(k)=ca*Ry(k)+(1-ca)/2*(Ry(k-1)+Ry(k+1));
end

%calculate power spectrum according to Moreau et al.
kappa=10;
Fs=1000;
Te=samplinginterval;
for f=1:50
    term2(f)=0;
    for k=1:P-1
        if f*k/Fs<kappa
            dkf=0.5*(1+cos(pi*f*k/Fs/kappa));
        else
            dkf=0;
        end
        term2(f)=term2(f)+dkf*Rr(k)*cos(2*pi*f*k*Te);
        %term2(f)=term2(f)+Rr(k)*cos(2*pi*f*k*Te);
    end
    PSm(f)=2*Te*(Ry0+2*term2(f));
end
PSmnormal=PSm;

%calculate power spectrum according to Adrian et al.
for i=1:2000
    R(i)=mean(signal(1:end-2000).*signal(1+i:end-2000+i));
end
R0=mean(signal(1:end-2000).*signal(1:end-2000));
```

```
for i=1:50
    S(i)=1/pi/1000*sum(R.*cos(2*pi*i*[1:length(R)]/1000));
end
S=S+R0/pi/1000;
plot(S)

Snorm=S;


%% BAV non leaflet
temp=dlmread('diffBAVnonwhole.txt');
time=temp(:,1);
signal=temp(:,2);

%create sample and hold re-sampled, uniformly spaced data
timeSH=round(time(5)):1:time(end-4);
signalSH=zeros(length(timeSH),1);
for i=timeSH(1):1:timeSH(end)
    disp(i)
    nl=find(time>i,1,'first')-1;
    signalSH(i-timeSH(1)+1)=signal(nl);
end
dlmwrite('BAVnonwholeSH',[timeSH' signalSH])

A=dlmread('BAVnonwholeSH');
time=A(:,1);
signal=A(:,2);
P=2000;

%calculate autocorrelation function according to Moreau et al.
meandatarate=length(time)/time(end)*1000; %Hz
samplinginterval=1/1000; %s
a=meandatarate*samplinginterval;
ca=(1+exp(-2*a))/(1-exp(-a))^2;

Ry=zeros(P,1);
for i=1:P
    Ry(i)=mean(signal(1:end-P).*signal(1+i:end-P+i));
end
Ry0=mean(signal(1:end-P).*signal(1:end-P));

Rr0=Ry0;
Rr(1)=ca*Ry(1)+(1-ca)/2*(Ry0+Ry(2));
for k=2:P-1
    Rr(k)=ca*Ry(k)+(1-ca)/2*(Ry(k-1)+Ry(k+1));
end

%calculate power spectrum according to Moreau et al.
kappa=10;
Fs=1000; %Hz
Te=samplinginterval; %s
for f=1:50
    term2(f)=0;
    for k=1:P-1
        if f*k/Fs<kappa
```

```
            dkf=0.5*(1+cos(pi*f*k/Fs/kappa));
        else
            dkf=0;
        end
        term2(f)=term2(f)+dkf*Rr(k)*cos(2*pi*f*k*Te);
        %term2(f)=term2(f)+Rr(k)*cos(2*pi*f*k*Te);
    end
    PSm(f)=2*Te*(Ry0+2*term2(f));
end
PSmBAVnon=PSm;

%calculate power spectrum according to Adrian et al.
for i=1:2000
    R(i)=mean(signal(1:end-2000).*signal(1+i:end-2000+i));
end
R0=mean(signal(1:end-2000).*signal(1:end-2000));
for i=1:50
    S(i)=1/pi/1000*sum(R.*cos(2*pi*i*[1:length(R)]/1000));
end
S=S+R0/pi/1000;

SBAVnon=S;


%% plot everything
%plot using Moreau et al's methods
loglog(PSmBAV,'k.-','linewidth',2,'markersize',18);
hold on
loglog(PSmBAVnon,'k.-','linewidth',2,'markersize',18,'color',[1 1
1]*0.6);
loglog(PSmnormal,'k.--','linewidth',2,'markersize',18,'color',[1 1
1]*0.3);
hold off
set(gca,'fontsize',14)
xlabel('Frequency (Hz)','FontSize',14,'FontWeight','Bold')
ylabel('Power (m^2/s^2)','FontSize',14,'FontWeight','Bold')
axis([1 50 10^-6 10^-2])
grid on
H=legend('BAV fused leaflet','BAV non-fused leaflet','normal valve
leaflet');
set(H,'position',  [0.1604    0.1552    0.4143    0.1802])

%plot using methods of Adrian et al
loglog(SBAV,'k.-','linewidth',2,'markersize',18);
hold on
loglog(SBAVnon,'k.-','linewidth',2,'markersize',18,'color',[1  1  1]*0.6);
loglog(Snorm,'k.--','linewidth',2,'markersize',18,'color',[1 1 1]*0.3);
hold off
set(gca,'fontsize',14)
xlabel('Frequency (Hz)','FontSize',14,'FontWeight','Bold')
ylabel('Power (m^2/s^2)','FontSize',14,'FontWeight','Bold')
axis([1 50 10^-7 10^-4])
grid on
H=legend('BAV fused leaflet','BAV non-fused leaflet','normal valve
leaflet');
set(H,'position',  [0.1604    0.1552    0.4143    0.1802])
```

B6. Fourier Low Pass Filter Codes

These code are subroutines to other codes. They perform a low pass filter curve fit using Fourier Transformation. They are called in some of the codes above.

```
function results=fouriersmooth3(A,freq)

%low pass filter to smooth out data (A)
%using fourier transformation, at cut off frequency (freq)
%Nt is the total number of points, dt is time resolution.
%this code uses the same time steps as input (A)

Nt=length(A);
Q0=sum(A)/Nt;
Q=A-Q0;
dt=0.002;
T=dt*Nt;

for i=1:Nt %freq
    F(i)=0;
    for j=1:Nt %timestep
        c=Q(j)*exp(-2*pi*sqrt(-1)*(i)*(j-1)/Nt);
        F(i)=F(i)+c;
    end
end


%------check if DFT was done properly
for i=1:Nt %timestep
    a(i)=0;
    for j=1:freq %freq
        c=F(j)/Nt*2*exp(2*pi*sqrt(-1)*(i-1)*(j)/Nt);
        a(i)=a(i)+c;
    end
end
%plot to check results
%plot(real(a)+Q0,'r')
%hold on
%plot(Q+Q0)
%hold off
results=real(a)+Q0;
```

```
function results=fouriersmooth4(A,freq,NNt)

%low pass filter to smooth out data (A)
%using fourier transformation, at cut off frequency (freq)
```

```
%Nt is the total number of points, dt is time resolution.
%the output can be set at different time steps from input
%NNT is the output # of data points (regular intervals).

Nt=length(A);
Q0=mean(A);
Q=A-Q0;
%dt=0.002;
%T=dt*Nt;

time1=linspace(0,Nt,Nt);
for i=1:freq %freq
    F(i)=0;
    for j=1:Nt %timestep
        %c=Q(j)*exp(-2*pi*sqrt(-1)*(i)*(j)/(Nt-1));
        c=Q(j)*exp(-2*pi*sqrt(-1)*(i)*time1(j)/(Nt));
        F(i)=F(i)+c;
    end
end


%------check if DFT was done properly
time2=linspace(0,NNt,NNt);
for i=1:NNt %timestep
    a(i)=0;
    for j=1:freq %freq
        c=F(j)/Nt*2*exp(2*pi*sqrt(-1)*time2(i)*(j)/(NNt));
        a(i)=a(i)+c;
    end
end
%plot to check results
%plot(real(a)+Q0,'r')
%hold on
%plot(Q+Q0)
%hold off

results=real(a)+Q0;
```

```
function results=fouriersmooth5(A,freq,NNt)

%low pass filter to smooth out data (A)
%using fourier transformation, at cut off frequency (freq)
%Nt is the total number of points, dt is time resolution.
%the output can be set at different time steps from input
%NNT is the output # of data points (regular intervals).
%this version uses first creates a periodic waveform by appending the
%mirror image of the data to itself before applying the filter

[s1 s2]=size(A);
if s1==1
    A=[fliplr(A) A(1) A];
    Nt=s2;
elseif s2==1
    A=[flipud(A);A(1);A];
```

```
    Nt=s1;
end

%Nt=length(A);
Q0=mean(A);
Q=A-Q0;
%dt=0.002;
%T=dt*Nt;

Nt2=Nt*2+1;
for i=1:freq %freq
    F(i)=0;
    for j=-Nt:Nt %timestep
        %c=Q(j)*exp(-2*pi*sqrt(-1)*(i)*(j)/(Nt-1));
        c=Q(j+Nt+1)*exp(-2*pi*sqrt(-1)*(i)*(j)/(Nt2));
        F(i)=F(i)+c;
    end
end


%------check if DFT was done properly
NNt2=2*NNt+1;
for i=-NNt:NNt %timestep
    index=i+NNt+1;
    a(index)=0;
    for j=1:freq %freq
        %c=F(j)/Nt*2*exp(2*pi*sqrt(-1)*(i+15)*(j)/(NNt2));
        c=F(j)/Nt2*2*exp(2*pi*sqrt(-1)*(i)*(j)/(NNt2));
        a(index)=a(index)+c;
    end
end
%plot to check results
%plot(real(a)+Q0,'r')
%hold on
%plot(Q+Q0)
%hold off

a=a(NNt+2:end);
results=real(a)+Q0;
```

```
function results=fouriersmooth7(t,A,T,freq)

%low pass filter to smooth out data (A)
%using fourier transformation, at cut off frequency (freq)
%Nt is the total number of points, dt is time resolution.
%non-uniform spacing of data considered
%However, please consider using more advanced code if power spectrum is
%desired

Nt=length(A);
%Q0=sum(A)/Nt;
%Q=A-Q0;
Q=A;
```

```
for i=0:freq %freq
    F(i+1)=0;
    for j=1:Nt-1 %timestep
        c=(Q(j)+Q(j+1))/2*exp(-2*pi*sqrt(-
1)*(i)*(t(j)+t(j+1))/2/T)*(t(j+1)-t(j));
        F(i+1)=F(i+1)+c;
    end
end

%------reconstruct curve
for i=1:Nt %timestep
    a(i)=0;
    a2(i)=0;
    for j=0:freq %freq
        c=F(j+1)/T*2*exp(2*pi*sqrt(-1)*t(i)*(j)/T);
        c2=F(j+1)/T*2*exp(2*pi*sqrt(-1)*t(i)*(j)/T) * (2*pi*sqrt(-
1)*j); %gradient
        a(i)=a(i)+c;
        a2(i)=a2(i)+c2;
    end
end
%plot to check results
%plot(real(a)+Q0,'r')
%hold on
%plot(Q+Q0)
%hold off

%results=[[real(a)+Q0]' [real(a2)]'];
results=[real(a)' real(a2)'];
```

APPENDIX C

HISTOLOGY ANALYSIS PROTOCOLS

1. HARVEST AND CULTURE OF PORCINE AORTIC VALVES

Materials and Reagents:

For tissue harvesting:

1. 1x 6-well plate Fisher #08-772-1B
2. 1x surgical scissors
3. 1x curved forceps
4. Dulbecco's phosphate buffered saline solution (dPBS) 500 mL Sigma #D5773
5. Ethanol/Methanol spray bottle
6. Stainless steel dissection tray (big) Fisher/VWR
7. Cooler with ice
8. Pipettor and sterile pipets
9. Sterilization pouch Fisher # 01-812-50

For cone and plate experiments:

1. 1x scalpel handle (no. 3) Fisher #08-915-2
2. Sterile scalpel blades EMS #72044-10
3. Glass slide coverslips as spacer between the cone apex and the plate.
4. Stainless steel dissection tray or sterile plastic tray
5. Blue absorption pad
6. 1x 6-well plate Fisher #08-772-1B
7. 1x straight forceps
8. 1x curved forceps

Cone and Plate Bioreactor:

1. The teflon cone and steel cone shaft
2. The plate dish and plate cover
3. The cone flange (holds the shaft in place and covers the plate)
4. The small peristaltic pump
5. Reservoir and reservoir lid
6. 3 lengths of 1/16 ID Tygon® tubing, two long and one short
7. 6x 4/40 screws (plate screws)
8. 3x 6/32 screws (cone and shaft screws)
9. 6x 6/32 screws (reservoir screws)
10. Suitable allen keys and cross-head screw drivers for all screws
11. Valve Leaflet "Cookie-cutting" tool (round rod with sharp edges to cut round valve leaflet samples)
12. For Dulbecco's Modified Eagles Medium (DMEM):
    - DMEM Powder Sigma #D5648 (formulation depends on experiment)

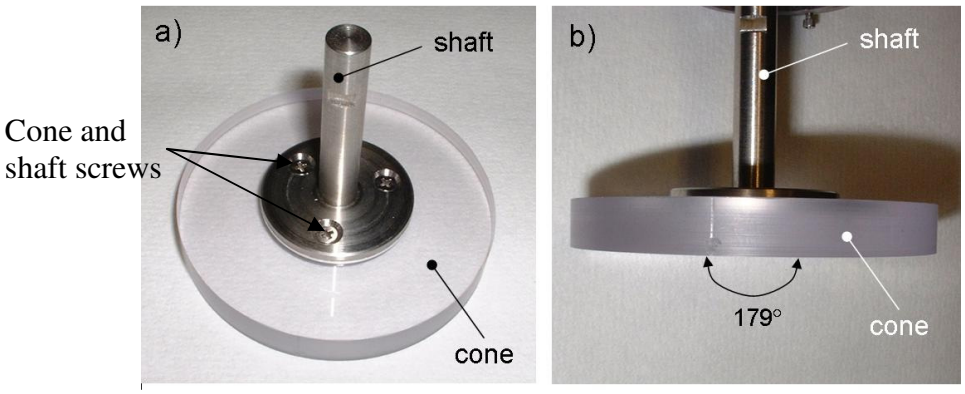

Figure 1. The cone and the cone shaft, attached by screws.

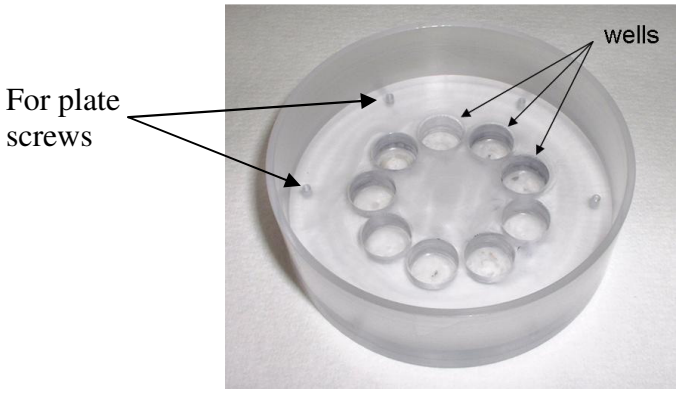

Figure 2. The cone dish.

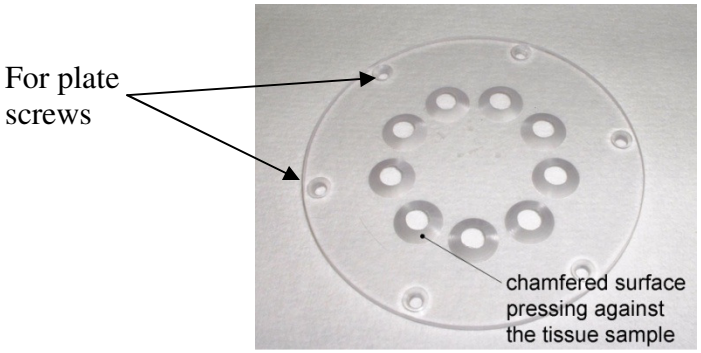

Figure 3. The dish cover.

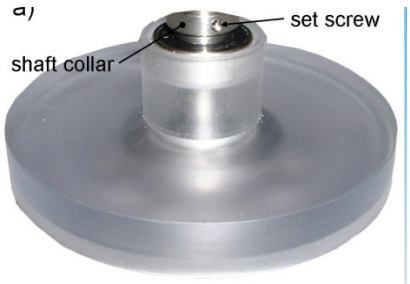

Figure 4. The cone flange.

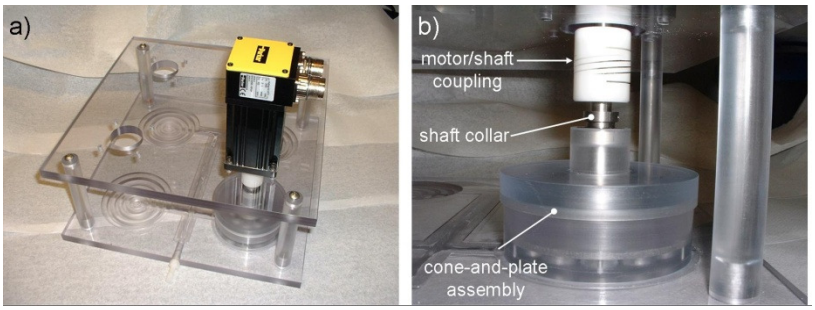

Figure 5. The cone and plate system assembly.

Procedure:

Day before

1. Autoclave scissors and forceps in small sterilization pouch.
2. Autoclave tray and absorption pad in large sterilization pouch.
3. Autoclave all spacers, razor blades, surgical tools, and screws in a small sterilization pouch.
4. Pack and sterilize cone and plate bioreactor and all screw drivers and tubing in ethylene oxide (EtO) sterilizer.
5. Place all sterilization pouches under UV overnight.
6. Autoclave dPBS and the agarose and put in fridge overnight.
7. On morning of slaughterhouse trip, fill cooler with ice and place dPBS bottle in it.

At slaughterhouse

1. Spray work area and tray thoroughly with alcohol.
2. Fill 6-well plate(s) with ice-cold dPBS.
3. Excise valve leaflets, wash in ice-cold dPBS and place in 6-well plate, keeping track of the anatomical position of each leaflet sample.
4. After tissue collection, place 6-well plate(s) in ice and return to lab.

Experiment setup

1. Use sterile techniques and a laminar flow hood at all times.
2. Place DMEM from fridge into incubator/water bath at 37°C.
3. Heat up agarose in a microwave to melt it.
4. Attach plate cover to plate dish, secure with plate screws.
5. Insert 0.725 ml of agarose into each well, leave it to solidify
6. Use Tissue “cookie-cutting” tool and scapel to cut round samples of tissues about 7-8 mm in diameter. Store all samples in sterile PBS after cutting.
7. Carefully detach the plate cover from the plate dish. Ensure no agarose gel is damaged too much in the process. Add 1-2 drops of agarose to the gel in each tissue well, so as to flatten the meniscus of the agarose surface. This will ensure the tissues can stay flushed to the plate cover surface. Allow the newly added agarose to solidify.
8. Couple the cone shaft to the cone and secure with screws. Insert the cone (with shaft) into the cone flange.

9. Place the tissues carefully on top of each agarose gel. Re-attach plate cover to the plate dish, thereby pressing the tissues to the agrose and securing them at the bottom of the plate, while exposing a small circular surface of the tissues via holes in the plate cover.
10. Place 1 glass coverslip slide in the center of the plate as spacer, attach the cone and the cone cover to the plate. Allow the cone to slide downwards to the plate to rest on the glass slide. Place the shaft collar around the cone shaft until it rests on the cone cover. Tighten the screw on the shaft collar to secure the cone at this position with respect to the cone cover.
11. Remove the cone and the cone flange, remove the glass slides, and re-attach the cone cover and cone. Ensure that the tissues do not dry out. Add some PBS to the tissues in the plate if necessary.
12. Attach the short Tygon® tubing from the reservoir outlet to the peristaltic pump inlet. Attach a long Tygon® tubing from the pump outlet to the cone and plate inlet (luer lock fitting with a lower elevation). Attach the other long Tygon® tubing from the plate outlet (luer lock fitting with a higher elevation) to the reservoir inlet (top of reservoir)
13. Pour the culture media into the reservoir, activate the peristaltic pump, and allow media to fill up all the Tygon® tubing and the cone and plate.
14. Attach the whole setup (reservoir, pump and cone and plate) the cone and plate frame. Attach the motor to the frame, and couple the motor to the cone shaft (figure 5).
15. Start the Controller Program and activate the motor. For details of operations on the controller and motor, please refer to the cone and plate manual in Appendix D.
16. Monitor bioreactor at least twice a day. Media should be changed every 1-2 days

NOTES:

- Sterile techniques must be used at all times. Wearing face masks is not absolutely necessary for porcine tissue, but must be worn at all times for other tissue types (eg: human, ovine etc).
- An alternative to 6-well plates is to use autoclaved plastic containers and excise out the entire aortic valve with the root and a portion of the aorta and place it in ice-cold dPBS. The individual cusps will then be excised in a laminar flow hood in the laboratory.

2. TISSUE POST-PROCESSING

Materials and Reagents:

For tissue harvesting:

1. 1x 6-well plate Fisher #08-772-1B
2. 1x straight forceps
3. 1x curved forceps
4. 1x scalpel handle and sterile blade
5. Sterile cold dPBS

For frozen block preparation:

1. Plastic molds EMS #70180-70184
2. OCT compound EMS #62550-01
3. Straight microdissection forceps
4. Long hemostat
5. Vacuum flask EMS #61891-02
6. Liquid nitrogen From IBB mechanical chase

For snap-freezing tissue (protein and RNA analysis):

1. Cryovials EMS #61800-1A
2. Cryovial holders ("canes") EMS #61080-10
3. Liquid nitrogen dewar

Procedure:

Stopping of experiment

1. Autoclave surgical tools and dPBS well in advance. Refrigerate dPBS.
2. On day of experiment, bring dPBS to 37ºC in incubator or water bath. Fill 6-well plate with dPBS.
3. Stop the controller program and return bioreactor to laminar flow hood.
4. Remove tissue from bioreactor.
5. Immerse leaflet in dPBS 3x to wash away DMEM. More washes may be necessary. Tissue should appear whitish and lose most of the pink color from the DMEM before proceeding to the next steps of the protocol. dPBS should not be colder than room temperature as that might result in thermal shock to the tissue samples.

Preparation of frozen blocks for histology

1. Label plastic molds accordingly.
2. Arrange tissue samples at the base of plastic mold in appropriate orientation.
3. Fill mold with OCT compound.
4. Using microdissection forceps "stand" the tissue in the OCT compound. If en face sections are required, tissue should be placed face down in the mold.
5. Fill vacuum flask with liquid nitrogen.
6. Using long hemostat, dip OCT block in liquid nitrogen. Ensure that the block is not submerged (liquid nitrogen should NEVER contact the OCT directly). Make

sure liquid nitrogen does not fall on the OCT compound as it will cause bubbles and cracks to develop in the block.

7. OCT blocks will start to solidify and turn opaque. Keep blocks in liquid nitrogen until just a small circle (approximately 5mm in diameter) of OCT on the top face of the block is left to be solidified. This will ensure that the block does not crack.
8. Place frozen blocks in -80°C freezer.

Snap-freezing of tissue for Arsenazo Assay

1. Label cryovials accordingly.
2. Place one tissue sample per cyrovial and snap vials into cyrovial holder.
3. Place entire cryovials into liquid nitrogen (in the dewar).
4. Transfer cryovials to -80°C freezer. Alternatively, cryovials can be maintained in liquid nitrogen, but care should be taken to ensure that the liquid nitrogen level is always topped up.

3. Pulverization of Valve Leaflet Tissues

Materials:

1. Mortar and pestle – the size of a Chinese tea cup
2. Liquid Nitrogen 2-3L
3. Thick Gloves
4. Tongs
5. Spatula
6. 1-2 Styrofoam box(es) (big enough to hold 2 – 3 L of liquid N2)
7. Funnel with a hole big enough to insert (slightly) into
8. Cryovials (At least 2.5" long so that boiling of N2 will not cause tissue to escape from vial)
9. Tube rack to hold cryovials (preferable one that can float in the liquid N2)

Procedure:

1. Place mortar and pestle, funnel, cryovials into Styrofoam box filled with ~ 2 L+ of liquid N2.
    - This is to ensure everything is at the same temp and that nothing will stick to the mortar and pestle (i.e. frozen grounded-up valve tissue).
2. Immerse tissue (you only need ~ 1 g for any biochemical study) into the liq. N2 for at least 1 minute.
3. Using the tongs, bring the mortar out and leave it half filled with liquid N2. Pull out the pestle and tissue and then in a twisting and pulsating downwards motion, push down on tissue, using one hand to hold the mortar down.
    - Don't push too fast or too hard because some liq. N2 and bits of tissue will spill out.
4. Continue grinding and pulverizing until the heart tissue is a very fine granular powder. This may take a few minutes.
    - At times the grinding takes so long that more liq. N2 will have to be added to the mortar.
    - Use a small plastic cup and be careful when pouring it in (else tissue might spill out).
    - Add enough liq. N2 to make a nice tissue slurry as this will be important in later steps.
5. When done grinding heart tissue up, use tongs to get the cryovial and funnel. Set the cryovial onto the test tube rack and sit it upright. Insert the small hole of the funnel into the mouth of the cryovial.
6. Using your gloves, quickly pour the tissue slurry into the funnel-cryovial. If there is tissue left in the mortar, use the spatula (dip it into liq. N2 first) and then scrape the remaining bits in. Finally, use the spatula and tap the side of the funnel so that the rest of the tissue funnels into the cryovial.

NOTES:

- Ground tissue should never be allowed to thaw. It should always be maintained in liquid nitrogen or in the -80°C freezer.

4. Alizarin Red Stain

Reagents:

1. Alizarin Red Solution
    a. Alizarin Red S 2g Sigma #05600
    b. dH2O 100 mL
    c. 0.5% Ammonium Hydroxide Sigma #320145

    Mix the solution, adjust the pH to 4.1 – 4.3 using 0.5% Ammonium Hydroxide. The pH is critical. Make fresh.

Procedure:

1. Deparaffinize slides and rehydrate to 70% alcohol.
2. Rinse in dH2O at RT, 2x for 3 min each.
3. Incubate in Alizarin Red S Solution, for 5 minutes. Check microscopically for an orange-red color.
4. Shake off excess dye and blot sections using Kimwipes.
5. Use autostainer in histology lab for Hematoxylin counterstain. (optional)
6. Dehydrate and clear.
7. Coverslip and store at RT.

5. Von Kossa Stain

Reagents:

1. 5% Silver Nitrate Solution (Stable for 1 year).
    a. Silver nitrate 25 g Sigma #S8157
    b. dH2O 500 mL

    Mix well and pour into clean brown bottle and store in refrigerator at 4°C.

2. 5% Sodium Thiosulfate (Make fresh)
    a. Sodium Thiosulfate 5 g Sigma #S7026
    b. dH2O 100 mL

3. Nuclear Fast Red (Kemechtrot) Solution
    a. Nuclear fast red 0.1 g Sigma #229113
    b. Aluminum sulfate 5 g Sigma #368458
    c. dH2O 100 mL
    d. Thymol 1 grain Sigam #T0501

    Dissolve aluminum sulfate in water. Add nuclear fast red and slowly heat to boil and cool. Filter and add a grain of thymol as a preservative.

Procedure:

1. Deparaffinize slides and rehydrate in dH_2O at RT.
2. Wash slides in dH_2O 2x for 3 min each.
3. Incubate slides in 5% silver nitrate solution placed under bright sunlight or under a 60W lamp. Place foil or mirror behind the jar/tray to reflect the light. Leave for 1 hour or until calcium turns black. (For best results use UV lamp)
4. Wash 3x dH2O for 5 min at RT.
5. Wash 1x in 5% sodium thiosulfate for 5 min at RT.
6. Wash 1x in tap water, 1x in dH2O.
7. Incubate slides in Nuclear Fast Red for 5 min at RT.
8. Wash briefly in dH2O.
9. Dehydrate and clear.
10. Coverslip and store at RT.

6. Calcium Arsenazo Assay

Reagents:

1. PBS Sigma #P5368
2. Acetic acid 1N Sigma #242843
3. Calcium reagent (Arsenazo III) DCL#140-24(1L)
4. Calcium standard 1 mg/mL Sigma #05-1050

Procedure:

1. Wash samples 3X with calcium-free PBS. This can be purchased.
2. Remove samples from wells/plates and place in microcentrifuge tube with 500 µL of 1N acetic acid.
3. Vortex samples overnight in refrigerator.
4. If needed, spin samples down in small centrifuge on maximum speed for 8-10 minutes, and remove supernatant into fresh tubes.
5. Prepare standards (maximum 100 µg/mL, and 6 serial dilutions; in 1N acetic acid).
6. Pipette 25 µL of standards and samples in triplicate to a clear Costar 96-well plate.
7. Add 300 µL of reagent to each well (dilute samples if color change is more than maximum standard).
8. Incubate for 30 seconds at room temperature.
9. Read samples on plate reader at 650 nM (color is stable for 30 minutes).

NOTES:

- For cells in plates, put acid in plate overnight at 4C. Next day use cell scraper to scrape off the cells, and transfer cells and acid to microcentrifuge tubes. Vortex samples overnight in refrigerator.
- Store samples at -20C.
- According to the reagent manual, when using 20µL of sample and 2 mL of reagent (1/100 ratio), the assay is linear up to 200µg/mL. The linearity will depend on the ratio of sample/reagent used. When using the ratio above, the relationship is linear for < 20 µg/mL, but a quadratic equation fits the standards very well. A fourth order polynomial equation fits the standards almost perfectly.
- In the case of the ratio above, the saturation limit of the assay is ~175 µg/mL.
- To figure out the dilutions required for each group, you can compare color change in 1-2 samples from each group with the standards using n=1.

APPENDIX D

RAW DATA FOR PLOTS

The following tables list values used for plotting results of the Arsenazo Assay in figures 6-51 and 6-54

For Figure 6-51a

	Fresh Control	Normal Valve	Sine 5 dyn/cm^2	Sine 10 dyn/cm^2	Sine 25 dyn/cm^2
Sample 1	0.111	0.225	0.635	0.116	0.259
Sample 2	0.047	0.160	0.091	0.153	0.190
Sample 3	0.172	0.082	1.770	0.126	0.306
Sample 4	0.055	0.144	0.379	0.238	0.154
Sample 5	0.336	0.118	0.132	0.228	0.293
Sample 6	0.096	0.124	0.141	0.193	0.273
Sample 7	0.230	0.126	0.684	0.142	0.266
Sample 8	0.157	0.096	1.274	0.132	-
Sample 9	-	0.211	0.192	0.149	-
ave	0.150	0.134	0.588	0.164	0.249
sterror	0.034	0.015	0.195	0.015	0.021

For Figure 6-51b

	Fresh Control	Normal Valve	Sine 1x frequency	Sine 2x frequency	Sine 4x frequency
Sample 1	0.111	0.225	0.116	0.364	1.423
Sample 2	0.047	0.160	0.153	0.090	0.375
Sample 3	0.172	0.082	0.126	0.207	2.456
Sample 4	0.055	0.144	0.238	0.437	0.243
Sample 5	0.336	0.118	0.228	0.111	0.080
Sample 6	0.096	0.124	0.193	0.246	0.725
Sample 7	0.230	0.126	0.142	0.135	0.274
Sample 8	0.157	0.096	0.132	0.166	0.337
Sample 9	-	0.211	0.149	0.132	0.374
ave	0.150	0.134	0.164	0.210	0.698
sterror	0.034	0.015	0.015	0.040	0.256

For Figure 6-54

	Fresh Control	Normal Valve	Sine 1x frequency	Sine 2x frequency	Sine 4x frequency
Sample 1	0.111	0.225	0.214	0.744	0.523
Sample 2	0.047	0.160	0.402	0.433	0.431
Sample 3	0.172	0.082	0.269	0.255	0.479
Sample 4	0.055	0.144	0.241	0.351	0.737
Sample 5	0.336	0.118	0.162	0.404	0.963
Sample 6	0.096	0.124	0.410	0.554	0.654
Sample 7	0.230	0.126	0.189	0.525	1.033
Sample 8	0.157	0.096	0.334	0.444	0.704
Sample 9	-	0.211	0.579	1.014	1.340
ave	0.150	0.134	0.311	0.525	0.763
sterror	0.034	0.015	0.045	0.076	0.099

APPENDIX E

CONE-AND-PLATE BIOREACTOR USER MANUAL

authors: Philippe Sucosky philippe.sucosky@gmail.com
Adnan Elhammali adnan.elhammali@gmail.com
updated: 4/11/2008

revision author: Choon Hwai Yap
choonhwai@gmail.com
updated: 4/22/2011

I. SYSTEM DESCRIPTION

Ex vivo tissue studies require the maintenance of mechanical and biochemical environments close to physiologic conditions. The present cone-and-plate tissue culture system has been designed to expose tissue samples to well-defined shear stress conditions. The design consists of a servo motor coupled to a cone placed on top of a stationary dish. The motor is controlled by a servo drive programmed via a computer. Fluid flows within the gap between the cone and the plate. In the present design, the cone features an angle of 0.5° and is located 200 microns above the surface of the plate. This particular geometry allows for the production of a nearly-uniform shear stress environment in the flow, and more particularly at the surface of the plate. Since the shear stress levels is directly related to the cone angular velocity, desired temporal shear stress variations can be imposed by rotating the cone at specific angular velocity waveforms. The production of a desired angular velocity waveform can be monitored in real time via a digital/analog acquisition card interfacing between the computer and the servo motor.

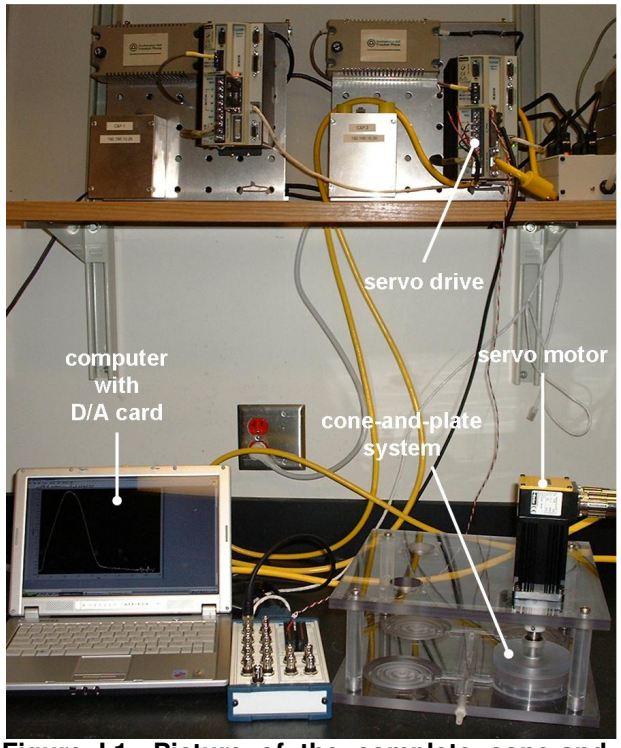

Figure I.1: Picture of the complete cone-and-plate tissue culture system.

Although similar devices have already been used extensively in biomedical research to subject cells to uniform shear stress environments, they have not been adapted to accommodate whole pieces of tissue. The present novel design, can accommodate circular tissue samples (7 mm diameter) flush mounted in the bottom plate to avoid any perturbation to the surrounding flow, and thus, to the uniformity of the surrounding shear stress environment. Nine equi-angularly spaced cylindrical wells are machined in the plate, each accommodating a sample holder. The tissue sample placed at the top of the holder is clamped in position by a plate cover such that the top surface of the sample coincides with that of the plate cover. The particular geometry of the plate cover exposes a circular sample region of 5 mm in diameter. The system can be used to expose various types of tissues to steady, pulsatile or oscillatory shear stress. A picture of the complete apparatus is shown in Figure I.1.

Cone assembly

As shown in Figure I.2, the cone assembly consists of a cone attached to a shaft. The cone is made of Delrin plastic while the shaft is made of stainless steel. The cone is coupled to the shaft via three screws. The cone features an angle of 0.5° and the conical surface

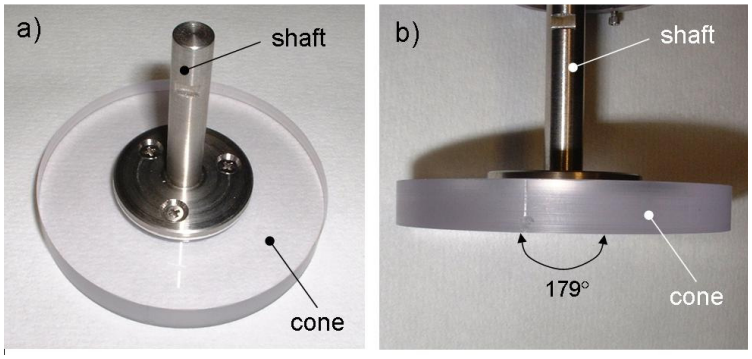

Figure I.2: Cone assembly: a) top view; and b) front view showing the nearly-flat angle of the cone.

is polished to ensure a maximum smoothness.

Plate

The plate (Figure I.3) is machined in a cylindrical rod of polycarbonate. Nine equi-angularly spaced cylindrical wells (7-mm diameter) are located at a radius r = 20 mm from the center. The internal and external lateral surfaces can be polished to enhance optical access, if needed. Each well can accommodate a tissue sample holder (see description below).

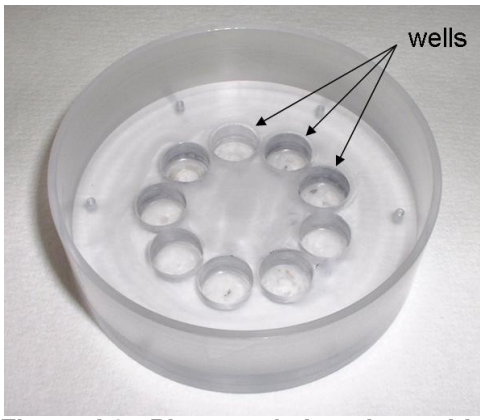

Figure I.3: Picture of the plate with the nine equi-angularly spaced cylindrical wells.

Plate cover

The function of the plate cover is two-fold: to expose a smooth flat piece of tissue to the flow, and to clamp the tissue samples in position on top of the holders. The plate cover is a thin circular plate of polycarbonate screwed on top of the tissue wells located in the plate. Nine equi-angularly spaced holes are machined in the plate cover, aligned with the wells of the plate. The holes are chamfered a an angle of 45° such that the hole diameter on the lower surface of the plate cover is equal to the diameter of the well machined in the plate, and the hole diameter on the upper surface of the plate cover is equal to the diameter of the circular surface at the top of the holder (i.e., 5 mm) (Figure I.4). The chamfered surface presses on the tissue sample to maintain it in position on top of the holder.

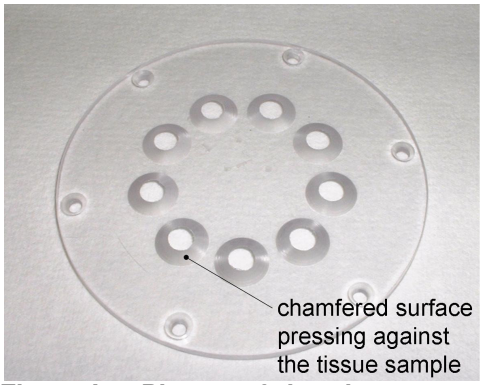

Figure I.4: Picture of the plate cover. The chamfered surface presses the tissue samples against the holders.

Agarose Bed Within Tissue Wells

The function of the agarose bed is to position the circular tissue samples at the center of the wells and to maintain them at a certain distance from the plate surface. 0.15% agarose was found to be well suited for this purpose. The agarose can be autoclaved to ensure sterility. Thereafter, they should be stored at 4 degrees refrigerator until use. Before insertion into the cone and plate, the bottle of agarose is first microwaved to liquefy the agarose for manipulation. To ensure the agarose bed had the suitable shape within the well, the plate cover is first coupled with the plate, such that the wells are empty spaces accessible through holes in the plate cover. 715 microliters of agarose is then pipetted into each well, and allowed to solidify. The plate cover is then removed, leaving the agarose in the required shape within the wells. However, care must be taken to minimize breakage of the agarose pieces during removal of the plate cover. To achieve this, a curved tweezer can be gently inserted between the plate cover and the agarose to loosen the contact before removing the plate cover. At this stage, however, the agarose has a meniscus to its top surface. 2 drops of agarose can be placed into this meniscus to flatten it after removing the place cover. Once the additional agarose solidifies, trimmed valve leaflets can be

Figure I.5: Plate, agaorose bed and cover assembly.

placed on the agarose, and the plate cover can be re-attached to the plate. Figure I.5 shows a picture of the plate, agarose bed and cover assembly.

Flange

The flange closes the system to ensure sterility and accommodates the two ball bearings driving the cone and shaft assembly in rotation. The lip machined on the edge ensures a correct centering of the flange with respect to the plate and the rest of the system. The flange is made of polycarbonate. A shaft collar placed on the cone shaft permits to adjust the vertical distance between the cone apex and the surface of the plate cover. The collar is maintained in position via a set screw. The first prototype is shown in Figure I.6a. A new flange has been designed. In this new design, nine holes are machined around the perimeter of the flange and intersect with a groove machined in the flat circular surface located at the bottom of the flange. The function of those channels is to ensure proper gas exchange by bringing air from the surroundings into the device. The axes of the holes machined on the perimeter of the flange are horizontal to prevent contamination (Figure I.6b).

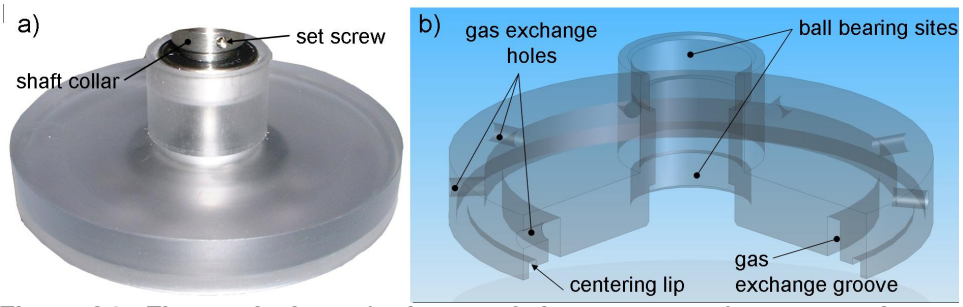

Figure I.6: Flange design: a) picture of the prototype (no gas exchange capability); and b) clipped CAD rendering of the newly designed flange (with gas exchange capability).

The Perfusion System

Since the cone and plate system has orifices to allow gas exchange, the small amount of media fluid within the bioreactor can easily dry out. To prevent this, a reservoir is attached to the system, allowing at least 50 ml of media to be stored, and a slow peristaltic pump (SP200FO, APT Instruments, Rochester, IL) is used to circulate the media into and out of the cone and plate system. Threaded luer lock fittings were installed on the plate portion of the bioreactor, and the reservoir, such that small diameter (1/8" ID) tygon® tubing (B-44-3, McMaster Carr, Atlanta, GA) can be used to connect the reservoir to the pump, from the pump to the plate portion of the bioreactor, and from the plate back to the reservoir (figure 1.7).

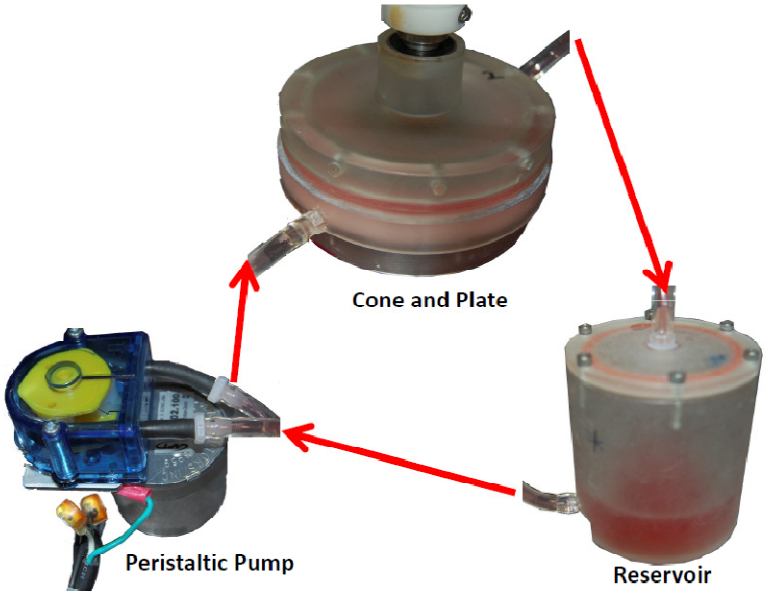

Figure I.7: Schematic of the perfusion system. The reservoir stores replenishment media to counter evaporation of media from the cone and plate. The slow perfusion system is driven by a commercial peristaltic pump. The flow is slow so as not to disturb the shear stress environment created by the cone and plate.

Suction table, suction lid, and motor table

A suction table has been designed to maintain the system in position while the cone is rotating. The table is made of polycarbonate and can accommodate four cone-and-plate systems. Four sets of concentric suction channels are machined in the table. Those channels are connected by two transversal channels and a central channel with inlet located at the front of the suction table. Four polycarbonate rods are screwed in at the corners of the suction table to support the motor table (Figure I.8). The diameter of the rods (19 mm) is large enough to stabilize the entire assembly even in presence of the inherent vibrations produced by the servo motor. Figure I.9 shows the different elements assembled and mounted on the motor and suction tables.

Driving system

The driving system used to rotate the cone at desired angular velocity waveforms consists of a rotary servo motor and a servo drive/controller. The single-axis controller/drive used in the present setup (Figure I.10) offers complex program and I/O capabilities. The servo drive/controller powered by a DC power block can be programmed using a commercial software package supplied with the product.

The rotary servo motor chosen in the current setup was dimensioned to provide the necessary torque and velocity to subject the tissue samples to a maximum shear stress of 100 dyn/cm^2.

Monitoring system

The monitoring system is capable of displaying in real time the actual angular velocity of the cone. An analog/digital acquisition card converts the analog velocity output provided by the motor feedback into a digital signal that can be visualized on a computer.

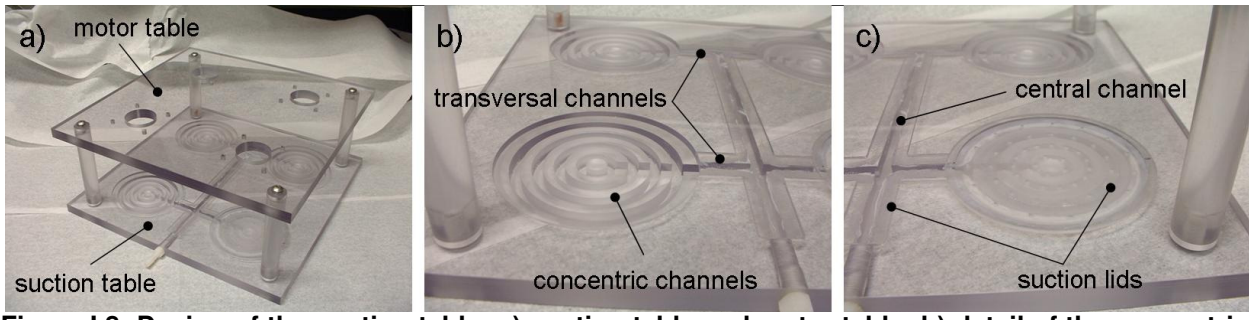

Figure I.8: Design of the suction table: a) suction table and motor table; b) detail of the concentric channels; and c) suction lids covering the suction channels.

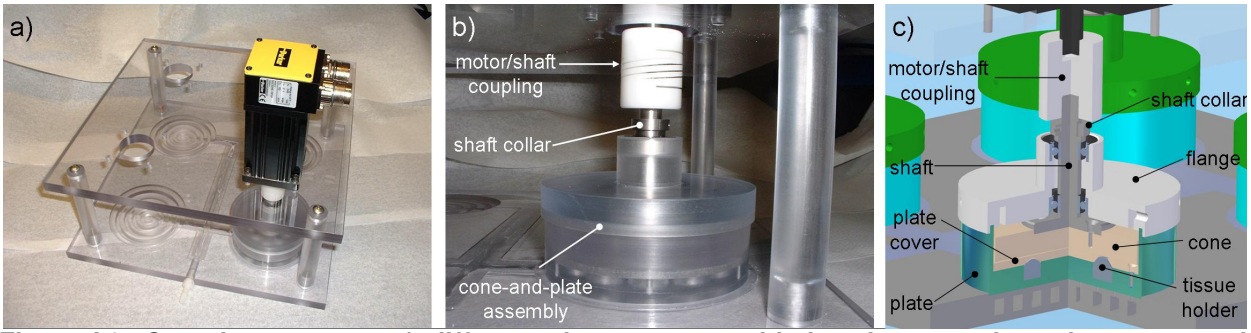

Figure I.9: Complete system: a) different elements assembled and mounted on the motor and suction tables; b) details of the cone-and-plate assembly mounted on the suction lid; and c) clipped CAD rendering of the whole assembly.

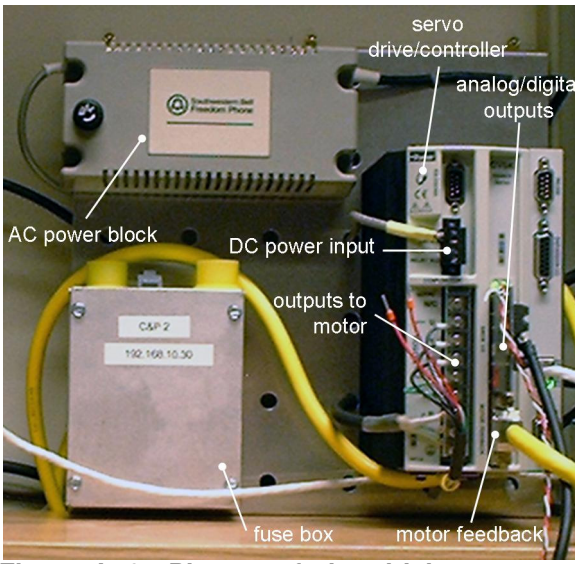

Figure I.10: Picture of the driving system setup.

II. Parker Servo Drive Programming, Feedback Monitoring, and Tuning

Programming the Servo Drive

We use the compiled waveform method to program all of our shear stress waveforms. This involves the sectioning off of the waveform into hundreds of small segments. For each segment, the velocity and the distance traversed under that velocity are programmed into the drive. A second program will then need to be created to compile the first program and then loop it:

Program 1:

```
del name  ---> This deletes anything stored under this program name.
def name  ---> This assigns the program the new name
mc01
A400      ---> Defines acceleration at which motor switches between
velocities
V0.82133  ---> Velocity in RPS
D28       ---> Distance traversed at this velocity (note: 4000 units per
rotation,
               double check that this is the setting for your specific
motor)
GOBUF1    ---> Command to complete segment
V2.0095   ---> Start of a new segment
D69
GOBUF1
V4.9618
D171
GOBUF1
V6.4744
D223
GOBUF1
end
```

notes: The distance D has to be a whole number. To rotate in the opposite direction,enter a negative distance. Once max desired velocity is reached, you will need to enter a deceleration command (ad instead of A as we did in line 4) right after the last GOBUF1 command of the accelerating segment and before inserting the new decelerating segments. This must be done every time the acceleration changes from positive to negative or vice versa.

Program 2:

```
del rname
DEF rname

PCOMP name  ---> compiles the segments of program “name”
L0          ---> begin loop
PRUN tauh   ---> run program
T0.31       ---> inserts a time delay of .31 seconds. Insert delay as
needed.
LN          ---> defines the infinite loop
END
```

Write these programs in the program editor and download to the servo drive. Once downloaded, you will only need to run the second program (type rname in the terminal). You will need to read the manual or contact tech support to learn the basic operations of the servo drive and motor (how to turn on and off and how to activate the motor).

Analog Monitoring

To monitor the waveform in real time, you will need to connect two sets of cables to the Data acquisition card. The analog cable which will output a voltage is connected from pin 21 and 25 (ground). Refer to page 75 of the hardware installation manual for a schematic. The digital output will be used as a trigger. This trigger will be programmed to function when the motor stops and starts running. Refer to page 73 of the Hardware installation guide for a schematic of the digital outputs.

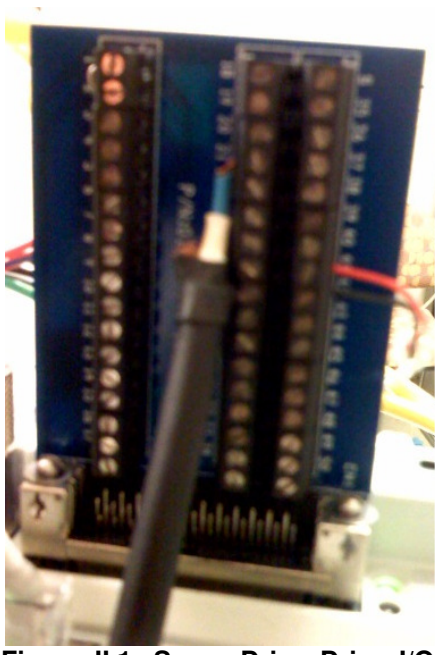

Figure II.1: Servo Drive Drive I/O connections

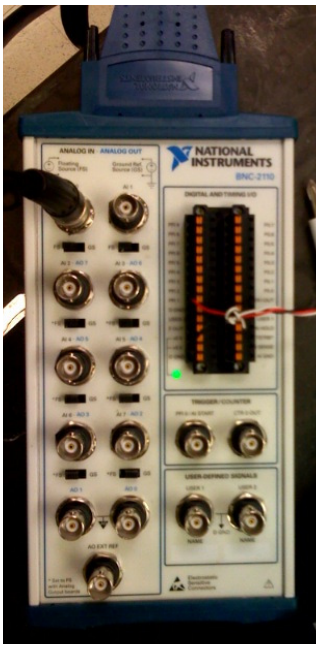

Figure II.2: DAQ BNC block

Analog outputs

There are a few commands to activate the analog output. Analog output A is on pin 21 and analog output B is on pin 22. They both do the same thing. Ground is on pin 25. A cable should connect these pins to the Analog In connections on the DAQ card (Figures 1 and 2).

The commands are:

DMONAV 5 – programs output A to velocity.

DMONBV 5- same as above but for output B

DMONAS- scaling factor 2000 corresponds to 1rps=.975V; 1000 corresponds to 1rps=.487V

- Determining the scaling is a bit tricky since it is drive specific. The easiest thing to do is run the motor at 1 rps and connect the probes of a voltage meter directly to pins 21 and 25 and measure the voltage. Alter the ratio of voltage/velocity with the DMONAS command. Remember, your max and min voltage has to be within -10 to +10 so scale in a manner such that you're max and min velocities are included.

DMONAV 24- This command will allow you to test if the outputs are functioning properly. Enter this command and rotate the shaft with your hand. You should notice voltage fluctuation on the instrument being used to measure (make sure you enter the drive0 command to deactivate the drive otherwise the shaft won't turn)

DMONBV 24- same as above but for output B.

Now you should have your analog outputs activated and should know the ratio of velocity to output voltage.

Digital outputs

You will need to connect two cables from pin 41 and 42 of the servo drive to the digital and timing I/O connections of the DAQ BNC block (Figures II.1 and II.2). 42 is the ground. Once connected, use the following command:

outfnc1-B: the 1 corresponds to pin 41 and the B defines the motion trigger. This trigger is initiated when the motor starts moving after a halt. When reading the waveform in LabView, we can use this trigger such that collection of data will begin only when the motor starts moving. This is appropriate for our purposes because it guarantees that our data corresponds to the beginning of the waveform. You do not need the trigger for continuous waveforms that have no halts.

LabView

We are using LabView 8 to carry out feedback. Open LabView and in the "Getting Started" section choose "vi from template". Then under "DAQ", choose "Data Acquisition with NI-DAQ.mx".

Follow the given instructions. On the screen for Analog data acquisition, you will see the trigger tab by double clicking on the DAQ block. Set it to digital and choose the appropriate inputs from the card. Be sure to program the appropriate slope under "custom scaling" in the configuration window. The slope should have been determined when running the DMONAS command as described above. Finally, make sure the timing settings are set so as to read at least one period of the waveform.

When back on the DAQ block, right click on the data tab and choose "create" and "graph indicator". Then right click on the white region, choose "File I/O" under programming and then choose "write spreadsheet file". Drag and place this next to the graph indicator and connect the two. (Note: You may want to wait to add the spreadsheet writing function until you have properly configured the feedback mechanism and can clearly see the graph in LabView)

Now, when you open the graph indicator and hit the arrow tab, the waveform will be read and you will be prompted to save the information immediately (assuming you created the spreadsheet write function as described above). Once saved, you will have to rename the file with the .txt extension. You will be given a series of velocity measurements. The number of measurements given will correspond to the frequency chosen in the "timing section" when double clicking on the DAQ block.

Tuning

Tuning can be very tedious since it must be carried out manually. Once you obtain a set of data from LabView, plot in Excel and compare with the original programmed waveform. Make adjustments to the Program as necessary. It is very common for the output velocity to come out one or two units lower than programmed velocity. Keep in mind that when raising the velocity of a segment in the program, you must also increase the distance D for that segment by the appropriate distance. Not doing so will result in

the shortening of the period of the waveform (Increasing V but not D will decreased the time).

Servo Drive Codes

A batch file is required to activate the connection between the laptop and the servo-motor controllers (connected through the LAN cables) This batch file's contents are as follows:

Filename: 6KARP.bat

Contents:
arp -s 192.168.10.30 00-90-55-00-56-E6 192.168.10.31
arp -s 192.168.10.29 00-90-55-00-56-E7 192.168.10.31

Tips on how to start the system running

Connect the cone and plate apparatus to the servo motor, and plug in the peristaltic perfusion pump. Turn on the laptop, plug in the LAN cable (cross-over cable) between the laptop and the servo motor controller. Allow some time for the laptop to detect the connection. Run the batch file "6KARP.bat" described above, and then start the servo motor controller program, "Motion Planner, version 4.3". Change the IP address on the program as necessary, and then request the program connect with the controller. You can now upload / download shear stress waveforms through the laptop program. To run the waveforms, enter command: "drive1" to engage the motor, and then enter the command to run the waveform, which would be the name of the waveform file. Usually cyclic programs start with a "r". To stop the program, press Ctrl-K, and then enter command "drive0" to dis-engage the motor.

III. Parts List

1. Custom machined Cone and Plate apparatus (please see Appendix A for dimensions and screw sizes and please see above for assembly information):
    a. Delrin cone, cone shaft, and shaft collar, shaft collar screw.
    b. Cone flange
    c. Plate, plate cover, and plate cover screws
    d. Reservoir, reservoir cover, and reservoir cover screws
    e. Mounting table and associated screws
2. Servo motor for rotating cone: model SM232AE-NPSN, Parker Hann Corp, Rohnert Park, CA
3. Servo motor controller: GV6k Servo Motor, Parker Hann Corp, Rohnert Park, CA
4. Perfusion peristaltic pump: Model SP202.100 APT Instruments, Rochester, IL
5. Incubator: Model 3110 CO_2 water Jacketed Incubator, Forma Scientific, Marrietta, OH.
6. Laptop: Dell Inspiron 710m, Dell, Round rock, TX.

BIBLIOGRAPHY

1. Lindroos, M., et al., *Prevalence of aortic valve abnormalities in the elderly: an echocardiographic study of a random population sample.* J Am Coll Cardiol, 1993. **21**(5): p. 1220-5.

2. Lloyd-Jones, D., et al., *Heart disease and stroke statistics--2010 update: a report from the American Heart Association.* Circulation, 2010. **121**(7): p. e46-e215.

3. Balachandran, K., et al., *Elevated cyclic stretch alters matrix remodeling in aortic valve cusps: implications for degenerative aortic valve disease.* Am J Physiol Heart Circ Physiol, 2009. **296**(3): p. H756-64.

4. Butcher, J.T., et al., *Transcriptional profiles of valvular and vascular endothelial cells reveal phenotypic differences: influence of shear stress.* Arterioscler Thromb Vasc Biol, 2006. **26**(1): p. 69-77.

5. Sucosky, P., et al., *Altered shear stress stimulates upregulation of endothelial VCAM-1 and ICAM-1 in a BMP-4- and TGF-beta1-dependent pathway.* Arterioscler Thromb Vasc Biol, 2009. **29**(2): p. 254-60.

6. Xing, Y., et al., *Cyclic pressure affects the biological properties of porcine aortic valve leaflets in a magnitude and frequency dependent manner.* Ann Biomed Eng, 2004. **32**(11): p. 1461-70.

7. Smith, K.E., S.A. Metzler, and J.N. Warnock, *Cyclic strain inhibits acute pro-inflammatory gene expression in aortic valve interstitial cells.* Biomech Model Mechanobiol, 2010. **9**(1): p. 117-25.

8. Stevens, T., et al., *NHLBI workshop report: endothelial cell phenotypes in heart, lung, and blood diseases.* Am J Physiol Cell Physiol, 2001. **281**(5): p. C1422-33.

9. Topper, J.N. and M.A. Gimbrone, Jr., *Blood flow and vascular gene expression: fluid shear stress as a modulator of endothelial phenotype.* Mol Med Today, 1999. **5**(1): p. 40-6.

10. Roberts, W.C., *The congenitally bicuspid aortic valve. A study of 85 autopsy cases.* Am J Cardiol, 1970. **26**(1): p. 72-83.

11. Ward, C., *Clinical significance of the bicuspid aortic valve.* Heart, 2000. **83**(1): p. 81-85.

12. Beppu, S., et al., *Rapidity of progression of aortic stenosis in patients with congenital bicuspid aortic valves.* Am J Cardiol, 1993. **71**(4): p. 322-7.

13. Freeman, R.V. and C.M. Otto, *Spectrum of calcific aortic valve disease: pathogenesis, disease progression, and treatment strategies.* Circulation, 2005. **111**(24): p. 3316-26.

14. Barron, V., et al., *Bioreactors for cardiovascular cell and tissue growth: a review.* Ann Biomed Eng, 2003. **31**(9): p. 1017-30.

15. Balachandran, K., *Aortic Valve Mechanobiology - the Effect of Cyclic Stretch*, in *Biomedical Engineering*. 2010, Georgia Institute of Technology: Atlanta.

16. Swanson, M. and R.E. Clark, *Dimensions and geometric relationships of the human aortic valve as a function of pressure.* Circ Res, 1974. **35**(6): p. 871-82.

17. Swanson, W.M. and R.E. Clark, *Aortic valve leaflet motion during systole. Numerical-graphical determination.* Circ Res, 1973. **32**(1): p. 42-8.

18. Yap, C.H., et al., *Dynamic deformation characteristics of porcine aortic valve leaflet under normal and hypertensive conditions.* Am J Physiol Heart Circ Physiol, 2010. **298**(2): p. H395-405.

19. Vesely, I. and A. Lozon, *Natural preload of aortic valve leaflet components during glutaraldehyde fixation: effects on tissue mechanics.* J Biomech, 1993. **26**(2): p. 121-31.

20. Christie, G.W., *Anatomy of aortic heart valve leaflets: the influence of glutaraldehyde fixation on function.* Eur J Cardiothorac Surg, 1992. **6 Suppl 1**: p. S25-32; discussion S33.

21. Grande-Allen, K.J., et al., *Mechanisms of aortic valve incompetence: finite-element modeling of Marfan syndrome.* J Thorac Cardiovasc Surg, 2001. **122**(5): p. 946-54.

22. Grande-Allen, K.J., et al., *Glycosaminoglycan profiles of myxomatous mitral leaflets and chordae parallel the severity of mechanical alterations.* J Am Coll Cardiol, 2003. **42**(2): p. 271-7.

23. Grande-Allen, K.J., et al., *Glycosaminoglycan synthesis and structure as targets for the prevention of calcific aortic valve disease.* Cardiovasc Res, 2007. **76**(1): p. 19-28.

24. Thubrikar, M., *The Aortic Valve*. 1990, Boca Raton, Fla: CRC Press.

25. Sacks, M.S., D.B. Smith, and E.D. Hiester, *The aortic valve microstructure: effects of transvalvular pressure.* J Biomed Mater Res, 1998. **41**(1): p. 131-41.

26. Hilbert, S.L., et al., *Allograft heart valves: the role of apoptosis-mediated cell loss.* J Thorac Cardiovasc Surg, 1999. **117**(3): p. 454-62.

27. Schenke-Layland, K., et al., *Cardiomyopathy is associated with structural remodelling of heart valve extracellular matrix.* Eur Heart J, 2009. **30**(18): p. 2254-65.

28. Hatle, L. and B. Angelsen, *Doppler Ultrasound in Cardiology Physical Principals and Clinical Applications*. 1985, Philadelphia: Lea and Febiger.

29. Nandy, S. and J.M. Tarbell, *Flush mounted hot film anemometer measurement of wall shear stress distal to a tri-leaflet valve for Newtonian and non-Newtonian blood analog fluids.* Biorheology, 1987. **24**(5): p. 483-500.

30. Nerem, R.M. and W.A. Seed, *An in vivo study of aortic flow disturbances.* Cardiovasc Res, 1972. **6**(1): p. 1-14.

31. Bellhouse, B.J. and K.G. Reid, *Fluid mechanics of the aortic valve.* Br Heart J, 1969. **31**(3): p. 391.

32. Reul, H. and N. Talukdar, *Heart Valve Mechanics*, in *Quantitative Cardiovascular Studies Clinical and Research Applications of Engineering Principles.*, G.D.R. Hwang N. H. C., Patel D. J., Editor. 1979, University Park Press: Baltimore. p. 527-564.

33. Kvitting, J.P., et al., *Flow patterns in the aortic root and the aorta studied with time-resolved, 3-dimensional, phase-contrast magnetic resonance imaging: implications for aortic valve-sparing surgery.* J Thorac Cardiovasc Surg, 2004. **127**(6): p. 1602-7.

34. Markl, M., et al., *Time-resolved three-dimensional magnetic resonance velocity mapping of aortic flow in healthy volunteers and patients after valve-sparing aortic root replacement.* Journal of Thoracic and Cardiovascular Surgery, 2005. **130**(2): p. 456-463.

35. Leyh, R.G., et al., *Opening and closing characteristics of the aortic valve after different types of valve-preserving surgery.* Circulation, 1999. **100**(21): p. 2153-60.

36. Bellhouse, B.J., *Velocity and Pressure Distribution in the Aortic Valve.* Journal of Fluid Mechanics, 1969. **37**: p. 587-600.

37. Ling, S.C., et al., *Application of heated-film velocity and shear probes to hemodynamic studies.* Circ Res, 1968. **23**(6): p. 789-801.

38. Yoganathan, A.P., Y.-R. Woo, and H.-W. Sung, *Turbulent shear stress measurements in the vicinity of aortic heart valve prostheses.* Journal of Biomechanics, 1986. **19**(6): p. 433-442.

39. Lim, W.L., et al., *Pulsatile flow studies of a porcine bioprosthetic aortic valve in vitro: PIV measurements and shear-induced blood damage.* J Biomech, 2001. **34**(11): p. 1417-27.

40. brands, P.J., et al., *A noninvasive method to measure wall shear rate using ultrasound.* Ultrasound in Med. & Biol., 1995. **21**(2): p. 171-185.

41. Efstathopoulos, E.P., et al., *Wall shear stress calculation in ascending aorta using phase contrast magnetic resonance imaging. Investigating effective ways to calculate it in clinical practice.* Phys Med, 2008.

42. Weston, M.W., D.V. LaBorde, and A.P. Yoganathan, *Estimation of the shear stress on the surface of an aortic valve leaflet.* Ann Biomed Eng, 1999. **27**(4): p. 572-9.

43. Ge, L. and F. Sotiropoulos, *Direction and magnitude of blood flow shear stresses on the leaflets of aortic valves: is there a link with valve calcification?* J Biomech Eng, 2010. **132**(1): p. 014505.

44. Morsi, Y.S., et al., *Transient fluid-structure coupling for simulation of a trileaflet heart valve using weak coupling.* J Artif Organs, 2007. **10**(2): p. 96-103.

45. De Hart, J., et al., *A three-dimensional computational analysis of fluid-structure interaction in the aortic valve.* J Biomech, 2003. **36**(1): p. 103-12.

46. Weinberg, E.J., et al., *Hemodynamic environments from opposing sides of human aortic valve leaflets evoke distinct endothelial phenotypes in vitro.* Cardiovasc Eng, 2010. **10**(1): p. 5-11.

47. Weinberg, E.J. and M.R. Kaazempur Mofrad, *Transient, three-dimensional, multiscale simulations of the human aortic valve.* Cardiovasc Eng, 2007. **7**(4): p. 140-55.

48. Lo, D. and I. Vesely, *Biaxial strain analysis of the porcine aortic valve.* Ann Thorac Surg, 1995. **60**(2 Suppl): p. S374-8.

49. Vesely, I., *The role of elastin in aortic valve mechanics.* J Biomech, 1998. **31**(2): p. 115-23.

50. Billiar, K.L. and M.S. Sacks, *Biaxial mechanical properties of the natural and glutaraldehyde treated aortic valve cusp--Part I: Experimental results.* J Biomech Eng, 2000. **122**(1): p. 23-30.

51. Stella, J.A., J. Liao, and M.S. Sacks, *Time-dependent biaxial mechanical behavior of the aortic heart valve leaflet.* J Biomech, 2007. **40**(14): p. 3169-77.

52. Doehring, T.C., E.O. Carew, and I. Vesely, *The effect of strain rate on the viscoelastic response of aortic valve tissue: a direct-fit approach.* Ann Biomed Eng, 2004. **32**(2): p. 223-32.

53. Dagum, P., et al., *Deformational dynamics of the aortic root: modes and physiologic determinants.* Circulation, 1999. **100**(19 Suppl): p. II54-62.

54. Kershaw, J.D., et al., *Specific regional and directional contractile responses of aortic cusp tissue.* J Heart Valve Dis, 2004. **13**(5): p. 798-803.

55. El-Hamamsy, I., et al., *Endothelium-dependent regulation of the mechanical properties of aortic valve cusps.* J Am Coll Cardiol, 2009. **53**(16): p. 1448-55.

56. Merryman, W.D., et al., *The effects of cellular contraction on aortic valve leaflet flexural stiffness.* J Biomech, 2006. **39**(1): p. 88-96.

57. Goldbarg, S.H., et al., *Insights into degenerative aortic valve disease.* J Am Coll Cardiol, 2007. **50**(13): p. 1205-13.

58. Stephan, P.J., et al., *Comparison of age, gender, number of aortic valve cusps, concomitant coronary artery bypass grafting, and magnitude of left ventricular-systemic arterial peak systolic gradient in adults having aortic valve replacement for isolated aortic valve stenosis.* Am J Cardiol, 1997. **79**(2): p. 166-72.

59. Yacoub, M.H. and J.J. Takkenberg, *Will heart valve tissue engineering change the world?* Nat Clin Pract Cardiovasc Med, 2005. **2**(2): p. 60-1.

60. Otto, C.M., et al., *Association of aortic-valve sclerosis with cardiovascular mortality and morbidity in the elderly.* N Engl J Med, 1999. **341**(3): p. 142-7.

61. Pai, R.G., *Degenerative valve disease.* J Am Coll Cardiol, 2006. **48**(12): p. 2601; author reply 2602.

62. Kim, K.M., et al., *Aging changes in the human aortic valve in relation to dystrophic calcification.* Human Pathology, 1976. **7**(1): p. 47-60.

63. Stewart, B.F., et al., *Clinical factors associated with calcific aortic valve disease. Cardiovascular Health Study.* J Am Coll Cardiol, 1997. **29**(3): p. 630-4.

64. Agmon, Y., et al., *Aortic valve sclerosis and aortic atherosclerosis: different manifestations of the same disease? Insights from a population-based study.* J Am Coll Cardiol, 2001. **38**(3): p. 827-34.

65. Sabet, H.Y., et al., *Congenitally bicuspid aortic valves: a surgical pathology study of 542 cases (1991 through 1996) and a literature review of 2,715 additional cases.* Mayo Clin Proc, 1999. **74**(1): p. 14-26.

66. Sievers, H.H. and C. Schmidtke, *A classification system for the bicuspid aortic valve from 304 surgical specimens.* J Thorac Cardiovasc Surg, 2007. **133**(5): p. 1226-33.

67. Espinola-Zavaleta, N., et al., *Anatomic three-dimensional echocardiographic correlation of bicuspid aortic valve.* J Am Soc Echocardiogr, 2003. **16**(1): p. 46-53.

68. Braverman, A.C., et al., *The bicuspid aortic valve.* Curr Probl Cardiol, 2005. **30**(9): p. 470-522.

69. den Reijer, P.M., et al., *Hemodynamic predictors of aortic dilatation in bicuspid aortic valve by velocity-encoded cardiovascular magnetic resonance.* J Cardiovasc Magn Reson, 2010. **12**: p. 4.

70. Brown, C., D.C. Sane, and D.W. Kitzman, *Bicuspid aortic valves in monozygotic twins.* Echocardiography, 2003. **20**(2): p. 183-4.

71. Clementi, M., et al., *Familial congenital bicuspid aortic valve: a disorder of uncertain inheritance.* Am J Med Genet, 1996. **62**(4): p. 336-8.

72. Kappetein, A.P., et al., *The neural crest as a possible pathogenetic factor in coarctation of the aorta and bicuspid aortic valve.* J Thorac Cardiovasc Surg, 1991. **102**(6): p. 830-6.

73. Fedak, P.W., et al., *Clinical and pathophysiological implications of a bicuspid aortic valve.* Circulation, 2002. **106**(8): p. 900-4.

74. Lee, T.C., et al., *Abnormal aortic valve development in mice lacking endothelial nitric oxide synthase.* Circulation, 2000. **101**(20): p. 2345-8.

75. Garg, V., et al., *Mutations in NOTCH1 cause aortic valve disease.* Nature, 2005. **437**(7056): p. 270-274.

76. Robicsek, F., et al., *The congenitally bicuspid aortic valve: how does it function? Why does it fail?* Ann Thorac Surg, 2004. **77**(1): p. 177-85.

77. Wallby, L., et al., *T lymphocyte infiltration in non-rheumatic aortic stenosis: a comparative descriptive study between tricuspid and bicuspid aortic valves.* Heart, 2002. **88**(4): p. 348-351.

78. Tutarel, O. and M. Westhoff-Bleck, *Bicuspid aortic valves and dilatation of the ascending aorta.* Ann Thorac Surg, 2005. **80**(4): p. 1562; author reply 1562-3.

79. Yasuda, H., et al., *Failure to prevent progressive dilation of ascending aorta by aortic valve replacement in patients with bicuspid aortic valve: comparison with tricuspid aortic valve.* Circulation, 2003. **108 Suppl 1**: p. II291-4.

80. Ge, L., et al., *Characterization of hemodynamic forces induced by mechanical heart valves: Reynolds vs. viscous stresses.* Ann Biomed Eng, 2008. **36**(2): p. 276-97.

81. Dasi, L.P., et al., *Vorticity dynamics of a bileaflet mechanical heart valve in an axisymmetric aorta.* Physics of Fluids, 2007. **19**(6): p. -.

82. Simon, H.A., et al., *Spatio-temporal flow analysis in bileaflet heart valve hinge regions: potential analysis for blood element damage.* Ann Biomed Eng, 2007. **35**(8): p. 1333-46.

83. Simon, H.A., et al., *Simulation of the three-dimensional hinge flow fields of a bileaflet mechanical heart valve under aortic conditions.* Ann Biomed Eng, 2010. **38**(3): p. 841-53.

84. Cannegieter, S.C., F.R. Rosendaal, and E. Briet, *Thromboembolic and bleeding complications in patients with mechanical heart valve prostheses.* Circulation, 1994. **89**(2): p. 635-41.

85. Yoganathan, A.P. and B. Travis, *Fluid Dynamics of Prosthetic Valves*, in *The Practice of Clinical Echocardiography*, C.M. Otto, Editor. 2008, W.B. Saunders Company: Philadelphia. p. 552-576.

86. Xing, Y., et al., *Effects of constant static pressure on the biological properties of porcine aortic valve leaflets.* Ann Biomed Eng, 2004. **32**(4): p. 555-62.

87. Platt, M.O., et al., *Cyclic pressure and shear stress regulate matrix metalloproteinases and cathepsin activity in porcine aortic valves.* J Heart Valve Dis, 2006. **15**(5): p. 622-9.

88. Balachandran, K., et al., *An ex vivo study of the biological properties of porcine aortic valves in response to circumferential cyclic stretch.* Ann Biomed Eng, 2006. **34**(11): p. 1655-65.

89. Balachandran, K., et al., *Elevated cyclic stretch induces aortic valve calcification in a bone morphogenic protein-dependent manner.* Am J Pathol, 2010. **177**(1): p. 49-57.

90. Butcher, J.T. and R.M. Nerem, *Valvular endothelial cells regulate the phenotype of interstitial cells in co-culture: effects of steady shear stress.* Tissue Eng, 2006. **12**(4): p. 905-15.

91. Metzler, S.A., et al., *Cyclic strain regulates pro-inflammatory protein expression in porcine aortic valve endothelial cells.* J Heart Valve Dis, 2008. **17**(5): p. 571-7; discussion 578.

92. Otto, C.M., et al., *Characterization of the early lesion of 'degenerative' valvular aortic stenosis. Histological and immunohistochemical studies.* Circulation, 1994. **90**(2): p. 844-53.

93. Warnock, J.N., et al., *Differential immediate-early gene responses to elevated pressure in porcine aortic valve interstitial cells.* J Heart Valve Dis, 2006. **15**(1): p. 34-41; discussion 42.

94. Merryman, W.D., et al., *Synergistic effects of cyclic tension and transforming growth factor-beta1 on the aortic valve myofibroblast.* Cardiovasc Pathol, 2007. **16**(5): p. 268-76.

95. Kaden, J.J., et al., *Inflammatory regulation of extracellular matrix remodeling in calcific aortic valve stenosis.* Cardiovascular Pathology. **14**(2): p. 80-87.

96. Butcher, J.T., C.A. Simmons, and J.N. Warnock, *Mechanobiology of the aortic heart valve.* J Heart Valve Dis, 2008. **17**(1): p. 62-73.

97. Rabkin, S.W., *The association of hypertension and aortic valve sclerosis.* Blood Press, 2005. **14**(5): p. 264-72.

98. Simmons, C.A., et al., *Spatial heterogeneity of endothelial phenotypes correlates with side-specific vulnerability to calcification in normal porcine aortic valves.* Circ Res, 2005. **96**(7): p. 792-9.

99. Konduri, S., et al., *Normal physiological conditions maintain the biological characteristics of porcine aortic heart valves: an ex vivo organ culture study.* Ann Biomed Eng, 2005. **33**(9): p. 1158-66.

100. Sucosky, P., et al., *Design of an ex vivo culture system to investigate the effects of shear stress on cardiovascular tissue.* J Biomech Eng, 2008. **130**(3): p. 035001.

101. Leo, H.L., *An In Vitro Investigation of the Flow Fields Through Bileaflet and Polymeric Prosthetic Heart Valves*, in *Biomedical Engineering*. 2005, Georgia Institute of Technology: Atlanta.

102. Weston, M.W. and A.P. Yoganathan, *Biosynthetic activity in heart valve leaflets in response to in vitro flow environments.* Ann Biomed Eng, 2001. **29**(9): p. 752-63.

103. Leo, H.L., et al., *A comparison of flow field structures of two tri-leaflet polymeric heart valves.* Ann Biomed Eng, 2005. **33**(4): p. 429-43.

104. Leo, H.L., et al., *Fluid dynamic assessment of three polymeric heart valves using particle image velocimetry.* Ann Biomed Eng, 2006. **34**(6): p. 936-52.

105. Yap, C.H., L.P. Dasi, and A.P. Yoganathan, *Dynamic hemodynamic energy loss in normal and stenosed aortic valves.* J Biomech Eng, 2010. **132**(2): p. 021005.

106. Cui, W., et al., *Systolic and diastolic time intervals measured from Doppler tissue imaging: normal values and Z-score tables, and effects of age, heart rate, and body surface area.* J Am Soc Echocardiogr, 2008. **21**(4): p. 361-70.

107. White, F.M., *Viscous fluid flow*. 3rd ed. McGraw-Hill series in mechanical engineering. 2006, New York, NY: McGraw-Hill Higher Education. xxi, 629 p.

108. Pope, S.B., *Turbulent flows*. 2000, Cambridge ; New York: Cambridge University Press. xxxiv, 771 p.

109. Adrian, R.J. and C.S. Yao, *Power spectra of fluid velocities measured by laser Doppler velocimetry.* Experiments in Fluids, 1986. **5**(1): p. 17-28.

110. Moreau, S., et al., *Estimation of power spectral density from laser Doppler data via linear interpolation and deconvolution.* Experiments in Fluids, 2011. **50**(1): p. 179-188.

111. Womersley, J.R., *Method for the calculation of velocity, rate of flow and viscous drag in arteries when the pressure gradient is known.* J Physiol, 1955. **127**(3): p. 553-63.

112. Powell, A.J., et al., *Phase-velocity cine magnetic resonance imaging measurement of pulsatile blood flow in children and young adults: in vitro and in vivo validation.* Pediatr Cardiol, 2000. **21**(2): p. 104-10.

113. Langerak, S.E., et al., *Improved MR flow mapping in coronary artery bypass grafts during adenosine-induced stress.* Radiology, 2001. **218**(2): p. 540-7.

114. Roman, M.J., et al., *Two-dimensional echocardiographic aortic root dimensions in normal children and adults.* Am J Cardiol, 1989. **64**(8): p. 507-12.

115. Stein, P.D. and H.N. Sabbah, *Turbulent blood flow in the ascending aorta of humans with normal and diseased aortic valves.* Circ Res, 1976. **39**(1): p. 58-65.

116. Clark, C., *Turbulent velocity measurements in a model of aortic stenosis.* J Biomech, 1976. **9**(11): p. 677-87.

117. Durst, F., et al., *The development lengths of laminar pipe and channel flows.* Journal of Fluids Engineering-Transactions of the Asme, 2005. **127**(6): p. 1154-1160.

118. Joseph, D.D., *Helmholtz decomposition coupling rotational to irrotational flow of a viscous fluid.* Proc Natl Acad Sci U S A, 2006. **103**(39): p. 14272-7.

119. Donal, E., et al., *Planimetric assessment of anatomic valve area overestimates effective orifice area in bicuspid aortic stenosis.* J Am Soc Echocardiogr, 2005. **18**(12): p. 1392-8.

120. Bonow, R.O., et al., *ACC/AHA 2006 guidelines for the management of patients with valvular heart disease: a report of the American College of Cardiology/American Heart Association Task Force on Practice Guidelines (writing committee to revise the 1998 Guidelines for the Management of Patients With Valvular Heart Disease): developed in collaboration with the Society of Cardiovascular Anesthesiologists: endorsed by the Society for Cardiovascular Angiography and Interventions and the Society of Thoracic Surgeons.* Circulation, 2006. **114**(5): p. e84-231.

121. Peskin, C.S. and A.W. Wolfe, *The aortic sinus vortex.* Fed Proc, 1978. **37**(14): p. 2784-92.

122. Ming, L. and K. Zhen-huang, *Study of the closing mechanism of natural heart valves.* Applied Mathematics and Mechanics, 1986. **7**(10): p. 955-964.

123. Hale, J.F., D.D. Mc, and J.R. Womersley, *Velocity profiles of oscillating arterial flow, with some calculations of viscous drag and the Reynolds numbers.* J Physiol, 1955. **128**(3): p. 629-40.

124. Thubrikar, M., et al., *The design of the normal aortic valve.* Am J Physiol, 1981. **241**(6): p. H795-801.

125. Guerraty, M.A., et al., *Side-specific expression of activated leukocyte adhesion molecule (ALCAM; CD166) in pathosusceptible regions of swine aortic valve endothelium.* J Heart Valve Dis, 2011. **20**(2): p. 165-7.

126. Feindel, C.M. and T.E. David, *Aortic valve sparing operations: basic concepts.* Int J Cardiol, 2004. **97 Suppl 1**: p. 61-6.

127. Bao, X., C. Lu, and J.A. Frangos, *Temporal gradient in shear but not steady shear stress induces PDGF-A and MCP-1 expression in endothelial cells: role of NO, NF kappa B, and egr-1.* Arterioscler Thromb Vasc Biol, 1999. **19**(4): p. 996-1003.

128. Bao, X., C.B. Clark, and J.A. Frangos, *Temporal gradient in shear-induced signaling pathway: involvement of MAP kinase, c-fos, and connexin43.* Am J Physiol Heart Circ Physiol, 2000. **278**(5): p. H1598-605.

129. Davies, P.F., *Hemodynamic shear stress and the endothelium in cardiovascular pathophysiology.* Nat Clin Pract Cardiovasc Med, 2009. **6**(1): p. 16-26.

130. Zeng, Z., et al., *Macromolecular transport in heart valves. II. Theoretical models.* Am J Physiol Heart Circ Physiol, 2007. **292**(6): p. H2671-86.

131. Butcher, J.T., et al., *Unique morphology and focal adhesion development of valvular endothelial cells in static and fluid flow environments.* Arterioscler Thromb Vasc Biol, 2004. **24**(8): p. 1429-34.

132. Li, Y.S., J.H. Haga, and S. Chien, *Molecular basis of the effects of shear stress on vascular endothelial cells.* J Biomech, 2005. **38**(10): p. 1949-71.

133. Ku, D.N., et al., *Pulsatile flow and atherosclerosis in the human carotid bifurcation. Positive correlation between plaque location and low oscillating shear stress.* Arteriosclerosis, 1985. **5**(3): p. 293-302.

134. De Paulis, R., et al., *Aortic valve-sparing operations and aortic root replacement.* J Cardiovasc Med (Hagerstown), 2007. **8**(2): p. 97-101.

135. Chatzizisis, Y.S., et al., *Role of endothelial shear stress in the natural history of coronary atherosclerosis and vascular remodeling: molecular, cellular, and vascular behavior.* J Am Coll Cardiol, 2007. **49**(25): p. 2379-93.

136. Kannel, W.B., et al., *Heart rate and cardiovascular mortality: the Framingham Study.* Am Heart J, 1987. **113**(6): p. 1489-94.

137. Palatini, P., *Elevated heart rate as a predictor of increased cardiovascular morbidity.* J Hypertens Suppl, 1999. **17**(3): p. S3-10.

138. Matsumoto, Y., et al., *Regular exercise training prevents aortic valve disease in low-density lipoprotein-receptor-deficient mice.* Circulation, 2010. **121**(6): p. 759-67.

139. Pate, G.E., *Association between aortic stenosis and hypertension.* J Heart Valve Dis, 2002. **11**(5): p. 612-4.

140. McEniery, C.M., et al., *Increased stroke volume and aortic stiffness contribute to isolated systolic hypertension in young adults.* Hypertension, 2005. **46**(1): p. 221-6.

141. Levy, R.L., P.D. White, and et al., *Transient tachycardia; prognostic significance alone and in association with transient hypertension.* Med Press Egypt, 1946. **38**(6): p. 207-12.

142. Palatini, P., et al., *Relationship of tachycardia with high blood pressure and metabolic abnormalities: a study with mixture analysis in three populations.* Hypertension, 1997. **30**(5): p. 1267-73.

143. Garg, V., et al., *Mutations in NOTCH1 cause congenital and adult cardiac disease.* Circulation, 2005. **112**(17): p. U576-U576.

144. Nigam, V. and D. Srivastava, *Notch1 represses osteogenic pathways in aortic valve cells.* J Mol Cell Cardiol, 2009. **47**(6): p. 828-34.

145. Russo, C.F., et al., *Aortic complications after bicuspid aortic valve replacement: long-term results.* Ann Thorac Surg, 2002. **74**(5): p. S1773-6; discussion S1792-9.

146. Davies, P.F., et al., *Turbulent fluid shear stress induces vascular endothelial cell turnover in vitro.* Proc Natl Acad Sci U S A, 1986. **83**(7): p. 2114-7.

147. Vesely, I. and D. Boughner, *Analysis of the bending behaviour of porcine xenograft leaflets and of natural aortic valve material: bending stiffness, neutral axis and shear measurements.* J Biomech, 1989. **22**(6-7): p. 655-71.

148. Saito, M., et al., *Possible link between large artery stiffness and coronary flow velocity reserve.* Heart, 2008. **94**(6): p. e20.

149. Cerny, L. and W. Walawender, *The flow of a viscous liquid in a converging tube.* Bulletin of Mathematical Biology, 1966. **28**(1): p. 11-24.

150. Ren-jing, C. and Q. Chan, *Boundary layer development of pulsatile blood flow in a tapered vessel.* Applied Mathematics and Mechanics, 1993. **14**(4): p. 319-326.

151. Rao, A.R. and R. Devanathan, *Pulsatile flow in tubes of varying cross-sections.* Zeitschrift für Angewandte Mathematik und Physik (ZAMP), 1973. **24**(2): p. 203-213.